

DISS. ETH NO. 14855

FINITE AND INFINITE
HETEROGENEITIES
UNDER PURE AND SIMPLE SHEAR

A dissertation submitted to the
SWISS FEDERAL INSTITUTE OF TECHNOLOGY ZURICH

for the degree of
Doctor of Natural Sciences

presented by
DANIEL WALTER SCHMID
Dipl. Natw. ETH
born 22. December, 1973
citizen of Full-Reuenthal, Aargau

accepted on the recommendation of

Prof. Dr. J.-P. Burg	ETH Zürich	examiner
Dr. Yu. Yu. Podladchikov	ETH Zürich	co-examiner
Prof. Dr. H. Schmeling	Universität Frankfurt a. M.	co-examiner

2002

To my parents

TABLE OF CONTENTS

ZUSAMMENFASSUNG	5
ABSTRACT	7
CHAPTER 1: INTRODUCTION	9
METHODS	10
THESIS STRUCTURE	11
<i>Chapter 2 - Mantled porphyroclast gauges</i>	<i>11</i>
<i>Chapter 3 - Analytical solutions for deformable elliptical inclusions in general shear</i>	<i>11</i>
<i>Chapter 4 - Muskhelishvili's method applied to elliptical and lubricated circular inclusions in general shear: Solution implementation in MATLAB</i>	<i>12</i>
<i>Chapter 5 - Are isolated stable rigid clasts in shear zones equivalent to voids?</i>	<i>12</i>
<i>Chapter 6 - Folding of Finite Length Layers</i>	<i>12</i>
<i>Chapter 7 - Numerical Modeling of Single Layer Folding in General Shear</i>	<i>13</i>
<i>Chapter 8 - Multilayer Folding</i>	<i>13</i>
RELATED WORK	14
REFERENCES	14
CHAPTER 2: MANTLED PORPHYROCLAST GAUGES.....	15
ABSTRACT	15
INTRODUCTION	16
NUMERICAL METHOD AND SETUP	18
CIRCULAR INCLUSIONS	22
<i>Initial Stages</i>	<i>22</i>
<i>Effect of Finite Strain</i>	<i>32</i>
ELLIPTICAL INCLUSION	33
<i>Initial Stages</i>	<i>33</i>
<i>Finite Strain</i>	<i>40</i>
LUBRICATED INCLUSION ROTATION MAPS (LIRM)	41
<i>Introduction</i>	<i>41</i>
<i>Dependence of Attractor Lines on Lubricant Viscosity</i>	<i>45</i>
ATTRACTOR MAPS	47
APPLICATION OF ATTRACTOR MAP METHOD	51
<i>Viscosity Contrast and Productivity Estimation</i>	<i>51</i>
<i>Shear Strain Estimation</i>	<i>53</i>
LIMITATIONS OF THE ATTRACTOR MAP METHOD	55
CONCLUSIONS	56
ACKNOWLEDGMENTS	57
REFERENCES	57
APPENDIX - CHECKS VERSUS ANALYTICAL SOLUTIONS	59

CHAPTER 3: ANALYTICAL SOLUTIONS FOR DEFORMABLE ELLIPTICAL INCLUSIONS IN GENERAL SHEAR.....	61
SUMMARY	61
INTRODUCTION.....	62
<i>Overview Muskhelishvili Method</i>	62
<i>Geological Relevance</i>	63
<i>Numerical Code Benchmarking</i>	65
<i>Solution Implementation And Availability</i>	66
BRIEF REVIEW OF MUSKHELISHVILI’S METHOD.....	66
<i>Basic Set Of Equations</i>	67
<i>Far-Field Flow Expressions In Complex Potentials</i>	70
CIRCULAR INCLUSION	71
<i>Solution</i>	71
<i>Applications</i>	72
CIRCULAR INCLUSION WITH A RIM.....	78
<i>Solution</i>	78
<i>Applications</i>	80
ELLIPTICAL INCLUSION	86
<i>Conformal Transformations</i>	86
<i>Far-Field Flow Conditions</i>	88
<i>Solution</i>	89
<i>Basic Set Of Equations</i>	90
<i>Applications</i>	91
DISCUSSION AND CONCLUSION	104
ACKNOWLEDGEMENTS.....	105
REFERENCES.....	106
APPENDIX: COEFFICIENTS FOR CIRCULAR INCLUSION WITH RIM	108
<i>Q-Coefficients</i>	108
<i>K-Coefficients</i>	109
APPENDIX: PRESSURE FIELD COMPARISON IN Z AND ζ	110

CHAPTER 4: MUSKHELISHVILI’S METHOD APPLIED TO ELLIPTICAL AND LUBRICATED CIRCULAR INCLUSIONS IN GENERAL SHEAR: SOLUTION IMPLEMENTATION IN MATLAB..... 111

INTRODUCTION.....	111
MATLAB SCRIPTS	114
<i>CYL_P_INTERF.M</i>	115
<i>CYL_P_INTERF_MAX.M</i>	116
<i>CYL_P_MATRIX.M</i>	117
<i>CYL_W_RIM</i>	118
<i>ELL_DYNAMIX.M</i>	122
<i>ELL_P_INTERF.M</i>	124
<i>ELL_ROT_RATE.M</i>	125
<i>ZHOUK_DEMO.M</i>	126

CHAPTER 5: ARE ISOLATED STABLE RIGID CLASTS IN SHEAR ZONES EQUIVALENT TO VOIDS?..... 127

ABSTRACT	127
INTRODUCTION.....	128
IGNORING THE CLAST TO STUDY THE CLAST.....	131
ROTATION DIRECTION OF PERFECTLY BONDED INCLUSIONS.....	133

EQUIVALENT VOID CONJECTURE	137
VERIFICATION	137
CONCLUSIONS	139
ACKNOWLEDGMENTS.....	139
REFERENCES.....	140
APPENDIX – MATLAB SCRIPT SUPPLEMENT TO FIGURE 4	141

CHAPTER 6: FOLDING OF FINITE LENGTH LAYERS..... 143

ABSTRACT	143
INTRODUCTION.....	144
BASIC STATE ANALYSIS.....	146
<i>Solution with Muskhelishvili’s Method</i>	148
<i>Viscous Layer in Viscous Matrix</i>	149
<i>Power-Law Layer in Viscous Matrix</i>	152
<i>Elastic Layer in Viscous Matrix</i>	153
LINEAR STABILITY ANALYSIS.....	155
<i>Viscous Layer in Viscous Matrix</i>	155
<i>Elastic Layer in Viscous Matrix</i>	157
TABLE 1 - SUMMARY OF FOLDING MODES	163
TABLE 2 - USED SYMBOLS	164
DISCUSSION.....	165
<i>Viscous Layer in Viscous Matrix</i>	165
<i>Elastic Layer in Viscous Matrix</i>	175
CONCLUSIONS	181
ACKNOWLEDGEMENTS.....	182
REFERENCES.....	182
APPENDIX ALUMINIUM FOIL EXPERIMENTS	184

NUMERICAL MODELING OF SINGLE LAYER FOLDING IN GENERAL SHEAR 189

ABSTRACT	189
INTRODUCTION.....	190
MODEL DESCRIPTION	191
VISUALIZATION	194
<i>Material</i>	194
<i>Active Flow</i>	194
<i>Effective Strain Rate</i>	195
<i>Longitudinal Strain</i>	195
<i>Effective Stress</i>	196
<i>Pressure</i>	196
RESULTS	197
<i>Pure Shear</i>	198
<i>Combined Pure and Simple Shear</i>	200
DISCUSSION AND INTERPRETATION OF PURE SHEAR EXPERIMENTS	201
<i>Geometrical Evolution and Active Flow Field</i>	201
<i>Effective Shear Strain Rate and Longitudinal Strain</i>	203
<i>Effective Shear Stress and Pressure</i>	204
DISCUSSION AND INTERPRETATION OF GENERAL SHEAR EXPERIMENTS	206
<i>Geometrical Evolution and Active Flow Field</i>	206
<i>Effective Shear Strain Rate and Longitudinal Strain</i>	211
<i>Effective Shear Stress and Pressure</i>	211
CONCLUSIONS	211
REFERENCES.....	213

CHAPTER 8: MULTILAYER FOLDING.....	215
ABSTRACT	215
INTRODUCTION.....	216
METHODS	218
THICK PLATE LINEAR STABILITY ANALYSIS	220
NUMERICAL ANALYSIS OF FINITE AMPLITUDE MORPHOLOGY	226
<i>Case 1</i>	227
<i>Case 2</i>	228
<i>Case 3</i>	229
<i>Case 4</i>	230
<i>Case 5</i>	231
FOLD MORPHOLOGY TABLE.....	232
DISCUSSION AND CONCLUSIONS	233
REFERENCES.....	234
 ACKNOWLEDGEMENTS.....	 235
 CURRICULUM VITAE	 237

ZUSAMMENFASSUNG

Diese Doktorarbeit identifiziert und beantwortet grundlegende Fragen der Strukturgeologie, welche entweder nicht gestellt oder nicht befriedigend gelöst worden waren. Der Themenbereich umfasst eine grosse Bandbreite von Problemen, welche von Einzelpartikelrotation zur Mehrschichtfaltung reicht. Dies sind Themen der klassischen Strukturgeologie, und trotzdem sind Effekte erster Ordnung nicht berücksichtigt worden. Faltung ist ein Beispiel. Die existierenden Theorien nehmen an, dass die faltenden Schichten unendlich lang sind oder die Kompression direkt durch starre Wände als Randbedingung an den Schichtenden angesetzt wird. Beide Annahmen sind selten relevant für die Geologie und wir zeigen, dass das Schichtlänge zu –dicke Verhältnis, zum Beispiel einer Quarzvene, einen entscheidenden Einfluss auf den Faltungsprozess ausübt. Dies resultiert in drei neuen Faltungsmodi welche gewisse Widersprüche der klassischen Theorien erklären. Wir geben eine Erklärung für die beobachteten kleinen Wellenlänge zu Schichtdicke Verhältnisse, welche im Widerspruch zu der grossen Variabilität natürlicher Viskositätskontraste stehen.

Ein weiteres Beispiel für die adressierten grundlegenden Fragen ist das Verhalten von Partikeln in Scherzonen. Diese Partikel zeigen oft eine regelmässige Ausrichtung (SPO), welche mit den klassischen Theorien nicht erklärt werden kann. Häufig sind diese Partikel von einem Mantel umgeben, welcher oft studiert wurde, dessen Funktion jedoch auf die eines passiven Deformationsaufzeichnungsgerät reduziert wurde. Dies steht im klaren Widerspruch zu der beobachteten Lokalisierung der Deformation im Mantelmaterial, welche ein Indikator für die Schmierwirkung des Mantels ist. Durch die explizite Modellierung des Mantels als separates, weiches Material entwickeln wir eine analytische Theorie, welche den Charakter der SPO erklärt. In Kombination mit einer grossen Anzahl numerischer Experimente schaffen wir ein Werkzeug das uns erlaubt die Mantelmaterialproduktivität, den Mantel-Matrix Viskositätskontrast und den totalen Scherbetrag abzuschätzen, basierend auf einfachen geometrischen Parametern, welche entweder im Feld oder anhand von Dünnschliffen bestimmt werden kann.

Intuitiv ist es akzeptiert, dass Kombinationen von reiner und einfacher Scherung zu asymmetrischen Falten führen. Frühere Studien mit analogen Materialien, analytischen

Theorien und numerischen Modellen konnten jedoch den Bezug zwischen einfacher Scherung und Faltenasymmetrie nicht darlegen. Wir zeigen hier unter welchen Bedingungen einfache Scherung tatsächlich asymmetrische Falten verursacht und wie dieser Zusammenhang benutzt werden kann, um ein Werkzeug zu entwickeln, welches dazu dient den Scherbetrag anhand der Faltengeometrie abzuschätzen.

Die letzte Frage welche wir in dieser Arbeit ansprechen bezieht sich auf die Bildung von Knicken in gefalteten Mehrschichtsequenzen. Dieses Phänomen wird normalerweise mit anisotropen und/oder nichtlinearen Rheologien verknüpft. Wir können jedoch zeigen, dass einfache, Newtonische Mehrschichtlagen Knicke ausbilden können, wenn sie unter kombinierter einfacher und reiner Scherung deformiert werden und eine starre Basis vorhanden ist. Konsequenterweise muss die Interpretation von Faltungsmechanismen und -bedingungen diese Resultate berücksichtigen und entsprechend angepasst werden.

Das Hauptwerkzeug, welches in dieser Arbeit angewandt wird, sind die Konzepte der Kontinuumsmechanik. Wir benützen analytische, numerische und kombinierte Techniken, welche auf die spezifischen Probleme abgestimmt sind und die Vorteile der benutzen Methode berücksichtigen. Diese Methoden umfassen die analytischen Formulierungen dünner und dicker Platten, die komplexe Potentialmethode von Muskhelishvili, Finite Differenzen, Finite Elemente und Spektralmethoden.

ABSTRACT

This thesis identifies, and gives solutions to, unanswered first order questions in structural geology concerning a wide range of problems from isolated clast behavior to multilayer folding. These are classical themes of research in structural geology and elsewhere; however, some of the basic problem characteristics have not been adequately accounted for in previous works. Folding is such an example, because the theory of folding assumes infinitely long layers or rigid wall boundary conditions directly applied to the layer extremities. Both assumptions are rarely appropriate for geology, e.g., we show that the aspect ratio of an isolated layer, such as a quartz vein, is a principal controlling factor of the folding process. Our analysis discovers three new folding modes that explain inconsistencies that are intrinsic to the classical theories. In particular, we give an explanation for the natural preference of small wavelength to layer thickness ratios that is in disagreement with the wide range of natural viscosity contrasts.

Another example for the addressed fundamental questions is the behavior of clasts in shear zones. Such clasts often show a shape preferred orientation (SPO) that cannot be explained by classical theories. The mantle that often surrounds these clasts had been the focus of many studies, however, it has been regarded as a passive strain recorder. This is in contradiction to the strain localization that takes place in the mantle, which is an indicator for the lubricant rheology of the mantle material. By the explicit introduction of a weak mantle material we succeed in developing an analytical theory that explains the character of the observed SPO, and in combination with a vast number of numerical experiments we develop a tool for estimating mantle material productivity, mantle-matrix viscosity contrast, and shear strain based on simple geometrical parameters that can be measured in the field.

It is intuitively accepted that combinations of pure and simple shear lead to asymmetric folds. However, previous analogue, analytical, and numerical experiments failed to identify the relationship between fold asymmetry and simple shear. We show under which conditions the simple shear – asymmetry conjecture is justified and outline how it can be used to estimate shear strains from natural folds.

The final question that we address is the formation of kinks in folded multilayer stacks. While this phenomenon is generally attributed to anisotropic and/or non-linear rheologies, we show that simple Newtonian multilayer stacks, subjected to general shear, and close to a no-slip base can exhibit kinking as well, which changes the interpretation of natural multilayer folds.

The key tool used to answer each question posed is the concept of continuum mechanics. We employ analytical, numerical, and combined techniques tailored to the requirements of the specific problems in such a way as to acknowledge the limitations of each method. These methods include thin and thick plate formulations, Muskhelishvili's complex potential method, finite differences, finite elements, and spectral codes.

CHAPTER 1: INTRODUCTION

In a time where it is fashionable to employ black-box codes to solve seemingly complicated problems with even more complex rheologies this thesis focuses on classical themes of structural geology such as clasts and folds. Both subjects have been intensely studied; yet, there is a trail of first order questions that were either not asked previously or solved unsatisfactory. Folding is such an example. All theories assume that folds grow due to layer parallel compression in infinitely long layers or in finite length layers with the boundary conditions applied through rigid walls directly onto the layer extremities. While this is the case for engineering problems for which the (elastic) theories were originally developed (Euler, 1744), it has rarely relevance to geology where infinitely long layers are certainly not possible and usually no rigid walls are in the proximity. A classical field example of folds are quartz veins in slates (Sherwin and Chapple, 1968). Such veins are likely to have aspect ratios in the range of 500-1000 (Vermilye and Scholz, 1995) and are isolated in the surrounding slate and “feel” the far-field compressional flow only through the slate. The question arises if classical folding theories are applicable to such configurations.

To address this folding question we first investigated the elliptical clast/inclusion embedded in a matrix and subjected to far-field flow conditions. The mantle that often surrounds porphyroclasts had been profoundly studied mainly for kinematic reasons (e.g., Passchier and Trouw, 1996) but it had been considered as a passive marker despite the fact that it causes strain localization and is likely to be the weakest phase in the system. Related to this inappropriate resolution of the mantle material is the fact that classical theories for clast rotation (Ghosh and Ramberg, 1976) fail to explain the shape preferred orientation common in natural shear zones (e.g., ten Grotenhuis et al., 2002).

Another problem addressed in this thesis is the condition for the development of fold asymmetry. Intuitive argumentation identifies simple shear as the cause. However, most previous studies involving analogue, analytical, and numerical modeling do not attribute any influence of simple shear on the folding process. A related topic is kinking, which is frequently observed in multilayer stacks. It is commonly believed that material anisotropy and/or material non-linearity is required for kinking. Yet, a much simpler

case of multilayer folding, a stack of Newtonian layers in combined pure and simple shear with a base nearby, also results in kink fold morphologies.

METHODS

The key tool used to answer the raised first order questions is the concept of continuum mechanics with its different analytical and numerical implementations. Where possible we derived analytical solutions, based on the theories of thin and thick plates, and the complex potential method of Muskhelishvili (1953). The latter is a powerful method to obtain analytical solutions for the bi-harmonic equation in relatively complex two-dimensional domains. Where it was not possible to obtain analytical solutions we sought numerical ones. Two different methods were used: a mixed spectral/finite difference method and the finite element method (FEM). Both methods were developed specifically for this work. Most of the development was done in MATLAB and, where speed requirements made it necessary, in FORTRAN90/95. The spectral code allows incompressible Newtonian and power-law rheologies, the FEM implements Newtonian, power-law, elastic and visco-elastic (Maxwell) rheologies. The reason why two different codes were developed is because each has its advantages and therefore they are suitable for different kinds of problems. For example, multilayer folding, as it is presented in this thesis, is ideally solved with the spectral code. The spectral code is optimized to take advantage of the periodic nature of the problem and is capable of giving results quickly when the multilayer stack consists of many layers that are all perturbed with a random noise signal – a task that would result in supercomputer scale FEM models. On the other hand, the lubricated rigid clast in a shear zone is better solved with the FEM code. The complex geometry resulting from the tail formation with very narrow films of weak materials, the material parameter variations over eight orders of magnitudes, and the focus on pressure as a key parameter are much better handled by the FEM code. The combination of numerical codes and analytical solutions has the advantage that for simpler problems the numerical codes can be tested and tuned, which assures that the more complex problems, where no analytical solutions can be found, will be resolved properly.

THESIS STRUCTURE

CHAPTER 2 - MANTLED PORPHYROCLAST GAUGES

This chapter introduces the characteristics of clast behavior in general (i.e., combined pure and simple) shear. Employing the FEM code the influence of boundary conditions, non-linear rheologies, intermediate layers between clast and matrix, geometry, and finite strain on the kinematic and dynamic parameters is investigated. It is shown that lubricated clasts can rotate syn- as well as antithetically to the applied simple shear flow and it is found that they stabilize at positive inclinations to the shear plane. Systematic analysis of more than 8000 experiments is used to construct so called “attractor maps” that can be used to obtain estimates for mantle material productivity and viscosity contrast between mantle and matrix, based on simple geometrical parameters that can be determined in the field or on thin sections. It is also shown how shear strain estimates can be obtained from mantled clasts alone, in absence of better strain recorders.

CHAPTER 3 - ANALYTICAL SOLUTIONS FOR DEFORMABLE ELLIPTICAL INCLUSIONS IN GENERAL SHEAR

This chapter presents a collection of analytical solutions for deformable inclusions. The technique employed is the complex potential method of Muskhelishvili (1953). In contrast to previous work our solutions are valid for finite viscosity contrasts between clast and matrix, covering the entire range from voids to rigid clasts. In addition we provide the solution for the mantled circular clast. The chapter focus is on the use of the solutions for geological problems, such as overpressure generation due to clasts in shear zones. The solutions are also an excellent opportunity for two-dimensional numerical code benchmarking and testing, because the problem solved is truly two-dimensional, exhibits sharp gradients in material properties and solutions, and must be solved accurately on a variety of scales simultaneously.

CHAPTER 4 - MUSKHELISHVILI'S METHOD APPLIED TO ELLIPTICAL AND LUBRICATED CIRCULAR INCLUSIONS IN GENERAL SHEAR: SOLUTION IMPLEMENTATION IN MATLAB

This chapter demonstrates the ease with which the complex potential solutions given in Chapter 3 can be implemented in MATLAB. Having native support for complex numbers, MATLAB is an ideal tool for this. These scripts are online available and are meant to support teaching and research.

CHAPTER 5 - ARE ISOLATED STABLE RIGID CLASTS IN SHEAR ZONES EQUIVALENT TO VOIDS?

Combining field data, analogue modeling, and our analytical and numerical results, this chapter gives an analytical explanation for the observed shape preferred orientation of clasts in natural shear zones. We show that it is possible to reduce the mantled clast, or more general the lubricated clast, to an equivalent void. This equivalent void has the rotational character of a real void, but cannot change its shape, which is supported by the rigid clast. The resulting theoretical curve for clast stabilization shows that the stable inclination angle decreases with increasing aspect ratio. The curve agrees well with field data, in contrast to previous theoretical work.

CHAPTER 6 - FOLDING OF FINITE LENGTH LAYERS

We investigate the influence of the finiteness and aspect ratio of layers on folding mechanism. This analytical work is a synthesis of the classical thin-plate theory with the Muskhelishvili solutions presented in Chapter 3. We show that the aspect ratio of the layer has a first order influence on the folding process and discover three new folding modes. In the viscous(layer)-viscous(matrix) case the new folding mode gives an explanation for the long standing problem of the natural preference of small wavelength to thickness ratios (Sherwin and Chapple, 1968), which cannot be explained by classical folding theories. The new folding modes in the elastic-viscous case show a dependence of the elastic folding process on the applied far field strain rate, which is verified with analogue experiments. Our new theory determines the value of the layer parallel

compressive stress, which is a significant advance because this stress component is difficult to evaluate, as it is not constant throughout the folding process.

CHAPTER 7 - NUMERICAL MODELING OF SINGLE LAYER FOLDING IN GENERAL SHEAR

The parameters that cause fold asymmetry are disputed and, in particular, it is unclear if asymmetric folds can be used as indicators of the simple shear component of the general shear far-field flow. This situation is exacerbated by the lack of a complete dataset of kinematic and dynamic parameters throughout single layer fold development. Such a dataset is required in order to evaluate the applicability of the geometric and kinematic tools that are in use for fold characterization and process identification. We show that combinations of layer parallel pure and simple shear indeed lead to asymmetric fold development, which is, however, a passive process. The resulting fold geometries and vergence are correct recorders of the simple shear component and can be used in combination with the strain map developed by Schmalholz and Podladchikov (2001) to get estimates for competence contrast, bulk shortening, and total shear strain.

CHAPTER 8 - MULTILAYER FOLDING

The multilayer folding chapter is a combination of analytical thick-plate theory and spectral code experiments. The analytical part investigates folding in a simple multilayer stack under pure shear and identifies a new folding mode. The numerical experiments show the fold morphologies that result in Newtonian multilayers under pure and general shear as a function of the presence of a nearby no-slip base. The general shear experiments develop kinks if the no-slip base is relatively close. This is an important finding because the rheologies employed are neither anisotropic nor non-linear, which was previously thought to be the requirement for kinking. Consequently the folding mechanism and -condition interpretation must take this into account and be adjusted accordingly.

RELATED WORK

During my PhD time I also co-authored several papers, which are not part of the thesis as it is presented here. The references are:

- Y. Y. Podladchikov, S. M. Schmalholz and D.W. Schmid. Inverse Modelling of Sedimentary Basins. Proceedings of the ECMI 2000 Conference. Springer-Verlag. Series on “Mathematics in Industry”.
- S. M. Schmalholz, Y. Y. Podladchikov and D.W. Schmid. A spectral/finite-difference method for simulating large deformations of heterogeneous, viscoelastic materials. *Geophys. J. Int.* (2001) 145, 199–208.
- H.A. Paul, S.M. Bernasconi, D.W. Schmid, and J.A. McKenzie. Oxygen isotopic composition of the Mediterranean Sea since the Last Glacial Maximum: constraints from pore water analyses. *Earth and Planetary Science Letters*, 192(1): 1-14.

REFERENCES

- Euler, L., 1744. Methodus inveniendi lineas curvas maximi minimive proprietate gaudentes sive solutio problematis isoperimetrici latissimo sensu accepti. Marcum-Michaellem Bousquet & Socios., Lausanne & Genève.
- Ghosh, S.K. and Ramberg, H., 1976. Reorientation of Inclusions by Combination of Pure Shear and Simple Shear. *Tectonophysics*, 34(1-2): 1-70.
- Muskhelishvili, N.I., 1953. Some basic problems of the mathematical theory of elasticity. Noordhoff Groningen, 704 pp.
- Passchier, C.W. and Trouw, R.A.J., 1996. *Microtectonics*. Springer, Berlin [etc.], 289 pp.
- Schmalholz, S.M. and Podladchikov, Y.Y., 2001. Strain and competence contrast estimation from fold shape. *Tectonophysics*, 340(3-4): 195-213.
- Sherwin, J.A. and Chapple, W.M., 1968. Wavelengths of Single Layer Folds - a Comparison between Theory and Observation. *American Journal of Science*, 266(3): 167-179.
- ten Grotenhuis, S.M., Passchier, C.W. and Bons, P.D., 2002. The influence of strain localisation on the rotation behaviour of rigid objects in experimental shear zones. *Journal of Structural Geology*, 24(3): 485-499.
- Vermilye, J.M. and Scholz, C.H., 1995. Relation between Vein Length and Aperture. *Journal of Structural Geology*, 17(3): 423-434.

CHAPTER 2: MANTLED PORPHYROCLAST GAUGES

(This chapter is submitted to “Journal of Structural Geology” by Daniel W. Schmid and Yuri Yu. Podladchikov. It is meant to be published together with the manuscript "Analogue modelling of the influence of aspect ratio and particle/matrix interface slip on the rotational behaviour of monoclinic and elliptical rigid particles in non-coaxial flow" by Stefano Ceriani, Neil Mancktelow and Giorgio Pennacchioni.)

ABSTRACT

We investigate the behavior of the isolated mantled porphyroclast in a shear zone. The method employed is a Finite Element Model. Three distinct phases, clast, mantle and matrix are present, the rheologies are power-law with exponents ranging from 1 to 5 and the far-field boundary condition is simple shear. The effective viscosity of the mantle is assumed to be less than those of the clast and the matrix. We show for which sets of parameters mantled porphyroclasts reach super-horizontal stabilization, relative to the shear plane and sense. Clasts in natural mylonites frequently exhibit similar orientation, which is interpreted as a stable inclination. The systematic examination of the matrix/mantle/clast system allows for the construction of attractor maps that can be directly used as gauges for (i) the effective viscosity contrast between matrix and mantle, (ii) the productivity of mantle material around the clast as a function of the bulk shear strain, and (iii) for the total shear strain. The necessary data required to use the attractor maps are simple geometrical parameters that can be measured in the field, clast aspect ratio, clast inclination versus the shear plane, mantle thickness, and mantle and clast area. This new method successfully reproduces the characteristics of natural porphyroclast and is in good agreement with data from natural shear zones.

Keywords:

Rotating clasts, Stabilization, Back-Rotation, Lubrication, Numerical Modeling, Rheology, Mantle Productivity, Shear Strain Estimation

INTRODUCTION

The frequent observation of mantled porphyroclasts in mylonitic shear zones together with their distinct geometries has stimulated a major quest to find possible applications as gauges capable of providing quantitative data on the rheology, kinematics and dynamics. While there appears to be common agreement on the usefulness of mantled porphyroclasts as indicators of shear sense (e.g., Hanmer and Passchier, 1991), all other possible interpretations as natural microgauges are still disputed. In particular, it is unclear if mantled porphyroclasts record information on the vorticity of the bulk flow and, more importantly, if they are reliable measures of rheology (Passchier et al., 1993; Bons et al., 1997; Pennacchioni et al., 2000). It was also seen that mantled porphyroclasts may actually rotate in opposite directions to the applied shear sense (Ghosh and Ramberg, 1976; Marques and Coelho, 2001; Pennacchioni et al., 2001; Mancktelow et al., 2002) and the parameters controlling potential back rotation are not unequivocally established.

We believe that much of the uncertainty stems from the fact that the most basic requirements to study mantled porphyroclasts in a shear zone were rarely met in previous works, namely that the mantled porphyroclast in a matrix represents a three phase system: the clast, the mantle and the matrix. Consequently three (possibly) different material properties must be employed. Given the large natural differences in grain sizes between clast and mantle material and the amount of strain localization in the mantle it seems a fair assumption that the mantle material is the weakest phase in the system. Most previous studies have however modeled the mantle as a passive strain tracker in the matrix, starting from Passchier and Simpson's pioneering work (1986).

The well known analytical solution for rigid particles in simple shear was derived by Jeffery (1922) and extended to contemporaneous pure and simple shear by Ghosh and Ramberg (1976). However, the interest in the behavior of isolated inclusions is not only restricted to geologists but is in fact of relevance to a large part of the scientific community. Based on the alternative analytical solutions by Muskhelishvili (1953) and Eshelby (1959), researchers in the fields of composites and defects in solids have recently derived expressions for an inclusion with imperfect bonding to the matrix (e.g., Mura, 1987; Furuhashi et al., 1992; Gao, 1995; Ru and Schiavone, 1997; Shen et al., 2001). A common finding of these recent works is that the so called Eshelby conjecture

(Mura, 2000) does not hold for a cylindrical or elliptical inclusion with a slipping interface. The Eshelby conjecture states that constant stresses applied at infinity cause constant stresses inside the inclusion, i.e., for arbitrary combinations of pure and simple shear, and arbitrary orientation and aspect ratio of the ellipsoidal inclusion, the stress state inside is homogenous and can be completely described by a single stress tensor. This result is of fundamental importance for geological applications, where the observed systems are not likely to show perfect bonding between clast and matrix (either due to interfacial slip or the presence of a third phase, i.e., the mantle). Inhomogeneous stress states inside the inclusion are not only expected to change the flow patterns, but may cause transitions into different deformation mechanisms fields, drive metamorphic reactions and be the cause for asymmetric zoning (e.g., myrmekite distribution, Simpson and Wintsch, 1989). Certainly the loss of homogeneity of the stresses inside the inclusion has a significant influence on texture evolution which, up to now, has been based on the Eshelby solution (e.g., Kocks et al., 1998).

The subject of this study is the three phase mantled porphyroclast system subject to simple shear, sufficiently isolated that the boundary conditions do not disturb the behavior of the clast and with no other clasts in the vicinity. Since we explicitly assume that the effective viscosity of the mantle material is less than that of the matrix, we will refer to it as a “lubricant”. This terminology has the advantage that it is geologically neutral and is also applicable to the end-member case where the thickness of the lubricant vanishes, but slip is allowed on the inclusion-matrix interface. Due to the plane strain assumption this study is restricted to two dimensions. The clast is assumed to be elliptical, including the degenerate case of a circular inclusion. Hence, strictly speaking, we assume that in three dimensions the clast is an infinitely long elliptical cylinder.

The analytical works mentioned above only provide closed-form solutions (solutions with a finite number of terms) for the case of lubricated circular inclusions (Shen et al., 2000). In the case of lubricated elliptical inclusions, the solutions are infinite series that usually converge to an acceptable error with only a few of the series terms used. However, since there is no significant difference between a truncated infinite analytical solution and a numerical model that approximates the governing Stokes equations locally with polynomials of chosen order, we prefer to use a Finite Element Method

(FEM). This has the advantage that arbitrary geometries, non-linear materials (here Non-Newtonian power-law) and finite strains can be studied.

In the first section of the paper the model method and setup are explained. Then the influence of a lubricating layer on the stress distribution and the rotation at initial and finite stages is demonstrated with examples of circular and elliptical inclusions. Finally we show under which conditions the lubricated inclusion has stable positions and how viscosity contrast between matrix and lubricant and the productivity rate of fine grained mantle material can be estimated from geometrical parameters by means of attractor maps.

NUMERICAL METHOD AND SETUP

The numerical model used is a personally developed two-dimensional FEM code using the seven node Crouzeix-Raviart triangle (Crouzeix and Raviart, 1973) to solve the Stokes equations for incompressible, viscous materials. A mixed method is employed, with linear interpolation of pressure, since this avoids spurious pressures usually appearing due to the incompressibility constraint (Brezzi and Fortin, 1991). The code has been extensively tested from simple flow problems to mantle convection. The specific check of the numerical model versus the solutions of Jeffery and Ghosh and Ramberg is given in Appendix 1.

The initial configuration of the numerical experiments is depicted in Figure 1. Since the presence of boundaries may influence the behavior of a rotating inclusion (Ildefonse et al., 1992; Bons et al., 1997; Marques and Coelho, 2001), care was taken to avoid such boundary effects. In all models, the length of the inclusion is only five percent of the shear zone width and the lateral boundaries are even farther apart, with the length of the ellipse only one to two percent of the box length. The thickness of the lubricating layer was in the range of zero to fifty percent of the short axis of the ellipse.

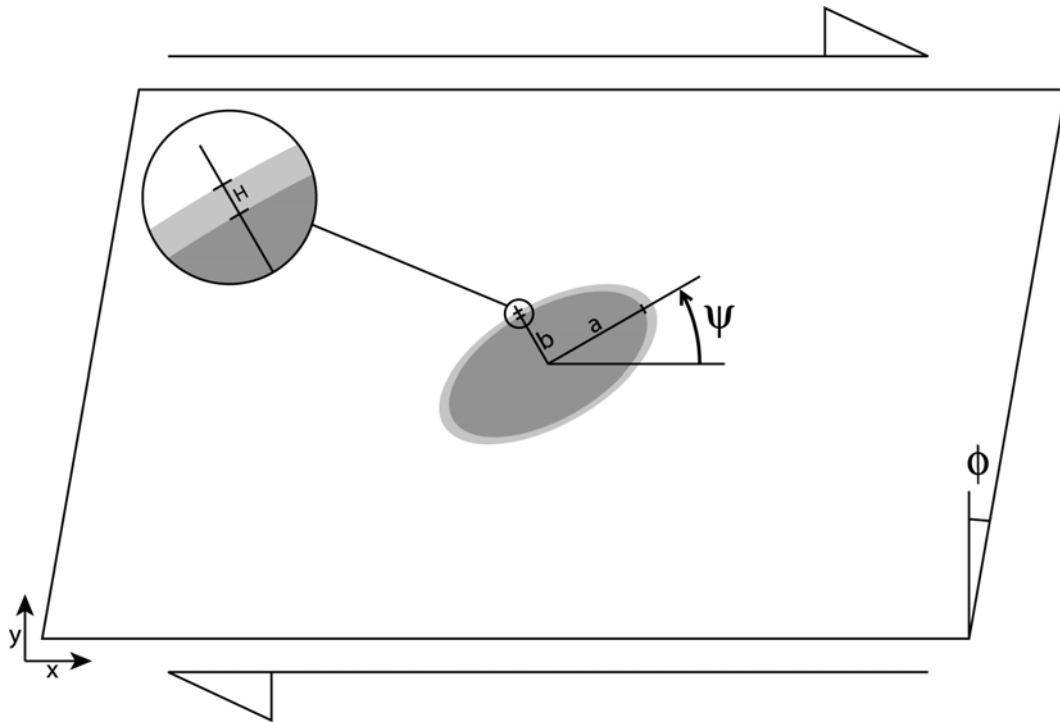


Figure 1

Initial configuration of the experiments. A competent ellipse (dark gray) is coated with a weak lubricant layer (light gray), and embedded in a matrix of intermediate effective viscosity. The sketch is not to scale with respect to the actual particle-matrix size relationship (see text). The aspect ratio of the ellipse is given with R which is the ratio of the two axes, a/b . The orientation of the inclusion is measured as the angle ψ , between the long axis and the shear plane, with $\psi > 0$ meaning counterclockwise. Due to the symmetry of the system ψ only varies from -90° to 90° . The thickness of the lubricant, H , is measured as the intersection of the line defined by the short axis of the ellipse and the lubricant layer and given in percent of b . The boundary condition applied is a constant shear velocity on top and bottom and a free surface condition at the lateral boundaries. The shear angle ϕ is a measure of the achieved shear strain γ , which is defined as $\gamma = \tan(\phi)$.

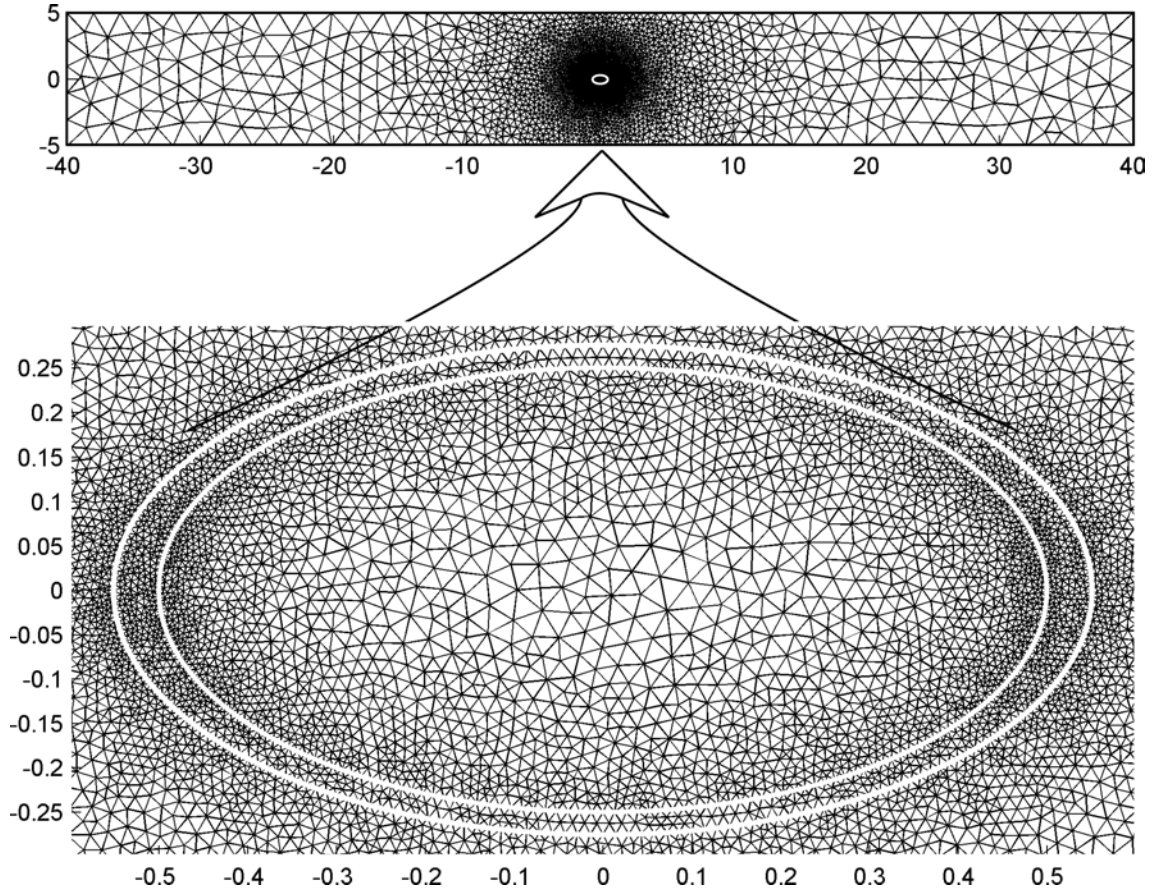


Figure 2

Typical mesh generated for an ellipse of aspect ratio 2:1 with a 10% lubricant layer between ellipse and matrix. Initial number of elements is more than 20'000.

The necessary resolution around the particle was achieved by mesh refinement, with a typical example displayed in Figure 2.

The boundary conditions applied are constant shear strain rate on top and bottom resulting in constant shear velocities, and stress free boundaries at the lateral sides. The definition of the shear strain rate $\dot{\gamma}$ is

$$\dot{\gamma} = \frac{\partial v_x}{\partial y} \quad (1)$$

where v_x is the horizontal velocity in the Cartesian coordinate system (Figure 1). Hence positive $\dot{\gamma}$ values mean top to the right shearing, which is the case for all experiments presented here.

The rheologies studied are Newtonian and Non-Newtonian power-law, for which the relationship between deviatoric stresses, τ_{ij} , and strain rates, $\dot{\epsilon}_{ij}$, can be written in general form as (e.g., Ranalli, 1995)

$$\tau_{ij} = 2\eta\dot{\epsilon}_{ij} \quad (2)$$

where η is the effective viscosity of the material and defined as

$$\eta = B\dot{\epsilon}_e^{\left(\frac{1}{n}-1\right)} \quad (3)$$

Here $\dot{\epsilon}_e$ is the effective strain rate, n is the power-law exponent and B is a pre-exponential material constant, which, in the case of a Newtonian material ($n = 1$), is the viscosity. The definition of $\dot{\epsilon}_e$ is

$$\dot{\epsilon}_e = \sqrt{\left(\frac{\dot{\epsilon}_{xx} - \dot{\epsilon}_{yy}}{2}\right)^2 + \dot{\epsilon}_{xy}^2} \quad (4)$$

and follows the Mohr circle construction (Jaeger and Cook, 1979) of the maximum or effective shear stress σ_e

$$\sigma_e = \sqrt{\left(\frac{\sigma_{xx} - \sigma_{yy}}{2}\right)^2 + \sigma_{xy}^2} \quad (5)$$

For scalability it is useful to give the viscosities as relative values. Unless stated otherwise, the “rigid” inclusion was assumed to be 1000 times more competent, i.e., viscous, than the matrix. The viscosity of the lubricant was a fraction of the matrix viscosity ranging from 1/2 to 1/50'000. Viscosity contrasts are clearly defined for Newtonian materials. The case of power-law materials is less straightforward, because strain rates enter the expression of the effective viscosities and these are not known a priori. As a first proxy, the applied far-field strain rate values may be used to evaluate the effective viscosities. However, due to the expected strain rate localization in the weak lubricant the calculated values will not correspond to the actual contrasts present in the experiment. Ten and Yuen (1999) have already pointed out that even a small difference in the B values of clast and matrix behaving as power-law materials can result in large effective viscosity contrasts. This topic will be discussed in the section considering power-law behavior.

Due to the large overall and local strains expected for the problem, continuous remeshing was applied for the finite strain runs, whereby the surrounding box was kept rectangular and only the contours of the lubricant layer and the elliptical inclusion were actually moved, generating a new mesh for every time step. With this procedure, the danger of mesh distortion is eliminated and the only restriction on achievable strains result from the increasing memory usage due to the ever-growing number of elements, caused by the formation of tails and thinning of the lubricant around the ellipse. Since neither Newtonian nor power-law rheology exhibits memory apart from the geometrical configuration, this permanent remeshing does not introduce additional problems since it does not involve interpolation of the stress tensor that would be required by, for example, viscoelastic rheologies.

CIRCULAR INCLUSIONS

INITIAL STAGES

The simplest type of inclusions are of circular shape since there is no dependence on orientation angle ψ . We therefore start to illustrate the problem for this basic shape. The characteristic effects of the presence of a lubricating layer on stress and strain rates are shown on in Figures 3 to 9. The parameters used to illustrate the problem are pressure, P , effective strain rate, $\dot{\epsilon}_e$, effective shear stress, σ_e , and the inclination of the maximum stretching direction, θ . The convention used here is that compressive pressures are positive. We display pressure perturbation values only, i.e., an arbitrary lithostatic component may be added without any influence on the results.

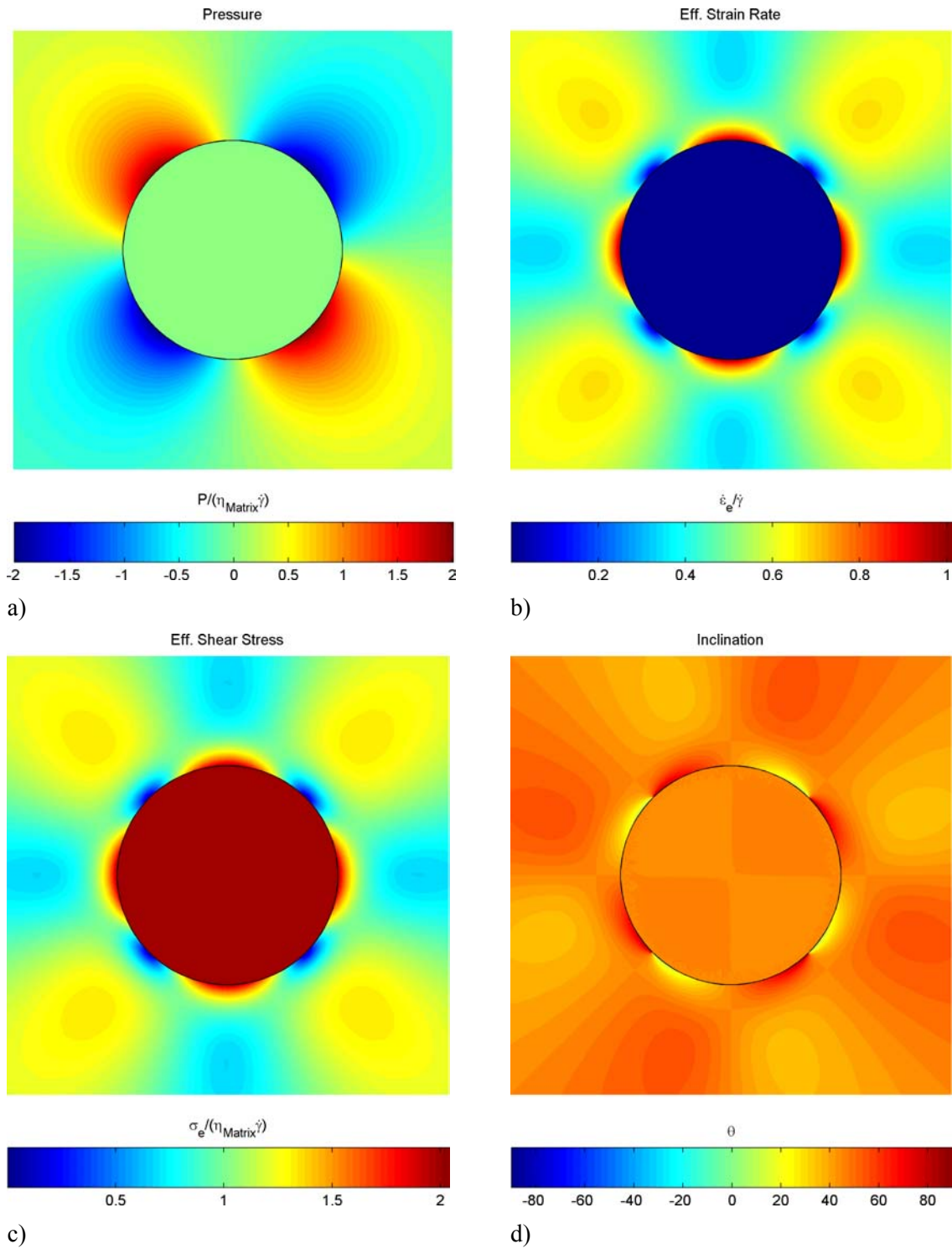


Figure 3

Rigid circular inclusion, no lubricant and perfect bonding between matrix and clast. For this and all other experiments the shear sense is top to the right. Note that only the region immediately surrounding the inclusion is displayed but the full model is much larger (c.f., Figure 2). $\eta_{clast} / \eta_{matrix} = 1000/1$

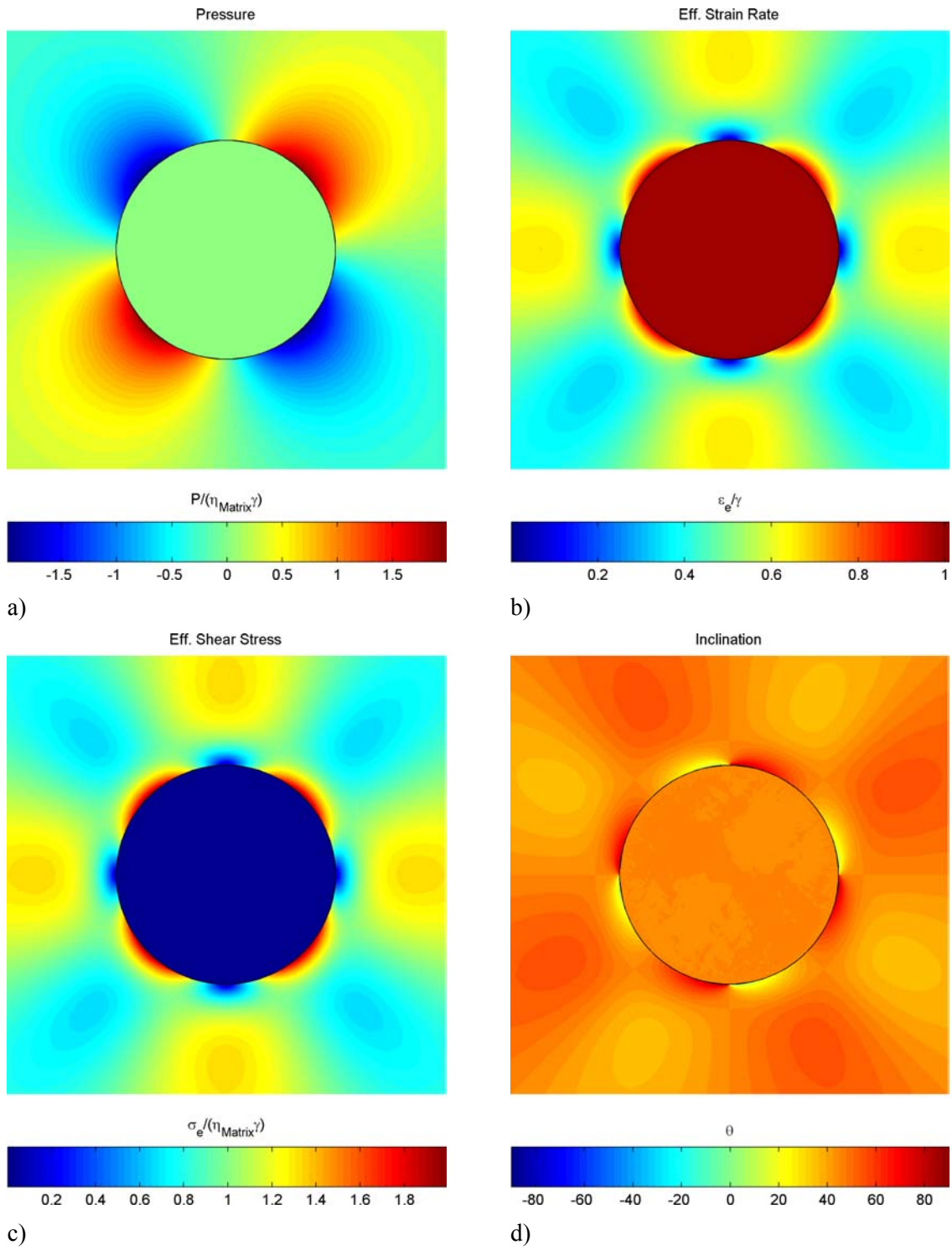


Figure 4

Weak circular inclusion, no lubricant and perfect bonding between matrix and clast.

$$\eta_{clast} / \eta_{matrix} = 1/1000$$

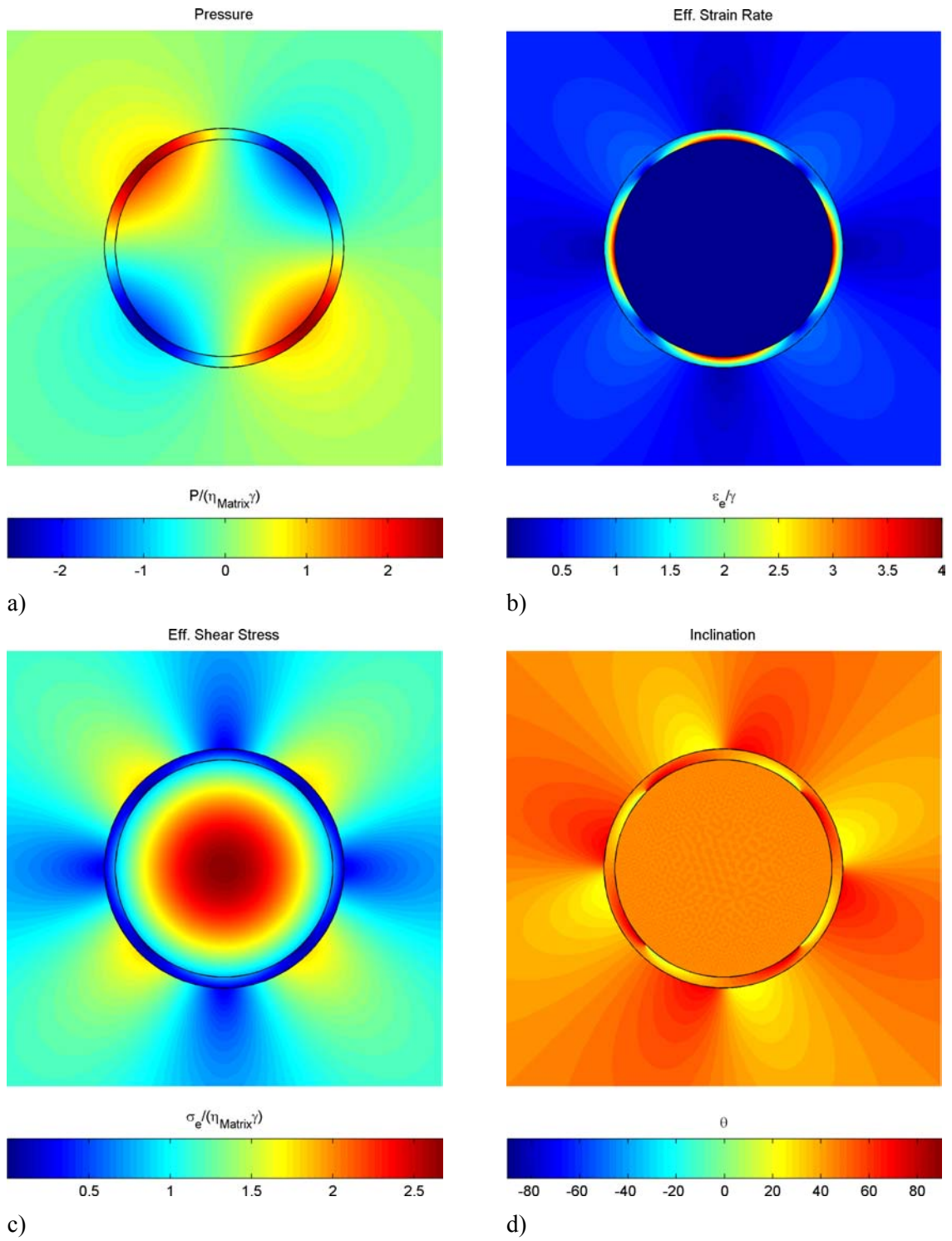


Figure 5

Rigid circular inclusion with a lubricant layer.

$$H = 10, \eta_{\text{lubricant}} / \eta_{\text{matrix}} = 1/10$$

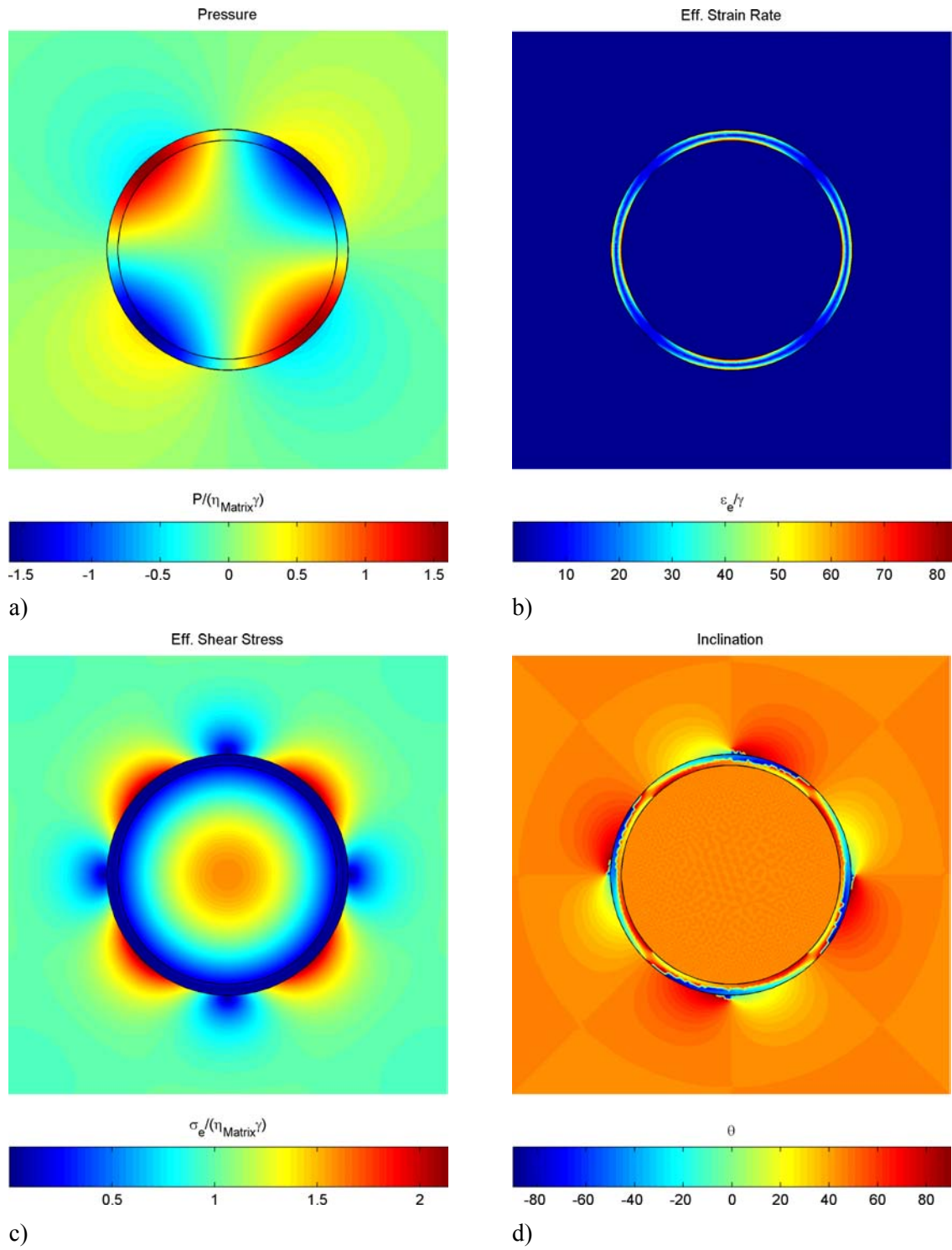


Figure 6
Rigid circular inclusion with a lubricant layer.
 $H = 10, \eta_{lubricant} / \eta_{matrix} = 1/1000$

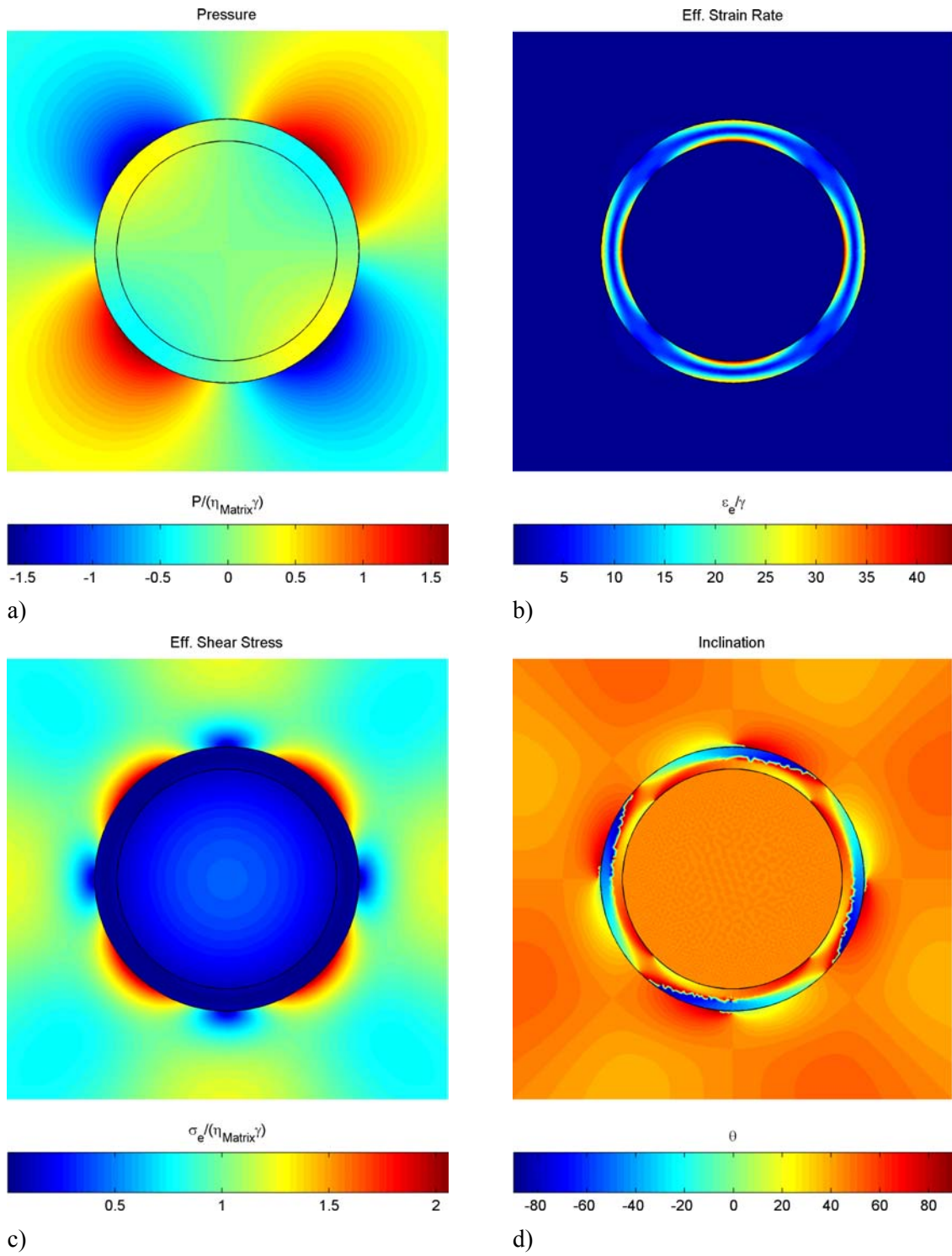


Figure 7

Rigid circular inclusion with a lubricant layer.

$$H = 20, \eta_{lubricant} / \eta_{matrix} = 1/1000$$

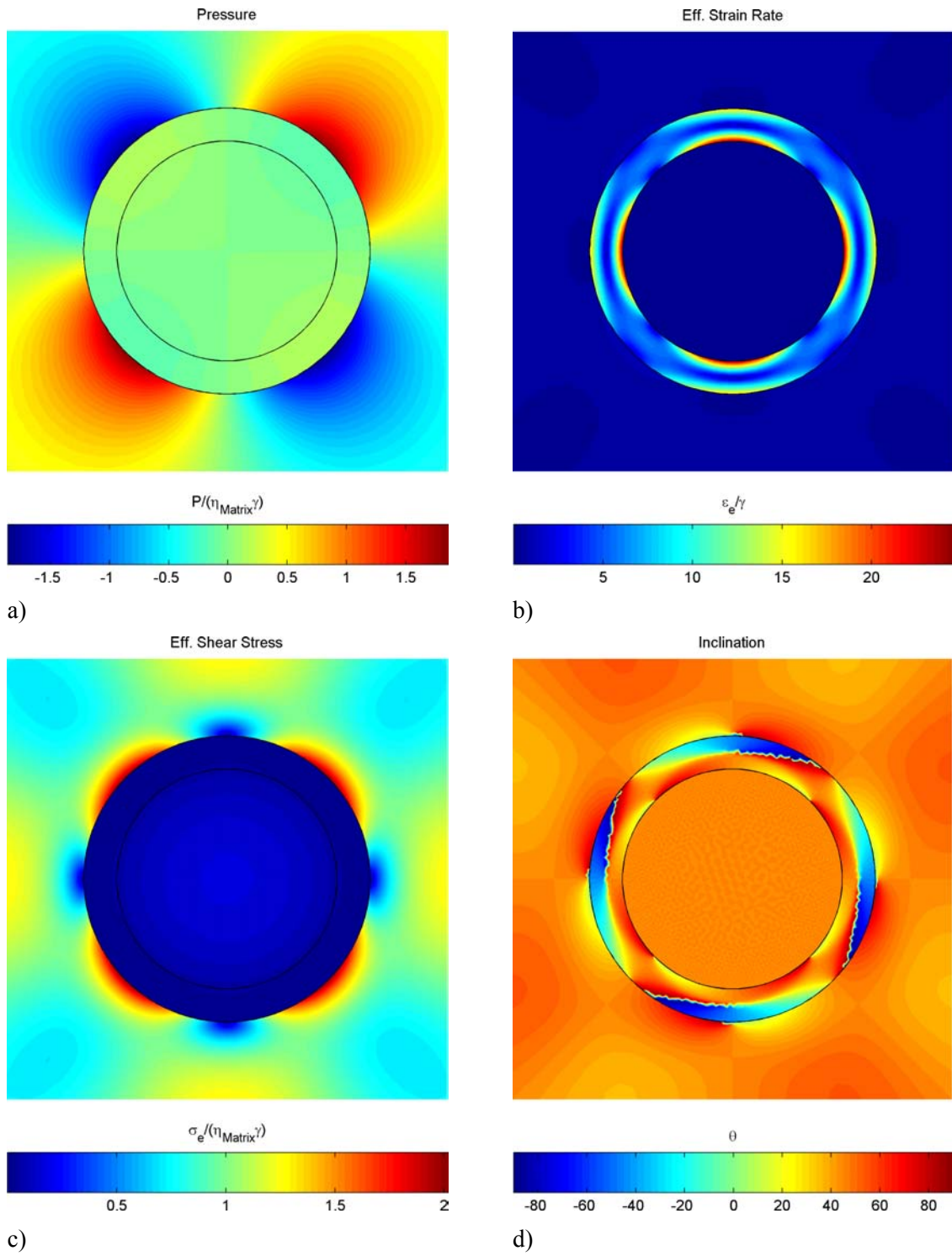


Figure 8
Rigid circular inclusion with a lubricant layer.
 $H = 30, \eta_{lubricant} / \eta_{matrix} = 1/1000$

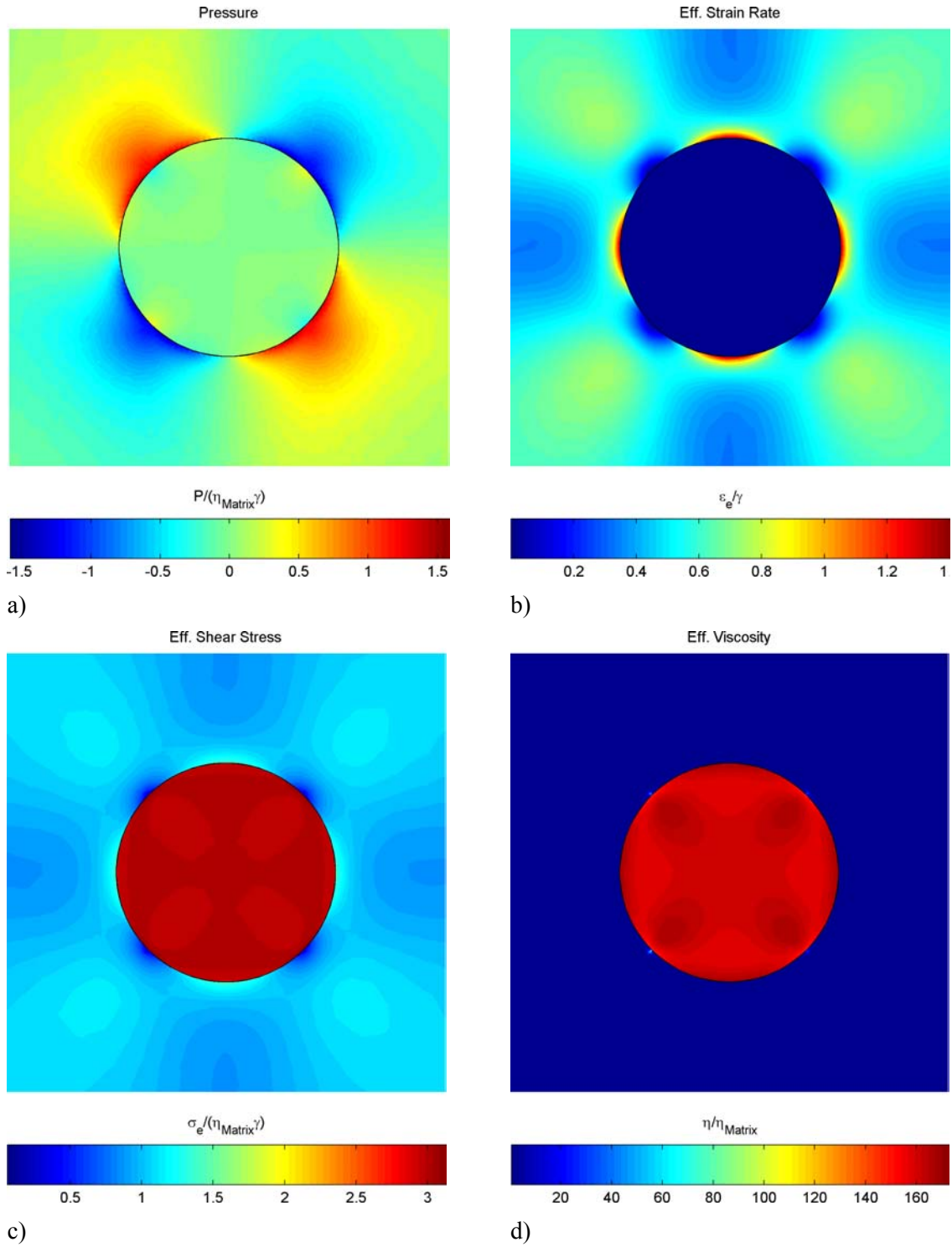


Figure 9

Rigid circular inclusion. Clast and matrix are power-law materials.

$$H = 0, n_{\text{clast}} = 3.3, n_{\text{matrix}} = 3.05, \eta_{\text{clast}} / \eta_{\text{matrix}} = 10/1$$

In order to understand the influence of a lubricant layer on the inclusion behavior it is necessary to first look at the two most simple end-member cases of inclusions: the very competent and the very weak. For contrasting this two end-members of inclusions they are compared in Figures 3 and 4. Not unexpectedly, high pressures develop adjacent to the rigid inclusion in the two quadrants where simple shear streamlines impinge on the inclusion. The other two quadrants are in relative extension, show low pressures and would in nature be the potential sites for the development of pressure shadows (e.g., Passchier and Trouw, 1996). Due to the symmetry of the system, the absolute amplitudes of the pressure perturbations in all four quadrants are equal. The effective strain rate is lowest in the inclusion; the maximum shear stresses are, however, found within the inclusion. With the exception of the matrix close to the inclusion the maximum stretching direction is everywhere around 45°.

If we introduce a weak instead of a strong inclusion not only the viscosity contrast is flipped but also p , $\dot{\epsilon}_e$, σ_e and θ . This means that compressive areas become extensive, regions with no shear strain rate become highly strained and the maximum shear stress is big where it was small before. The pressure in the inclusion is still zero, however, it is now the location of the highest effective strain rates and the lowest effective stresses. All of this although the applied simple shear boundary condition remained unchanged (top to the right).

The significance of the Eshelby conjecture is shown by this two end-member cases: although changing the relative viscosity contrast completely changes the kinematic and dynamic parameters, the inside of the inclusion stays homogeneous with all displayed parameters having a constant value. The introduction of a slipping interface (Figure 5), achieved through the explicit introduction of a lubricating layer, results in a dramatic change to a heterogeneous stress and strain rate distribution in the inclusion, consistent with published analytical solutions (Shen et al., 2001). Qualitatively, the weak mantle allows propagation of the outside pressures into the inclusion. On the other hand, increasing lubrication (i.e., decreasing viscosity of the weak mantle) progressively inverts the pressure distribution in the matrix surrounding the inclusion so that, for a lubricant layer with viscosity of 1/1000 and a thickness of 10% (Figure 6), the originally compressive quadrants have become extensive and vice versa. The reason for this progressive change in the matrix pressure distribution is that, with decreasing viscosity

of the lubricant, the matrix does not “feel” the inclusion anymore, and the pressure distribution in the matrix comes to resemble the case of a weak inclusion (Figure 4). This effect is further amplified if the thickness of the lubricating layer is increased (Figures 7 and 8), thus progressively masking the rigid inclusion until the stress state in the inclusion is almost homogenous, as shown for the weak inclusion (Figure 8).

The effect of the lubricant layer on the effective shear strain rate, $\dot{\epsilon}_e$, is that it acts as a strain concentrator and exhibits the highest effective strain rates. The amplitude of $\dot{\epsilon}_e$ increases with decreasing lubricant viscosity, but decreases with increasing lubricant thickness.

The influence of a lubricant layer on the effective shear stress is that, analogous to the behavior of P , the matrix values approach the case of a weak inclusion with decreasing lubricant viscosity and increasing H . The values of σ_e in the lubricant are smallest. Interestingly the values within the clast decrease, with decreasing $\eta_{lubricant}$ and increasing H , from the rim, but remain highest in the center of the clast, an observation made previously by Kenkmann (2000).

Another case where the Eshelby conjecture does not hold, even without the presence of a lubricant, is when the employed rheologies are Non-Newtonian (Figure 9). Here both materials, clast and matrix, have a power-law exponent $n=3$. The inclusion values become inhomogeneous only because of the Non-Newtonian character of the matrix, i.e., a power-law inclusion alone still follows the Eshelby conjecture. While the general features of the corresponding Newtonian case (e.g., Figure 3) are preserved the power-law has an important influence on the viscosity distribution. Although the effective viscosity contrast was scaled, using the boundary condition strain rate values, to be 10:1 its actual value is around 150:1 (Figure 9d) and follows the findings of Ten and Yuen (1999). The reason for the discrepancy between the predicted and the actual effective viscosity contrast is that the boundary condition strain rates not a reliable proxy for the effective strain rate that enters the expression of the effective viscosity of a power-law material, eqn. (3). Indeed it can readily be seen from the Newtonian case (Figure 3b) that the effective strain rate in the strong inclusion is very low and consequently the effective viscosities expected for a power-law material will be high.

EFFECT OF FINITE STRAIN

The finite strain behavior is illustrated in Figure 10, based on the already discussed rigid circular inclusion with $H=10$, $\eta_{lubricant} / \eta_{matrix} = 1/1000$ (Figure 6). The achieved shear strain was $\gamma=0.56$ (cf. Figure 1 for the definition of γ). Although this is a relatively small γ value, it is sufficient to significantly decrease the lubricant thickness in the compressive quadrants and to form tails. The geometry of the clast is ϕ -type (Passchier and Trouw, 1996) which would evolve into a σ -type with increasing strain (Ceriani et al., 2002). The stress distribution still closely looks like the corresponding initial situation, but the increasingly sharp tail tips start acting as stress concentrators, like the tips of a crack (Jaeger and Cook, 1979).

Interestingly, the kinematics of the circular clast are almost unaffected by the presence of a lubricating layer (Figure 11). This is astonishing, given that in the presented case the lubricant viscosity is very small. Initially the synthetic rotation of the clast slows down and then accelerates to a value slightly higher than the analytical value of the perfectly bonded case, which is $\psi / \dot{\gamma} = -0.5$.

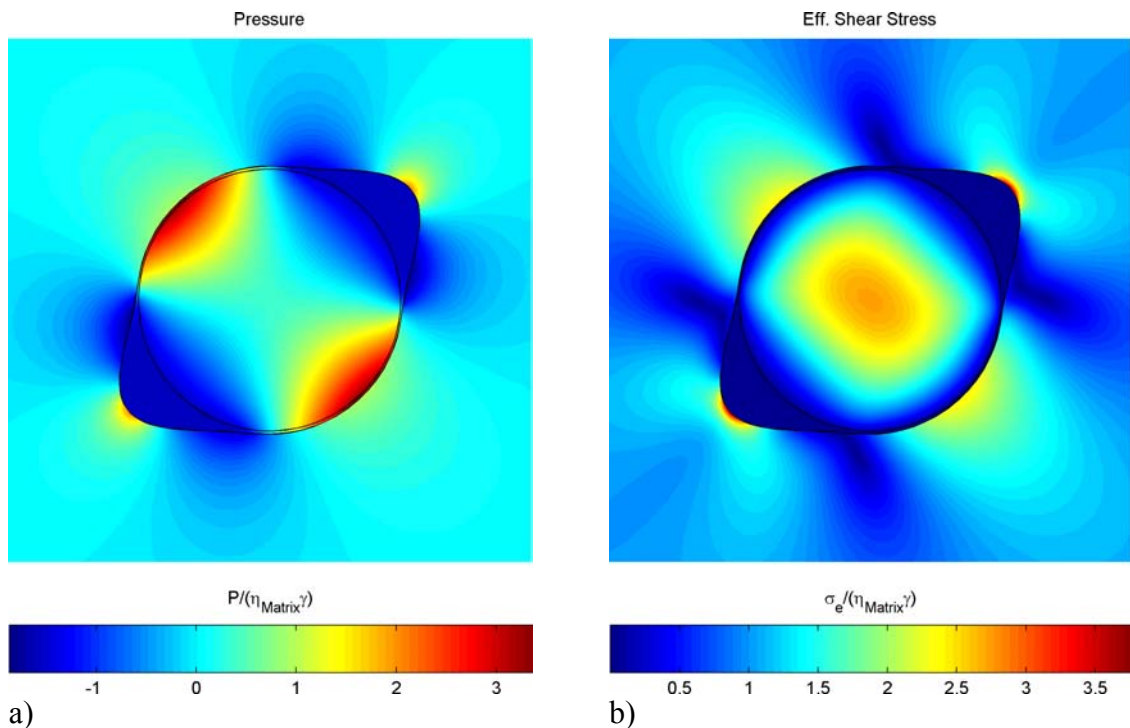


Figure 10

Finite strain experiment with a circular inclusion. $H=10$, $\eta_{lubricant} / \eta_{matrix} = 1/1000$.

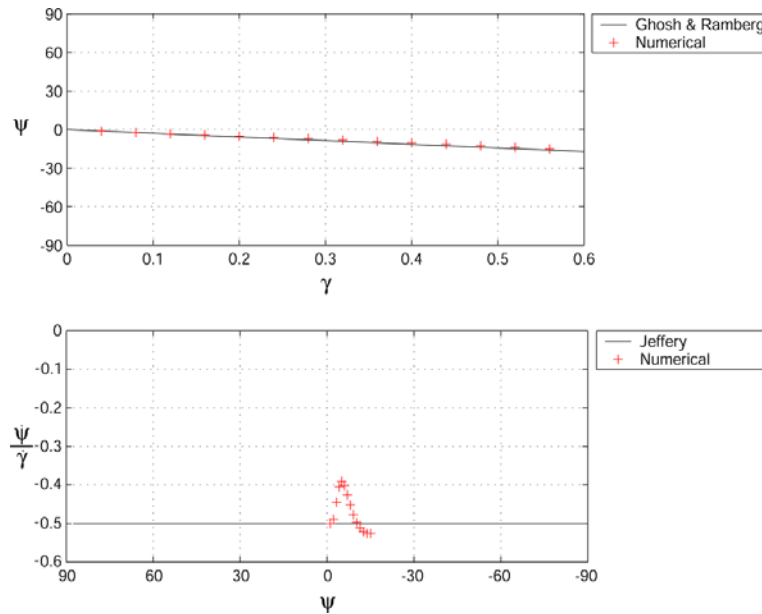


Figure 11

Comparison of the rotational behavior of the lubricated circular clast versus the analytical solutions derived for the perfectly bonded case.

ELLIPTICAL INCLUSION

INITIAL STAGES

The fundamental behavior of an elliptical inclusion is discussed here using the example of an ellipse with an aspect ratio of 2:1, Figure 12. The basic characteristics of stress and strain rate distributions and amplitudes of the case of a circular inclusion (Figure 3) are preserved. However, the inclination of the inclusion, ψ , plays now also an important role (Figure 14). The introduction of a lubricant with $\eta_{lubricant} = 1/1000$ and $H=10$ (Figure 13) already causes the pressure and effective shear stress to vanish within the inclusion. This reflects the analytical prediction of Stagni (1991) who found that an elliptical inclusion with imperfect bonding to the matrix should remain stress free when subjected to remote simple shear parallel to the long axis of the ellipse. The particular interface condition employed by Stagni was that the normal tractions are continuous but the shear tractions vanish. Vanishing stresses can also be observed for the vertical ellipse (Figure 15), which may simply be looked at as a degenerate case of a horizontal ellipse.

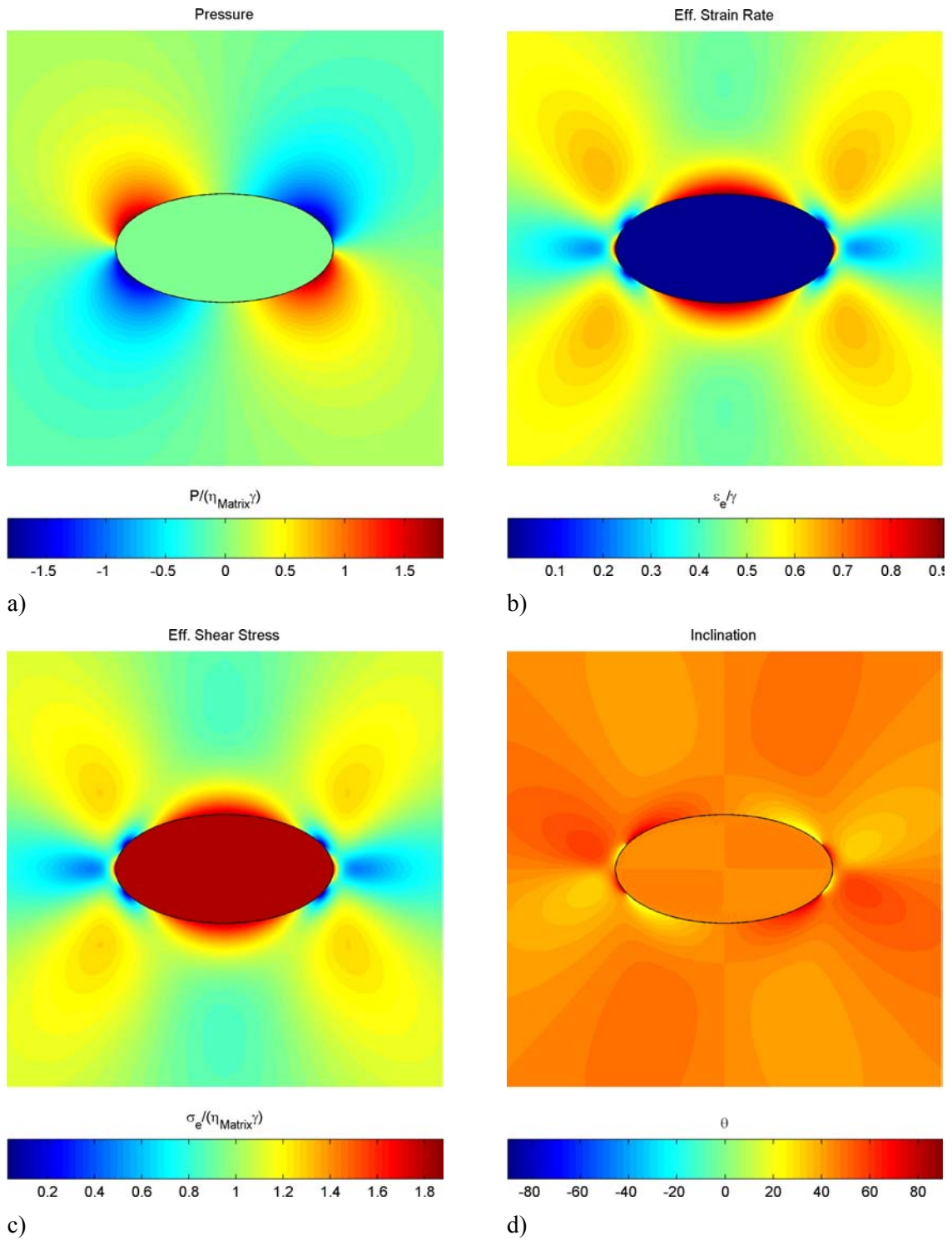


Figure 12

Rigid elliptical inclusion with perfect bonding between clast and matrix.

$H=0$, $R=2$, $\psi=0^\circ$

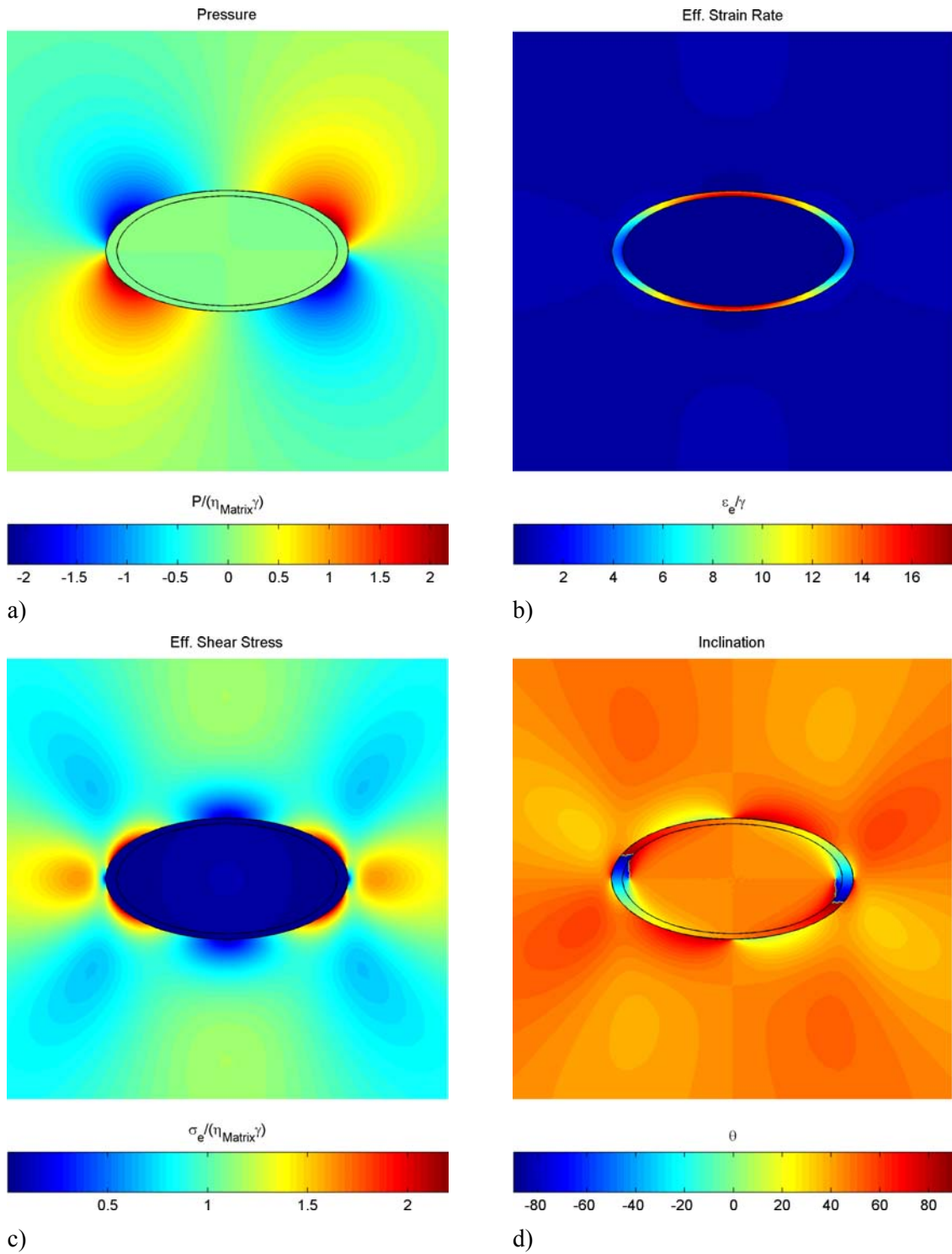


Figure 13

Rigid elliptical inclusion with a lubricant layer.

$H = 10$, $\eta_{lubricant} / \eta_{matrix} = 1/1000$, $R = 2$, $\psi = 0^\circ$

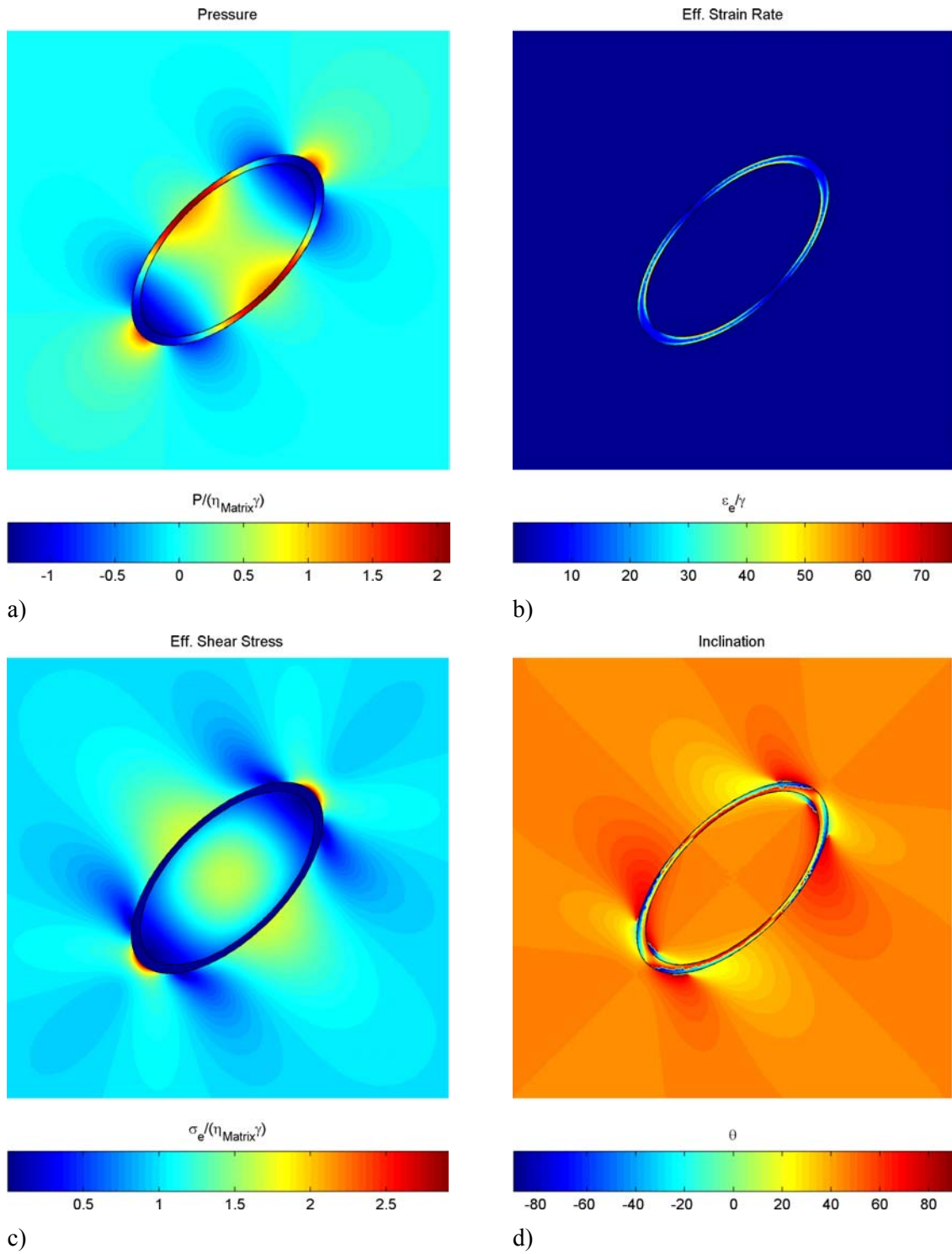


Figure 14

Rigid elliptical inclusion with a lubricant layer.

$H = 10$, $\eta_{lubricant} / \eta_{matrix} = 1/1000$, $R = 2$, $\psi = 45^\circ$

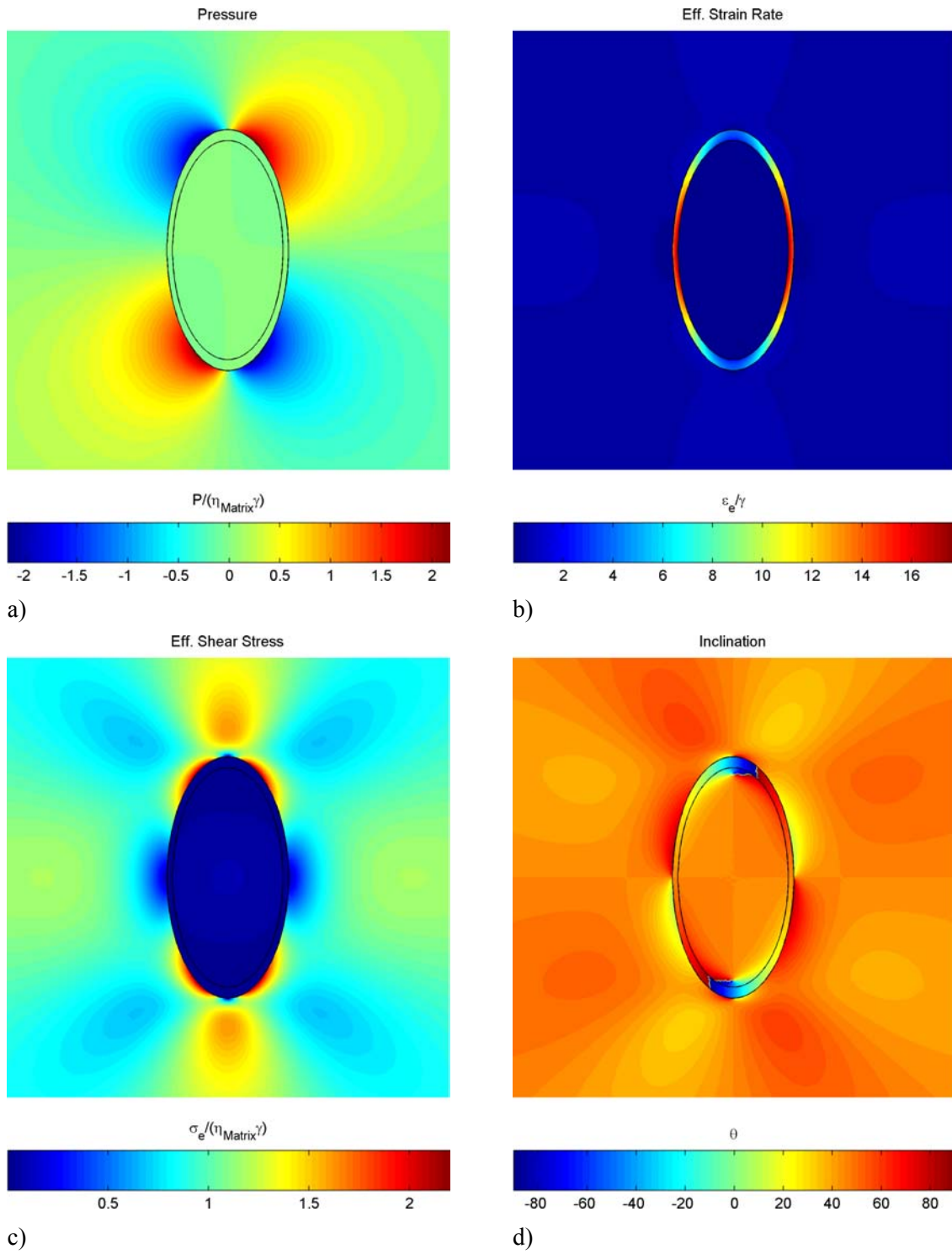


Figure 15

Rigid elliptical inclusion with a lubricant layer.

$H = 10$, $\eta_{lubricant} / \eta_{matrix} = 1/1000$, $R = 2$, $\psi = 90^\circ$

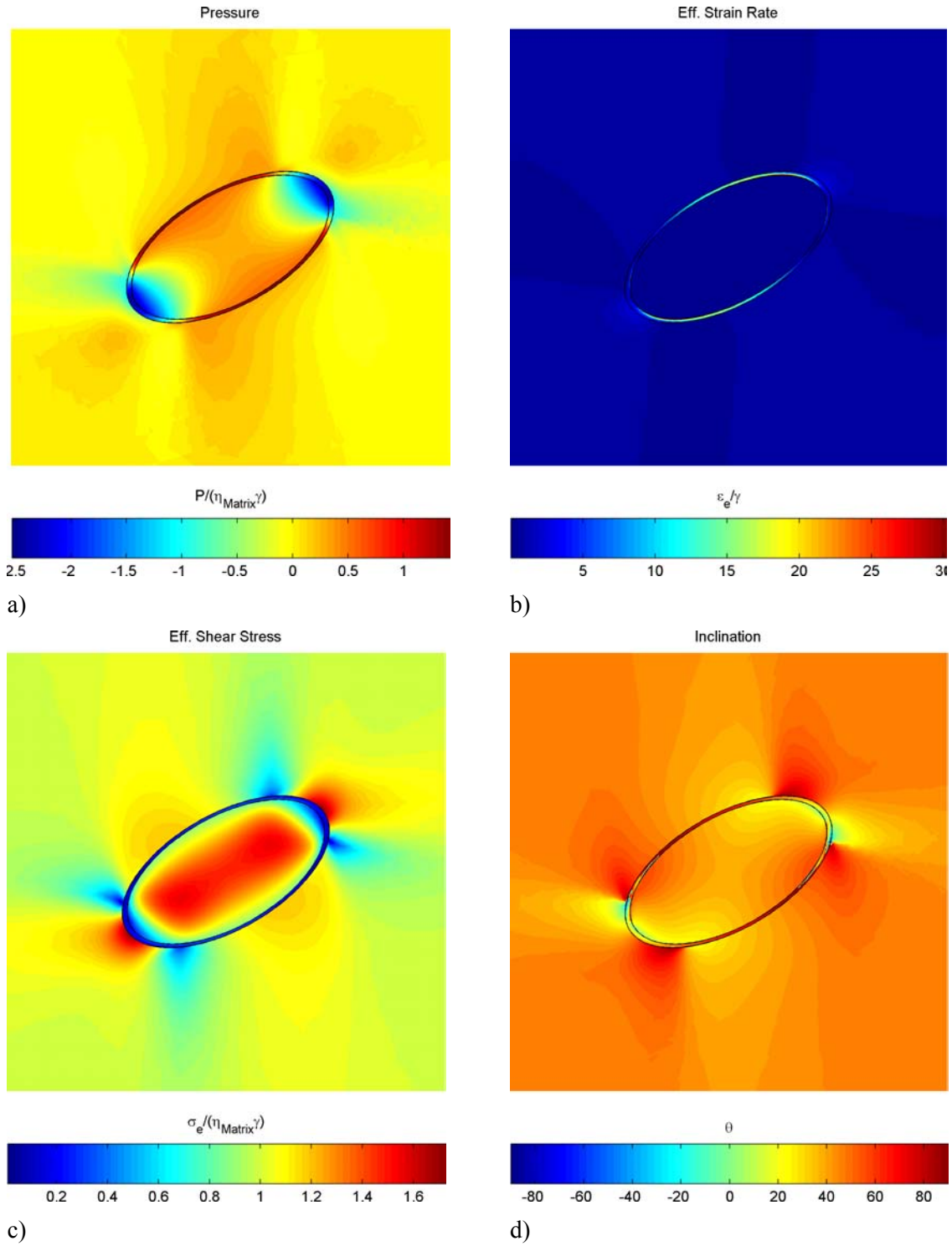


Figure 16

Rigid elliptical inclusion with a lubricant layer.

Lubricant and matrix are **power-law**.

$$H = 10, n_{clast} = 1, n_{matrix} = 3, n_{lubricant} = 3, \eta_{lubricant} / \eta_{matrix} = 1/10, R = 2, \theta = 30^\circ$$

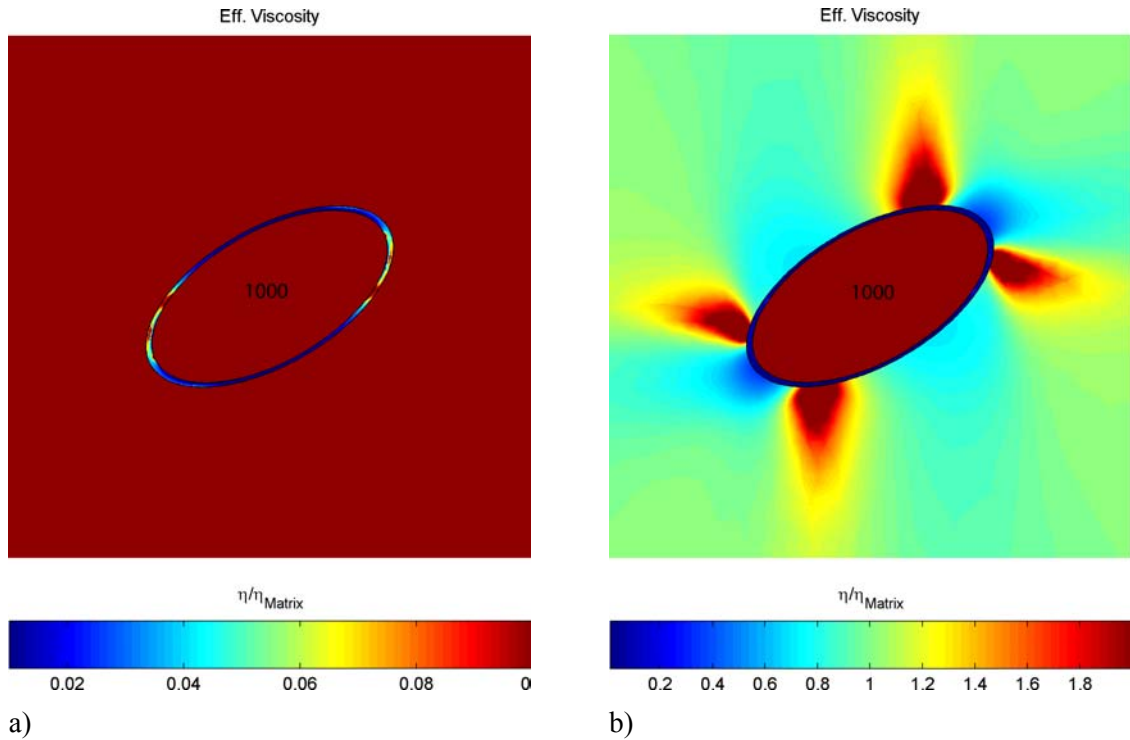


Figure 17

Effective viscosities corresponding to Figure 16.

a) Effective viscosity values in the range 0.01:0.1. The lubricant values are almost everywhere ten times too low compared to the predicted value of 0.1 using the background strain rate.

b) Effective viscosity values in the range 0.1:2. The matrix values are close to 1, the value predicted with the background strain rate.

If power-law instead of Newtonian materials are used the Eshelby conjecture does not hold anymore, as already observed for the circular inclusion. The predicted effective viscosities are again incorrect. In particular the effective viscosities in the lubricant are approximately one order of magnitude wrong (Figure 17a), approximately 0.01 in most of the lubricant instead of the predicted 0.1. The reason are the high observed effective strain rates in the lubricant layer (Figure 16b). Interestingly the prediction of effective viscosity values largely holds for the matrix (Figure 17b), which is due to the corresponding $\dot{\epsilon}_e$ values, that do not deviate much from the predicted values deduced from the boundary condition.

FINITE STRAIN

The finite strain behavior is illustrated based on the rigid elliptical inclusion with an aspect ratio of 2:1, $H=10$ and $\eta_{\text{lubricant}} / \eta_{\text{matrix}} = 1/1000$ (Figure 13). The achieved shear strain was $\gamma = .86$. Again, this is a relatively small γ but it is sufficient to substantially decrease the lubricant thickness in the compressive quadrants to form σ -type tails and bring the particle into a meta-stable position. As in the case of the circular inclusion the progressively increasing sharpness of the tail tips acts as a stress concentrator.

In contrast to the circular case the introduction of a lubricant layer has a drastic effect on the kinematic behavior of the elliptical inclusion (Figure 11). Starting from its initial position parallel to the shear flow the inclusion rotates “backwards”, i.e., antithetically against the applied simple shear flow. With increasing shear strain the inclusion approaches a quasi-static inclination of approximately 30° to the shear plane. This inclination is not truly static due to continuous movement of lubricant towards the tails. With decreasing thickness the particle is expected to move towards the shear plane and eventually rotate again according to Jeffery’s theory.

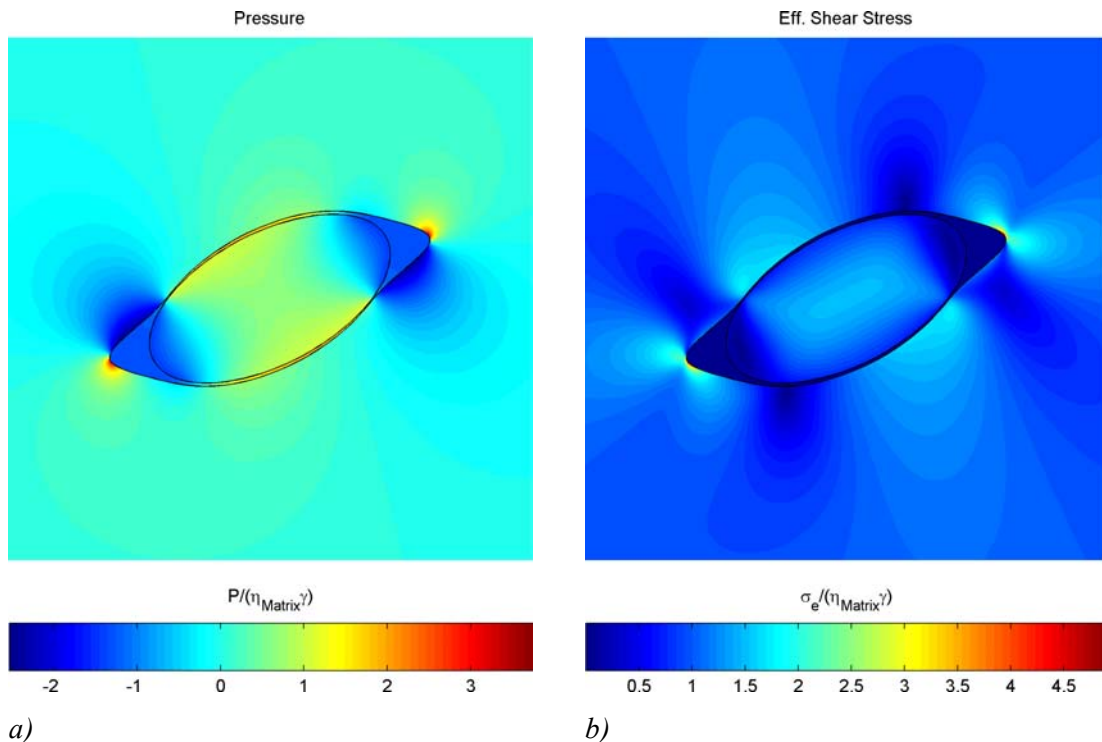


Figure 18

Finite strain experiment with an elliptical inclusion performed to $\gamma = .86$.

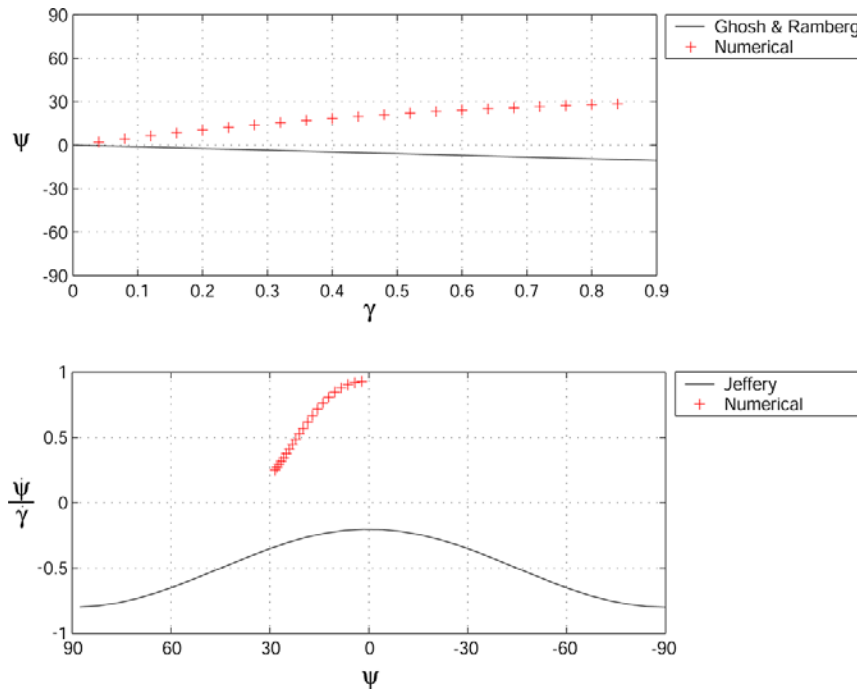


Figure 19

Comparison of the rotational behavior of the lubricated clast versus the analytical solutions derived for the perfectly bonded case. Aspect ratio of clast is 2:1.

LUBRICATED INCLUSION ROTATION MAPS (LIRM)

INTRODUCTION

The introduction of a lubricant layer drastically changes the dynamics and the kinematics of elliptical inclusions. On the other hand, the progressive development of tails does not appear to significantly influence the dynamics or the kinematic behavior of the inclusion. The tails only slightly alter the stress distribution through the change in geometry of the lubricant layer. However, the stress distribution in the direct vicinity of the inclusion remains almost identical to the case of a lubricated porphyroclast without tails. Analogue modeling shows that the kinematic behavior is not changed by the presence of tails (Ceriani et al., 2002). The influence of the tails is purely one of mass balance – the formation of tails reduces the thickness of lubricant material around the inclusion. We therefore conclude that tail formation is not a first order effect and we test this hypothesis by comparing instantaneous, single time-step experiments with finite

strain experiments. This is done with the aid of so-called “lubricated inclusion rotation maps” (LIRM). Each LIRM summarizes several hundred single time step experiments in which, for a given aspect ratio and lubricant viscosity, the rotation rate $\dot{\psi}$ and the lubricant thickness change rate \dot{H} , were measured as a function of orientation angle ψ and lubricant thickness H .

$$\dot{H} = f(H, \psi) \quad (6)$$

$$\dot{\psi} = g(H, \psi) \quad (7)$$

where f and g are constructed as lookup tables from more than 8000 numerical experiments.

The reason why \dot{H} is a key parameter is that it determines the lubricant behavior over the largest part of the inclusion surface, i.e., the sides parallel to the long axis. Hence \dot{H} controls if this channel-like region increases or decreases in thickness, in competition with the tails. In contrast to the tails, these lubricant channels exert tractions on the inclusion and therefore must be considered when studying the behavior of an elongated, lubricated inclusion. In fact, the comparison with a channel flow, driven by pressure gradients is even more appropriate if the pressure along the channel is taken into account. It is clear from the previous section that pressures are highest near the center of the channel and lowest in the pressure shadow zones into which the material is expelled.

The two building blocks of a LIRM, $\dot{\psi}$ and \dot{H} as a function of ψ and H , are shown in Figure 20 and Figure 21, respectively, with the example of an inclusion of aspect ratio 2:1 and lubricant viscosity 1/1000. As already demonstrated the introduction of a lubricant layer has a strong influence on the rotation rates (Figure 20). With increasing H , the rotation rates go rapidly from Jeffery’s solution (zero lubricant) into a steady field in which back-rotation (positive $\dot{\psi}$) occurs for orientations close to the shear direction. In this case of a strong viscosity contrast between matrix and lubricant, this steady field is already reached with only 2% lubricant. Interestingly the $\dot{\psi}$ field is always symmetric around $\psi = 0$. On the other hand, \dot{H} is more sensitive to the amount of lubricant and does not show a steady state with respect to H . Based on the measured values of $\dot{\psi}$ and \dot{H} a first LIRM can be constructed (Figure 22).

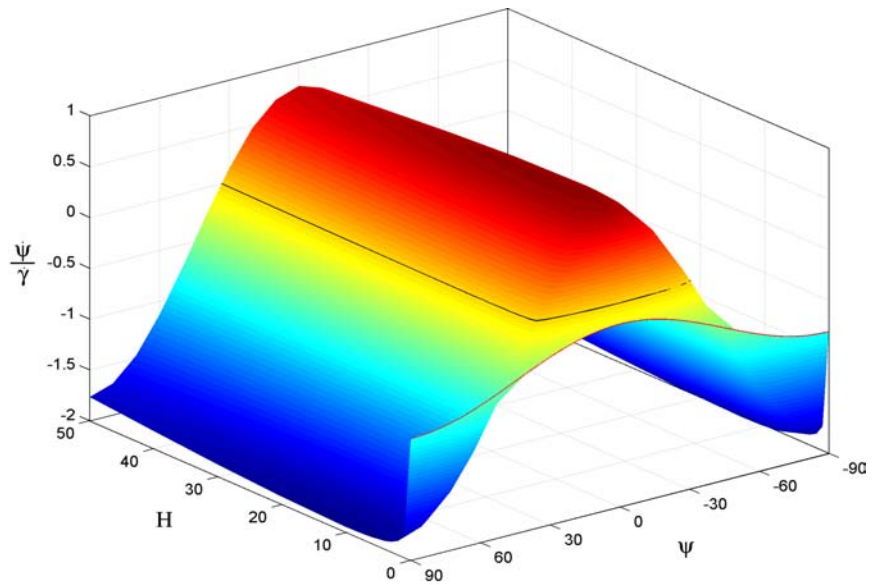


Figure 20

Normalized rotation rate as a function of inclusion inclination and the thickness of the lubricant. The red line in the foreground represents the analytical solution from Jeffery. The black line is the zero rotation rate contour. Above the zero contour back-rotation occurs, below the rotation is synthetic.

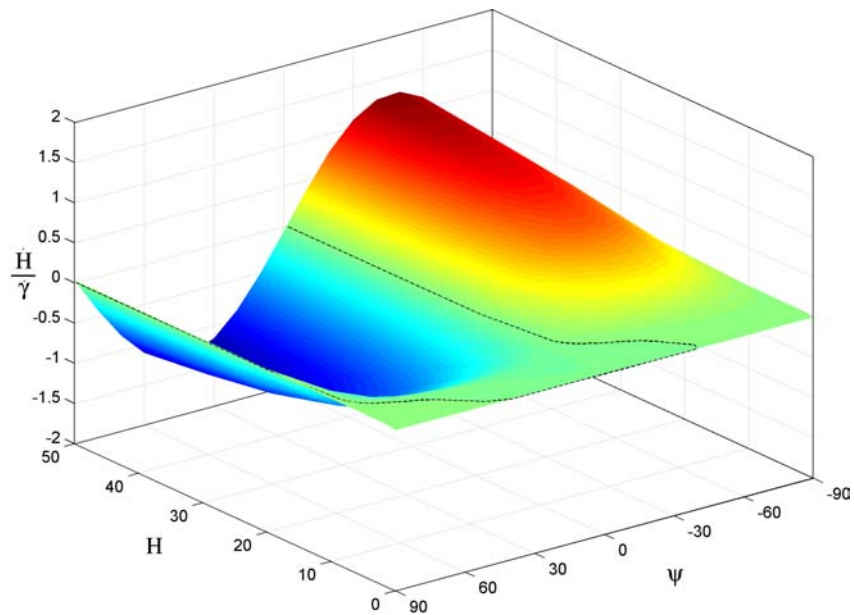


Figure 21

Normalized thickness change rate as a function of inclusion inclination and the thickness of the lubricant. The black dotted line is the zero thickness change rate contour.

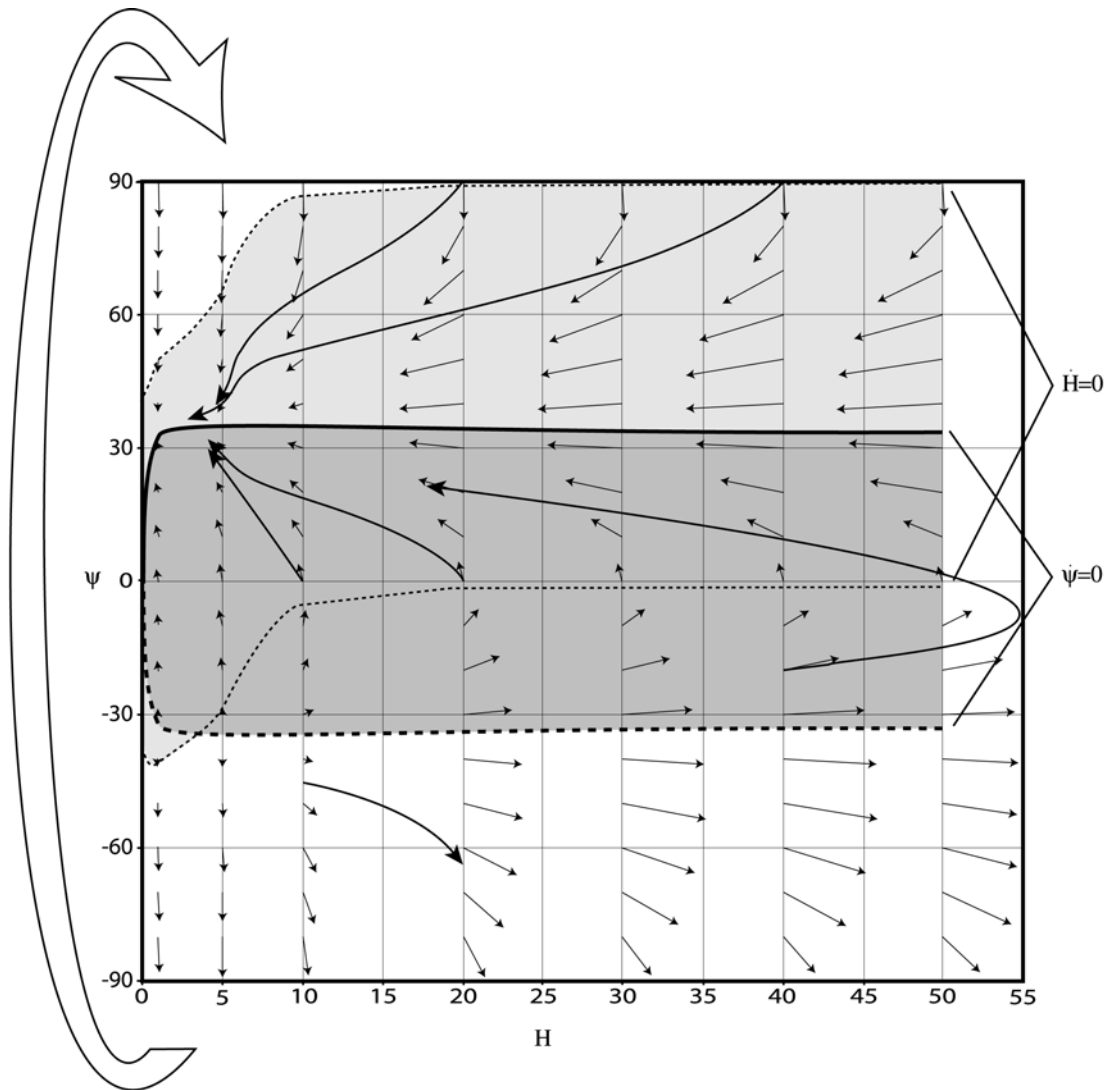


Figure 22

LIRM for a lubricated inclusion of aspect ratio 2:1 and lubricant viscosity 1/1000. Thin straight arrows symbolize the inclusion flow direction derived from single time step experiments. Thick arrows show the path of actual finite strain experiments. The field of decreasing H (negative \dot{H} , light gray) is overlain by the field of back-rotation (positive $\dot{\psi}$, dark gray).

The basic assumption of a LIRM is that the knowledge of $\dot{\psi}$ and \dot{H} from the instantaneous experiments are sufficient to describe the movement of an inclusion in the $\psi-H$ plane. The measured values of $\dot{\psi}$ and \dot{H} are hereby translated into velocity vectors in the $\psi-H$ plane. The amount of information needed can, however, be reduced to the position of the zero contours of $\dot{\psi}$ and \dot{H} . These define entirely how a lubricated inclusion moves in the $\psi-H$ plane.

Inside the field bounded by $\dot{\psi}=0$ (dark gray) back rotation occurs and the inclusion is rotated towards positive ψ values. Outside this field, synthetic rotation takes place. If only the vertical velocity (due to $\dot{\psi}$) is taken into account, the entire zero contour of $\dot{\psi}$ would summarize the locations of stable orientations of the inclusion since the inclination should not change once the contour is reached. This is only true for the positive leg of the $\dot{\psi}=0$ line which acts as an attractor line, able to attract inclusions from the entire $\psi-H$ plane due to the vertical periodicity of the system. The negative leg is unstable and small disturbances will move the inclusion away from it towards the attractor line. Since the steady field of $\dot{\psi}=0$ with respect to H is already reached here with $H \approx 2\%$ it is expected that natural inclusions with the given aspect ratio and viscosity contrast are most likely to be found at a positive inclination towards the shear plane of $H \approx 35^\circ$.

The interpretation of the $\dot{H}=0$ contour follows similar arguments. Inside the contour (light gray) the values are negative and hence the lubricant thickness decreases, which is to be expected for positive inclinations. Therefore the inclusion will be moved towards smaller H values inside the contour and the opposite is true for locations outside the contour. If the zero contours of \dot{H} and $\dot{\psi}$ would intersect at positive inclinations a true stable attractor point would be found. This is however not the case here nor in any other experiment with no lubricant productivity, which will be discussed later.

In order to verify the predictive power of LIRMs finite strain runs were performed with randomly chosen starting positions in $\psi-H$ plane and their trace plotted on the presented LIRM (Figure 22). The lines follow the velocities derived from single time step experiments quite well and clearly indicate the attraction potential of the attractor line. This again demonstrates that the tails are not a key parameter in the mantled porphyroclast system.

DEPENDENCE OF ATTRACTOR LINES ON LUBRICANT VISCOSITY

The functionality of LIRM was discussed above with the example of a relatively high viscosity contrast between matrix and lubricant of 1000:1. In order to check the influence of the viscosity contrast on the position of the attractor line LIRMs were

constructed for a range of different viscosity contrasts. The resulting attractor lines are shown in Figure 23. The characteristic behavior is that with decreasing lubricant viscosity less lubricant material is needed for back rotation to occur, the field of back rotation becomes larger with respect to ψ and tends towards a maximum value. If the viscosity of the lubricant is too close to the matrix value, no attractor line exists and hence no back rotation occurs. This was checked here with a lubricant value of 1/2, for which no back rotation occurred in the investigated H range. On the other hand, lowering the viscosity contrast below 1/1000 has no further significant influence on the results. The case of 1/50'000 was checked and yields almost identical values to the 1/1000 case.

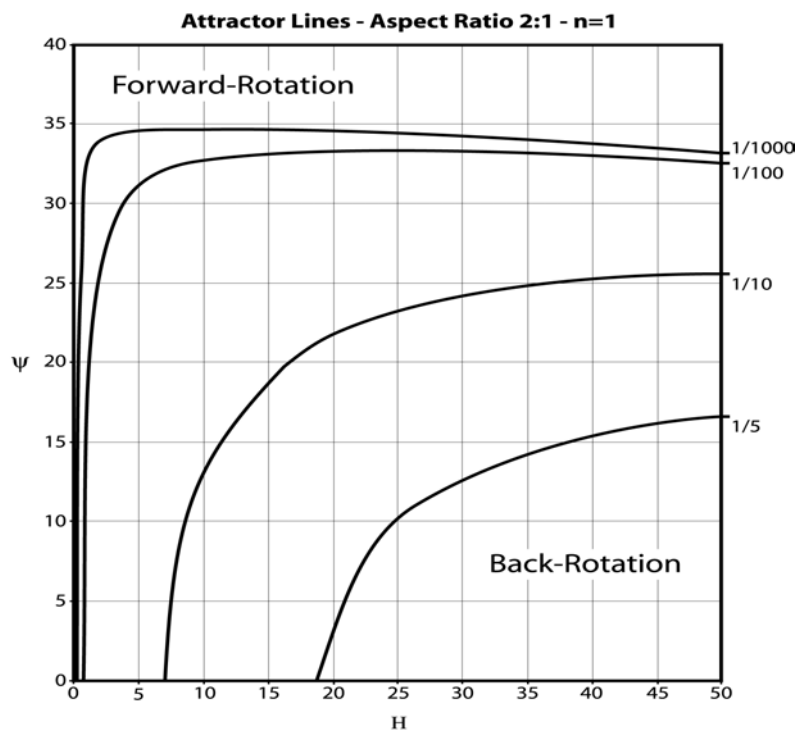


Figure 23

Attractor lines for an inclusion with aspect ratio 2:1. The viscosity contrast $\eta_{lubricant} / \eta_{matrix}$ is given on the right border. The field of back-rotation is a function of the viscosity contrast between matrix and mantle as indicated by the iso-viscosity contours.

ATTRACTOR MAPS

The cases presented so far of inclusions with a given initial lubricant thickness are somewhat arbitrary since in natural mylonites the lubricant mantle would be expected to develop progressively during ongoing deformation. With the onset of deformation, local stress concentrations around the porphyroclast could lead to local cataclasis (e.g., Tullis and Yund, 1987) or crystal-plastic re-crystallization. Here it is important to note the difference in scaling between velocities and stresses. While, for given shear strain rate, the absolute values of the velocities around the clast decrease with decreasing size of the clast, this is not the case for the amplitudes of the local stresses. It is clear from dimensional and analytical arguments (Jaeger and Cook, 1979) that the stresses are independent of clast size and do not decrease with decreasing clast size, contrarily to proposed by Passchier and Simpson (1986).

In order to account for productivity of mantle material during deformation we add a productivity rate, Π , to the LIRM. Π is defined analogous to \dot{H} and describes the change in the thickness solely due to the productivity. The total change in lubricant thickness is now the sum of $\Pi + \dot{H}$ and therefore the zero contour lines of the (total) thickness change rate will be altered, depending on the value of Π . The effect of this addition of Π is shown in Figure 24. Note that the productivity values are given normalized with $\dot{\gamma}$ and for readability of the plots multiplied by 100.

$$\bar{\Pi} = 100 \frac{\Pi}{\dot{\gamma}} \quad (8)$$

We can express $\bar{\Pi}$ as

$$\bar{\Pi} = 100 \dot{H} = 100 \frac{dH}{d\gamma} \quad (9)$$

Hence the meaning of the measured $\bar{\Pi}$ value is that per one γ , $\bar{\Pi}/100$ percent mantle material is produced.

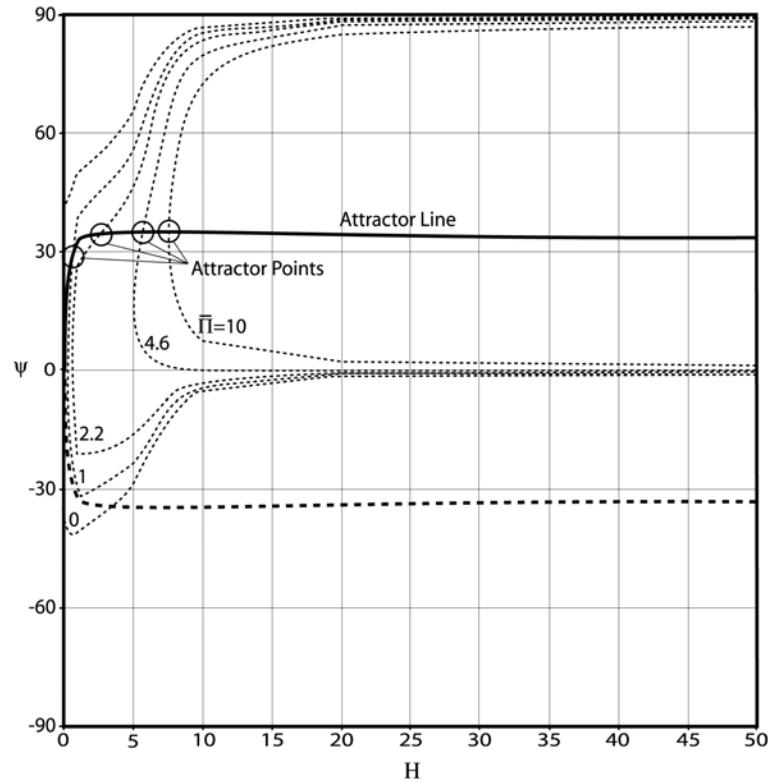
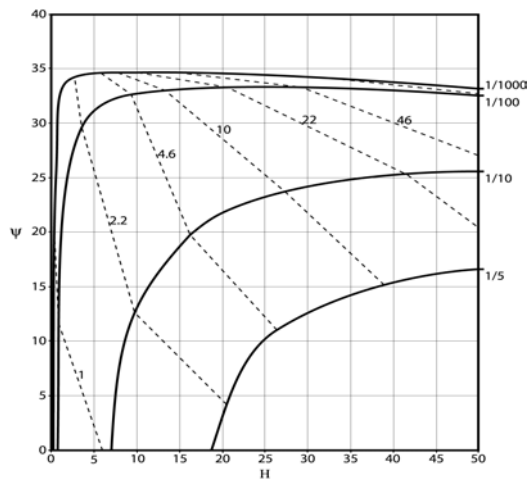


Figure 24

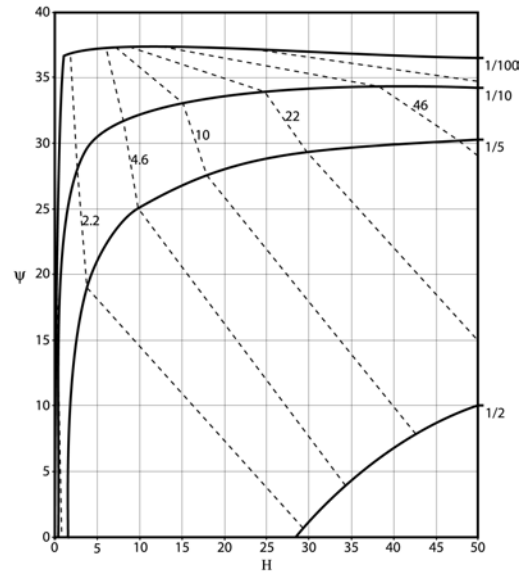
LIRM with added productivity for an ellipse with aspect ratio 2:1 and lubricant viscosity 1/1000.

The important effect of adding Π is that, for certain values, the zero contours of \dot{H} now intersect the attractor line. These intersection points are stable attractor points that attract inclusions from the entire $\psi - H$ plane and, once the attractor point is reached, the inclusion will remain in this inclination with the corresponding value of lubricant thickness for as long as the productivity Π remains unchanged. For a given aspect ratio two parameters greatly affect the location of the attraction point: $\bar{\Pi}$ and $\eta_{matrix} / \eta_{mantle}$ (cf. Figures 23 and 24). Conversely, many points in the $\psi - H$ plane may become attraction points for a particular combination of $\bar{\Pi}$ and $\eta_{matrix} / \eta_{mantle}$.

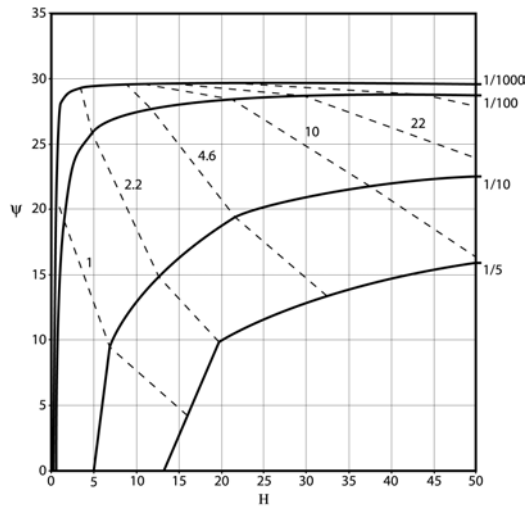
In order to summarize the existence of attractor points for different aspect ratios, viscosity contrasts, productivity rates, and power-law exponents we have produced the attractor maps displayed in Figure 25.



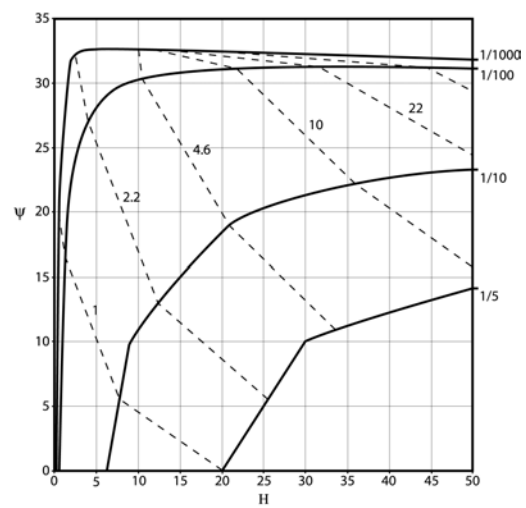
a) $R=2, n_{\text{lubricant}}=1, n_{\text{matrix}}=1$



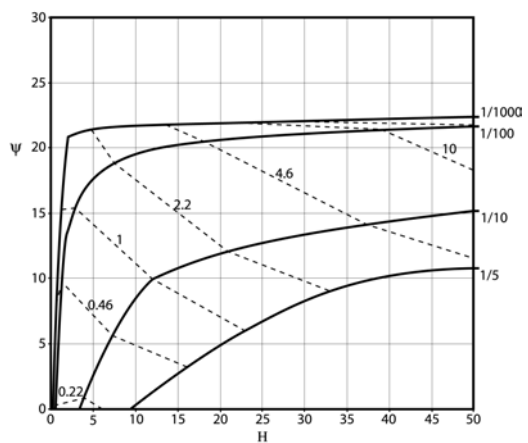
b) $R=2, n_{\text{lubricant}}=3, n_{\text{matrix}}=3$



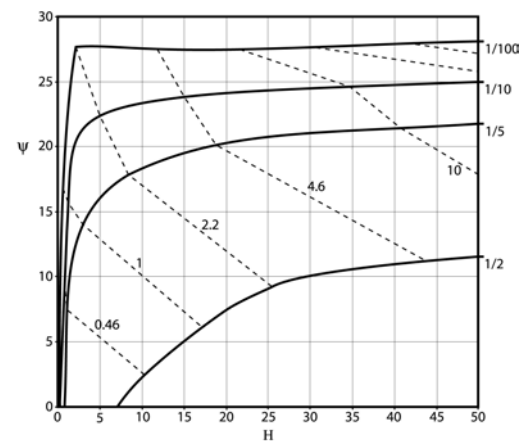
c) $R=3, n_{\text{lubricant}}=1, n_{\text{matrix}}=1$



d) $R=3, n_{\text{lubricant}}=1, n_{\text{matrix}}=3$



e) $R=6, n_{\text{lubricant}}=1, n_{\text{matrix}}=1$



f) $R=6, n_{\text{lubricant}}=3, n_{\text{matrix}}=5$

Figure 25

Attractor maps for various aspect ratios and power-law exponents.

For given $\psi - H$ couples (and aspect ratio) the attractor maps yield the values of the matrix-mantle viscosity contrast and mantle productivity rate that allow the particle to maintain its inclination, ψ . The values of $\bar{\Pi}$ and $\eta_{matrix} / \eta_{mantle}$ can be by interpolation between the corresponding iso-contour lines (solid=viscosity contrast, dashed=mantle productivity). The attractor maps also allow a comprehensive overview over the size of the fields in which stable inclinations occur and thus at which particle inclination back-rotation is to be expected. In particular the attractor maps yield the maximum possible inclination angle.

The characteristics of the attractor maps are:

1. The iso-viscous attractor lines show, for all aspect ratios and rheologies, the same tendency, namely that decreasing the viscosity of the lubricant widens the field of back rotation in the $\psi - H$ plane.
2. Once the viscosity of the lubricant is $<1/1000$ of the viscosity of the matrix the behavior of the inclusion is no more sensitive to further decreases in lubricant viscosity for the range of H considered. Zooming into the map would make the dependence on larger viscosity contrasts visible.
3. Increasing the aspect ratio leads to a decrease in the maximum stable inclination angle.
4. For all Newtonian rheologies, the lubricant viscosity has to be less than $1/2$ that of the matrix for back rotation to occur (given that the maximum lubricant thickness is ≤ 50).
5. The introduction of power-law rheology increases the maximum stable inclination angle.
6. The introduction of a power-law lubricant allows stabilization to occur already for an effective viscosity contrast of $1/2$ (due to the underestimation of the actual effective viscosity contrast).
7. Productivities that produce stable attractor points lie in the range $0.22 \leq \bar{\Pi} \leq 100$, i.e., $(0.002\%-1\%)*b$ per $\Delta\gamma = 1$.

APPLICATION OF ATTRACTOR MAP METHOD

VISCOSITY CONTRAST AND PRODUCTIVITY ESTIMATION

The primary use of the presented attractor maps is for estimating the rate at which the clast material was turned into mantle material and for approximating the effective viscosity contrast between mantle and the matrix. The required information are simple geometrical parameters, measurable in the field or thin sections. This procedure is demonstrated with the example of the mica fish in Figure 26. The mica is embedded in a quartz rich matrix, the shear sense is top to the left and the shear plane is horizontal. Relative to the shear plane, the clast shows a positive inclination, which is assumed to be stable. The clast is surrounded by finer grained material that is derived from the clast and long but very thin tails exist, as indicated by the trace of fine grained mica material at the top right and bottom left of the clast.

The geometrical parameters needed for the attractor map method are aspect ratio, inclination and mantle thickness. The first two parameters are easily determined and the values are $a/b = 3.5$ and $\psi = 14^\circ$. The attractor map that comes closest to the measured aspect ratio was generated for $a/b = 3$, which is assumed to be applicable. Since the clast is not perfectly elliptical, several ways exist in which to determine H , as shown in the insert of Figure 26. However, the average value is around $H \approx 17$, and it is obvious from the corresponding attractor map, Figure 27, that variations on the observed scale are not significant. The measured values of ψ and H allow for the construction of an intersection point on the attractor map.

This intersection point yields the estimates of mantle material productivity and viscosity contrast between matrix and mantle material, which are found by interpolating between the solid lines (viscosity contrast) and dashed lines (mantle productivity). Doing this reveals that the viscosity contrast between the matrix and the mantle was rather small, in the range of 1:5 to 1:10. The mantle material productivity is approx. $\bar{\Pi} \approx 2.5$. Thus, if the position of the mica is indeed stable, it needs to produce 0.025% mantle material (relative to b) per γ to maintain the present inclination. Both obtained parameters, the effective mantle-matrix viscosity contrast and the mantle material productivity rate, are in a reasonable range that may be expected for natural mylonites.

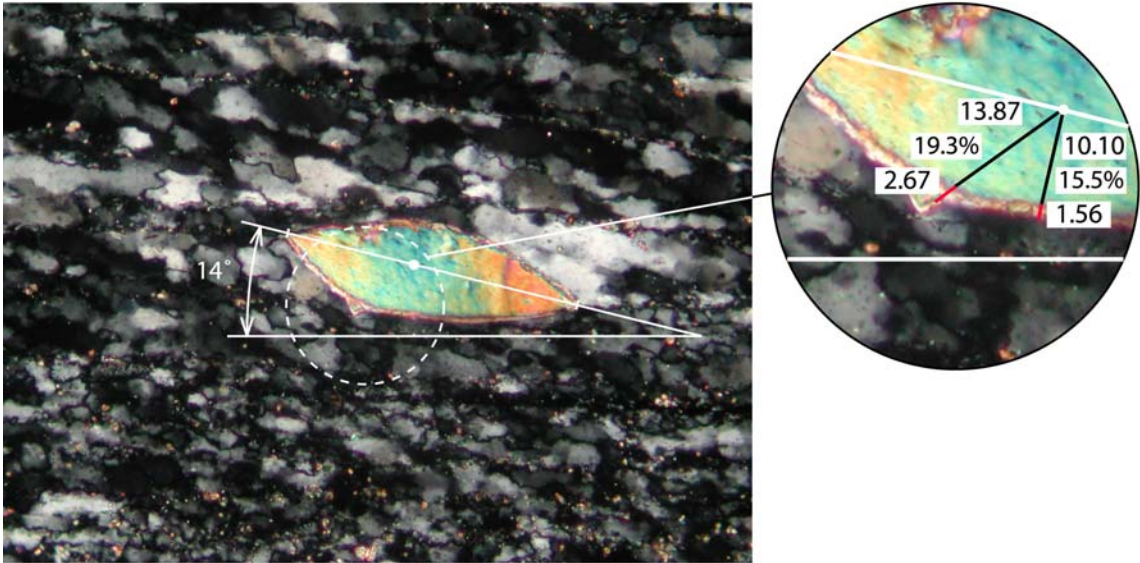


Figure 26

Mica fish from the Dent Blanche nappe. Height of picture is $70\mu\text{m}$. Shear sense is top to left, shear plane is horizontal. Measured aspect ratio is $R=3.5$, inclination $\psi = 14^\circ$, and mantle thickness is ca. $H=17$ (average of two different measurements).
(Photo courtesy G. Pennacchioni)

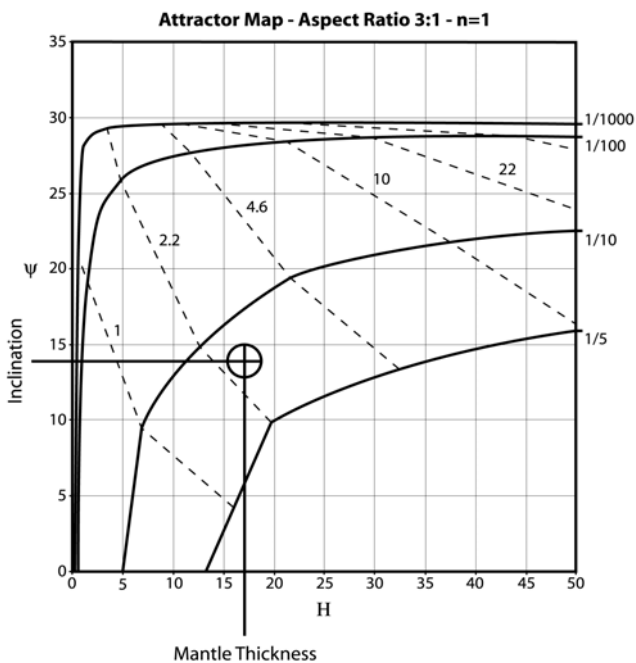
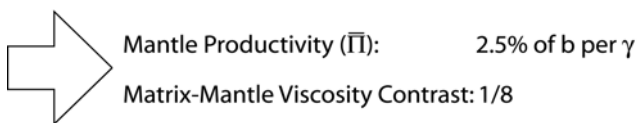


Figure 27

Interpretation of Figure 26 on the corresponding attractor map. Solid are the iso-viscosity-contrast lines, dashed are the iso-mantle-productivity lines (normalized $\rightarrow \bar{\Pi}$).



SHEAR STRAIN ESTIMATION

The attractor map method has been derived as a tool for estimating the productivity of mantle material and the viscosity contrast between matrix and mantle. However, if it is possible to determine the total area of mantle material, M , we can use the mantle productivity value to estimate the total amount of shear strain. The corresponding equation is

$$\gamma = 100 \frac{M}{cb\bar{\Pi}} \quad (10)$$

where M is the area of the mantle and c is the circumference of the ellipse. Since the exact expression of the circumference of an ellipse is an infinite series, we must use an approximated form. The simplest form is (given by Kepler (c.f., Kepleri, 1860))

$$c = \pi(a + b) \quad (11)$$

which has a maximum error of $\approx 21\%$. Better approximations, notably the ones by Ramanujan, can be found in Almkvist and Berndt (1988).

The clast example given in Figure 26 has very narrow tails that are almost impossible to identify and consequently, the total mantle area is difficult to determine. Therefore, we demonstrate the shear strain estimation with a hypothetical case, Figure 28. The attractor map yields a mantle material productivity rate of $\bar{\Pi} \approx 3$. Substituting the additional geometrical parameters into eqn. (10), we obtain a shear strain approximation of $\gamma \approx 5.3$.

Cases like the one shown in Figure 26 where the area of the mantle material cannot be determined, either because it is too narrow at places or dissolved, may still yield shear strains if the original size of the clast can be estimated. In Figure 28a), the dashed black line represents such a hypothetical original clast. In nature, statistics of clast sizes inside and outside shear zones may be used to approximate the amount of mantle material produced. Or it may simply be assumed that the largest clast size outside the shear zone corresponds to the largest clast size within the shear zone.

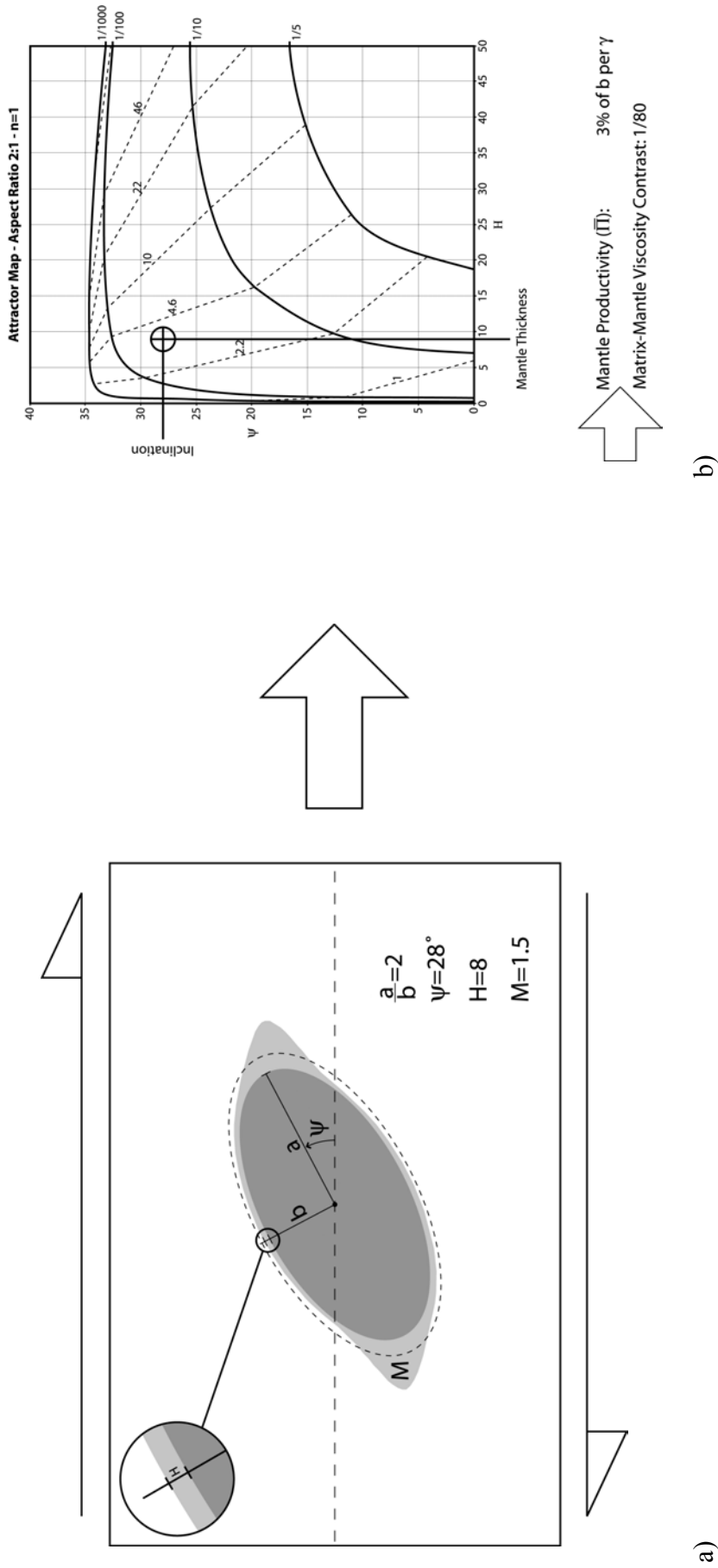


Figure 28

Hypothetical mantled clast in a stable position (a) and the interpretation on the corresponding attractor map (b). The additional parameters needed to calculate the shear strain are the absolute values of the ellipse radii and the area of the mantle (M), which are (normalized by b): $a=2$, $b=1$, and $M=1.5$. In a) the dashed black line depicts the circumference of an ellipse that has the same aspect ratio as the smaller ellipse, but contains the total area of smaller ellipse and mantle together

The strain estimate formula for this case is

$$\gamma = \frac{100}{\bar{\Pi}} \left(\frac{b_o}{b_c} - 1 \right) \quad (12)$$

where b_o and b_c are the original and current minimum clast radius, respectively.

More generally, the method may be applicable to polyphase rocks that show a distinct orientation and grain size when subject to shear, a hypothesis that should be tested either by laboratory experiments with torsion rigs, with field examples or numerically.

LIMITATIONS OF THE ATTRACTOR MAP METHOD

In order to be able to tackle the complexity of the mantled porphyroclast system we have restricted our investigation to elliptical shapes. Clasts in natural mylonites can have more complex forms. However, it has been shown by Ferguson (1979) and Arbaret et al. (2001) for the classical Jeffery solution that even if strongly non-elliptical objects are used, the ellipse shape based theory remains an excellent approximation of the rotational behavior. We expect to see a similar insensitivity to actual clast shape concerning the validity of the presented attractor maps. Indeed, Mancktelow et al. (2002) have shown that lubricated rhomboidal particles show the same characteristic back-rotational and stable inclination behavior as observed here.

Another objection that might be considered is that natural clasts with systematic orientation are observed but they do not have a mantle. It is likely that such clasts have an imperfect bonding to the matrix which can be looked at as the limiting case of a lubricant layer, where the thickness goes to zero, normal tractions are continuous but shear tractions vanish. Therefore the clast behavior will effectively follow the descriptions above. Yet, the attractor maps will not be applicable since there is no actual lubricant layer that is perfectly bonded to the clast and the matrix.

Previous explanations of systematic clast stabilization have been mostly based on the combined effect of pure and simple shear. Here we focus only on simple shear and ignore possible pure shear components. If an additional pure shear component is present the results may be altered, however, mylonites are characterized by the large amounts of

shear displacement accumulated in relatively narrow zones and therefore clearly simple shear dominated the system. Under these conditions, the combined pure and simple shear theory does not exhibit stable inclinations and can be ruled out. We therefore conclude that, apart from very particular cases, the effects of contemporaneous pure shear are minor.

Care has been taken to avoid boundary or clast interaction effects. This simplifies the analysis but is to some extent unrealistic since the clast densities in mylonites may lead to clast interaction. It has been shown by Ildefonse et al. (1992) that the interaction effects become significant if individual clasts are closer than one diameter, and this distance is assumed to be the limit of applicability of the presented work.

Another important aspect is that natural shear zones accommodate large amounts of strain through strain partitioning whereby large areas do not deform much and most strain is concentrated in the narrow zones that make up the so-called C-S fabrics (Berthe et al., 1979; Lister and Snoke, 1984). If a C-S fabric is present then local shear flows may differ from the bulk shear and consequently the shear strain recorded by a clast may not be representative for the bulk of the rock mass.

CONCLUSIONS

We have investigated the mantled porphyroclast in a shear zone as a three phase system where the viscosity of the mantle material is lower than the matrix and the “rigid” clast. The introduction of a weak mantle has a strong influence on the distribution and amplitudes of effective strain rates, pressures and maximum shear stresses. The most prominent effects of the weak mantle are found in the clast kinematics. We have shown that for a large set of parameters the clast has meta-stable positions that are always at positive inclinations relative to the shear plane and direction. In order to reach this positions the clast can either rotate with the applied shear or against it, depending on the starting position. If a mantle material productivity rate is added, which is clearly the case in nature, stable inclination angles result. These inclination angles range from 40° to 0°, depending on the viscosity contrast between matrix and mantle, the power law exponent of the materials, the thickness of the mantle, the mantle material productivity,

and the aspect ratio. Generally the stable inclination angle decreases with growing aspect ratio, which is in agreement with observations of clasts in natural shear zones (ten Grotenhuis et al., 2002).

Systematic investigation of the behavior of the lubricated clast in a shear zone results in attractor maps. These maps are a novel tool for estimating the mantle material productivity and the viscosity contrast between mantle and matrix by means of simple geometrical parameters. In combination with the area of the clast and the mantle, the knowledge of the mantle material productivity rate yields an approximation for the total shear strain. In absence of conventional shear strain markers, such as vein offsets, the new method is the only tool that can provide estimates for the shear strain.

ACKNOWLEDGMENTS

This research was supported by the ETH Zurich, grant TH 0-20650-99. We wish to thank Jean-Pierre Burg, Stefano Ceriani, Neil Mancktelow, Fernando Ornelas and Karel Schulmann for helpful and inspiring discussions.

REFERENCES

- Almkvist, G. and Berndt, B., 1988. Gauss, Landen, Ramanujan, the Arithmetic-Geometric Mean, Ellipses, Pi, and the Ladies-Diary. *American Mathematical Monthly*, 95(7): 585-608.
- Arbaret, L., Mancktelow, N.S. and Burg, J.P., 2001. Effect of shape and orientation on rigid particle rotation and matrix deformation in simple shear flow. *Journal of Structural Geology*, 23(1): 113-125.
- Berthe, D., Choukroune, P. and Jegouzo, P., 1979. Orthogneiss, Mylonite and Non Coaxial Deformation of Granites - Example of the South-Armorican-Shear-Zone. *Journal of Structural Geology*, 1(1): 31-42.
- Bons, P.D., Barr, T.D. and tenBrink, C.E., 1997. The development of delta-clasts in non-linear viscous materials: A numerical approach. *Tectonophysics*, 270(1-2): 29-41.
- Brezzi, F. and Fortin, M., 1991. Mixed and hybrid finite elements methods. Springer series in computational mathematics ; 15. Springer-Verlag, New York, ix, 350 pp.
- Ceriani, S., Mancktelow, N.S. and Pennacchioni, G., 2002. Analogue modelling of the influence of aspect ratio and particle/matrix interface slip on the rotational behavior of monoclinic and elliptical rigid particles in non-coaxial flow. *Journal of Structural Geology*, This volume(This issue).

- Crouzeix, M. and Raviart, P.A., 1973. Conforming and Nonconforming Finite-Element Methods for Solving Stationary Stokes Equations. *Revue Francaise D Automatique Informatique Recherche Operationnelle*, 7(DEC): 33-75.
- Eshelby, J.D., 1959. The Elastic Field Outside an Ellipsoidal Inclusion. *Proceedings of the Royal Society of London Series a- Mathematical and Physical Sciences*, 252(1271): 561-569.
- Ferguson, C.C., 1979. Rotations of Elongate Rigid Particles in Slow Non-Newtonian Flows. *Tectonophysics*, 60(3-4): 247-262.
- Furuhashi, R., Huang, J.H. and Mura, T., 1992. Sliding Inclusions and Inhomogeneities with Frictional Interfaces. *Journal of Applied Mechanics-Transactions of the Asme*, 59(4): 783-788.
- Gao, Z., 1995. A Circular Inclusion With Imperfect Interface: Eshelby's Tensor and Related Problems. *Journal of Applied Mechanics-Transactions of the Asme*, 62: 860-866.
- Ghosh, S.K. and Ramberg, H., 1976. Reorientation of Inclusions by Combination of Pure Shear and Simple Shear. *Tectonophysics*, 34(1-2): 1-70.
- Hanmer, S. and Passchier, C.W., 1991. Shear sense indicators: a review. *Geological Survey of Canada*, 90: 1-71.
- Ilddefonse, B., Sokoutis, D. and Mancktelow, N.S., 1992. Mechanical Interactions between Rigid Particles in a Deforming Ductile Matrix - Analog Experiments in Simple Shear-Flow. *Journal of Structural Geology*, 14(10): 1253-1266.
- Jaeger, J.C. and Cook, N.G.W., 1979. *Fundamentals of rock mechanics*. Chapman & Hall, London, XXII, 593 pp.
- Jeffery, G.B., 1922. The motion of ellipsoidal particles immersed in a viscous fluid. *Proceedings of the Royal Society of London*, A102: 161-179.
- Kenkmann, T., 2000. Processes controlling the shrinkage of porphyroclasts in gabbroic shear zones. *Journal of Structural Geology*, 22(4): 471-487.
- Kepleri, J., 1860. *Astronomia Nova. Opera Omnia*, 3. Heyder & Zimmer, Frankfurt.
- Kocks, U.F., Tomé, C.N., Wenk, H.-R., Mecking, H. and Beaudoin, A.J., 1998. *Texture and anisotropy preferred orientations in polycrystals and their effect on materials properties*. Cambridge University Press, Cambridge, XII, 676 S. pp.
- Lister, G.S. and Snoke, A.W., 1984. S-C Mylonites. *Journal of Structural Geology*, 6(6): 617-638.
- Mancktelow, N.S., Arbaret, L. and Pennacchioni, G., 2002. Experimental observations on the effect of interface slip on rotation and stabilisation of rigid particles in simple shear and a comparison with natural mylonites. *Journal of Structural Geology*, 24(3): 567-585.
- Marques, F.O. and Coelho, S., 2001. Rotation of rigid elliptical cylinders in viscous simple shear flow: analogue experiments. *Journal of Structural Geology*, 23(4): 609-617.
- Mura, T., 1987. *Micromechanics of defects in solids*. Nijhoff, Dordrecht etc., XIII, 587 S. pp.
- Mura, T., 2000. Some new problems in the micromechanics. *Materials Science and Engineering a-Structural Materials Properties Microstructure and Processing*, 285(1-2): 224-228.
- Muskhelishvili, N.I., 1953. *Some basic problems of the mathematical theory of elasticity*. Noordhoff, Groningen, 704 S. pp.
- Passchier, C.W. and Simpson, C., 1986. Porphyroclast Systems as Kinematic Indicators. *Journal of Structural Geology*, 8(8): 831-843.
- Passchier, C.W., Tenbrink, C.E., Bons, P.D. and Sokoutis, D., 1993. Delta-Objects as a Gauge for Stress Sensitivity of Strain-Rate in Mylonites. *Earth and Planetary Science Letters*, 120(3-4): 239-245.
- Passchier, C.W. and Trouw, R.A.J., 1996. *Microtectonics*. Springer, Berlin [etc.], XIII, 289 S. pp.
- Pennacchioni, G., Di Toro, G. and Mancktelow, N.S., 2001. Strain-insensitive preferred orientation of porphyroclasts in Mont Mary mylonites. *Journal of Structural Geology*, 23(8): 1281-1298.

- Pennacchioni, G., Fasolo, L., Cecchi, M.M. and Salasnich, L., 2000. Finite-element modelling of simple shear flow in Newtonian and non-Newtonian fluids around a circular rigid particle. *Journal of Structural Geology*, 22(5): 683-692.
- Ranalli, G., 1995. *Rheology of the Earth*. Chapman & Hall, London [etc.], XV, 413 S. pp.
- Ru, C.Q. and Schiavone, P., 1997. A circular inclusion with circumferentially inhomogeneous interface in antiplane shear. *Proceedings of the Royal Society of London Series a-Mathematical Physical and Engineering Sciences*, 453(1967): 2551-2572.
- Shen, H., Schiavone, P., Ru, C.Q. and Mioduchowski, A., 2000. Analysis of internal stress in an elliptic inclusion with imperfect interface in plane elasticity. *Mathematics and Mechanics of Solids*, 5(4): 501-521.
- Shen, H., Schiavone, P., Ru, C.Q. and Mioduchowski, A., 2001. Stress analysis of an elliptic inclusion with imperfect interface in plane elasticity. *Journal of Elasticity*, 62(1): 25-46.
- Simpson, C. and Wintsch, R.P., 1989. Evidence for Deformation-Induced K-Feldspar Replacement by Myrmekite. *Journal of Metamorphic Geology*, 7(2): 261-275.
- Stagni, L., 1991. Elastic field perturbation by an elliptic inhomogeneity with a sliding interface. *Journal of Applied Mathematics and Physics*, 42: 881-819.
- Ten, A.A. and Yuen, D.A., 1999. Time-dependent formation of mantled inclusion structures for different rheologies under a simple shear. *Earth and Planetary Science Letters*, 165(1): 25-35.
- ten Grotenhuis, S.M., Passchier, C.W. and Bons, P.D., 2002. The influence of strain localisation on the rotation behaviour of rigid objects in experimental shear zones. *Journal of Structural Geology*, 24(3): 485-499.
- Tullis, J. and Yund, R.A., 1987. Transition from Cataclastic Flow to Dislocation Creep of Feldspar - Mechanisms and Microstructures. *Geology*, 15(7): 606-609.

APPENDIX - CHECKS VERSUS ANALYTICAL SOLUTIONS

In order to check the numerical code for the specific problem, several finite strain runs with a rigid clast in a weak matrix ($\eta_{clast} / \eta_{matrix} = 1000$) were performed and compared to the solutions of Jeffery (1922) and Ghosh and Ramberg (1976). Since continuous remeshing is applied the achievable strains are unlimited and the experiments simply stopped after they had eaten enough CPU time. The comparison shows that numerical values coincide with the analytical solutions. The only case where a slight deviation is observed is for large γ values in the $\psi - \gamma$ plot. This is due to the accumulation of smallest deviations from the analytical values that add up in this plot since it is plotted versus γ together with the application of a simple time stepping scheme (Euler).

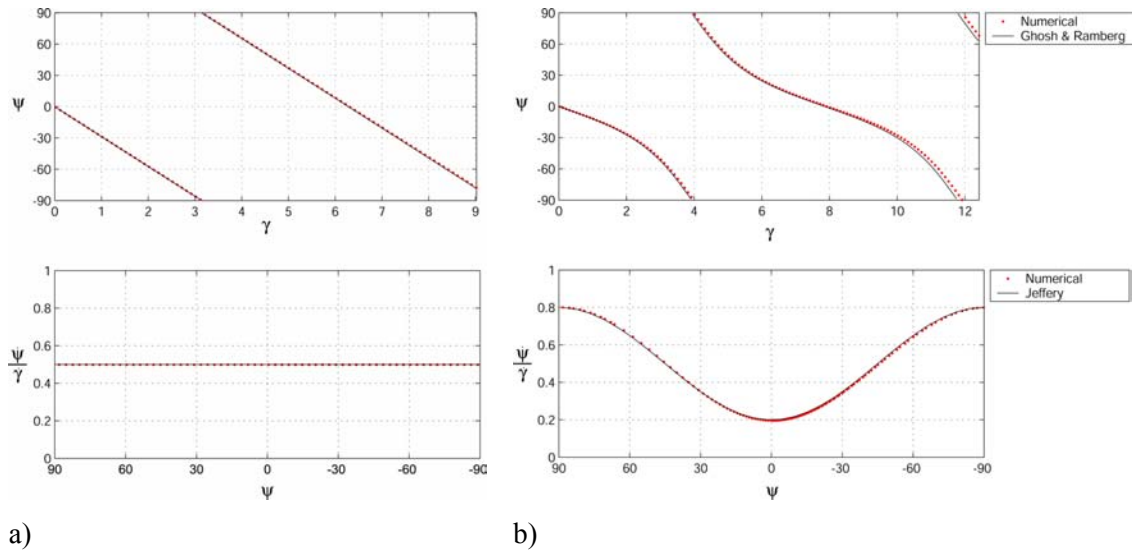


Figure 29

Comparison of numerical code versus analytical solutions.

a) Circular inclusion

b) Elliptical inclusion with aspect ratio 2:1

CHAPTER 3: ANALYTICAL SOLUTIONS FOR DEFORMABLE ELLIPTICAL INCLUSIONS IN GENERAL SHEAR

(This chapter is submitted to “Geophysical Journal International” by Daniel W. Schmid and Yuri Yu. Podladchikov)

SUMMARY

Using Muskhelishvili’s method, we present closed-form analytical solutions for isolated elliptical inclusions in general shear far-field flows. The inclusion is either perfectly bonded to the matrix or to an intermediate layer, termed the “mantle”. The solutions are valid for incompressible all-elastic or all-viscous systems. The actual values of the shear modulus or viscosity in the inclusion, mantle and matrix can be different and no limits are imposed on the possible contrasts. The presented solutions are complete two-dimensional solutions and the parameters that can be analysed include all kinematic (stream functions, velocities, strain rates, strains) and dynamic parameters (pressure, maximum shear stress, etc.). Refraining from giving the tedious derivation of the presented solutions we focus on how to use the solutions, how to extract the parameters of interest and how to apply and verify them. Since we want to demonstrate the usefulness of Muskhelishvili’s method for slow viscous flow problems, we apply our results to the mantled porphyroclast in a shear zone. Another important application is the benchmarking of numerical codes for which the presented solutions are most suitable due to the infinite range of viscosity contrasts and the strong local gradients of properties and results. In order to stimulate a more widespread use of the Muskhelishvili’s method, all solutions are implemented in MATLAB and downloadable from the web.

INTRODUCTION

The aim of this paper is threefold: i) to demonstrate the power of Muskhelishvili's complex variable method (Muskhelishvili, 1953) for solving two dimensional viscous as well as elastic problems, ii) provide a set of analytical solutions that are of major importance for various geological and geophysical applications, and iii) present a set of benchmarks that allow thorough testing of numerical codes solving incompressible, variable viscosity problems in two dimensions.

OVERVIEW MUSKHELISHVILI METHOD

The original motivation for the development of the Muskhelishvili method was to obtain analytical formulae for stress concentration around holes and recesses in engineering structures and machines (Savin, 1961). This was important because it had been noticed that, for example, canon holes in battle ships may cause a large reduction in strength so that even collisions with small vessels could cause the battle ship to break apart (Muskhelishvili, 1953). Kolosov (1907) first derived the analytical expression for stress concentration around an elliptical hole through the use of complex potentials. In the twenties and early thirties, Muskhelishvili generalized the method through the use of conformal mapping. With his method it is possible to solve the problem of an elastic plate containing holes of virtually any shape and many other problems of torsion, contact and bending. His work was published in book form in 1933 as "Some fundamental Problems of the Mathematical Theory of Elasticity" and the English translation became available in 1953.

Based on this historical excursion it may seem that the method is restricted to problems in elasticity. However, the instantaneous elastic and viscous problems are mathematically identical and, therefore, the method is equally valid for problems of slow viscous flow. Another perception may be that the method is only applicable to holes or voids. In fact, the method is mainly applied to problems involving voids such as cracks or tunnels (e.g., Jaeger and Cook, 1979), yet it is not limited to such applications as we will show here.

GEOLOGICAL RELEVANCE

In order to demonstrate the power of Muskhelishvili's method for problems of slow viscous flow, we will provide the analytical solutions for three different problems and emphasize how to use them. The solutions given are applicable to many different problems in geology and geophysics. We choose here to principally relate the solutions to the mantled porphyroclast in a mylonitic shear zone. The term "mantled porphyroclast system" is defined as follows (cf. Figure 1): a two-dimensional, mantled porphyroclast system

1. is a three phase system (clast, mantle and matrix), with three, possibly different, viscosities
2. is subjected to general shear, i.e., any combination of arbitrary inclined pure and simple shear
3. contains inclusion and mantle with elliptical shapes that are confocal
4. includes all degenerate cases such as circular shapes, infinite aspect ratios and zero mantle thickness.

The classical analytical solution for this problem was determined by Jeffery (1922) who derived the complete three dimensional solution for the rotational behaviour of a rigid ellipsoidal inclusion in a Newtonian matrix deforming in simple shear. By combining Jeffery's and Muskhelishvili's solutions, Ghosh and Ramberg (1976) derived how a rigid elliptical inclusion behaves in general two-dimensional shear. Yet, both Jeffery's and Ghosh and Ramberg's solutions only describe the kinematics of the rigid inclusion and do not give the dynamic parameters such as the stress components. In recent years interest in obtaining the distribution and amplitudes of the stresses in and around inclusions has been expressed. The pressures and differential stresses around inclusions are needed to interpret localized metamorphic reactions (e.g., Simpson and Wintsch, 1989) and for understanding deformation mechanisms (e.g., Kenkmann and Dresen, 1998). Local stress deviations caused by the presence of almost rigid clasts may, for example, cause over- or under-pressures in the geologic system that can hamper the P-T path interpretation and hence, the conversion of pressures into burial depth (e.g., Tenczer et al., 2001). Another shortcoming of the mentioned solutions is that they are strictly only valid for infinite viscosity contrasts between the clast and matrix. There is

no existing solution used for the analysis of deforming media that accounts for clasts that are either mantled or do not have perfectly bonded interfaces. Since finite viscosity contrasts and slipping interfaces are more likely to be the normal case than the exception, it is essential to have the analytical solution of the mantled porphyroclast system, not only in terms of kinematics, but also dynamics. The similarity between the mantled clast and the slipping interface clast is that at the limit of vanishing mantle viscosity and small mantle thickness, the normal traction and velocity are continuous through the interface, but the shear tractions and tangential velocity vanish, which are the characteristics of a slipping interface. Thus, the slipping interface clast is an end-member case of the mantled clast.

Two relatively straightforward methods are available to obtain exact analytical solutions for the described problem: the mentioned Muskhelishvili method and Eshelby's solution (Eshelby, 1959). The solution found by Eshelby is capable of dealing with three-dimensional spherical inclusions and is used frequently in fracture mechanics (e.g., Rice, 1968). It has also been used occasionally to analyse the behaviour of clasts in viscous shear flows (Bilby et al., 1975; Freeman, 1987). However, even proponents of Eshelby's solution affirm that "for plane strain or plane stress inhomogeneity problems, the complex potential method of Muskhelishvili (1953) is more effective than the equivalent inclusion method (i.e., Eshelby's solution)" (Mura, 1987).

The interest in isolated lubricated or perfectly bonded particles is not restricted to the geological community but is in fact inherent to a many other fields of science. The importance of the behaviour of composites has mainly stimulated researchers in recent years to derive the analytical solution for problems similar to the one posed here. As expected, the methods used are those of Eshelby and Muskhelishvili. Since the relevant references stem from different fields of science, it is difficult to answer the question concerning who the original authors of the principal solutions are. Additional complication comes from the fact that a large portion of the literature was originally written in Russian and was either never translated or is difficult to obtain. The books by Muskhelishvili (1953) and Savin (1961) contain most of the individual building blocks that make up the described problem. Therefore, we leave further research up to the interested reader and simply list the related literature: Mura (1987), Stagni (1991),

Furuhashi et al. (1992), Huang et al. (1993), Gao (1995), Ru and Schiavone (1997), Shen et al. (2001).

Common findings of the more recent works are that (1) the Eshelby conjecture does not hold for imperfect bonding between matrix and clast, and (2) the lubricated ellipse does not have a closed-form solution. The first finding simply means that the stress and strain (rate) components inside the inclusion cannot be described by a single value, which is the case for the perfect bonding between clast and matrix. The second finding means that the solution is an infinitely long series (Shen et al., 2001). For this reason we refrain from presenting the mantled elliptical inclusion here. Instead we concentrate on the cases for which finite series solutions can be found.

NUMERICAL CODE BENCHMARKING

The merit of analytical solutions is that they are the final answer to the question asked. In addition the answer to the follow-up questions are usually directly deducible from the solutions found. This is especially true for Muskhelishvili solutions which are complete two dimensional solutions and come with a set of rules on how to extract any desired kinematic or dynamic parameter. Yet, cases for which analytical solutions can be found are the minority and generally asymptotic methods (e.g., Barenblatt, 1996) combined with numerical models must be used instead or in addition. Nevertheless, analytical solutions retain their importance because numerical codes must be tested. The majority of analytical benchmark tests in use are restricted to essentially one dimensional viscosity profiles (Moresi et al., 1996). These may be difficult enough as demonstrated by Pelletier et al. (1989), nevertheless two dimensional codes should be benchmarked versus appropriate analytical solutions. “Essentially one dimensional” refers to the category of tests that are based on linear stability analysis such as two-dimensional folding (e.g., Biot, 1961; Fletcher, 1974) or diapirism (Chandrasekhar, 1961). Mathematically, in these problems the viscosity contrast does not affect the left-hand-side, i.e., the stiffness matrix of the system, but only contributes to the right hand side of the system of linear equations generated by the discretisation process. These problems do not account for any interaction between different harmonics (in frequency space) and are therefore only partly suitable for two dimensional benchmarking.

The solutions presented here implement genuine two dimensional problems. The complete solution is described using simple polynomials for complex potentials. The entire viscosity contrast range is covered and strong local gradients of properties and solutions can be present (such as within the rim), features which are crucial for proper code benchmarking.

SOLUTION IMPLEMENTATION AND AVAILABILITY

We choose to present the solutions without cumbersome derivation, because it is our aim to demonstrate how the basic set of equations allows for the derivation of any desired parameter and how the results can be applied and verified. Naturally, the solutions fulfil mass and force balance, rheological equations and far-field boundary conditions. They are obtained by matching the tractions and the velocities through the interfaces and solving the linear system of equations for the coefficients of the polynomial representations of complex potentials. In the same manner one can verify the presented solutions.

In order to stimulate a more widespread use of Muskhelishvili's method in general, and application of our results in particular, all MATLAB scripts used within this paper will be made available. MATLAB can directly deal with complex numbers and is therefore most suitable for visualizing solutions in terms of complex potentials. In addition, the scripts generate color plots that are more meaningful than the grayscale images presented here. The scripts are downloadable free of charge through the e-collection of the ETH Zürich under <http://e-collection.ethbib.ethz.ch/show?type=bericht&nr=188>. Figures in this paper that have a corresponding MATLAB script contain the name of the generating script in brackets at the end of the figure caption.

BRIEF REVIEW OF MUSKHELISHVILI'S METHOD

An in-depth introduction to Muskhelishvili's method is beyond the scope of this paper. Instead we will just provide the most important equations and describe how the various parameters of interest can be extracted from the obtained solution. Since the

documentation of Muskhelishvili's method is not easily obtainable, we give a few, hopefully helpful, references. Readers who are completely unfamiliar with the concept of complex potentials may start with the related fields of fluid dynamics, heat conduction and electrostatics, where the equations are Laplacian instead of double Laplacian, and consequently the solutions are simpler (only one complex potential). In addition, more literature on this subject exists, for example, the classical textbook by Batchelor (1967) and the very detailed introduction by Spiegel (1964). Muskhelishvili's method is best explained in the original author's work. This book is not common to all libraries and we allow ourselves to point out that it is available again through Kluwer's "Printing on Demand" (PoD) program; unfortunately at a somewhat expensive price. A more recent book providing a detailed introduction to the subject is Lu (1995). Readily accessible is the book by Jaeger and Cook (1979) which gives quite a broad introduction to the use of the method, mainly for the concentrations of stress around holes.

BASIC SET OF EQUATIONS

Muskhelishvili's method makes use of the fact that problems in two dimensions can conveniently be expressed in terms of a complex coordinate z . This is related to the usual, real $x - y$ Cartesian coordinates through

$$z = x + iy \quad (1)$$

where i is

$$i = \sqrt{-1} \quad (2)$$

In polar coordinates we can write z as

$$z = r \cos \theta + ir \sin \theta \quad (3)$$

where r is the radius, or the distance of the point to the origin and the angle θ is a measure of the angular distance to the horizontal. The latter form can be further converted with Euler's formula to

$$z = re^{i\theta} \quad (4)$$

The basis of the Muskhelishvili method is that the bi-harmonic equation, which describes the two-dimensional plane stress or plane strain elasticity problem, has a

general solution that can be expressed in terms of two complex functions, $\phi(z)$ and $\psi(z)$. The conditions imposed on $\phi(z)$ and $\psi(z)$ are that they must conform with the applied boundary conditions and be analytic, i.e., satisfy the Cauchy-Riemann equations (e.g., Jaeger and Cook, 1979). In simple terms, this means that complex potentials must be “normal” functions of z , such as $\sin(z)$, $\ln(z)$, z^2 , but not \bar{z} , $\Re(z)$ or $\Im(z)$. The over-bar denotes conjugation, \Re means the real part and \Im the imaginary part.

As already mentioned the instantaneous elastic and viscous problems are identical and the method equally applicable. Since we advocate a more widespread use of the method to slow flow problems, we provide here the three fundamental equations of the Muskhelishvili method for slow, incompressible, viscous flow in plane strain:

$$\sigma_{xx} + \sigma_{yy} = 4\Re(\phi'(z)) \quad (5)$$

$$\frac{\sigma_{yy} - \sigma_{xx}}{2} + i\sigma_{xy} = \bar{z}\phi''(z) + \psi'(z) \quad (6)$$

$$v_x + iv_y = \frac{\phi(z) - z\phi'(z) - \overline{\psi(z)}}{2\mu} \quad (7)$$

σ_{xx} , σ_{yy} and σ_{xy} are the components of the stress tensor, v_x and v_y are the horizontal and vertical velocities, μ is the viscosity of the material for which $\phi(z)$ and $\psi(z)$ are valid, prime and double prime denote the first and second derivatives versus z . Once the analytical expressions of $\phi(z)$ and $\psi(z)$ are obtained, stresses, velocities and a variety of other parameters can be evaluated. For example, the pressure (p) is obtained through eqn. (5) as

$$p = -2\Re(\phi'(z)) \quad (8)$$

Since the force balance equations determine the pressure only up to a constant, p is the pressure perturbation, i.e., an arbitrary (lithostatic) value may be added without any influence on the result. The sign convention used is that compressive pressure perturbations are positive.

Another useful parameter is the effective or maximum shear stress (τ), which is calculated as (e.g., Ranalli, 1995)

$$\tau = \sqrt{\left(\frac{\sigma_{xx} - \sigma_{yy}}{2}\right)^2 + \sigma_{xy}^2} \quad (9)$$

The Cartesian components of the velocity, v_x and v_y , are obtained from eqn. (7) by taking the real and imaginary parts, respectively. Another practical parameter for the analysis of two-dimensional flows is the stream function, Θ , (Turcotte and Schubert, 1982). The contour lines of Θ are used to visualize the flow of individual particles in steady state. The Cartesian definition of the Θ is

$$v_x = -\frac{\partial\Theta(x, y)}{\partial y} \quad (10)$$

$$v_y = +\frac{\partial\Theta(x, y)}{\partial x} \quad (11)$$

Hence, Θ can be obtained by integrating either v_x or v_y .

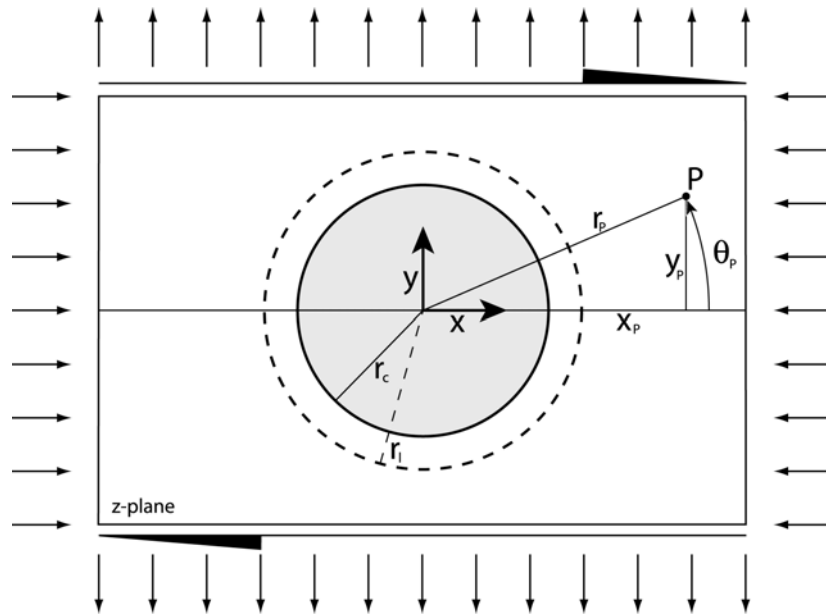


Figure 1

Setup of circular inclusion problem. A clast with radius r_c is embedded in a matrix and subjected to combined pure and simple shear far-field flows. In the case of a mantled circular inclusion, a layer of constant thickness is introduced between clast and matrix. The layer-matrix interface is defined through radius r_l . The origin of all coordinate systems is chosen to be the centre of the clast. The position of a point P in the z -plane can be expressed by three different coordinate systems, $P(z_p)$, $P(x_p, y_p)$, $P(r_p, \theta_p)$. Note that the presented analytical solutions are based on the assumption that the box boundaries are far from the clast and hence the size ratio of the box to the rest is not to scale.

FAR-FIELD FLOW EXPRESSIONS IN COMPLEX POTENTIALS

The kinematic boundary condition used in this work are pure shear (ps) strain rate, $\dot{\epsilon}$, and/or simple shear (ss) strain rate. In terms of complex potentials we write:

Pure Shear

$$\phi(z)_{ps} = 0 \quad (12)$$

$$\psi(z)_{ps} = -2\mu z \dot{\epsilon} \quad (13)$$

which through (7) give

$$v_x + iv_y = \bar{z} \dot{\epsilon} \quad (14)$$

using the identity given in eqn. (1) the typical pure shear flow field is obtained

$$v_x = \dot{\epsilon} x \quad (15)$$

$$v_y = -\dot{\epsilon} y \quad (16)$$

Simple Shear

$$\phi(z)_{ss} = -\frac{i}{2} \mu z \dot{\gamma} \quad (17)$$

$$\psi(z)_{ss} = i \mu z \dot{\gamma} \quad (18)$$

$$u_x + iv_y = -\frac{i}{2} (z - \bar{z}) \dot{\gamma} \quad (19)$$

$$v_x = y \dot{\gamma} \quad (20)$$

$$v_y = 0 \quad (21)$$

General Boundary Conditions

The addition of these shear flows yields the general, combined pure and simple shear (gps) boundary conditions:

$$\phi(z)_{gps} = -\frac{i\mu\dot{\gamma}z}{2} \quad (22)$$

$$\psi(z)_{gps} = (i\dot{\gamma} - 2\dot{\epsilon})\mu z \quad (23)$$

CIRCULAR INCLUSION

SOLUTION

The circular inclusion in a matrix of different viscosity subject to the general boundary conditions can be solved with Muskhelishvili's method and a detailed account for this problem has been given in Jaeger and Cook. Naturally, we need two sets of $\phi(z)$ and $\psi(z)$ to describe the result. One set, $\phi(z)_c$ and $\psi(z)_c$, describes the result within the inclusion/clast and is valid from the origin, chosen to be the centre of the clast, to the clast radius, r_c . The second set of complex potentials, $\phi(z)_m$ and $\psi(z)_m$, determines the solution in the matrix. Subscripts "c" and "m" are used to distinguish clast and matrix values, respectively.

Clast

$$\phi(z)_c = -\frac{i}{2}\mu_c z \dot{\gamma} \quad (24)$$

$$\psi(z)_c = 2(i\dot{\gamma} - 2\dot{\epsilon})\frac{\mu_c\mu_m}{\mu_c + \mu_m}z \quad (25)$$

Matrix

$$\phi(z)_m = -\frac{i}{2}\mu_m \dot{\gamma}z - (i\dot{\gamma} + 2\dot{\epsilon})Ar_c^2 z^{-1} \quad (26)$$

$$\psi(z)_m = (i\dot{\gamma} - 2\dot{\epsilon})\mu_m z - (i\dot{\gamma} + 2\dot{\epsilon})Ar_c^4 z^{-3} \quad (27)$$

with

$$A = \frac{\mu_m(\mu_c - \mu_m)}{\mu_c + \mu_m} \quad (28)$$

APPLICATIONS

Clast Kinematics

With this solution in terms of complex potential solution, it is possible to derive useful expressions such as the complete kinematics of the clast by plugging $\phi(z)_c$ and $\psi(z)_c$ into the velocity expression (eqn. (7)):

$$v_x + iv_y = \frac{\mu_m}{\mu_m + \mu_c} (i\dot{\gamma} + 2\dot{\epsilon})\bar{z} - \frac{i}{2}\dot{\gamma}z \quad (29)$$

This expression is valid for all possible viscosity contrasts between clast and matrix and for arbitrary combinations of simple and pure shear. It allows us to study the rotational behaviour of a circular clast in a mylonitic shear zone. Jeffery (1922) has shown that the rigid inclusion rotates with a rate that is half the applied shear rate. In order to reproduce this result, we need to derive the rotation rate, $\dot{\omega}$, that is inherent to eqn. (29). In Cartesian coordinates the rotation rate is defined as

$$\dot{\omega} = \frac{1}{2} \left(-\frac{\partial v_x}{\partial y} + \frac{\partial v_y}{\partial x} \right) \quad (30)$$

and is closely related to the shear strain rate, $\dot{\epsilon}_{xy}$, that is

$$\dot{\epsilon}_{xy} = \frac{1}{2} \left(\frac{\partial v_x}{\partial y} + \frac{\partial v_y}{\partial x} \right) \quad (31)$$

Hence in simple shear only ($\dot{\epsilon} = 0$), the clast rotation rate, inherent to eqn. (29) is

$$\dot{\omega} = -\frac{\dot{\gamma}}{2} \quad (32)$$

which is identical to Jeffery's result. If we apply a top to the right (positive) shear strain rate, then the clast rotates with the simple shear flow in a clockwise sense, at a rate that is half the applied shear rate. However, the rotation rate which we derived is not only valid for rigid clasts, but for arbitrary viscosity contrasts between clast and matrix. Therefore the factor two difference between the applied shear rate and the rotation rate persists independently of the actual viscosities. However, only the kinematics of the infinitely rigid inclusion are reducible to a rigid body rotation. All other circular clasts will show some shear deformation that is

$$\dot{\epsilon}_{xy} = \frac{\mu_m}{\mu_m + \mu_c} \dot{\gamma} \quad (33)$$

As predicted $\dot{\epsilon}_{xy} \rightarrow 0$ for $\mu_c \rightarrow \infty$ and the maximum shear rate is obtained for the infinitely weak inclusion, $\mu_c \rightarrow 0$. Naturally when $\mu_c = \mu_m$ the shear strain rate in the clast is equal the far-field value in the matrix. It is noteworthy that already a clast that is only a hundred times more competent than the matrix will already exhibit a shear deformation that is smaller than one percent of the matrix value. This could be used as a viscosity contrast measure in shear zones.

Clast Dynamics

One of the driving forces of phase transitions and metamorphic reactions is the pressure. The pressure inside the clast is obtained by plugging $\phi(z)_c$ into eqn. (8) which yields

$$p_c = 0 \quad (34)$$

Eqn. (34) holds irrespective of the boundary conditions and viscosities – the clast itself stays at the background (lithostatic) pressure.

The second important driving force is the differential or maximum shear stress, τ_c . Analogous to the pressure τ_c inside the inclusion has the property that it can be described with one single constant value

$$\tau_c = 2\sqrt{4\dot{\epsilon}^2 + \dot{\gamma}^2} \frac{\mu_c \mu_m}{\mu_c + \mu_m} \quad (35)$$

In the case of an infinitely weak inclusion the maximum shear stress vanishes. In contrast, for the rigid inclusion, τ_c is a function of the kinematic boundary conditions and the viscosity of the matrix:

$$\tau_c = 2\sqrt{4\dot{\epsilon}^2 + \dot{\gamma}^2} \mu_m \quad (36)$$

This value is likely to be characteristic for most competent clasts since a viscosity contrast between clast and matrix of 10:1, yields already a maximum shear stress value that deviates less than 10% from the $\mu_c \rightarrow \infty$ case.

Matrix Dynamics

The matrix values of p and τ do not show the property of single constant values sometimes referred to as ‘‘Eshelby conjecture’’ (e.g., Mura, 2000), but are by no means more complicated to derive. Using the given complex potentials of the matrix, the pressure is

$$p_m = -2r_c^2 \frac{\mu_m (\mu_c - \mu_m)}{\mu_c + \mu_m} \Re \left(\frac{i\dot{\gamma} + 2\dot{\epsilon}}{z^2} \right) \quad (37)$$

Reverting to polar coordinates this expression simplifies to

$$p_m = -2 \frac{\mu_m (\mu_c - \mu_m)}{\mu_c + \mu_m} \frac{r_c^2}{r^2} (\dot{\gamma} \sin(2\theta) + 2\dot{\epsilon} \cos(2\theta)) \quad (38)$$

If we are interested in the matrix pressure on the clast-matrix boundary we simply set $r = r_c$ to obtain

$$p_m = -2 \frac{\mu_m (\mu_c - \mu_m)}{\mu_c + \mu_m} (\dot{\gamma} \sin(2\theta) + 2\dot{\epsilon} \cos(2\theta)) \quad (39)$$

We can immediately see that in simple as well as pure shear there are two pressure maxima and minima along an entire clast circumference. The amplitudes of these extrema depend on the viscosities and the applied far-field flow, but not on the clast size. This is also the case for all other stress and strain rate components and contradicts the proposition of Passchier and Simpson (1986) that the amplitude of the driving forces of clast re-crystallization should decrease with decreasing clast size. It is also important

to realize that pressure, in contrast to for example traction components, is not required to be continuous through an interface ($p_c = 0$ within the inclusion).

Plotting eqn. (39) for various viscosity contrasts and simple shear only results in Figure 2. As for the differential stresses in the clast (τ_c), we see that the infinite viscosity contrast pressure limit is approached rapidly and therefore this limit may be taken to be representative for the majority of natural clasts.

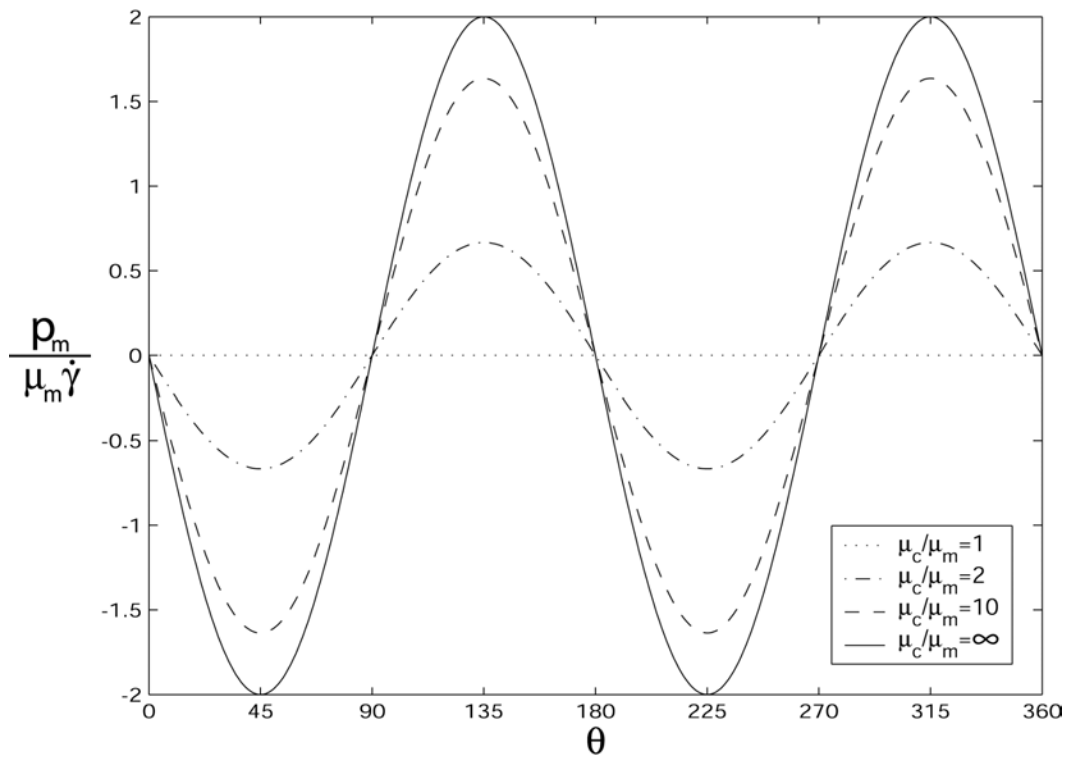


Figure 2

Pressure around cylindrical inclusions with different clast-matrix viscosity contrasts in simple shear. θ is in Figure 1.

(The name of the generating Matlab script is `cyl_p_interf.m`)

The value of this infinite pressure limit is obtained by setting $\mu_c \rightarrow \infty$ and $\theta = 3/4\pi$ which results in

$$p_m = 2\mu_m\dot{\gamma} \quad (40)$$

Therefore the maximum over-pressure in the matrix is two times the applied far-field stress ($\mu_m\dot{\gamma}$). Tenczer et al. (2001) obtained a normalized pressure value of 1.5 (see

their Figure 5). Interestingly, their numerical Newtonian experiments clearly agree with the theory presented here, but still show an approximate error of ca. 7% from the correct solution. This is a case where proper benchmarking could have been fruitful in order to determine the resolution required and the efficiency of the numerical implementation. Only afterwards more complex rheologies such as power-law should be modelled.

Eqn. (39) is equally applicable to competent as well as to weak inclusions ($\mu_c < \mu_m$). Thus we are able to plot the matrix pressures extrema at the interface and $\theta = 3/4\pi$ for the entire range of μ_c / μ_m (Figure 3). The behaviour of the weak inclusion is the inverse of the competent inclusion, i.e., the loci of compression become extensive and vice versa. This is interesting, because the applied simple shear far-field flow is still the same, i.e., the top left and the bottom right quarter (relative to the clast) are still “streamed” at by the background component of the flow. However, if the clast is weaker than the matrix this quadrants go into relative extension, while the originally extensive quadrants become compressional (cf., Figure 6b in Tenczer et al., 2001). It can be shown that this is characteristic for all dynamic and kinematic parameters.

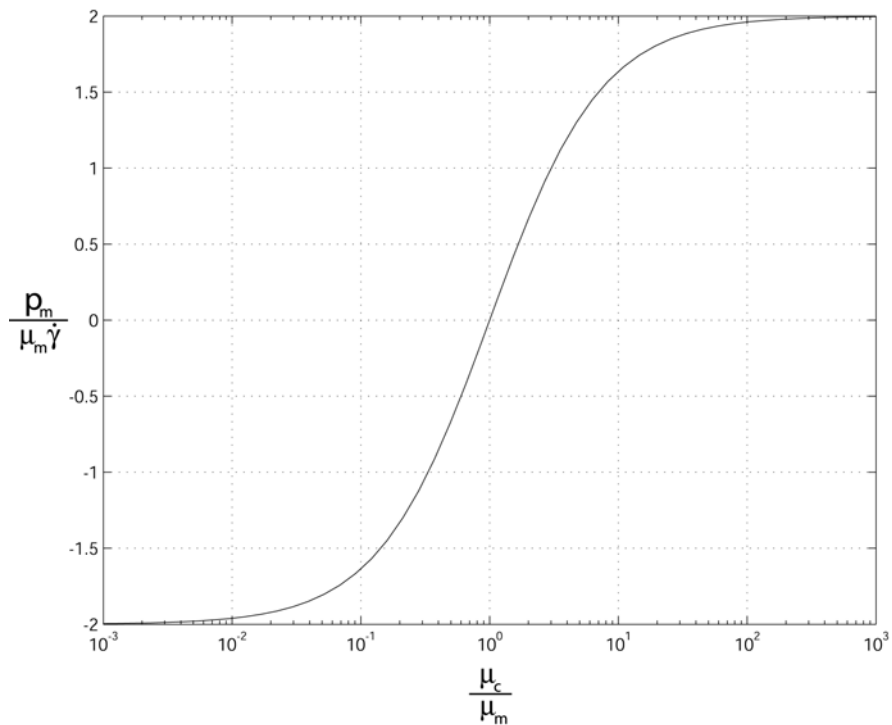


Figure 3

Pressure extrema in the matrix as function of μ_c / μ_m . (*cyl_p_interf_max.m*)

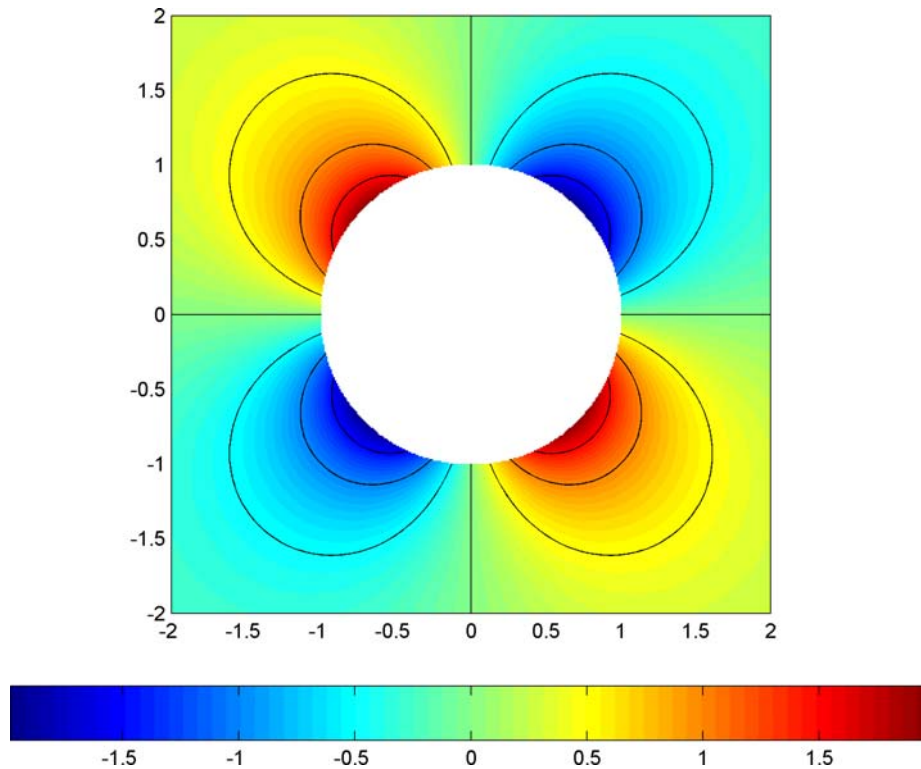


Figure 4

Pressure field around competent clast embedded in a weak matrix and subjected to simple shear. (*cyl_p_matrix.m*)

```
%CYL_P_MATRIX.M
%FAR-FIELD FLOW - VISCOSITIES - GEOMETRY
gr      = 1;
er      = 0;
mm      = 1;
mc      = 1e6;
rc      = 1;

%PRESSURE CALCULATION IN THE Z-PLANE
[X,Y]   = meshgrid(-2:.01:2);
Z       = X+i*Y;
P       = -2.*mm.*(mc-mm)./(mc+mm).* ...
          real(rc^2./Z.^2.*(i*gr+2*er));
P(abs(Z)<rc) = NaN;

%PLOTING
pcolor(X,Y,P)
axis image;
shading interp;
hold on;
contour(X,Y,P, [-1.5,-1,-.5,0,.5,1,1.5], 'k');
colorbar('horiz');
```

Eqn. (37) does not only contain interface information, but was in fact derived to show the complete analytical expression for the two-dimensional pressure perturbation field outside a circular clast, cf. Figure 4. Since complex numbers, potentials and cryptic letters like \Re have a certain deterrence potential we demonstrate the ease of using eqn. (37) explicitly by means of the complete MATLAB script that produces Figure 4.

Although based on a simple script, Figure 4 displays the entire characteristics of pressure perturbations around rigid clasts in simple shear. The size and the shape of the over- and under-pressure regions can be captured and hence the estimated dimensions of possible pressure shadows. The pressure field expectably shows a perfect point symmetry around the clast centre. Using a different method Masuda and Ando (1988) could not obtain this perfect point symmetry although their analytical series solution had 24 terms.

CIRCULAR INCLUSION WITH A RIM

SOLUTION

The circular inclusion with a rim is a three phase system where a zone of constant thickness (termed “layer” in the following) and possibly different viscosity is introduced between the clast and the matrix. Accordingly the solution consists now of three different sets of $\phi(z)$ and $\psi(z)$ for clast, matrix and layer for which the subscript “l” is introduced. Note that the solutions in clast and matrix are also altered due to the presence of the rim.

The additional parameters introduced are the viscosity of the layer, μ_l , and the radius of the layer-matrix interface, c.f., Figure 1. For geometrical reasons the condition imposed on r_l is

$$r_l \geq r_c \tag{41}$$

If $r_l = r_c$ the rim has zero thickness and the previous solution is recovered. In order to reduce the number of parameters involved we normalize by μ_m and r_c . Therefore the

viscosities present are $\tilde{\mu}_c$ and $\tilde{\mu}_l$ and the remaining radius is \tilde{r}_l , where the tilde means normalization.

Due to the increasing complexity of the geometry and number of parameters, the solution for the mantled circular inclusion is significantly more involved in terms of coefficients, but not in terms of the form of the solution:

Clast

$$\tilde{\phi}(z)_c = -\frac{i}{2}\dot{\gamma}\tilde{\mu}_c z + (i\dot{\gamma} - 2\dot{\epsilon})Q_1 z^3 \quad (42)$$

$$\tilde{\psi}(z)_c = (i\dot{\gamma} - 2\dot{\epsilon})Q_2 z \quad (43)$$

Layer

$$\tilde{\phi}(z)_l = (i\dot{\gamma} + 2\dot{\epsilon})Q_3 - \frac{i}{2}\dot{\gamma}\tilde{\mu}_l z + (i\dot{\gamma} - 2\dot{\epsilon})Q_4 z^3 \quad (44)$$

$$\tilde{\psi}(z)_l = (i\dot{\gamma} + 2\dot{\epsilon})Q_5 z^{-3} + (i\dot{\gamma} - 2\dot{\epsilon})Q_6 z \quad (45)$$

Matrix

$$\tilde{\phi}(z)_m = (i\dot{\gamma} + 2\dot{\epsilon})Q_7 z^{-1} - \frac{i}{2}\dot{\gamma} z \quad (46)$$

$$\tilde{\psi}(z)_m = (i\dot{\gamma} + 2\dot{\epsilon})Q_8 z^{-3} + (i\dot{\gamma} - 2\dot{\epsilon})z \quad (47)$$

The coefficients Q_1 to Q_8 depend only on $\tilde{\mu}_c$, $\tilde{\mu}_l$, and \tilde{r}_l , are therefore real, and are given in the Appendix. The general form of the solution in terms of which powers of z are present can be explained as follows. Inside the clast only positive powers of z are admissible because otherwise the functions would not be analytic since division by zero would occur in the centre of the clast, ($z = 0$). On the other hand, in the matrix all values of stress, strain rate and velocities, and hence $\phi(z)$ and $\psi(z)$, must decay towards the background/far-field state with increasing distance from the layer/clast. Therefore the solution in the matrix consists of the far-field flow and negative powers of z . The complex potentials within the layer have the task to match the matrix and the clast and hence the polynomials contain both, negative and positive powers of z .

APPLICATIONS

Clast Kinematics

We have seen that the circular clast with perfect, direct bonding to the matrix rotates in simple shear with a rate that is half the applied shear rate, irrespective of μ_c / μ_m . The question that arises is what influence an intermediate layer, strong or weak, between clast and matrix has on the rotation rate. Evaluating the Cartesian velocity components within the clast we obtain

$$\frac{v_x}{r_c} = \left(+\frac{1}{2} \tilde{y} + \frac{Q_2}{2\tilde{\mu}_c} \tilde{y} + \frac{2Q_1}{\tilde{\mu}_c} \tilde{y}^3 \right) \dot{\gamma} + \left(\frac{6Q_1}{\tilde{\mu}_c} \tilde{y}^2 \tilde{x} + \frac{Q_2}{\tilde{\mu}_c} \tilde{x} + \frac{2Q_1}{\tilde{\mu}_c} \tilde{x}^3 \right) \dot{\varepsilon} \quad (48)$$

$$\frac{v_y}{r_c} = \left(-\frac{1}{2} \tilde{x} + \frac{Q_2}{2\tilde{\mu}_c} \tilde{x} + \frac{2Q_1}{\tilde{\mu}_c} \tilde{x}^3 \right) \dot{\gamma} - \left(\frac{6Q_1}{\tilde{\mu}_c} \tilde{x}^2 \tilde{y} + \frac{Q_2}{\tilde{\mu}_c} \tilde{y} + \frac{2Q_1}{\tilde{\mu}_c} \tilde{y}^3 \right) \dot{\varepsilon} \quad (49)$$

We can see that the first term in the simple shear part is a rigid body rotation at a rate that is half the applied shear rate. Setting $\dot{\varepsilon} = 0$ and evaluating the expression for the rotation rate (cf. eqn. (30)) results in

$$\dot{\omega} = -\frac{1}{2} \dot{\gamma} - \frac{3Q_1}{\tilde{\mu}_c} \dot{\gamma} (y^2 - x^2) \quad (50)$$

which confirms the above observation. However, clearly the Eshelby conjecture is violated since the rotation rate is not constant within the clast. Yet, for the infinitely rigid clast the second term of eqn. (50) vanishes. This result is noteworthy since it implies that the rotation of a circular, rigid clast is independent of a strong ($\mu_l > \mu_m$) or very weak/lubricant rim ($\mu_l \ll \mu_m$).

We conclude here our investigation about the rotation rates of circular clast: The rigid circular clast always rotates with $\dot{\omega} = -\dot{\gamma}/2$, irrespective of the matrix viscosity and the presence of additional interfaces/layers between clast and matrix. If the clast is not rigid the presence of a layer between the clast and the matrix disturbs this equality. Yet, if the clast is directly and perfectly coupled to the matrix it will always rotate with $\dot{\omega} = -\dot{\gamma}/2$, irrespective of the viscosity contrast between clast and matrix.

For completeness we also give the related shear strain rate, which is

$$\dot{\varepsilon}_{xy} = \frac{Q_2}{2\tilde{\mu}_c} \dot{\gamma} + \frac{3Q_1}{\tilde{\mu}_c} \dot{\gamma} (y^2 + x^2) \quad (51)$$

As expected $\dot{\varepsilon}_{xy}$ vanishes for rigid clasts.

Dynamics

The exceptional characteristics of the circular clast embedded in a matrix and subject to uniform far-field boundary conditions are that the inside of the clast shows constant dynamic values and in particular no pressure perturbation is generated in simple shear. Plugging the $\phi(z)$'s of the three different phases into the pressure equation the following expressions are obtained

$$\frac{P_c}{\mu_m} = -2\Re(3i\dot{\gamma}Q_1z^2 - 6\dot{\varepsilon}Q_1z^2) \quad (52)$$

$$\frac{P_l}{\mu_m} = -2\Re((-i\dot{\gamma} - 2\dot{\varepsilon})Q_3z^{-2} + 3(i\dot{\gamma} - 2\dot{\varepsilon})Q_4z^2) \quad (53)$$

$$\frac{P_m}{\mu_m} = -2\Re((-i\dot{\gamma} - 2\dot{\varepsilon})Q_7z^{-2}) \quad (54)$$

Setting $\dot{\varepsilon} = 0$ and reverting to polar coordinates the non-dimensional pressures are

$$\frac{P_c}{\dot{\gamma}\mu_m} = 6Q_1\tilde{r}^2 \sin(2\theta) \quad (55)$$

$$\frac{P_l}{\dot{\gamma}\mu_m} = \left(\frac{2Q_3}{\tilde{r}^2} + 6Q_4\tilde{r}^2 \right) \sin(2\theta) \quad (56)$$

$$\frac{P_m}{\dot{\gamma}\mu_m} = \frac{2Q_7}{\tilde{r}^2} \sin(2\theta) \quad (57)$$

Eqn. (55) generally indicates that the property of zero pressure perturbation in the clast is lost. Interestingly the pressures inside the clast is now synchronized with the outside. Both, eqn. (55) and (57), exhibit two minima and two maxima around the clast circumference at exactly the same locations. In the matrix, this was already obtained for the case of perfect direct bonding between circular clast and matrix. Indeed eqns. (57)

and (38) are very similar and naturally are identical if the viscosity of the layer is equal the matrix value.

Although the property of zero pressure perturbation within the clast is lost, certain limits still exhibit this characteristic. (1) When the viscosity of the layer is equal to the matrix value ($\tilde{\mu}_l = 1$) then Q_1 is zero and consequently $p_c = 0$. (2) If the layer becomes very lubricant ($\tilde{\mu}_l \rightarrow 0$) Q_1 also vanishes and the clast pressure is lithostatic.

Plotting the complete two-dimensional pressure perturbation, stream function, and maximum shear stress fields is straightforward. The only information required are $\dot{\gamma}$, $\dot{\varepsilon}$, $\tilde{\mu}_c$, $\tilde{\mu}_l$ and \tilde{r}_l . Results for selected sets of parameters are displayed in Figures 5 to 7.

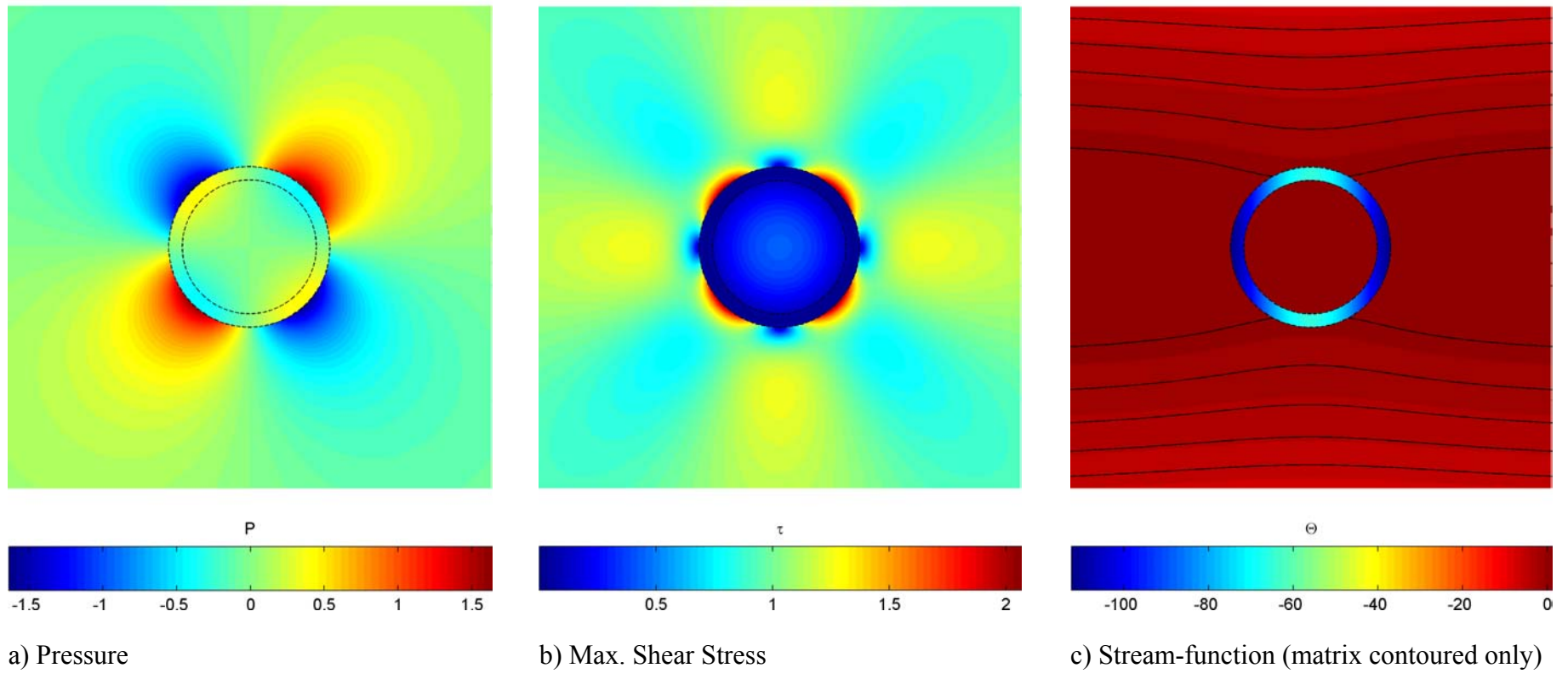


Figure 5

Competent cylindrical inclusion surrounded by a weak layer, subjected to simple shear.

$\dot{\epsilon} = 0$, $\dot{\gamma} = 1$, $r_l = 1.2$, $\tilde{\mu}_c = 1000$, $\tilde{\mu}_l = 1/1000$ (*cyl_w_rim.m*)

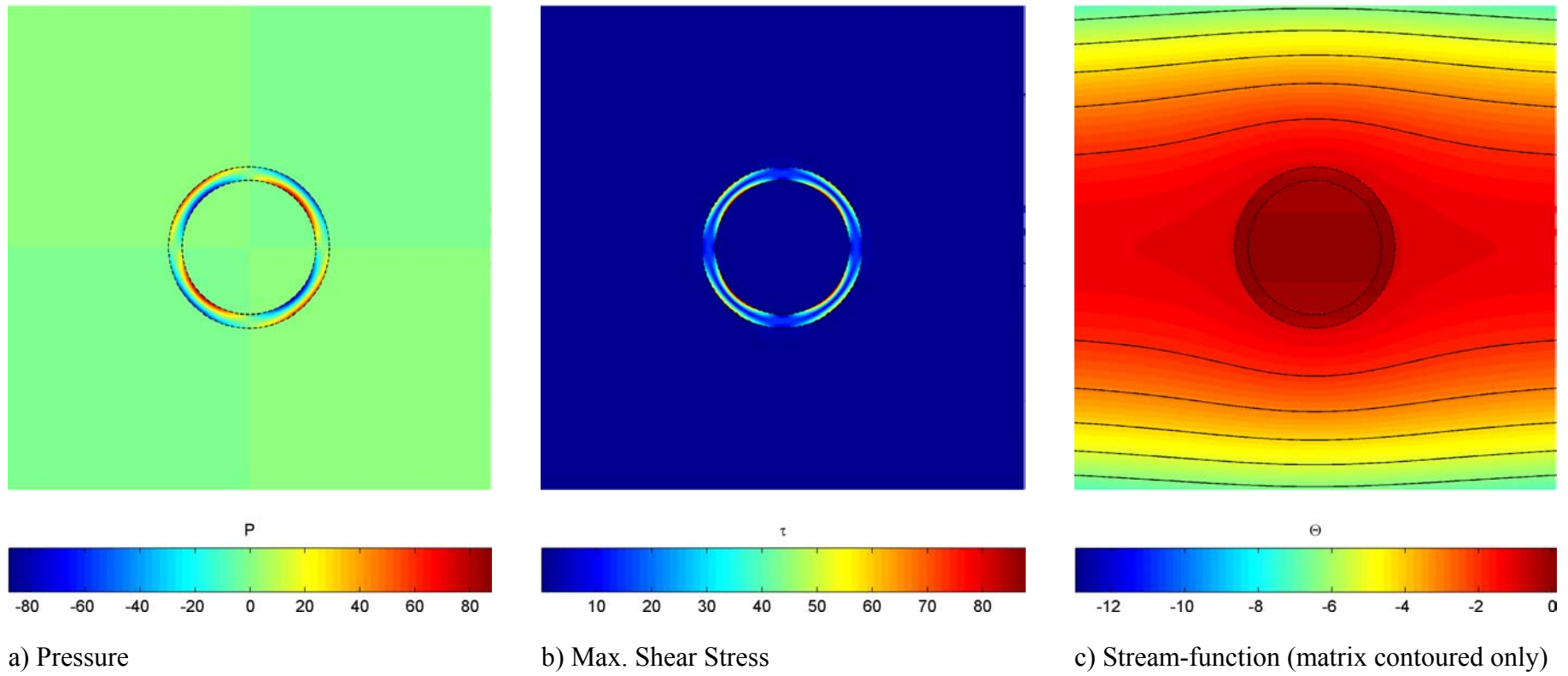


Figure 6

Weak cylindrical inclusion surrounded by a strong layer, subjected to simple shear.

$\dot{\epsilon} = 0$, $\dot{\gamma} = 1$, $\tilde{r}_i = 1.2$, $\tilde{\mu}_c = 1/1000$, $\tilde{\mu}_i = 1000$ (*cyl_w_rim.m*)

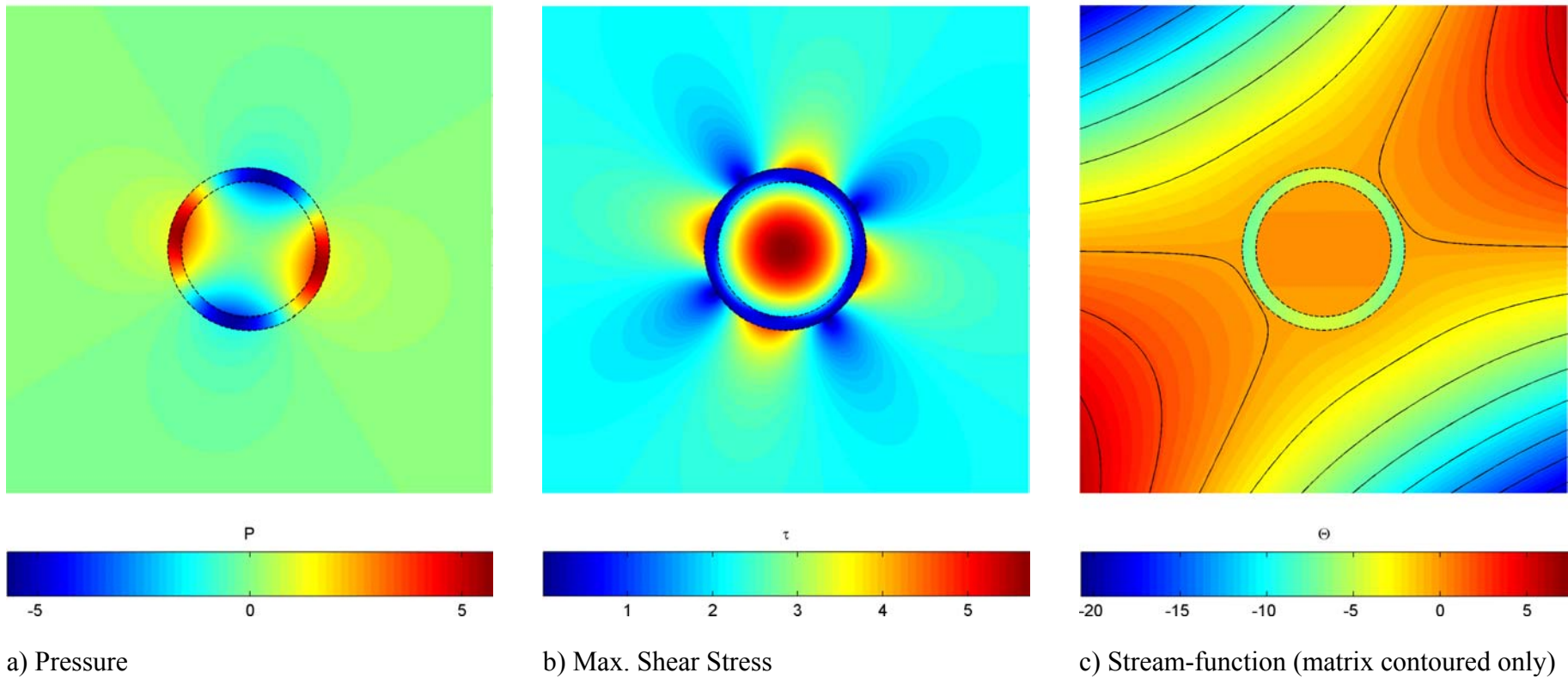


Figure 7

Competent cylindrical inclusion surrounded by a weak layer, subjected to combined pure and simple shear (horizontal compression and horizontal simple shear).

$$\dot{\epsilon} = -1, \dot{\gamma} = 1, r_i = 1.2, \tilde{\mu}_c = 1000, \tilde{\mu}_l = 1/10 \text{ (cyl_w_rim.m)}$$

ELLIPTICAL INCLUSION

CONFORMAL TRANSFORMATIONS

Until now we have focused on circular inclusion problems. Given the geometry, these solutions could have been found also in cylindrical coordinate systems, though without the convenience of already existing expressions for all kinematic and dynamic parameters. However, the genuine strength of Muskhelishvili's method is that conformal transformations may be applied. Conformal transformation means a coordinate transformation that is analytic, i.e., fulfills the Cauchy-Riemann equations. The geometrical meaning of conformal transformation is that the mapping is unique and that both amplitude and sense of angles are preserved.

The reason why conformal transformations are useful is because they allow solution finding for complex physical problems (z -plane) in geometrically simpler image planes (ζ). The most famous usage of conformal solution transformation maybe by due to N.E. Joukowski who succeeded in 1906 to calculate the lift of an airfoil. He reduced the problem to calculating the flow around a rigid cylinder in the image plane and then, using what is now called Joukowski transform, translated his solution to the physical domain, where the cylinder becomes an airfoil (this class of airfoils now being called Joukowski airfoils).

The Joukowski transform is not only suitable to study airplane wings, but is also appropriate for the study of elliptical inclusion. The most general definition of the Joukowski transform is

$$z = R \left(\zeta + \frac{m}{\zeta} \right) \quad (58)$$

However, for our study R and m can both be set to 1, since for elliptical shapes they are not needed. The characteristic effect of the Joukowski transform is explained in Figure 8. Certain off-centre circles in the ζ -plane become airfoil-like shapes in z . Since we are interested in elliptical inclusions in z , we restrict the possible circles in ζ to the class whose centre coincides with the coordinate system origin. Due to the condition of uniqueness of the mapping we have to restrict the possible circle radii, ρ , to

$$\rho \geq 1 \quad (59)$$

The circle with $\rho=1$ becomes a slit in z and has an infinity aspect ratio t . The definition of t is

$$t = \frac{a}{b} \quad (60)$$

The relationship between ρ and t is inverse, i.e., the aspect ratio in z decreases as ρ increases in ζ . The explicit relationship is

$$\rho = \frac{\sqrt{(t-1)(t+1)}}{t-1} \quad (61)$$

Hence, for a given physical problem with an elliptical inclusion of aspect ratio t we can set up the corresponding problem in z , where we have the matrix from infinity to ρ and the inclusion from ρ to 1. Therefore the inclusion is a ring in ζ , cf. Figure 22 in the appendix.

The conservation of amplitudes and sense of angles is an important feature for the analysis of the results since it facilitates switching between ζ to z . This property can be seen from Figure 8, where the point Π in ζ corresponds to P in z . While (in polar coordinates) ρ_{Π} can be different from r_p , θ_{Π} must be identical with θ_p .

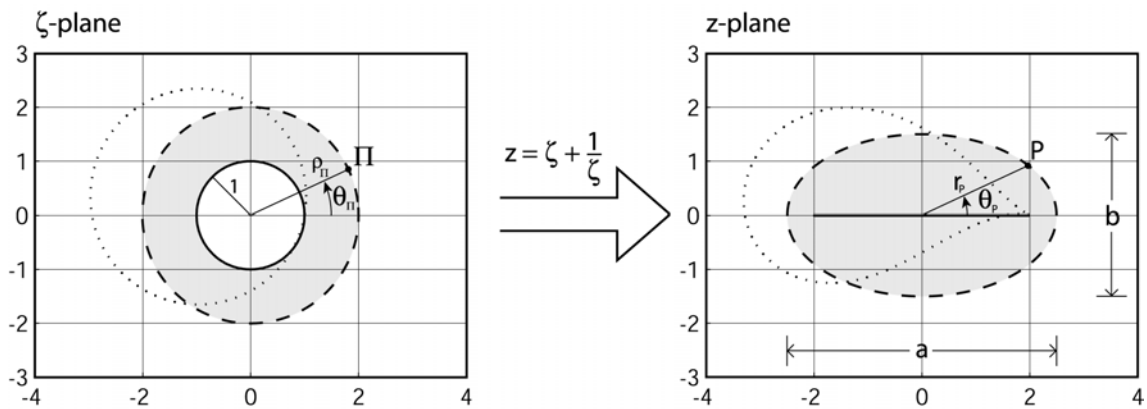


Figure 8

Joukowski transform. The transform maps the image plane, ζ , to the physical plane, z . (zhouk_demo.m)

FAR-FIELD FLOW CONDITIONS

The far-field flow conditions in the physical domain are still pure shear and/or simple shear. Since we solve the problem in the image plane ζ , we must translate the boundary conditions from z to ζ . This is done by replacing z with the expression of the Joukowski transform. Given that we are dealing with a non-circular inclusion the angle (α) between the boundary condition flow and the long axis of the ellipse must also be considered (Figure 9). The definition of α used is that it is measured from the horizontal of the boundary conditions and positive values are counter-clockwise. For this system the we can write the combined pure and simple shear boundary conditions with the inclination α as

$$\phi(\zeta(z))_{gps} = -\frac{i\mu\dot{\gamma}}{2}\left(\zeta + \frac{1}{\zeta}\right) \quad (62)$$

$$\psi(\zeta)_{gps} = (i\dot{\gamma} - 2\dot{\epsilon})\mu\left(\zeta + \frac{1}{\zeta}\right)e^{-2i\alpha} \quad (63)$$

Setting $\alpha = 0$ restores the general horizontal boundary conditions (eqns. (22) and (23)).

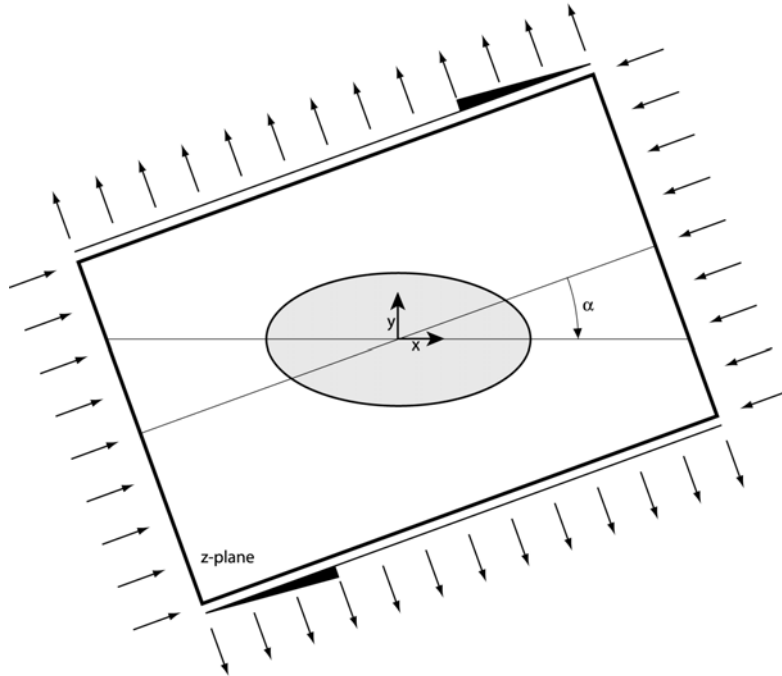


Figure 9

Boundary condition for the elliptical inclusion. In this example $\alpha = -20^\circ$.

SOLUTION

The solution for the elliptical inclusion with inclined arbitrary combinations of pure and simple shear is:

$$\phi(\zeta(z))_m = -\frac{i}{2}\dot{\gamma}\left(\zeta + \frac{1}{\zeta}\right) + B_3\tilde{\rho}_c^2\left(\frac{i\Im(\mathbf{B})}{B_1} - \frac{\Re(\mathbf{B})}{B_2}\right)\frac{1}{\zeta} \quad (64)$$

$$\psi(\zeta(z))_m = -(\Re(\mathbf{B}) + i\Im(\mathbf{B}))\left(\zeta + \frac{1}{\zeta}\right) + B_5\left(\frac{i\Im(\mathbf{B})}{B_1} - \frac{\Re(\mathbf{B})}{B_2}\right)\frac{1}{\zeta^3 - \zeta} \quad (65)$$

$$\phi(\zeta(z))_c = \left(\frac{i\tilde{\mu}_c B_4 \dot{\gamma}}{2B_1} - \tilde{\rho}_c^2(\tilde{\mu}_c - 1)\left(\frac{i\tilde{\mu}_c \Im(\mathbf{B})}{B_1} - \frac{\Re(\mathbf{B})}{B_2}\right)\right)\left(\zeta + \frac{1}{\zeta}\right) \quad (66)$$

$$\psi(\zeta(z))_c = -2\tilde{\mu}_c\tilde{\rho}_c^4\left(\frac{i\Im(\mathbf{B})}{B_1} + \frac{\Re(\mathbf{B})}{B_2}\right)\left(\zeta + \frac{1}{\zeta}\right) \quad (67)$$

where \mathbf{B} contains rotated boundary condition terms

$$\mathbf{B} = (2\hat{\varepsilon} - i\dot{\gamma})e^{-2i\alpha} \quad (68)$$

and B_1 to B_5 are real-valued combinations of $\tilde{\mu}_c$ and $\tilde{\rho}_c$

$$B_1 = \tilde{\mu}_c\tilde{\rho}_c^4 + \tilde{\mu}_c + \tilde{\rho}_c^4 - 1 \quad (69)$$

$$B_2 = \tilde{\mu}_c\tilde{\rho}_c^4 - \tilde{\mu}_c + \tilde{\rho}_c^4 + 1 \quad (70)$$

$$B_3 = \tilde{\mu}_c\tilde{\rho}_c^4 - \tilde{\mu}_c - \tilde{\rho}_c^4 + 1 \quad (71)$$

$$B_4 = -\tilde{\mu}_c\tilde{\rho}_c^4 - \tilde{\mu}_c - \tilde{\rho}_c^4 + 1 \quad (72)$$

$$B_5 = \tilde{\mu}_c\tilde{\rho}_c^8 - \tilde{\mu}_c - \tilde{\rho}_c^8 + 1 \quad (73)$$

As before we have used μ_m to normalize the viscosities, and the inside radius of the inclusion ring in ζ to normalize all length parameters, hence the tildes.

BASIC SET OF EQUATIONS

The original basic set of equations at the beginning of this paper was given for the physical plane z . The solution presented above is written in terms of the image plane coordinates ζ . We must therefore analyze how to transfer the solutions. The only complication caused by the use of two different coordinate systems is that for spatial derivatives the chain rule of differentiation must be applied. Taking $\phi(\zeta(z))$ as an example the first derivative versus z becomes:

$$\frac{\partial \phi(\zeta(z))}{\partial z} = \frac{\partial \phi(\zeta(z))}{\partial \zeta} \frac{\partial \zeta}{\partial z} \quad (74)$$

This is convenient, since $\partial \phi(\zeta(z))/\partial \zeta$ can be directly computed and $\partial \zeta/\partial z$ is the inverse of $\partial z/\partial \zeta$:

$$\frac{\partial \phi(\zeta(z))}{\partial z} = \frac{\partial \phi(\zeta(z))}{\partial \zeta} \left(\frac{\partial z}{\partial \zeta} \right)^{-1} \quad (75)$$

In analogy we can find the second derivative as

$$\frac{\partial^2 \phi(\zeta(z))}{\partial z^2} = \frac{\partial^2 \phi(\zeta(z))}{\partial \zeta^2} \left(\frac{\partial z}{\partial \zeta} \right)^{-2} + \frac{\partial \phi(\zeta(z))}{\partial \zeta} \frac{\partial}{\partial \zeta} \left(\left(\frac{\partial z}{\partial \zeta} \right)^{-1} \right) \left(\frac{\partial z}{\partial \zeta} \right)^{-1} \quad (76)$$

Writing ϕ and ψ instead of $\phi(\zeta(z))$ and $\psi(\zeta(z))$ the basic set of equations under conformal Joukowski mapping becomes:

$$p = -2\Re \left(\frac{1}{1-\zeta^{-2}} \frac{\partial \phi}{\partial \zeta} \right) \quad (77)$$

$$\frac{\sigma_{yy} - \sigma_{xx}}{2} + i\sigma_{xy} = \overline{\left(\zeta + \frac{1}{\zeta} \right)} \left(\frac{1}{(1-\zeta^{-2})^2} \frac{\partial^2 \phi}{\partial \zeta^2} + \frac{-2}{(1-\zeta^{-2})^3} \frac{\partial \phi}{\partial \zeta} \right) + \frac{\partial \psi}{\partial \zeta} \frac{1}{1-\zeta^{-2}} \quad (78)$$

$$v_x + iv_y = \frac{\phi - \overline{\left(\zeta + \frac{1}{\zeta} \right)} \left(\frac{1}{1-\zeta^{-2}} \frac{\partial \phi}{\partial \zeta} \right) - \overline{\psi}}{2\mu} \quad (79)$$

APPLICATIONS

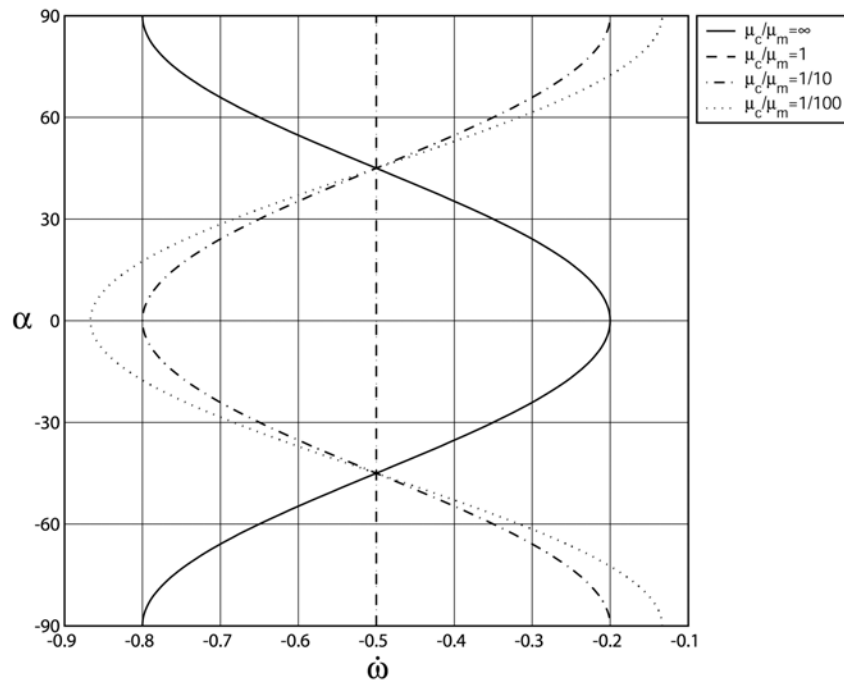
Clast Kinematics

Based on Muskhelishvili's method, Ghosh and Ramberg (1976) have derived the kinematic behaviour of the rigid elliptical clast in combined pure and simple shear. With the solution provided here it is possible to obtain the expression for the kinematic behavior of any kind of elliptical inclusion, competent or weak, in combined pure and simple shear. Analyzing the complex potential expressions of the clast it is evident that it is possible to rewrite them directly for the z -domain. Both, $\phi(\zeta(z))_c$ and $\psi(\zeta(z))_c$, are a function of $(\zeta + 1/\zeta)$, which is the definition of the used Joukowski transform (eqn. (58)). Therefore we can replace $(\zeta + 1/\zeta)$ by z to obtain expressions that are valid in z . This greatly simplifies the analysis, since coordinate transformations are no longer employed and consequently the simpler z -set of the basic equations can be used. The resulting expression for the rotation rate is

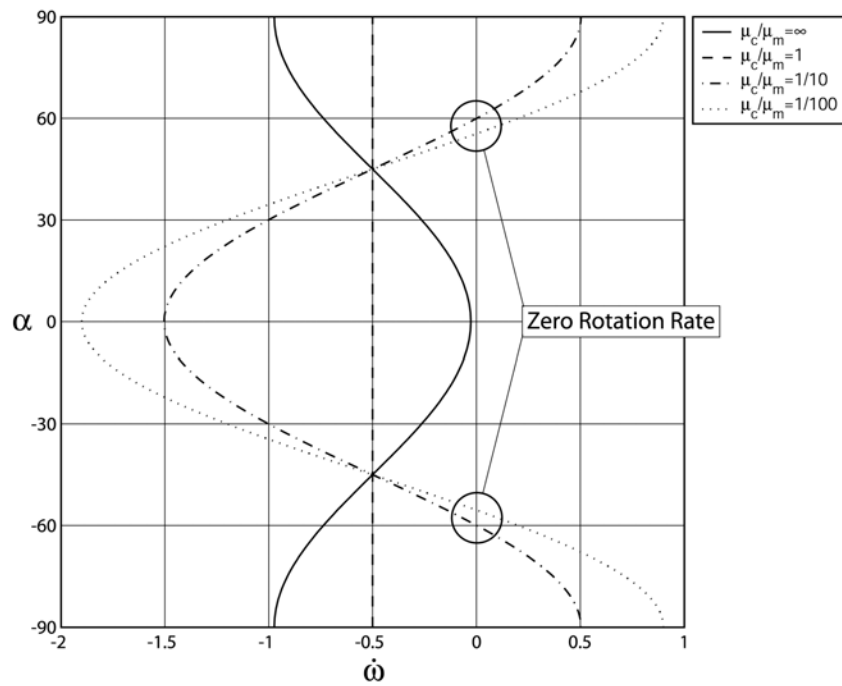
$$\dot{\omega} = \frac{\tilde{\mu}_c - \tilde{\mu}_c t^2 + t^2 + 1}{\tilde{\mu}_c + \tilde{\mu}_c t^2 + 2t} \sin(2\alpha) \dot{\epsilon} + \frac{-\tilde{\mu}_c + \tilde{\mu}_c t^2 - t^2 + 1}{2\tilde{\mu}_c + 2\tilde{\mu}_c t^2 + 4t} \cos(2\alpha) \dot{\gamma} - \frac{1}{2} \dot{\gamma} \quad (80)$$

This expression successfully reproduces Ghosh & Ramberg's $\tilde{\mu}_c \rightarrow \infty$ case and can be used to explore the entire field of $\tilde{\mu}_c - t$. We can, for example, set $\dot{\epsilon} = 0$ and vary $\tilde{\mu}_c$ and t as in done in Figure 10 for different aspect ratios t . It can be observed that if the clast aspect ratio is big enough and the viscosity is less than the matrix value, a field of back rotation comes into existence (Figure 10b) which is limited by the intersections with the $\dot{\omega} = 0$ line. If the inclusion is inclined with an angle corresponding to this field, it will rotate against the applied shear sense towards the lower intersection point. Since this field of back rotation only exists for weak inclusions, it must be realized that the corresponding shear strain rates are not negligible and may overprint the back rotation. The expression for the minimum required aspect ratio for back-rotation to occur in the case of the infinitely weak inclusion is

$$t = 1 + \sqrt{2} \quad (81)$$



a)



b)

Figure 10

Rotation rates for elliptical inclusions with aspect ratio 2 (a) and 6 (b).

(ell_rot_rate.m)

Clast Pressure

The Eshelby conjuncture holds for circular as well as any kind of elliptical inclusion subjected to homogeneous far-field stresses. To verify this we derive the pressure expression within the clast as

$$\frac{p_c}{\mu_m} = (2\dot{\epsilon} \cos(2\alpha) + \dot{\gamma} \sin(2\alpha)) \frac{2(1 - \tilde{\mu}_c) \tilde{\rho}_c^2}{\tilde{\rho}_c^4 + \tilde{\rho}_c^4 \tilde{\mu}_c - \tilde{\mu}_c + 1} \quad (82)$$

Since only constants are involved, this expression yields a constant pressure value within the inclusion. We can also see that the horizontal simple shear ($\dot{\epsilon} = 0$ and $\alpha = 0$) does not cause a pressure perturbation within the elliptical inclusion. The same is true for a pure shear only case where the boundary condition is 45° inclined. In the limit of a circular inclusion, $\tilde{\rho} \rightarrow \infty$, the pressure perturbation is likewise 0. It is also obvious that in simple as well as pure shear the rotating inclusion goes through two maxima and two minima in one full rotation. For the combined pure and simple shear an interesting parameter is the inclination angle at which, for given boundary condition amplitudes, the maximum absolute pressure deviation from the background state occurs. Taking the derivative of p_c versus α , equating to 0 and solving for α we obtain

$$\alpha = \frac{1}{2} \arctan\left(\frac{1}{2} \frac{\dot{\gamma}}{\dot{\epsilon}}\right) \quad (83)$$

For simple shear only this yields $\alpha = 45^\circ$, for pure shear only $\alpha = 0^\circ$. Substituting eqn. (83) into (82) results in the actual expression for the maximum, absolute pressure perturbation within the elliptical inclusion:

$$\max \left| \frac{p_c}{\mu_m} \right| = \left| \frac{2\tilde{\rho}_c^2 (1 - \tilde{\mu}_c) \sqrt{\dot{\gamma}^2 + 4\dot{\epsilon}^2}}{\tilde{\rho}_c^4 \tilde{\mu}_c - \tilde{\mu}_c + \tilde{\rho}_c^4 + 1} \right| \quad (84)$$

This expression can be used to derive the maximum pressure perturbation occurring in the rigid ($\tilde{\mu}_c \rightarrow \infty$) elliptical inclusion in pure shear:

$$\frac{p_c}{-2\mu_m \dot{\epsilon}} = \frac{t^2 - 1}{2t} \quad (85)$$

This shows that the maximum pressure perturbation, equal the overpressure, is roughly equal to $t/2$ times the characteristic far-field matrix stress value.

Pressure Around Rigid Elliptical Clast

Substituting the complex potentials of the matrix into the Joukowski transformation adjusted pressure expression, we obtain the corresponding pressure perturbation values:

$$\frac{P_m}{\mu_m} = -2\Re\left(-\frac{B_3\tilde{\rho}_c^2}{\zeta^2-1}\left(\frac{i\Im(B)}{B_1}-\frac{\Re(B)}{B_2}\right)\right) \quad (86)$$

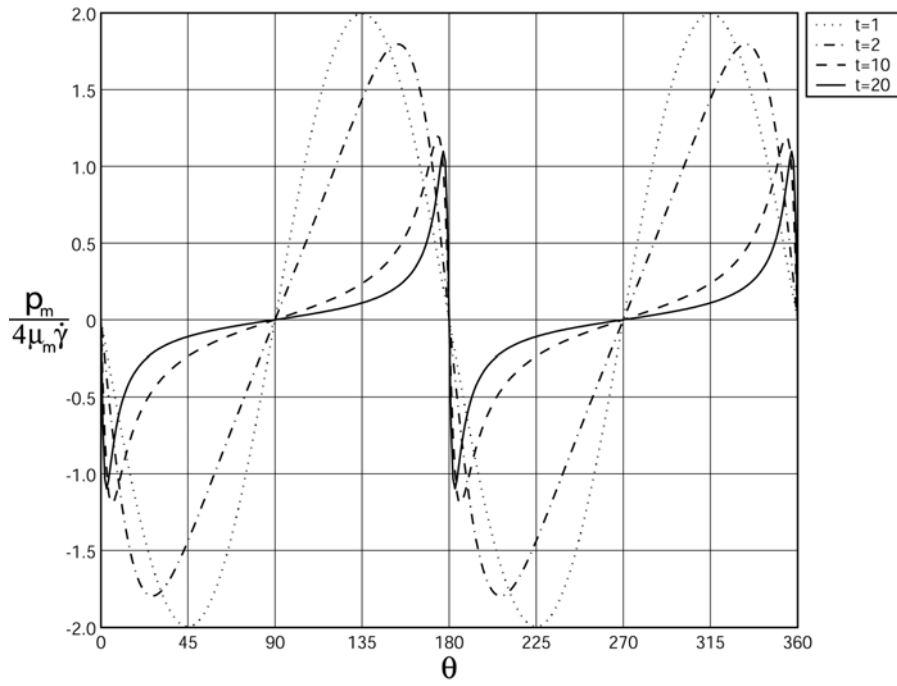
which can be written

$$\frac{P_m}{\mu_m} = -2\frac{B_3}{B_1B_2}\tilde{\rho}_c^2 * \Re\left(\frac{(-\dot{\gamma}\sin(2\alpha)-2\dot{\epsilon}\cos(2\alpha))B_1+i(-\dot{\gamma}\cos(2\alpha)+2\dot{\epsilon}\sin(2\alpha))B_2}{\zeta^2-1}\right) \quad (87)$$

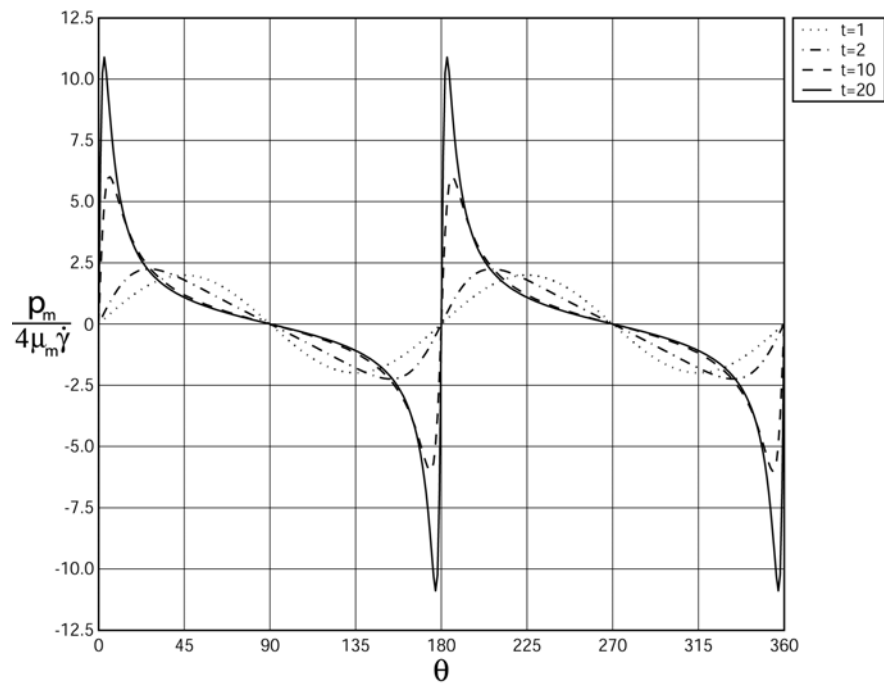
This expression is again closely related to the matrix pressure expression around the circular clast (eqn. (38)). Namely, if we set $\alpha = 0$, $\dot{\epsilon} = 0$ and investigate the small aspect ratio case, $\tilde{\rho}_c \rightarrow \infty$, the two expressions are identical.

Setting $\tilde{\rho} = \tilde{\rho}_c$, and $\alpha = 0$ the expression for the matrix pressure around the clast-matrix interface subjected to ellipse long axis parallel far-field flow can be derived. Results for different t and μ_c in simple shear are shown in Figure 11, and pure shear in Figure 12. In order to synchronize the plots, we scale the pressure values by the characteristic far-field matrix stress. This is $4\mu_m\dot{\gamma}$ in simple shear and $-2\mu_m\dot{\epsilon}$ in pure shear. The minus sign takes care of the pressure sign convention.

In all four cases the maximum pressure perturbation around the circular clast is two times the matrix stress value. Inversion of the clast-matrix viscosity contrast causes a sign flip of the pressure perturbation. The behaviour of the elliptical inclusion is more complicated. In simple shear the competent elliptical clast causes progressively less pressure perturbation with increasing aspect ratio, the inverse is true for the weak inclusion. An additional effect, that can be observed is that the more elongated the elliptical inclusion in simple shear, the closer the pressure extrema are to the tips.



a)



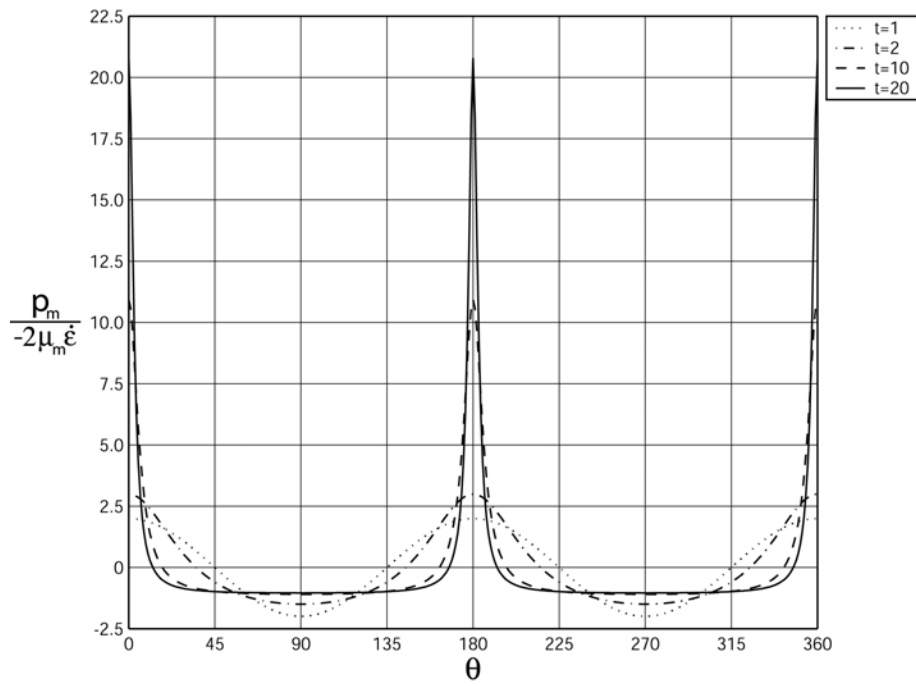
b)

Figure 11

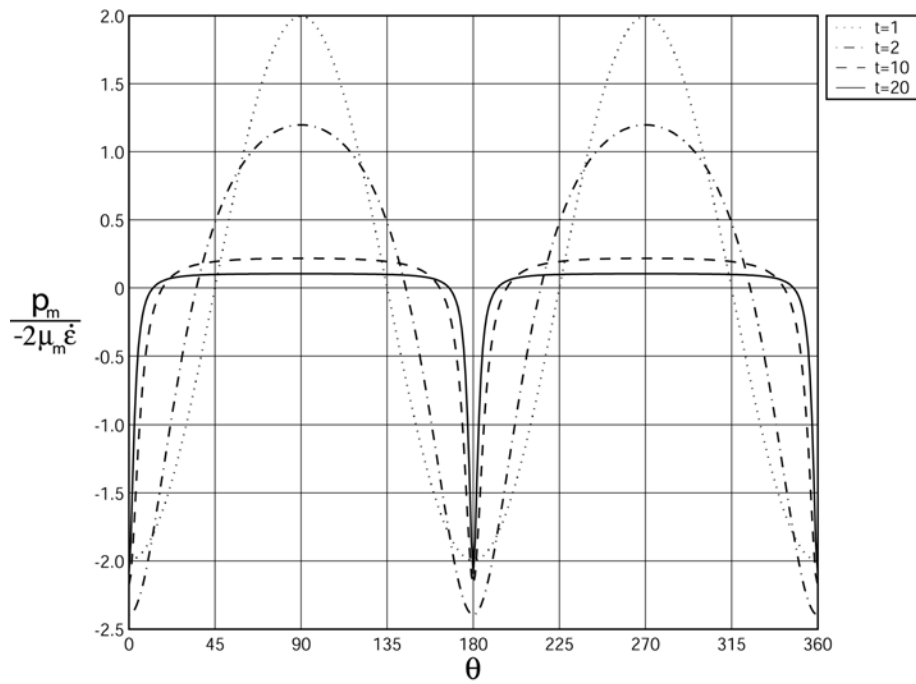
Matrix pressure at the clast-matrix interface for ellipse parallel simple shear.

(a) $\mu_c / \mu_m = 1000$, (b) $\mu_c / \mu_m = 1/1000$

(ell_p_intf.m)



a)



b)

Figure 12

Matrix pressure at the elast-matrix interface for ellipse parallel pure shear.

(a) $\mu_c / \mu_m = 1000$, (b) $\mu_c / \mu_m = 1/1000$

(ell_p_intf.m)

Interestingly the effect of increasing the aspect ratio of the competent inclusion is opposite in simple shear and pure shear. In pure shear the pressure perturbation around the competent elliptical inclusion grows with increasing aspect ratio. It appears that the maximum pressure (at the tips, $\theta = 0$) grows linearly with t . On the other hand the maximum absolute pressure perturbation driven by the presence of a weak inclusion first increases with increasing t , but then decreases again. Deriving the analytical expression for the maximum pressure perturbation generated by ellipse parallel pure shear in the tips, yields:

$$\frac{p_m}{-2\mu_m \dot{\epsilon}} = 2t \frac{(t+1)(\tilde{\mu}_c - 1)}{2\tilde{\mu}_c t + t^2 + 1} \quad (88)$$

Indeed, the limit of this expression for the rigid inclusion is

$$\frac{p_m}{-2\mu_m \dot{\epsilon}} = t + 1 \quad (89)$$

and for the infinitely weak inclusion

$$\frac{p_m}{-2\mu_m \dot{\epsilon}} = -2 \frac{t(t+1)}{t^2 + 1} \quad (90)$$

Plotting the latter yields Figure 13, and it can be seen that the pressure perturbation has a maximum at $t = 1 + \sqrt{2}$. The amplitude of this pressure perturbation is however minor.

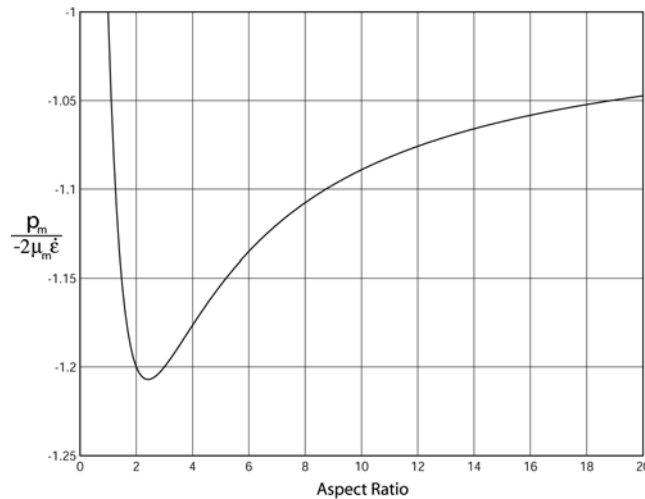


Figure 13

Maximum pressure perturbation caused in the tips by the infinitely weak elliptical inclusion as a function of the aspect ratio.

Complete Pressure Field

For convenience the presented solution consists of a redundant set of parameters. It is clear that at any instant, for any kind of combined pure and simple shear a set of principal axis can be found along which no shear stress occurs. Hence the instantaneous, arbitrary inclined, combined simple and pure shear problem can be reduced to one of inclined pure shear only. To give an idea of the pressure field in two-dimensions it is therefore sufficient to illustrate it based on inclined pure shear, as done in Figures 14 to 17. The difference between a competent and a weak inclusion is depicted in Figures 14 and 15. The transition causes a flip in the pressure field and the tips of the weak elliptical inclusion become regions of relative extension although they lie in the direction of maximum compression.

If the pure shear is inclined at 45° to the ellipse long axis the equivalent pressure field of horizontal simple shear is obtained (compare Figures 16 and 11a). Figure 17 shows how with larger aspect ratios the elliptical inclusion causes pressure concentrations near the tips, although the inclination of the boundary condition does not coincide with the major axis of the ellipsoidal inclusion. For a comparison of the pressure field in z and ζ please refer to the Appendix.

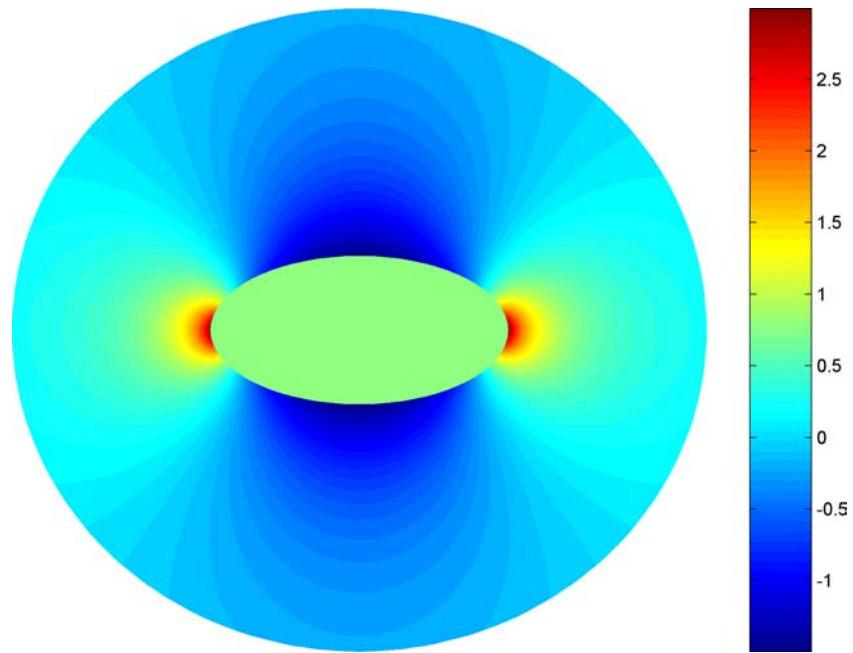


Figure 14

Pressure field around elliptical inclusion

$t = 2$, $\dot{\gamma} = 0$, $\dot{\epsilon} = -0.5$, $\alpha = 0^\circ$, $\mu_c = 1000$. (*ell_dynamix.m*)

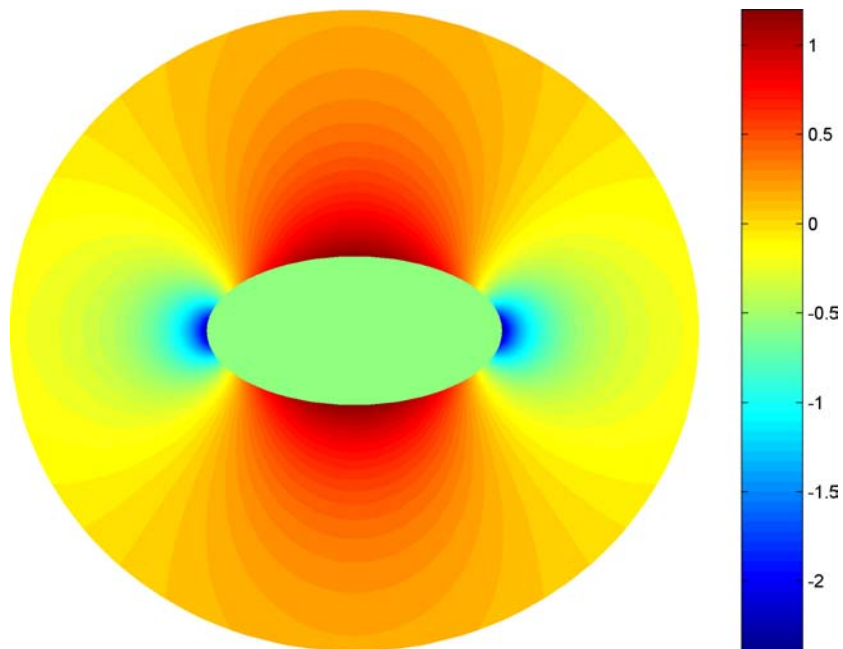


Figure 15

Pressure field around elliptical inclusion

$t = 2$, $\dot{\gamma} = 0$, $\dot{\epsilon} = -0.5$, $\alpha = 0^\circ$, $\mu_c = 1/1000$. (*ell_dynamix.m*)

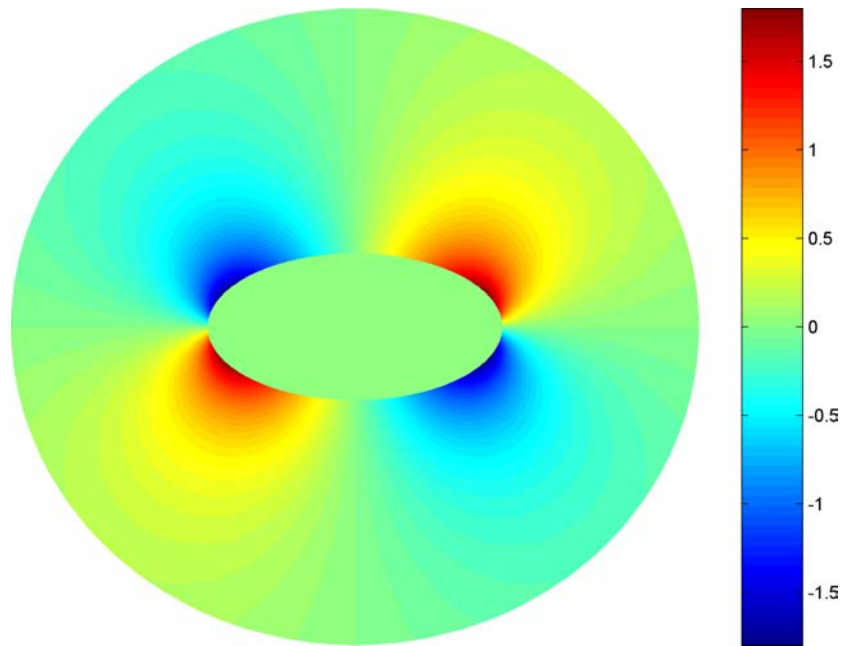


Figure 16

Pressure field around elliptical inclusion

$t = 2, \dot{\gamma} = 0, \dot{\epsilon} = -0.5, \alpha = -45^\circ, \mu_c = 1000$. (*ell_dynamix.m*)

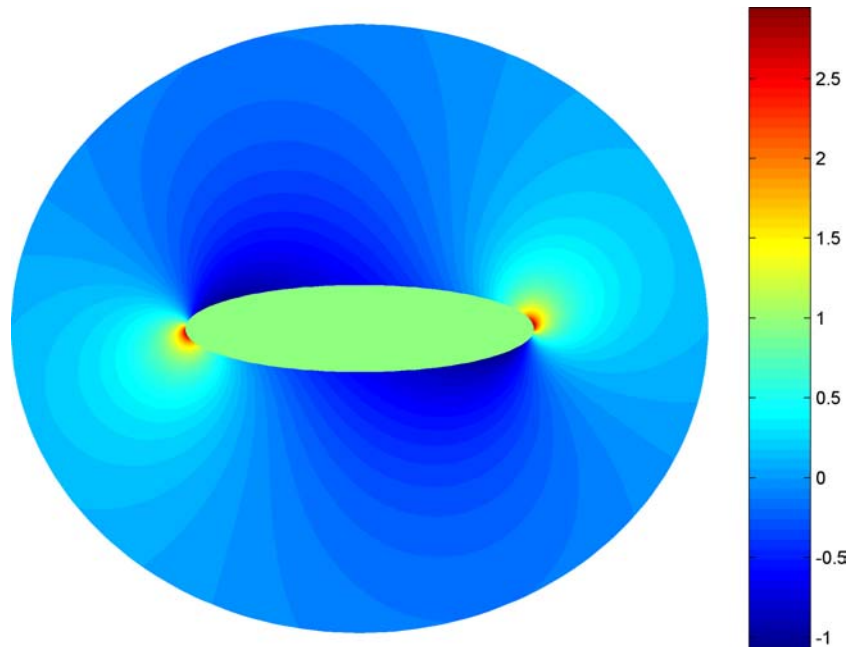


Figure 17

Pressure field around elliptical inclusion

$t = 4, \dot{\gamma} = 0, \dot{\epsilon} = -0.5, \alpha = -30^\circ, \mu_c = 1000$. (*ell_dynamix.m*)

Clast Maximum Shear Stress

The complete confirmation of the Eshelby conjuncture is that with eqn. (78) the following expression for the elliptical inclusion can be derived:

$$\frac{\sigma_{yy} - \sigma_{xx}}{2} + i\sigma_{xy} = -2\mu_c \rho_c^4 \left(\frac{i\Im(\mathbf{B})}{B_1} + \frac{\Re(\mathbf{B})}{B_2} \right) \quad (91)$$

Together with the fact that we have already shown that the pressure inside the inclusion is always homogenous, it can be deduced from eqn. (91) that all stress components are homogenous since only coordinate independent constants are involved. The corresponding expression for the maximum shear stress is

$$\frac{\tau}{\mu_m} = 2\tilde{\rho}_c^4 \tilde{\mu}_c \sqrt{\left(\frac{\dot{\gamma} \sin(2\alpha) + 2\dot{\epsilon} \cos(2\alpha)}{\tilde{\rho}_c^4 + \tilde{\rho}_c^4 \tilde{\mu}_c - \tilde{\mu}_c + 1} \right)^2 + \left(\frac{-\dot{\gamma} \cos(2\alpha) + 2\dot{\epsilon} \sin(2\alpha)}{\tilde{\rho}_c^4 + \tilde{\rho}_c^4 \tilde{\mu}_c + \tilde{\mu}_c - 1} \right)^2} \quad (92)$$

In simple shear only the maximum τ experienced by a rotating inclusion is

$$\frac{\tau}{4\mu_m |\dot{\gamma}|} = \frac{1}{4} \frac{(t+1)^2 \tilde{\mu}_c}{t^2 + 2\tilde{\mu}_c t + 1} \quad (93)$$

For clast in a shear zone where generally $\tilde{\mu}_c \gg t$ we can derive a simpler expression for the maximum τ :

$$\frac{\tau}{4\mu_m |\dot{\gamma}|} = \frac{(t+1)^2}{8t} \quad (94)$$

For clasts with pressure insensitive visco-plastic rheology eqn. (94) can be used to determine if the clast is behaving viscously or starts to yield. It can be seen that at least an aspect ratio of 6:1 is required to produce a maximum shear stress value within the clast that exceeds the far-field shear stress value ($4\mu_m |\dot{\gamma}|$).

Complete Maximum Shear Stress Field

Evaluating the maximum shear stress for the matrix as well, we are in the position to plot the complete two-dimensional maximum shear stress field. If the materials behave plastically according to a von Mises failure criterion, Figures 18 to 21 can be interpreted as displaying the proximity to failure.

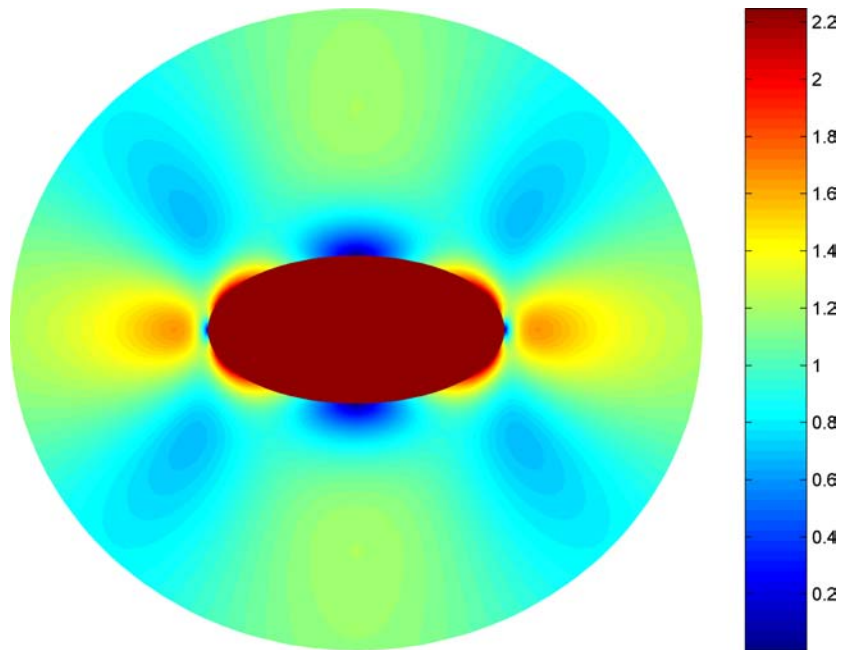


Figure 18

Maximum shear stress field around a strong elliptical inclusion

$t = 2, \dot{\gamma} = 0, \dot{\varepsilon} = -0.5, \alpha = 0^\circ, \tilde{\mu}_c = 1000.$

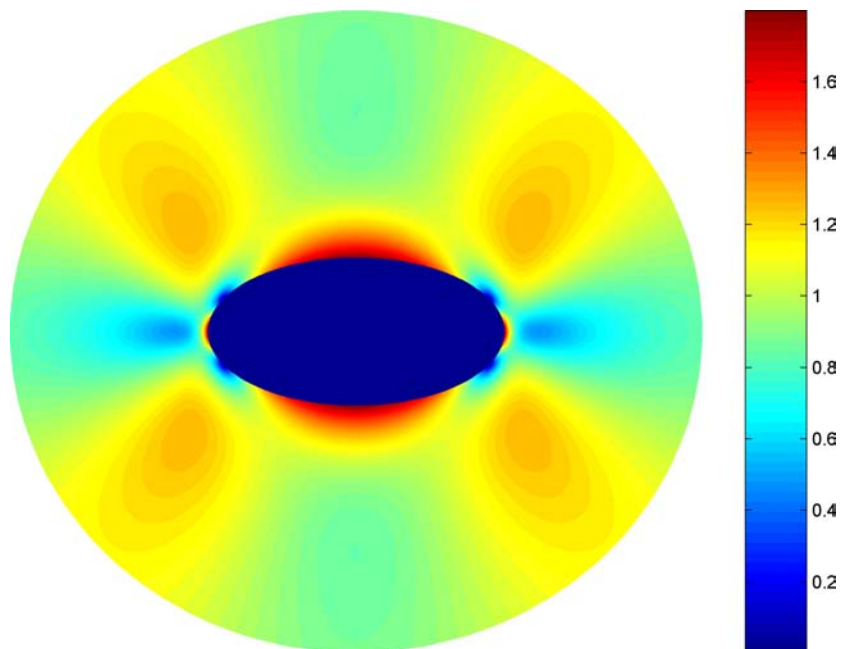


Figure 19

Maximum shear stress field around a weak elliptical inclusion

$t = 2, \dot{\gamma} = 0, \dot{\varepsilon} = -0.5, \alpha = 0^\circ, \tilde{\mu}_c = 1/1000.$

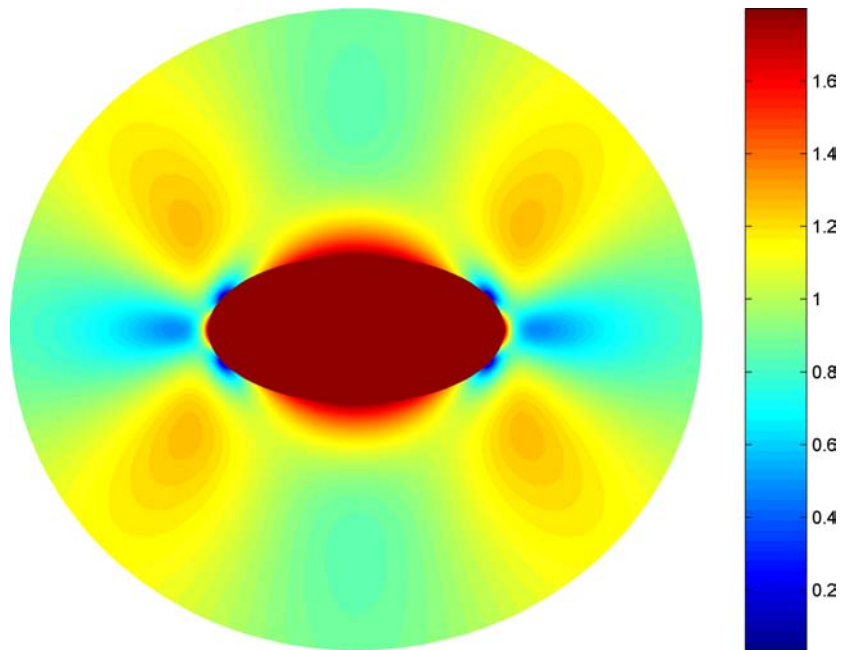


Figure 20

Maximum shear stress field around a strong elliptical inclusion

$t = 2$, $\dot{\gamma} = 0$, $\dot{\varepsilon} = -0.5$, $\alpha = -45^\circ$, $\tilde{\mu}_c = 1000$.

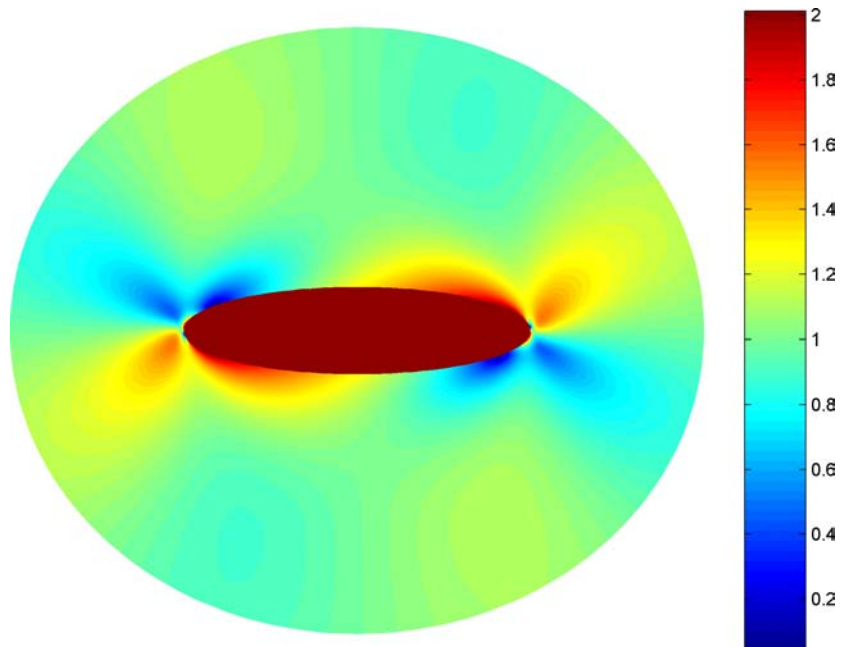


Figure 21

Maximum shear stress field around a strong elliptical inclusion

$t = 4$, $\dot{\gamma} = 0$, $\dot{\varepsilon} = -0.5$, $\alpha = -30^\circ$, $\tilde{\mu}_c = 1000$.

DISCUSSION AND CONCLUSION

We have presented the complete set of possible closed-form analytical solutions for isolated, deformable elliptical inclusions subjected to general shear, far-field flows. Our aim was to demonstrate how the essential parameters can be extracted from the two complex potentials that form the solution based on Muskhelishvili's method.

The rheologies used in this work are all Newtonian. It is clear that for geological purposes a more adequate rheology would be more complex, such as power-law. The method as it is presented here is applicable to incompressible all-elastic and all-viscous problems. Due to the established validity of Eshelby's conjecture for inclusions with perfect bonding to the matrix, it is possible to introduce more complex rheologies for the inclusion since the uniformity of the inclusion values largely facilitates the analysis. For example, it is possible to introduce a power-law or visco-elasto-plastic rheology for the inclusion. However, for the matrix, or even the layer between inclusion and matrix, this is not possible. Yet, it must be emphasized that the analytical analysis of the Newtonian case is of utmost importance.

(1) The presented analytical solutions allow for verification, testing and tuning (e.g., necessary mesh resolution) of numerical codes for the Newtonian case. This should be the pre-requisite before investigating non-linear rheologies.

(2) Only analytical solutions allow for elegant handling of large parameter-spaces. Especially, if the characteristics of the system are unexpected, as shown here, analytical solutions are the fastest possible way to capture the systematics and to train the intuition. Based on the understanding from the analytical solutions, the analysis can be continued with combined asymptotic and numerical methods.

(3) Generally, the power-law results are a variation of the Newtonian results preserving many of the Newtonian characteristics. This is true for mantled porphyroclasts (Schmid and Podladchikov, 2002) and another example is the folding of a Newtonian layer (Biot, 1961) compared to a power-law layer (Fletcher, 1974).

(4) Analytical solutions allow for direct and precise analysis of key-parameters throughout the domain, which with numerical models can only be achieved through systematic runs that may involve thousands of experiments.

Our application to a "real" geological problem is to the mantled porphyroclast in a shear zone. The results have important implications concerning the: i) distribution and amplitudes of the driving forces of phase changes, metamorphic reactions and deformation mechanisms, ii) estimation of clast-matrix viscosity contrasts, iii) kinematic clast behaviour and development of shape preferred orientations, iv) strain estimation from clasts in natural shear zones, v) general understanding of the clast as a function of geometry, present phases and viscosity contrasts. However, we leave it to the reader to explore further applications of geological problems. The possibilities are vast and promising applications include dikes with or without chilled rims, magma chambers, faults surrounded by damaged zone areole, cracks filled with another phase, zonation of crystals, etc. The number of additional problems that can be solved with Muskhelishvili's method is infinite. Through the use of Schwarz-Christoffel transformations (Spiegel, 1964; Driscoll and Trefethen, 2002), arbitrary single polygons can be treated. Combined with the variational principles of conformal transformations (Lavrentev and Schabat, 1967), the resulting analytical tools are capable of dealing with a huge variety of two-dimensional problems in elasticity and slow viscous flows. However, it should be realized that the number of problems already solved with Muskhelishvili's method is immense and these solutions just await applications in geology and geophysics.

ACKNOWLEDGEMENTS

This research was supported by the ETH Zurich, grant TH 0-20650-99. We wish to thank Jean-Pierre Burg, Boris Kaus and Stefan Schmalholz for helpful and inspiring discussions.

REFERENCES

- Barenblatt, G.I., 1996. Scaling, self-similarity, and intermediate asymptotics. Cambridge texts in applied mathematics ; 14. Cambridge University Press, Cambridge ; New York, xv, 386 pp.
- Batchelor, G.K., 1967. An introduction to fluid dynamics. University Press, Cambridge, 615 S. pp.
- Bilby, B.A., Eshelby, J.D. and Kundu, A.K., 1975. Change of Shape of a Viscous Ellipsoidal Region Embedded in a Slowly Deforming Matrix Having a Different Viscosity. *Tectonophysics*, 28(4): 265-274.
- Biot, M.A., 1961. Theory of Folding of Stratified Viscoelastic Media and Its Implications in Tectonics and Orogenesis. *Geological Society of America Bulletin*, 72(11): 1595-1620.
- Chandrasekhar, S., 1961. Hydrodynamic and hydromagnetic stability. Clarendon Press, Oxford., 652 pp.
- Driscoll, T.A. and Trefethen, L.N., 2002. Schwarz-Christoffel mapping. Cambridge University Press, New York, cm. pp.
- Eshelby, J.D., 1959. The Elastic Field Outside an Ellipsoidal Inclusion. *Proceedings of the Royal Society of London Series a- Mathematical and Physical Sciences*, 252(1271): 561-569.
- Fletcher, R.C., 1974. Wavelength selection in the folding of a single layer with power-law rheology. *Am. J. Sci.*, 274(11): 1029-1043.
- Freeman, B., 1987. The Behavior of Deformable Ellipsoidal Particles in 3- Dimensional Slow Flows - Implications for Geological Strain Analysis. *Tectonophysics*, 132(4): 297-309.
- Furuhashi, R., Huang, J.H. and Mura, T., 1992. Sliding Inclusions and Inhomogeneities with Frictional Interfaces. *Journal of Applied Mechanics-Transactions of the Asme*, 59(4): 783-788.
- Gao, Z., 1995. A Circular Inclusion With Imperfect Interface: Eshelby's Tensor and Related Problems. *Journal of Applied Mechanics-Transactions of the Asme*, 62: 860-866.
- Ghosh, S.K. and Ramberg, H., 1976. Reorientation of Inclusions by Combination of Pure Shear and Simple Shear. *Tectonophysics*, 34(1-2): 1-70.
- Huang, J.H., Furuhashi, R. and Mura, T., 1993. Frictional Sliding Inclusions. *Journal of the Mechanics and Physics of Solids*, 41(2): 247-265.
- Jaeger, J.C. and Cook, N.G.W., 1979. Fundamentals of rock mechanics. Chapman & Hall, London, XXII, 593 pp.
- Jeffery, G.B., 1922. The motion of ellipsoidal particles immersed in a viscous fluid. *Proceedings of the Royal Society of London*, A102: 161-179.
- Kenkmann, T. and Dresen, G., 1998. Stress gradients around porphyroclasts: palaeopiezometric estimates and numerical modelling. *Journal of Structural Geology*, 20(2-3): 163-173.
- Kolosov, G.V., 1907. Dissertation, St. Petersburg.
- Lavrentev, M.A. and Schabat, B.V., 1967. Methoden der komplexen Funktionentheorie. VEB Deutscher Verlag der Wissenschaften, Berlin, 846 S. pp.
- Lu, J.-K., 1995. Complex variable methods in plane elasticity. Series in pure mathematics ; v. 22. World Scientific, Singapore ; River Edge, NJ, viii, 230 pp.
- Masuda, T. and Ando, S., 1988. Viscous-Flow around a Rigid Spherical Body - a Hydrodynamical Approach. *Tectonophysics*, 148(3-4): 337-346.

- Moresi, L., Zhong, S.J. and Gurnis, M., 1996. The accuracy of finite element solutions of Stokes' flow with strongly varying viscosity. *Physics of the Earth and Planetary Interiors*, 97(1-4): 83-94.
- Mura, T., 1987. *Micromechanics of defects in solids*. Nijhoff, Dordrecht etc., XIII, 587 S. pp.
- Mura, T., 2000. Some new problems in the micromechanics. *Materials Science and Engineering a-Structural Materials Properties Microstructure and Processing*, 285(1-2): 224-228.
- Muskhelishvili, N.I., 1953. *Some basic problems of the mathematical theory of elasticity*. Noordhoff Groningen. Available through Kluwer's Printing on Demand (POD) program (www.wkap.com), 704 pp.
- Passchier, C.W. and Simpson, C., 1986. Porphyroclast Systems as Kinematic Indicators. *Journal of Structural Geology*, 8(8): 831-843.
- Pelletier, D., Fortin, A. and Camarero, R., 1989. Are Fem Solutions of Incompressible Flows Really Incompressible - (or How Simple Flows Can Cause Headaches). *International Journal for Numerical Methods in Fluids*, 9(1): 99-112.
- Ranalli, G., 1995. *Rheology of the Earth*. Chapman & Hall, London [etc.], XV, 413 S. pp.
- Rice, J.R., 1968. A Path Independent Integral and Approximate Analysis of Strain Concentration by Notches and Cracks. *Journal of Applied Mechanics*, 35(2): 379-&.
- Ru, C.Q. and Schiavone, P., 1997. A circular inclusion with circumferentially inhomogeneous interface in antiplane shear. *Proceedings of the Royal Society of London Series a- Mathematical Physical and Engineering Sciences*, 453(1967): 2551-2572.
- Savin, G.N., 1961. *Stress concentration around holes*. Pergamon Press, New York,, 430 pp.
- Schmid, D.W. and Podladchikov, Y.Y., 2002. Mantled porphyroclast gauges. *Journal of Structural Geology*, submitted.
- Shen, H., Schiavone, P., Ru, C.Q. and Mioduchowski, A., 2001. Stress analysis of an elliptic inclusion with imperfect interface in plane elasticity. *Journal of Elasticity*, 62(1): 25-46.
- Simpson, C. and Wintsch, R.P., 1989. Evidence for Deformation-Induced K-Feldspar Replacement by Myrmekite. *Journal of Metamorphic Geology*, 7(2): 261-275.
- Spiegel, M.R., 1964. *Schaum's outline of theory and problems of complex variables with an introduction to conformal mapping and its applications [including 640 solved problems]*. Schaum Publishing, New York, 313 pp.
- Stagni, L., 1991. Elastic field perturbation by an elliptic inhomogeneity with a sliding interface. *Journal of Applied Mathematics and Physics*, 42: 881-819.
- Tenczer, V., Stuwe, K. and Barr, T.D., 2001. Pressure anomalies around cylindrical objects in simple shear. *Journal of Structural Geology*, 23(5): 777-788.
- Turcotte, D.L. and Schubert, G., 1982. *Geodynamics applications of continuum physics to geological problems*. Wiley, New York, ix, 450 pp.

APPENDIX:
COEFFICIENTS FOR CIRCULAR INCLUSION WITH RIM

Q-COEFFICIENTS

$$Q_0 = K_2^2 + K_2 K_3 (-4\tilde{r}_l^2 + 6\tilde{r}_l^4 - 4\tilde{r}_l^6) + K_3^2 \tilde{r}_l^8 \quad (\text{A1})$$

$$Q_1 = \frac{4K_1 K_2 (\tilde{r}_l^2 - \tilde{r}_l^4)}{Q_0} \quad (\text{A2})$$

$$Q_2 = \frac{4K_1 (-4K_2 \tilde{r}_l^2 + 3K_2 \tilde{r}_l^4 + K_3 \tilde{r}_l^8)}{Q_0} \quad (\text{A3})$$

$$Q_3 = \frac{2K_2 K_4 (-K_2 \tilde{r}_l^2 + K_3 \tilde{r}_l^8)}{Q_0} \quad (\text{A4})$$

$$Q_4 = \frac{2K_2 (\tilde{\mu}_l + K_1) (\tilde{r}_l^2 - \tilde{r}_l^4)}{Q_0} \quad (\text{A5})$$

$$Q_5 = \frac{2K_2 K_4 (-K_2 \tilde{r}_l^4 + K_3 \tilde{r}_l^8)}{Q_0} \quad (\text{A6})$$

$$Q_6 = \frac{K_3 (K_2 K_5 (-8\tilde{r}_l^2 + 6\tilde{r}_l^4) + 2(\tilde{\mu}_l^2 + K_1) \tilde{r}_l^8)}{Q_0} \quad (\text{A7})$$

$$Q_7 = \frac{-K_2 K_6 \tilde{r}_l^2 + 4K_2 K_7 \tilde{r}_l^4 - 6K_2 K_7 \tilde{r}_l^6 + 4K_8 \tilde{r}_l^8 - K_3 K_7 \tilde{r}_l^{10}}{Q_0} \quad (\text{A8})$$

$$Q_8 = \frac{-K_2 K_6 \tilde{r}_l^4 + 4K_2 K_7 \tilde{r}_l^6 - 2K_9 \tilde{r}_l^8 + 4K_2 K_7 \tilde{r}_l^{10} - K_3 K_7 \tilde{r}_l^{12}}{Q_0} \quad (\text{A9})$$

K-COEFFICIENTS

$$K_1 = \tilde{\mu}_l \tilde{\mu}_c \quad (\text{A10})$$

$$K_2 = (\tilde{\mu}_l - \tilde{\mu}_c)(\tilde{\mu}_l - 1) \quad (\text{A11})$$

$$K_3 = (\tilde{\mu}_l + \tilde{\mu}_c)(\tilde{\mu}_l + 1) \quad (\text{A12})$$

$$K_4 = \frac{\tilde{\mu}_l}{\tilde{\mu}_l - 1} \quad (\text{A13})$$

$$K_5 = \frac{\tilde{\mu}_l}{\tilde{\mu}_l + 1} \quad (\text{A14})$$

$$K_6 = (\tilde{\mu}_l - \tilde{\mu}_c)(\tilde{\mu}_l + 1) \quad (\text{A15})$$

$$K_7 = (\tilde{\mu}_l + \tilde{\mu}_c)(\tilde{\mu}_l - 1) \quad (\text{A16})$$

$$K_8 = (\tilde{\mu}_l - \tilde{\mu}_c)(\tilde{\mu}_l + \tilde{\mu}_c)(1 - \tilde{\mu}_l + \tilde{\mu}_l^2) \quad (\text{A17})$$

$$K_9 = (\tilde{\mu}_l - \tilde{\mu}_c)(\tilde{\mu}_l + \tilde{\mu}_c)(3 - 8\tilde{\mu}_l + 3\tilde{\mu}_l^2) \quad (\text{A18})$$

APPENDIX:
PRESSURE FIELD COMPARISON IN Z AND ζ

The power of the described method is that a solution for a problem with a complex geometry in the physical domain (z) can be solved through the help of conformal mapping in a geometrically simpler image domain (ζ). Figure 8 shows how the Joukowski transformation works. As a farther illustration we show here a direct comparison of the pressure fields in z and ζ for an elliptical inclusion.

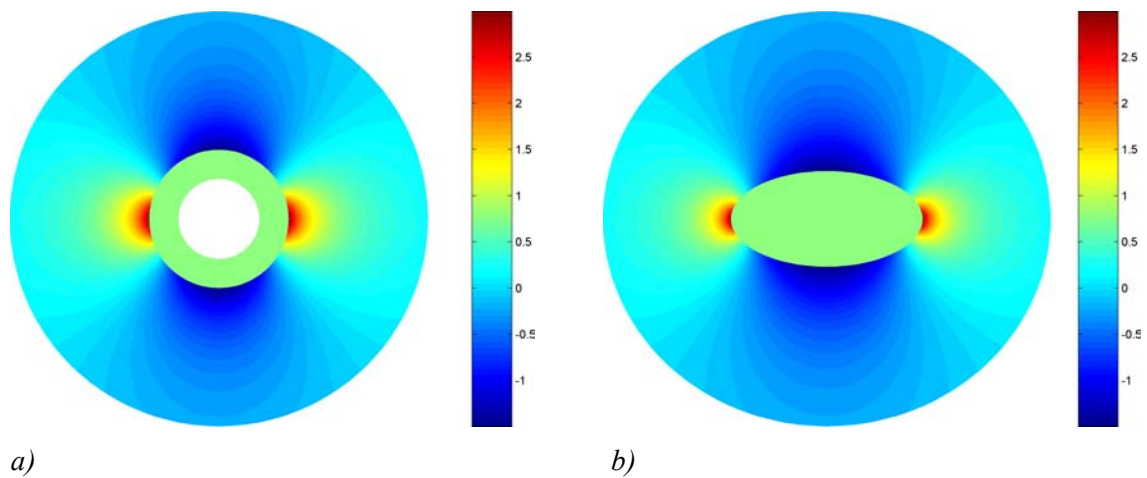


Figure 22

Comparison of the two-dimensional pressure field in image domain ζ (a) and physical domain z (b).

$t = 2$, $\dot{\gamma} = 0$, $\dot{\epsilon} = -0.5$, $\alpha = 0^\circ$, $\mu_c = 1000$.

CHAPTER 4: MUSKHELISHVILI'S METHOD APPLIED TO ELLIPTICAL AND LUBRICATED CIRCULAR INCLUSIONS IN GENERAL SHEAR: SOLUTION IMPLEMENTATION IN MATLAB

(This chapter is published in the e-collection of the ETH Zurich by Daniel Schmid and Yuri Podladchikov. It can be downloaded free of cost under the following URL

<http://e-collection.ethbib.ethz.ch/cgi-bin/show.pl?type=bericht&nr=188>)

Keywords: Muskhelishvili Method, Circular and Elliptical Inclusions, Lubricated Inclusions, Mantled Inclusions, Pure and Simple Shear, Viscous Rheology, Elastic Rheology, Incompressibility

INTRODUCTION

Two-dimensional problems in elasticity can be solved analytically by means of Muskhelishvili's method¹. This method is based on the fact that the result of the bi-harmonic equation can be represented by two complex potentials, called $\phi(z)$ and $\psi(z)$. The classical application of the method are circular and elliptical holes. At the beginning of the 20th century engineers had to face the problem that openings for the cannons on battle ships or for windows in airplanes could weaken the bulk structure so much that small forces/collisions could cause complete failure. This prompted the school of Kolosov and later Muskhelishvili to develop a method capable of solving such problems analytically.

In elastic geo-engineering problems such as tunnel building, Muskhelishvili's method is frequently applied, but rarely in the related field of slow viscous flow. Yet, the two problems are mathematically identical and consequently Muskhelishvili's method

¹ Muskhelishvili, N.I., 1953. Some basic problems of the mathematical theory of elasticity. Noordhoff, Groningen, 704S.

Through Kluwer's PoD program the book is available again and can be printed on demand, www.wkap.nl.

equally well applicable. We have recently shown ² the applicability of the method to slow viscous flow and we have derived all possible closed form solutions for mantled inclusions. “Mantled inclusions” means that we are dealing with a three phase system (inclusion, mantle and matrix), of incompressible materials with three, possibly different, viscosities. The inclusion is elliptical, including all shapes from infinite aspect ratio to circular inclusion. The inclusion is subjected to far-field general shear flows, i.e., arbitrary combinations of inclined pure and simple shear. Since, the solution for the mantled elliptical inclusion is an infinite series, we only present here the closed form solutions, which are: circular inclusion perfectly bonded to the matrix, circular inclusion perfectly bonded to an intermediate layer (mantle) which is perfectly bonded to the matrix, and the elliptical inclusion perfectly bonded to the matrix.

In order to stimulate a more widespread use of Muskhelishvili’s method which may be hampered by the fact that it makes use of “obscure” complex potentials we give here the complete set of MATLAB^{®3} scripts which we used to implement the solutions and visualize the results. The eight scripts provided have the following tasks:

CYL_P_INTERF.M

Pressure in the matrix at the circular clast-matrix interface.

CYL_P_INTERF_MAX.M

Maximum pressure in the matrix at the circular clast-matrix interface as a function of the viscosity contrast between clast and matrix.

CYL_P_MATRIX.M

Pressure around circular inclusion.

CYL_W_RIM

Complete two-dimensional field of pressure, maximum shear stress and stream function, when there is a third material between cylindrical inclusion and matrix.

ELL_DYNAMIX.M

2D pressure, stress and maximum shear stress caused by an elliptical inclusion

² ETH PhD Thesis by Dani Schmid, 2002.

³ MATLAB is a registered trademark of The MathWorks, Inc., 3 Apple Hill Drive, Natick, MA 01760-2098, USA, info@mathworks.com, <http://www.mathworks.com>

ELL_P_INTERF.M

Pressure in the matrix at the elliptical elast-matrix interface.

ELL_ROT_RATE.M

Analytical formula for the rotation rate of an ellipse in combined, inclined simple and pure shear.

ZHOUK_DEMO.M

Demonstration of the Joukowski transform.

These scripts also allow extraction of numerous other parameters with the help of the three basic formulae of Muskhelishvili's method:

$$p = -2\Re(\phi'(z)) \quad (1)$$

$$\frac{\sigma_{yy} - \sigma_{xx}}{2} + i\sigma_{xy} = \bar{z}\phi''(z) + \psi'(z) \quad (2)$$

$$v_x + iv_y = \frac{\phi(z) - z\overline{\phi'(z)} - \overline{\psi(z)}}{2\mu} \quad (3)$$

Where p is the pressure perturbation, σ is the total stress tensor, μ the viscosity, z the complex coordinate, v the velocity vector, x and y the usual Cartesian coordinates, ' means the first derivative versus z and '' the second, i is equal $\sqrt{-1}$, the over bar denotes conjugation, and \Re means the real part.

These expressions are only valid if no conformal mapping is applied. For cases where the Joukowski transformation is used, i.e., elliptical inclusions, care must be taken concerning the spatial derivatives. Since the problem is solved in a geometrically simpler image plane ζ , but the spatial derivatives must still be taken versus z , i.e., the complex coordinate of the physical plane, the relevant expressions are more complicated and the following set of equations must be employed:

$$p = -2\Re\left(\frac{1}{1-\zeta^{-2}}\frac{\partial\phi}{\partial\zeta}\right) \quad (4)$$

$$\frac{\sigma_{yy} - \sigma_{xx}}{2} + i\sigma_{xy} = \overline{\left(\zeta + \frac{1}{\zeta}\right)}\left(\frac{1}{(1-\zeta^{-2})^2}\frac{\partial^2\phi}{\partial\zeta^2} + \frac{-2}{(1-\zeta^{-2})^3}\frac{\partial\phi}{\zeta^3}\frac{\partial\phi}{\partial\zeta}\right) + \frac{\partial\psi}{\partial\zeta}\frac{1}{1-\zeta^{-2}} \quad (5)$$

$$v_x + iv_y = \frac{\phi - \left(\zeta + \frac{1}{\zeta}\right)\overline{\left(\frac{1}{1-\zeta^{-2}}\frac{\partial\phi}{\partial\zeta}\right)} - \bar{\psi}}{2\mu} \quad (6)$$

MATLAB SCRIPTS

Please note, that since these scripts are provided free of cost we put a big disclaimer on all of them and do not take any liability for correctness, errors, loss or whatever may happen; you use it at your own risk. Therefore the following applies to all of them:

%=====

DISCLAIMER OF WARRANTY:

Since the Software is provided free of charge, it is provided on an as is basis, without warranty of any kind, including without limitation the warranties of merchantability, fitness for a particular purpose and non-infringement. The entire risk as to the quality and performance of the Software is borne by the user. Should the Software prove defective, the user will assume the entire cost of any service and repair.

LIMITATION OF LIABILITY:

Under no circumstances and under no legal theory, tort, contract, or otherwise, shall the authors be liable to the user or any other person for any indirect, special, incidental, or consequential damages of any character including, without limitation, damages for loss of goodwill, work stoppage, computer failure or malfunction, or any and all other commercial damages or losses.

%=====

CYL_P_INTERF.M

```
=====
% CYL_P_INTERF.M
%
% Pressure in the matrix at the circular clast-matrix interface.
%
% 2002, Dani Schmid
%
=====
%SETUP ANGLES
theta    = 0:2*pi/359:2*pi;

%VISCOSITIES
mm       = 1;
mcs     = [1,2,10,1e6];

%FAR FIELD FLOW
er       = 0;
gr       = 1;

%CALCULATE AND PLOT
Styles   = {':k', '-.k', '--k', '-k'};
figure(1);
clf
counter=1;
for mc=mcs;
    Pressure    = 2.*mm.*(-2.*mc.*cos(2.*theta).*er- ...
                  mc.*gr.*sin(2.*theta)+2.*mm.*cos(2.*theta).* ...
                  er+mm.*gr.*sin(2.*theta))./(mc+mm);
    plot(theta/pi*180, Pressure, Styles{counter});
    hold on;
    counter     = counter+1;
end

axis([0 360 -2 2]);
set(gca, 'XTick', [0:45:360]);
xlabel('\theta');
ylabel('p/(\mu_m\gamma)', 'Rotation', 0);
title('Pressure Around Cylindrical Inclusion')
legend('\mu_c/\mu_m=1', '\mu_c/\mu_m=2', '\mu_c/\mu_m=10', ...
       '\mu_c/\mu_m=\infty', -1);
```

CYL_P_INTERF_MAX.M

```
%=====
% CYL_P_INTERF_MAX.M
%
% Maximum pressure in the matrix at the circular clast-matrix
% interface as a function of the viscosity contrast between clast
% and matrix.
%
% 2002, Dani Schmid
%
%=====

%LOGARITHMIC RANGE OF VISCOSITIES
mm      = 1;
mc      = logspace(-3,3);

%FAR FIELD FLOW
gr      = 1;

%MAXIMUM PRESSURE EXPRESSION
Pressure = 2.*mm.*(mc-mm)./(mc+mm).*gr;

%PLOT PRESSURE vs. THETA
figure(1);
clf
plot(mc, Pressure, '-k');
set(gca, 'XScale', 'log');
grid on;
set(gca, 'XMinorgrid', 'off');

xlabel('\mu_c/\mu_m');
ylabel('p/(\mu_m\gamma)', 'Rotation', 0);
title('Max. Pressure as f(\mu_c/\mu_m)')
```


CYL_P_MATRIX.M

```
%=====
% CYL_P_MATRIX.M
%
% Pressure around circular inclusion
%
% 2002, Dani Schmid
%
%=====
%FAR FIELD FLOW - VISCOSITIES - GEOMETRY
gr    = 1;
er    = 0;
mm    = 1;
mc    = 1e6;
rc    = 1;

%PRESSURE CALCULATION IN THE Z-PLANE
[X,Y] = meshgrid(-2:.01:2);
Z      = X+i*Y;
P      = -2.*mm.*(mc-mm)./(mc+mm).*real(rc^2./Z.^2.*(i*gr+2*er));

%PRESSURE IS ONLY FOR THE OUTSIDE OF THE CLAST
P(abs(Z)<rc) = NaN;

%PLOTTING
pcolor(X,Y,P)
axis image;
shading interp;
hold on;
contour(X,Y,P, [-1.5,-1,-.5,0,.5,1,1.5], 'k');
colorbar('horiz');
```

CYL_W_RIM

```

=====
% CYL_W_RIM
%
% Complete two-dimensional field of pressure, maximum shear stress
% and stream function
%
% 2002, Dani Schmid
%
=====
%DEFINE i
i   = sqrt(-1);
I   = sqrt(-1);

%INPUT PARAMETERS
er  = -0;    %Negative values indicate horizontal compression
gr  = 1;     %Positive value indicate top to the left shear
rl  = 1.2;
ml  = 1e+3;
mc  = 1e+3;

%DESIRED BOX SIZE
bs  = 3;    %Times rl

%K's
K1  = ml*mc;
K2  = (ml-mc)*(ml-1);
K3  = (mc+ml)*(ml+1);
K4  = ml/(ml-1);
K5  = ml/(ml+1);
K6  = (ml-mc)*(ml+1);
K7  = (mc+ml)*(ml-1);
K8  = (ml-mc)*(mc+ml)*(1-ml+ml^2);
K9  = (ml-mc)*(mc+ml)*(3-8*ml+3*ml^2);

%Q's
Q0  = K2^2+K2*K3*(-4*rl^2+6*rl^4-4*rl^6)+K3^2*rl^8;
Q1  = 4*K1*K2*(rl^2-rl^4)/Q0;
Q2  = (-16*K1*K2*rl^2+12*K1*K2*rl^4+4*K1*K3*rl^8)/Q0;
Q3  = K2*K4*(-2*K2*rl^2+2*K3*rl^8)/Q0;
Q4  = K2*(ml^2+K1)*(2*rl^2-2*rl^4)/Q0;
Q5  = K2*K4*(-2*K2*rl^4+2*K3*rl^8)/Q0;
Q6  = K3*(K2*K5*(-8*rl^2+6*rl^4)+2*(ml^2+K1)*rl^8)/Q0;
Q7  = (-K2*K6*rl^2+4*K2*K7*rl^4-6*K2*K7*rl^6+4*K8*rl^8 ...
      -K3*K7*rl^10)/Q0;
Q8  = (-K2*K6*rl^4+4*K2*K7*rl^6-2*K9*rl^8+4*K2*K7*rl^10 ...
      -K3*K7*rl^12)/Q0;

%RESOLUTION
nr   = 100;
nt   = 200;
Theta = 0:2*pi/nt:2*pi;

```

```

%CLAST
[R, THETA] = meshgrid(0:1/nr:1, Theta);
z          = R.*exp(i*THETA);
x          = real(z);
y          = imag(z);
Z_CLAST   = z; %Save z's for later contour plots

%Pressure
figure(1);
clf
PRES_CLAST = -6*Q1*real(z.^2*(-2*er+i*gr));
pcolor(real(z), imag(z), PRES_CLAST);
hold on;
%Streamfun
figure(2);
clf
STREAM_FUN_CLAST = er.*(-2./mc.*Q1.*y.^3.*x-1./mc.*Q2.*y.*x ...
    -2./mc.*Q1.*x.^3.*y)+(-1./4.*y.^2-1./4.*1./mc.*Q2.*y.^2 ...
    -1./2.*1./mc.*y.^4.*Q1).*gr;
pcolor(real(z), imag(z), STREAM_FUN_CLAST);
hold on;
%TAU
figure(3);
clf
TAU_CLAST = sqrt((-2.*Q2.*er+6.*Q1.*real(conj(z).*z.*(I.*gr ...
    -2.*er))).^2+(Q2.*gr+6.*Q1.*imag(conj(z).*z.*(I.*gr-2.*er))).^2);
pcolor(real(z), imag(z), TAU_CLAST);
hold on;

%LUBR
[R, THETA] = meshgrid(1:(rl-1)/nr:rl, Theta);
z          = R.*exp(i*THETA);
x          = real(z);
y          = imag(z);
Z_LUBR    = z;
%Pressure
figure(1);
PRES_LUBR = 2*real((i*gr+2*er)*Q3./z.^2-3*(-2*er+i*gr)*Q4*z.^2);
pcolor(real(z), imag(z), PRES_LUBR);
%Streamfun
figure(2);
STREAM_FUN_LUBR = ...
    -1./2./ml.*er.*(4.*x.*y.^3.*Q4+2.*y.*Q3./(x.^2+y.^2).*x ...
    -2.*Q5.*y.*x./(x.^2+y.^2).^2-x.*(-2.*Q3./(x.^2+y.^2).*y ...
    -6.*Q4.*(x.^2.*y-1./3.*y.^3))-2.*Q4.*(x.^3.*y ...
    -y.^3.*x)+2.*Q6.*y.*x)-1./2.*1./ml.*gr.*(1./2.*y.^2.*ml ...
    -x.*(Q3./(x.^2+y.^2).*x-3.*Q4.*x.*y.^2) ...
    -3./2.*Q4.*x.^2.*y.^2+3./4.*Q4.*y.^4-x.^2.*Q3./(x.^2+y.^2) ...
    -Q4.*(3./2.*x.^2.*y.^2-1./4.*y.^4)-Q5.*( ...
    -x.^2./(x.^2+y.^2).^2+1./2./(x.^2+y.^2))+1./2.*Q6.*y.^2);

pcolor(real(z), imag(z), STREAM_FUN_LUBR);
%TAU
figure(3);
TAU_LUBR = sqrt(real( ...
    -conj(z).* (2.*(I.*gr+2.*er).*Q3./z.^3+6.*(I.*gr ...
    -2.*er).*Q4.*z)+3.*(I.*gr+2.*er).*Q5./z.^4-(I.*gr ...
    -2.*er).*Q6).^2+imag(-conj(z).* (2.*(I.*gr+2.*er).*Q3./z.^3 ...

```

```

+6.*(I.*gr-2.*er).*Q4.*z)+3.*(I.*gr+2.*er).*Q5./z.^4-(I.*gr ...
-2.*er).*Q6).^2);
pcolor(real(z), imag(z), TAU_LUBR);

%MAT
[R, THETA] = ...
meshgrid(rl:(sqrt(2*bs^2*rl^2)-rl)/nr:sqrt(2*bs^2*rl^2), Theta);
z          = R.*exp(i*THETA);
x          = real(z);
y          = imag(z);
Z_MAT     = z;
%Pressure
figure(1)
PRES_MAT  = 2*real((i*gr+2*er)*Q7./z.^2);
pcolor(real(z), imag(z), PRES_MAT);
%Streamfun
figure(2)
STREAM_FUN_MAT = ...
er.*(-2.*Q7.*y.*x./(x.^2+y.^2)+Q8.*y.*x./ ...
(x.^2+y.^2).^2-x.*y)+(-1./2.*y.^2+Q7.*x.^2./ ...
(x.^2+y.^2)+1./2.*Q8.*(-x.^2./(x.^2+y.^2).^2+1./2./ ...
(x.^2+y.^2))).*gr;
pcolor(real(z), imag(z), STREAM_FUN_MAT);
%TAU
figure(3);
TAU_MAT   = ...
sqrt((-2.*er+real(2.*conj(z).* (I.*gr+2.*er).*Q7./z.^3 ...
-3.*(I.*gr+2.*er).*Q8./z.^4)).^2+(gr+imag(2.*conj(z).* ...
(I.*gr+2.*er).*Q7./z.^3-3.*(I.*gr+2.*er).*Q8./z.^4)).^2);
pcolor(real(z), imag(z), TAU_MAT);

%FINALIZE PLOTS=====
%Complex coordinates of clast and layer
Clast  = exp(i*Theta);
Layer  = rl*exp(i*Theta);

figure(1)
axis off
axis equal
axis([-bs*rl bs*rl -bs*rl bs*rl]);
shading interp;
plot(real(Clast), imag(Clast), '--k');
plot(real(Layer), imag(Layer), '--k');
title(['P \epsilon:', num2str(er), ' \gamma:', num2str(gr), ...
' \mu_c: ', num2str(mc), ' \mu_l: ', num2str(ml), ...
' r_l: ', num2str(rl)]);
cb_h    = colorbar('horiz. ');
pos_cb  = get(cb_h, 'pos');
set(cb_h, 'pos', [.26666, pos_cb(2), .504, pos_cb(4)])
set(get(cb_h, 'Title'), 'String', 'P');

figure(2)
axis equal
axis([-bs*rl bs*rl -bs*rl bs*rl]);
shading interp;
plot(real(Clast), imag(Clast), '--k');
plot(real(Layer), imag(Layer), '--k');
colorbar('horiz. ');

```

```

Z          = [ Z_MAT          ];
STREAM_FUN = [ STREAM_FUN_MAT ];
contour(real(Z), imag(Z), STREAM_FUN, 10, 'k')
axis off;
axis equal
axis([-bs*rl bs*rl -bs*rl bs*rl]);
shading interp;
plot(real(Clast), imag(Clast), '--k');
plot(real(Layer), imag(Layer), '--k');
title(['\Theta \epsilon:', num2str(er), ' \gamma:', num2str(gr), ...
' \mu_c: ', num2str(mc), ' \mu_l: ', num2str(ml), ' r_l: ', ...
num2str(rl)]);
cb_h      = colorbar('horiz. ');
pos_cb    = get(cb_h, 'pos');
set(cb_h, 'pos', [.26666, pos_cb(2), .504, pos_cb(4)])
set(get(cb_h, 'Title'), 'String', '\Theta');

figure(3)
axis off
axis equal
axis([-bs*rl bs*rl -bs*rl bs*rl]);
shading interp;
plot(real(Clast), imag(Clast), '--k');
plot(real(Layer), imag(Layer), '--k');
title(['\tau \epsilon:', num2str(er), ' \gamma:', num2str(gr), ...
' \mu_c: ', num2str(mc), ' \mu_l: ', num2str(ml), ' r_l: ', ...
num2str(rl)]);
cb_h      = colorbar('horiz. ');
pos_cb    = get(cb_h, 'pos');
set(cb_h, 'pos', [.26666, pos_cb(2), .504, pos_cb(4)])
set(get(cb_h, 'Title'), 'String', '\tau');

```

ELL_DYNAMIX.M

```
%=====
% ELL_DYNAMIX.M
%
% 2D pressure, stress and maximum shear stress caused by an
% elliptical inclusion
%
% 2002, Dani Schmid
%=====

%COMPLEX NUMBER DEFINITION
I      = sqrt(-1);
i      = sqrt(-1);

%VISCOSITY CONTRAST BETWEEN CLAST AND MATRIX
mc     = 1000;

%FAR FIELD FLOW
er     = -.5;
gr     = 0;
alpha  = -30/180*pi;

%ASPECT RATIO, t CANNOT BE 1 or SMALLER, USE t=1.001 FOR CIRCULAR
INCLUSION APPROXIMATION
t      = 4;
rc     = sqrt((t-1)*(t+1))/(t-1);

%SOLUTION CONSTANTS
BC     = (2.*er-I.*gr).*exp(+2.*I.*alpha);
B1     = rc.^4.*mc+rc.^4-1+mc;
B2     = rc.^4.*mc+rc.^4-mc+1;
B3     = rc.^4.*mc-mc-rc.^4+1;
B4     = -rc.^4.*mc-mc-rc.^4+1;
B5     = rc.^8.*mc-mc-rc.^8+1;

%RESOLUTION
rs     = 100;
ts     = 200;

%CLAST GRID IS FROM 1..rc
[rho, theta] = meshgrid(1:(rc-1)/rs:rc, 0:2*pi/ts:2*pi);
zeta_clast  = rho.*exp(i*theta);
p_clast     = real(-I.*mc.*B4./B1.*gr+2.*rc.^2.* ...
    (mc-1).*(I.*mc.*imag(BC)./B1-real(BC)./B2));
tau_clast   = -2.*mc.*rc.^4.*(I.*imag(BC)./B1+real(BC)./B2);
tau_clast   = sqrt((real(tau_clast)).^2 ...
    + (imag(tau_clast)).^2);

%Correct size of arrays
p_clast     = ones(size(rho))*p_clast;
tau_clast   = ones(size(rho))*tau_clast;

%MATRIX
[rho, theta] = meshgrid(rc:2*rc/rs:3*rc, 0:2*pi/ts:2*pi);
zeta_mat     = rho.*exp(i*theta);
```

```

p_mat          = -2.*rc.^2.*real(B3.*(-I.*imag(BC).*B2+ ...
                    real(BC).*B1)./(zeta_mat.^2-1)./B1./B2);
str_mat        = conj(zeta_mat+1./zeta_mat).* ...
                ((-I.*gr./zeta_mat.^3+2.*B3.*rc.^2.*(I.*imag(BC)./B1- ...
                    real(BC)./B2)./zeta_mat.^3)./(1-1./zeta_mat.^2)).^2- ...
                2.*(-1./2.*I.*gr.*(1-1./zeta_mat.^2))-B3.*rc.^2.* ...
                (I.*imag(BC)./B1-real(BC)./B2)./zeta_mat.^2)./(1- ...
                1./zeta_mat.^2)).^3./zeta_mat.^3)+(-real(BC)+I.*imag(BC)) ...
                .* (1-1./zeta_mat.^2))-B5.*(I.*imag(BC)./B1-real(BC) ...
                ./B2)./(zeta_mat.^3-zeta_mat).^2.*(3.*zeta_mat.^2-1))./ ...
                (1-1./zeta_mat.^2));

tau_mat        = sqrt((real(str_mat)).^2 + (imag(str_mat)).^2);

%TRANSLATE zeta -> z
z_clast        = zeta_clast+1./zeta_clast;
z_mat          = zeta_mat+1./zeta_mat;

%PLOT IN ZETA (IMAGE) DOMAIN
figure(1);
clf
subplot(211)
pcolor(real(zeta_clast), imag(zeta_clast), p_clast);
hold on;
pcolor(real(zeta_mat),    imag(zeta_mat),    p_mat);
shading interp;
axis image; axis off;
title('Pressure')
colorbar('vert')

subplot(212)
pcolor(real(zeta_clast), imag(zeta_clast), tau_clast);
hold on;
pcolor(real(zeta_mat),    imag(zeta_mat),    tau_mat);
shading interp;
axis image; axis off;
title('\tau')
colorbar('vert')

%PLOT IN Z (PHYSICAL) DOMAIN
figure(2);
clf
subplot(211)
pcolor(real(z_clast), imag(z_clast), p_clast);
hold on;
pcolor(real(z_mat),    imag(z_mat),    p_mat);
shading interp;
axis image; axis off;
title('Pressure')
colorbar('vert')

subplot(212)
pcolor(real(z_clast), imag(z_clast), tau_clast);
hold on;
pcolor(real(z_mat),    imag(z_mat),    tau_mat);
shading interp;
axis image; axis off;
%title('\tau')
colorbar('vert')

```

ELL_P_INTERF.M

```
=====
% ELL_P_INTERF.M
%
% Pressure in the matrix at the elliptical clast-matrix interface.
%
% 2002, Dani Schmid
=====

%CLEAR FIGURE
figure(1); clf

%COMPLEX NUMBER DEFINITION
I      = sqrt(-1);
i      = sqrt(-1);

%VISCOSITY CONTRAST BETWEEN CLAST AND MATRIX
mc     = 1e+3;

%FAR FIELD FLOW
er     = -1;
gr     = 0;
alpha  = 0/180*pi;

%ASPECT RATIO, t CANNOT BE <=1, USE t=1.001 FOR CIRCULAR INCLUSION
t      = [1.0001, 2, 10, 20];
Styles = {':k', '-.k', '--k', '-k'};

%CIRCUMFERENCE
theta  = 0:2*pi/360:2*pi;

for m=1:length(t)
    %TRANSLATE ASPECT RATIO INTO RADIUS
    rc  = sqrt((t(m)-1)*(t(m)+1))/(t(m)-1);
    %PRESSURE ON RADIUS
    press=(2.*mc.*rc.^4-2.*mc-2.*rc.^4+2).*rc.^2./...
    (mc.*rc.^4+mc-1+rc.^4)...
    ./((1+rc.^4+mc.*rc.^4-mc).*((rc.^2.*(cos(theta).^2-sin(theta) ...
    .^2)-1)./((rc.^2.*(cos(theta).^2-sin(theta).^2)-1).^2+4.*rc.^4 ...
    .*sin(theta).^2.*cos(theta).^2).*(-2.*er.*cos(2.*alpha)-gr ...
    .*sin(2.*alpha)).*(mc.*rc.^4+mc-1+rc.^4)+2.*rc.^2.*sin(theta) ...
    .*cos(theta)./((rc.^2.*(cos(theta).^2-sin(theta).^2)-1).^2+4.* ...
    rc.^4.*sin(theta).^2.*cos(theta).^2).*(-gr.*cos(2.*alpha)+ ...
    2.*er.*sin(2.*alpha)).*(1+rc.^4+mc.*rc.^4-mc));

    %PLOTTING
    plot(theta/pi*180, press, Styles{m});
    hold on;
end
achsen = axis;
axis([0 360 axsen(3:4)]);
set(gca, 'Xtick', [0:45:360])
grid on;

title('Pressure around elliptical inclusion');
xlabel('\theta'); ylabel('Pressure');
legend('t=1','t=2','t=10','t=20', -1);
```


ELL_ROT_RATE.M

```
%=====
% ELL_ROT_RATE.M
%
% Analytical formula for the rotation rate of an ellipse in
% combined, inclined simple & pure shear
%
% 2002, Dani Schmid
%
%=====
%CLEAR FIGURE
figure(1);
clf;

%FAR FIELD FLOW
er      = 0;
gr      = 1;
alpha   = -pi/2:(pi/2)/100:pi/2;

%ELLIPSE ASPECT RATIO
t       = 6;

%VISCOSITIES
mc      = [1e6,      1,  1/10, 1/100];
Styles  = {':k', '-.k', '--k', '-k'};

for m=1:length(mc)
    %ROTATION RATE
    rot_rate = (-1./2.*(t.^2-mc(m).*t.^2+mc(m)-1)./ ...
                (mc(m).*t.^2+mc(m)+2.*t).*cos(2.*alpha)-1./2).*gr ...
                -1./2.*(2.*mc(m).*t.^2-2.*t.^2-2.*mc(m)+2)./ ...
                (mc(m).*t.^2+mc(m)+2.*t).*sin(2.*alpha).*er;

    %PLOT
    plot(rot_rate, alpha/pi*180, Styles{m});
    hold on;
end
grid on;
xlabel('Rotation Rate/Shear Rate');
ylabel('\alpha');
legend('\mu_c/\mu_m=\infty', '\mu_c/\mu_m=1', ...
       '\mu_c/\mu_m=1/10', '\mu_c/\mu_m=1/100', -1);
```

ZHOUK_DEMO.M

```
%=====
% ZHOUK_DEMO.M
%
% Demonstration of the Joukowski transform
%
% 2002, Dani Schmid
%
%=====
%RESOLUTION
nt          = 200;
Theta       = 0:2*pi/nt:2*pi;

%SETUP THREE DIFFERENT CIRCLES
SLIT        = exp(i*Theta);
ELLE        = 2*exp(i*Theta);
JOUK        = 2*exp(i*Theta)-0.9696+i*0.3473;

%PLOT IN ZETA
figure(1)
clf
subplot(121)
hold on;
plot(real(SLIT), imag(SLIT), '-k');
plot(real(ELLE), imag(ELLE), '--k');
plot(real(JOUK), imag(JOUK), ':k');
axis equal
grid on
title('\zeta-Plane');

%TRANSFORM
SLIT        = SLIT + 1./SLIT;
ELLE        = ELLE + 1./ELLE;
JOUK        = JOUK + 1./JOUK;

%PLOT IN Z
subplot(122)
hold on;
plot(real(SLIT), imag(SLIT), '-k');
plot(real(ELLE), imag(ELLE), '--k');
plot(real(JOUK), imag(JOUK), ':k');
axis equal;
grid on
title('z-Plane');
```

CHAPTER 5: ARE ISOLATED STABLE RIGID CLASTS IN SHEAR ZONES EQUIVALENT TO VOIDS?

(This chapter is submitted “Tectonophysics” by Daniel W. Schmid and Yuri Yu. Podladchikov)

ABSTRACT

Isolated rigid clasts in shear zones often exhibit systematic inclinations with respect to the shear plane at shallow positive angles. This shape preferred orientation cannot be explained by any of the analytical theories used in geology. It was recently recognized that a weak mantle surrounding the clast or a slipping clast-matrix interface may be responsible for the development of the observed inclinations. Physical considerations lead us to conjecture that such mantled rigid clasts can be treated effectively as voids. The resulting theory agrees well with field data, in contrast to previous models. The theory has implications for our understanding of: clast rotation, shape preferred orientation development, strain estimation, and far-field flow reconstructions.

Keywords: clasts, inclusions, shear zones, stabilization, theory

INTRODUCTION

Geological field observations sometimes deliver counterintuitive and seemingly coincidental patterns. Careful examination often resolves these paradoxes by correcting our intuition, which is usually based on oversimplified or non-direct analogies. The “strange coincidences” do not call for special physics; they call for more quantitative evaluation of classical physics predictions compared to quick qualitative intuition-based reasoning. We see the ongoing active discussion on synchronous stabilization of apparently non-interacting rigid particles in shear zones tending towards instantaneous stretching directions, instead of being continuously rotated, as an excellent example of such a paradox.

If one considers a simple thought experiment whereby a Swiss cheese is sheared, its holes will deform to ellipses, initially aligned towards the stretching direction at 45° to the shear plane. Why do we see an almost identical picture for rigid particles in shear zones, having large inclination angles to the shear zone, even after the surrounding matrix accommodated enormous amounts of shear strain (Figure 1)? A picture of an airfoil, welded to something out of the observation plane, resisting the action of the gas flow that tries to turn and to lift it comes to mind. What holds the clasts in mylonitic shear zones? Why do they all have (coincidentally?) similar inclination angles after thousands percent of strain? The resolution discussed here is that presence of a seemingly unimportant thin, and weak, boundary layer, or imperfect welding of the clast to the matrix turns the clast into a hybrid of quasi-rigid and quasi-void behaviors. This mantle causes the clast to back-rotate toward the stretching direction as a void would, but the presence of the clast allows this void to keep its overall shape as a rigid particle.

The behavior of particles embedded in a matrix and subjected to boundary conditions remains a problem of fundamental interest for many branches of science. The analytical theories used in geology go back Jeffery (1922) who, based on Einstein (1906), developed a theory that explains the behavior of a rigid ellipsoid immersed in a viscous fluid subjected to far field simple shear flow. The most important addition was made by Ghosh and Ramberg (1976) who combined Jeffery’s theory and Muskhelishvili’s (1953) complex variable method to a two dimensional theory that explains the behavior of rigid elliptical particles embedded in a viscous fluid subjected to arbitrary combinations of pure and simple shear.

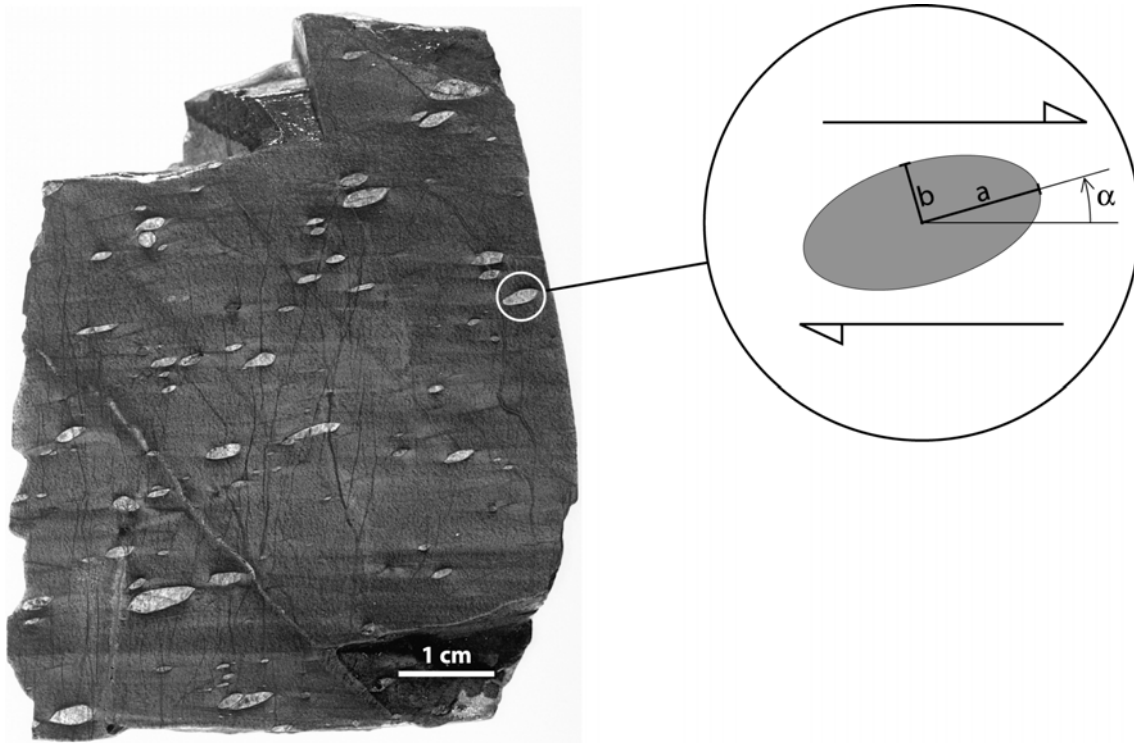


Figure 1

Ultramafic mylonite showing a clear shape preferred orientation of olivine porphyroclasts inclined at a low angle to the shear plane (horizontal). Shear sense is top to the right. Site location is near Finero in the Italian western alps. The inclination angle measure convention is displayed in the insert. (Photo courtesy G. Pennacchioni)

Other fields of science developed more complex theories in order to respond to the specific needs. Based on the alternative analytical solutions by Muskhelishvili (1953) and Eshelby (1959), researchers in the fields of composites and defects in solids derived in recent years the expressions for inclusions with imperfect bonding to the matrix (e.g., Mura, 1987; Furuhashi et al., 1992; Gao, 1995; Ru and Schiavone, 1997; Shen et al., 2001). A common finding of these works is that the so called Eshelby conjecture does not hold for a cylindrical or elliptical inclusion with a slipping interface. The Eshelby conjecture states that stresses applied at infinity cause constant stresses inside the inclusion, i.e., for arbitrary combinations of pure and simple shear, and arbitrary orientation and aspect ratio of the ellipsoidal inclusion, the stress state inside is homogenous and can be completely described by a single stress tensor.

The invalidity of Eshelby's conjecture is of fundamental importance for geological applications, where the observed systems are not likely to show perfect bonding

between clast and matrix (either due to interfacial slip or the presence of a third, weak phase, i.e., the mantle). Inhomogeneous stress states inside the inclusion are not only expected to change the flow patterns, but may cause transitions into different deformation mechanism fields, drive metamorphic reactions and be the cause for asymmetric zoning (e.g., myrmekite distribution, Simpson and Wintsch, 1989).

The focus of this study is the kinematic behavior of isolated, rigid clasts in shear zones. The term rigid is used here to describe a phase that has a much higher resistance to flow than all other phases present, thus termed weak. A clast that only interacts with the homogenous surrounding matrix and not with nearby clasts is designated an isolated clast. Ildefonse et al. (1992) have shown that the interaction effects become significant if individual clasts are closer than one diameter, and this distance is assumed to be the limit of applicability of the presented work.

The motivation for this study is the aforementioned observation that natural shear zones often exhibit systematic inclinations of porphyroclasts (Passchier and Trouw, 1996; Snoke et al., 1998). Analysis of natural data sets reveals that these inclinations are at shallow, positive angles with respect to the shear plane (e.g., Figure 1 and Mancktelow et al., 2002) and that there is a general trend for more elongated clasts to be less inclined with respect to the shear plane (Pennacchioni et al., 2001; ten Grotenhuis et al., 2002, cf. Figure 4). If large numbers of clasts show these inclinations then they must be stable or at least meta-stable, with the clast rotation rates, $\dot{\omega}$, vanishing compared to the shear rate, $\dot{\gamma}$. Existing analytical theories used in structural geology fail to give an explanation for the observed stable positions, either because no stable positions exists (Jeffery, 1922) or because the location and trend of the stable position does not correspond to the field data (Ghosh and Ramberg, 1976, cf. Figure 4). However, there is evidence from field data and analogue modeling that the observed stable orientations are due to interfacial slip or a weak mantle (Ildefonse and Mancktelow, 1993; Marques and Coelho, 2001; Mancktelow et al., 2002). If this is indeed the reason for clast stabilization then we need to rethink the possible applications, such as deciphering the far-field flow conditions during deformation (Ghosh and Ramberg, 1976; Passchier, 1987) and strain determinations (see Arbaret et al., 2000, for a review).

IGNORING THE CLAST TO STUDY THE CLAST

Mantled porphyroclasts exhibit the largest strains in the fine-grained mantle material. Consequently, it is likely that the mantle material has the smallest resistance to flow and thus the smallest viscosity of the system. We term such clasts “lubricated”. If the clast does not generate any mantle and behaves rigidly, slip is likely to occur between the matrix and clast. This interfacial slip case is simply an end-member of the lubricated clast in the limit of vanishing mantle viscosity.

If the weak mantle of the lubricated clast is either sufficiently thick (compared to the clast size) or has a vanishing viscosity compared to the matrix (the clast is assumed rigid), then the presence of the clast will be effectively masked by the mantle, e.g., the matrix does not “feel” the shear resistance of the clast. Practically matrix-mantle viscosity contrasts of 100:1 are already enough to “hide” the clast (Schmid and Podladchikov, 2002b). Since vanishing shear tractions cannot be responsible for the clast kinematics, the normal traction components must be analyzed. For example the pressure distribution in the matrix can be used as a proxy to determine if the clast-mantle couple behaves effectively as a rigid clast or as a void. Figure 2 shows the comparison of a lubricated clast to these two end-member cases. Although the lubricated clast has undergone substantial finite strain and developed complex mantle geometry it clearly corresponds to the weak clast case, which exhibits almost the same pressure perturbation pattern, i.e., pressure shadows. Hence, with respect to the normal tractions the presence of the rigid clast is again hidden from the matrix and the far-field flow. Therefore the lubricated clast can be reduced to a void.

It is tempting to use pressure or another stress component to explain clast rotation and stabilization based on the intuition that everything flows from high to low pressure areas and to argue that the high pressure zones adjacent to the clast push it towards the pressure lows (e.g., Marques and Coelho, 2001). Yet, because inertial effects are negligible the net forces and torques acting on any particle are always zero, irrespective of the particle rotation, and cannot determine the rotation direction. We therefore need to find an admissible explanation.

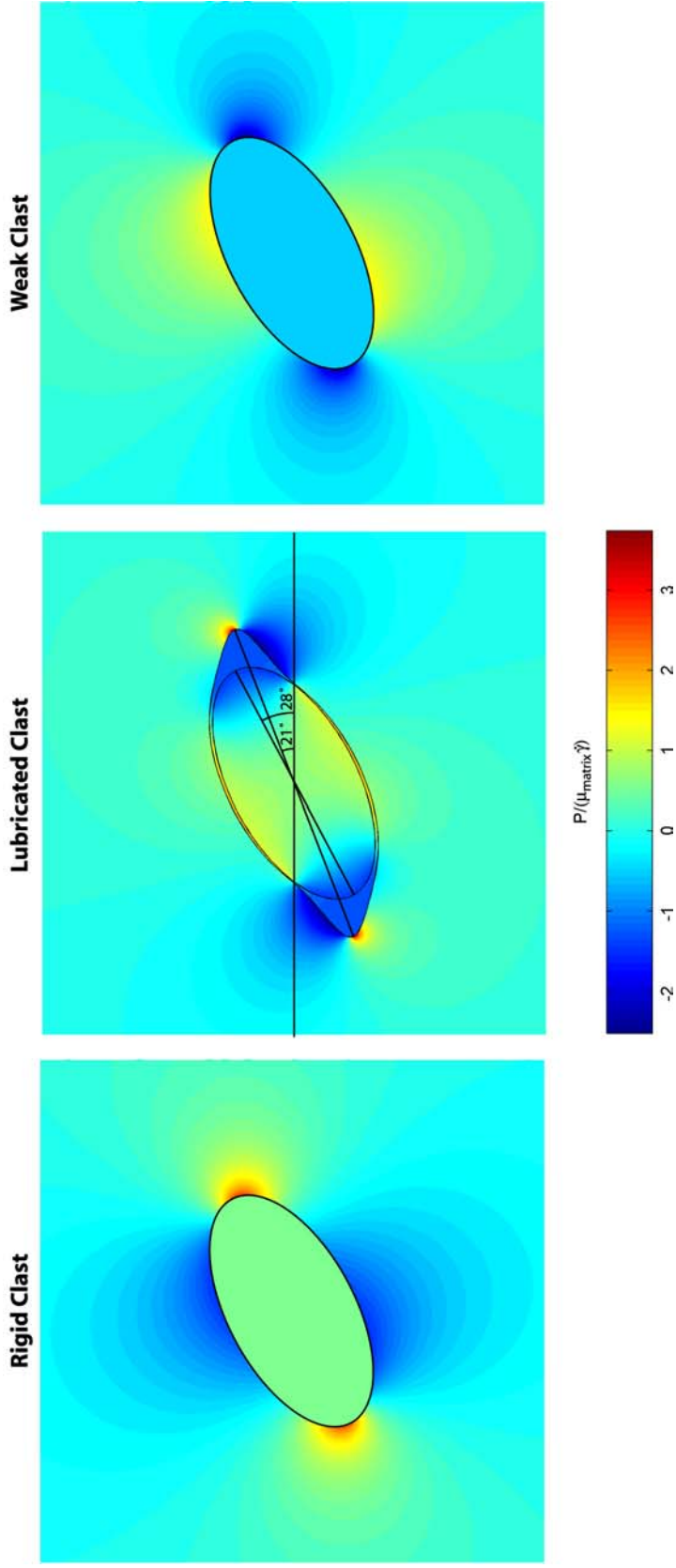


Figure 2

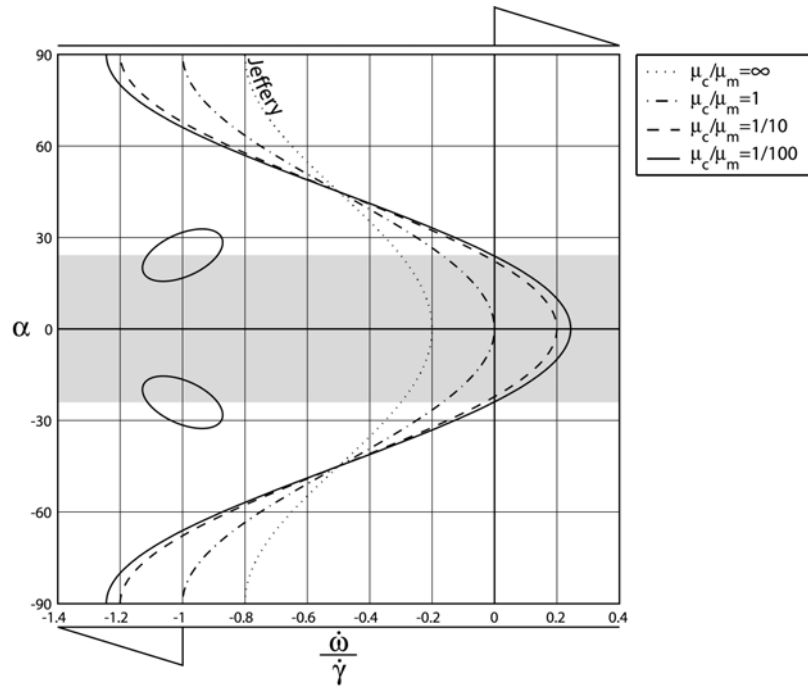
Finite Element Method based comparison of clast end-member cases, rigid and weak, to a finite strain mantled/lubricated clast experiment. The aspect ratio of the clast is in all three cases 2:1. The rigid and the weak clast are instantaneous experiments with a clast-matrix viscosity contrast of $1e6$ and $1e-6$, respectively.

The finite strain experiment has a clast-matrix viscosity contrast of 1000 and mantle-matrix contrast of 1/1000. The starting position was horizontal with the mantle material surrounding the clast equably with constant thickness. The achieved shear strain is 0.86, the measured aspect ratio of the weak layer 2.5, the inclination of the clast 28° , and the inclination of the weak mantle 21° . The data plotted is the pressure perturbation (P) normalized by the shear stress in the matrix.

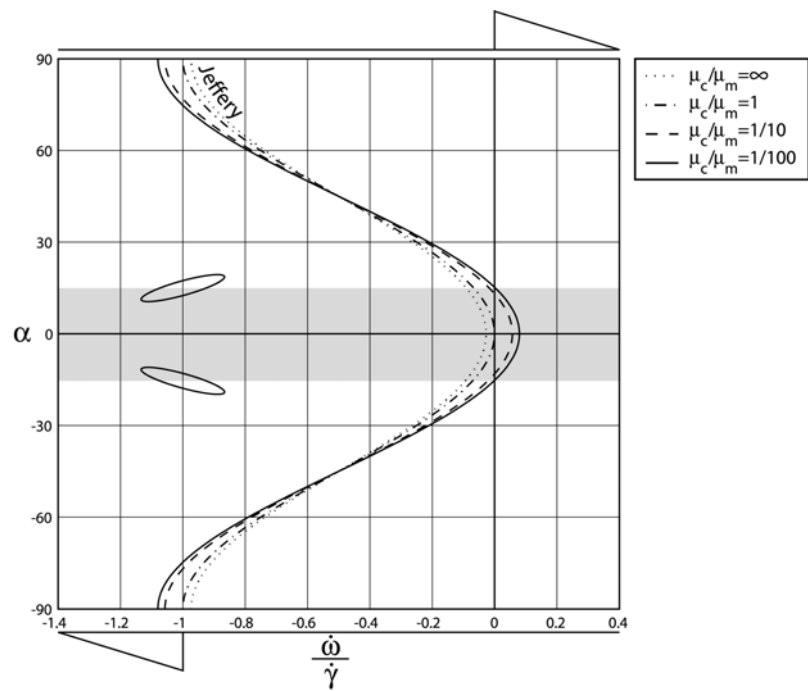
ROTATION DIRECTION OF PERFECTLY BONDED INCLUSIONS

Stable clast inclinations are the result of vanishing rotation rates. The rotational behavior of different kind of clast is of considerable complexity and illustrated here by means of some model cases. For example, the rigid circular clast always rotates with the applied shear sense, i.e., clockwise in top to the right simple shear. Jeffery (1922) showed that this rotation rate is half of the applied shear rate. If the circular clast has the same viscosity as the matrix material, then it is just a recorder of the homogeneous finite simple shear strain. The initially circular form will be instantaneously deformed into an ellipse with the long axis near vertical. With increasing strain this ellipse will become progressively elongated and the inclination will tend towards the shear plane (Ramsay and Huber, 1983). In contrast to this behavior is that of a circular void, which also cannot maintain its shape. Being pulled into the instantaneous stretching direction, the first ellipse appearance of the void is at 45° to the shear plane – as described with the Swiss cheese example in the introduction. The finite strain behavior is again that the ellipse becomes more elongated and approaches asymptotically the shear plane. Thus for all cases considered, the rotation direction of an elliptical shape derived from initially circular inclusion is synthetic with applied shear sense. This observation is dramatically altered for initially non-circular inclusions.

The behavior of clasts that are elliptical to start with requires knowledge of the initial inclination – for now we assume that the long axis is parallel to the shear plane. If rigid, such a clast will still rotate synthetically with the shear sense. However, due to its elliptical shape the rotational behavior is pulsating. If the particle is shear plane parallel, the simple shear flow easily streams around the particle, which consequently rotates slowest in this position. On the other hand, if the particle is inclined vertically to the shear plane it is a relatively large obstacle to the shear flow and consequently rotates fastest. The analytical expression describing this behavior goes again back to Jeffery's work and is displayed in Figure 3. If the elliptical clast in the shear plane parallel position has the same viscosity as the matrix the ellipse will be passively deformed. Although the simple shear flow has only shear plane parallel velocities the ellipse will initially undergo apparent back-rotation, antithetically against the shear sense. This can be easily checked with any drawing program. For finite strains the ellipse is progressively stretched and approaches the shear plane.



a)



b)

Figure 3

Rotational behavior of elliptical inclusions. The field where weak inclusions rotate backwards/antithetically is underlain gray.

a) Aspect ratio $R=2$

b) Aspect ratio $R=6$

The passive ellipse is a case of no viscosity contrast between the clast and the matrix, whereas the rigid case corresponds to the infinite contrast of viscosities. Therefore, lowering clast/matrix viscosity contrast from infinity to unity causes change in rotation direction from synthetic to antithetic.

The last and most relevant example is the shear plane parallel void, a case of infinitely small clast/matrix viscosity contrast. It may be speculated that it rotates backwards, extending the tendency of the passive ellipse compared to the rigid particle due to further drop of the clast-matrix viscosity contrast. The void can accommodate by deformation the pull towards the instantaneous stretching direction, which adds an extra component to the back-rotation compared to the passive ellipse case. This intuitive reasoning is rigorously verified by an exact analytical solution. We used Muskhelishvili's method (cf. Schmid and Podladchikov, 2002a) to derive the expression for the elliptical clast rotation, $\dot{\alpha}$, for simplicity approximated by the tangential velocity at the tip and divided by the tip to clast-clast center distance:

$$\frac{\dot{\alpha}}{\dot{\gamma}} = \cos(2\alpha) \frac{\tilde{\mu}_c R^2 + 2R - \tilde{\mu}_c + 2}{2\tilde{\mu}_c R^2 + 2\tilde{\mu}_c + 4R} - \frac{1}{2} \quad (1)$$

Here $\dot{\gamma}$ is the applied shear strain rate ($\dot{\gamma} = \partial v_x / \partial y$), x and y are Cartesian coordinates parallel and orthogonal to the shear plane, respectively, v the velocity vector, α the inclination of the ellipse to the simple shear flow, $\tilde{\mu}_c$ the viscosity ratio between clast and matrix (μ_c / μ_m), and R the aspect ratio of the elliptical inclusion. The sign convention used is that top to the right shearing is positive and all positive angular quantities mean counter-clockwise. The rigid limit ($\tilde{\mu}_c \rightarrow \infty$) of eqn. (1) is identical to Jeffery's expression (1922), cf. Figure 3. However, our interest is the infinitely weak inclusion, $\tilde{\mu}_c \rightarrow 0$, for which we obtain

$$\frac{\dot{\alpha}}{\dot{\gamma}} = -\sin(\alpha)^2 \frac{R+1}{R} + \frac{1}{2R} \quad (2)$$

This expression has the interesting property that positive rotation rates result when

$$\sin(\alpha)^2 < \frac{1}{2R+2} \quad (3)$$

($\dot{\gamma}$ always assumed to be positive). This means that the elliptical void indeed rotates backwards from a shear plane parallel position. However, it can be deduced from eqn. (3) that the maximum α for which back-rotation occurs is

$$\alpha = \arcsin\left(\frac{1}{\sqrt{2R+2}}\right) \quad (4)$$

which only yields 30° for $R \rightarrow 1$ as the maximum possible value for α , contrasting the 45° degrees that represent the direction of maximum instantaneous extension.

The characteristic rotational behavior of elliptical inclusions according to eqn. (1) is depicted in Figure 3. The rigid inclusion rotates according to Jeffery's theory, always in agreement with the applied shear sense. The distinctive effect of decreasing the inclusion viscosity is to amplify the behavior of the rigid inclusion, i.e., to accelerate the rotation where it is already fast and to slow it down where it is slow. If $\tilde{\mu}_c < 1$ the slow field even goes into back-rotation. The larger the aspect ratio is the smaller the size of the back-rotation field.

The expression of the maximum angle for which back-rotation occurs has a second significance: it represents meta-stable and stable clast inclinations. At the inclination angle described by eqn. (4) the rotation rate is zero and there is a mirror angle with respect to the shear plane that also has this characteristic. This negative, mirror angle is a meta-stable inclination, since the inclusion will stay at this inclination once it is there, but even the smallest perturbation will cause the inclusion to move towards the positive zero-rotation inclination. In fact, inclusions from all possible inclinations will either rotate forwards or backwards towards the positive inclination, which is why the positive inclination is stable.

Figure 3 also illustrates a seeming contradiction to our argumentation: the shear plane parallel passive ($\mu_c / \mu_m = 1$) ellipse is predicted to have zero rotation rate, which is opposed to the suggested drawing program exercise. This is the drawback of our simplified expression for the elliptical shape rotation rate, which may be nonzero even if material point at the tip does not move. Nevertheless, the tangential tip velocity is an accurate proxy for the rotation velocity. In addition we are really dealing with a lubricated clast that has only some characteristic of void as explained in the following.

EQUIVALENT VOID CONJECTURE

Lubricated rigid clasts, such as are common in natural shear zones, can be reduced to equivalent voids. The equivalent void has an elliptical shape, approximating the size of the clast. The rotational behavior of the equivalent void is given by the tangential tip velocity of real voids. This velocity pulls the equivalent void into a stable inclination that is at shallow positive angles to the shear zone. In contrast to real voids, shear deformations of the equivalent void can be ignored because its shape is given and supported by the contained rigid clast. The rigid clast is assumed to follow the pull of the tips and stabilize at approximately the angles predicted by the equivalent void theory.

VERIFICATION

To verify the validity of our assumption of void behavior, we compare the equivalent void theory with the geometry resulting from the presented finite strain experiment, Figure 3 (mid section). The clast-lubricant system has rotated backwards from the initially horizontal position into the present inclination, which is stable. The measured aspect ratio of the weak phase is 2.5:1, which, according to eqn. (4), should have a stable inclination at 22°. This theoretical value is remarkably close to the measured value of 21°. The aspect ratio of the clast itself is 2:1 and its inclination 28°. This is steeper than what our void theory predicts (24°) and is characteristic for all finite strain experiments performed. However, the measured deviations were never large, considering the simplifying assumptions made. The required shear strain to reach the stable orientation is < 1 , i.e., the total angle of the shear deformation $< 45^\circ$.

The most important test case of any geological theory is the comparison with field data. Figure 4 shows the comparison of the equivalent void theory versus natural data and the Ghosh and Ramberg theory. Ghosh and Ramberg (1976) derived their stable positions for a perfectly bonded clast in combined pure and simple shear. For given relative intensity of this two shear components the clast may have stable positions, depending on the aspect ratio. However, for any given far-field flow the stability curves lie in the gray areas and follow the trends indicated by the dashed lines. This trend conflicts with

the field data. In contrast, our equivalent void theory, shows excellent agreement with the field data, both in trend and absolute amplitudes of the angles.

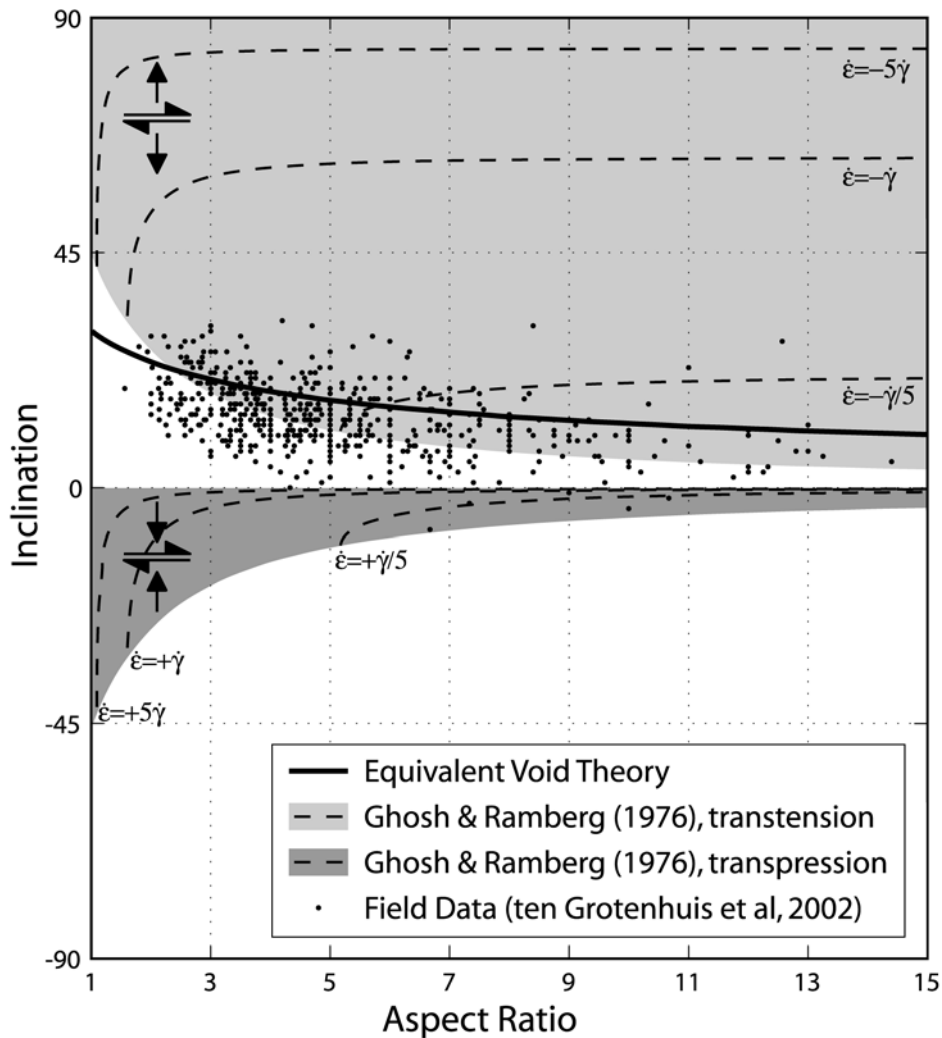


Figure 4

Comparison of natural data points collected by ten Grotenhuis et al (2002) to the presented void theory (bold solid line). The gray fields indicate the location of possible stable inclinations according to Ghosh and Ramberg’s combined pure and simple shear theory. Examples resulting from particular shear flow combinations are the dashed lines. The meaning of the terms “transpression” and “transtension” is explained through the arrows.

CONCLUSIONS

The combination of field, analogue, numerical and analytical results reduces the problem of the back-rotating and stabilizing competent clast in a shear zone to the one of an isolated void of fixed elliptical shape. Based on Muskhelishvili's (1953) method we have derived a theoretical curve for stable clast inclination that agrees well with natural data and represents an improvement compared to classical theories. The characteristics of the stable positions are that they are at shallow positive angles to the shear plane and the stable inclination angle decreases with increasing clast aspect ratio. The prerequisite for the theory to be applicable is the presence of a weak phase (weaker than the matrix) between rigid clast and matrix or imperfect bonding between clast and matrix, both of which are often the case in natural shear zones.

The equivalent void theory has the following important geological implications. i) Clasts in shear zones can have stable positions in simple shear without the requirement of an additional pure shear component. ii) The stable orientation can be approached either syn- or antithetically, hence the clast can rotate against the applied shear sense. iii) The strain needed to develop a strong shape preferred orientation is small ($\gamma \approx 1$) and therefore evaluations based on other theories may overestimate strain by orders of magnitudes. iv) The reconstruction of far-field shear flow conditions and the kinematic vorticity analysis must be modified to incorporate these new findings.

ACKNOWLEDGMENTS

This research was supported by the ETH Zurich, grant TH 0-20650-99. We wish to thank Jean-Pierre Burg, Stefano Ceriani, James Connolly, Neil Mancktelow, Fernando Ornelas and Karel Schulmann for helpful and inspiring discussions. Giorgio Pennacchioni is acknowledged for the photograph in Figure 1 and Saskia ten Grotenhuis for providing her field data file.

REFERENCES

- Arbaret, L. et al., 2000. Analogue and numerical modelling of shape fabrics: application to strain and flow determination in magmas. *Transactions of the Royal Society of Edinburgh-Earth Sciences*, 91: 97-109.
- Einstein, A., 1906. Eine neue Bestimmung der Moleküldimensionen. *Annalen der Physik*, 19: 289-306.
- Eshelby, J.D., 1959. The Elastic Field Outside an Ellipsoidal Inclusion. *Proceedings of the Royal Society of London Series a- Mathematical and Physical Sciences*, 252(1271): 561-569.
- Furuhashi, R., Huang, J.H. and Mura, T., 1992. Sliding Inclusions and Inhomogeneities with Frictional Interfaces. *Journal of Applied Mechanics-Transactions of the Asme*, 59(4): 783-788.
- Gao, Z., 1995. A Circular Inclusion With Imperfect Interface: Eshelby's Tensor and Related Problems. *Journal of Applied Mechanics-Transactions of the Asme*, 62: 860-866.
- Ghosh, S.K. and Ramberg, H., 1976. Reorientation of Inclusions by Combination of Pure Shear and Simple Shear. *Tectonophysics*, 34(1-2): 1-70.
- Ildefonse, B. and Mancktelow, N.S., 1993. Deformation around Rigid Particles - the Influence of Slip at the Particle Matrix Interface. *Tectonophysics*, 221(3-4): 345-359.
- Ildefonse, B., Sokoutis, D. and Mancktelow, N.S., 1992. Mechanical Interactions between Rigid Particles in a Deforming Ductile Matrix - Analog Experiments in Simple Shear-Flow. *Journal of Structural Geology*, 14(10): 1253-1266.
- Jeffery, G.B., 1922. The motion of ellipsoidal particles immersed in a viscous fluid. *Proceedings of the Royal Society of London*, A102: 161-179.
- Mancktelow, N.S., Arbaret, L. and Pennacchioni, G., 2002. Experimental observations on the effect of interface slip on rotation and stabilisation of rigid particles in simple shear and a comparison with natural mylonites. *Journal of Structural Geology*, 24(3): 567-585.
- Marques, F.O. and Coelho, S., 2001. Rotation of rigid elliptical cylinders in viscous simple shear flow: analogue experiments. *Journal of Structural Geology*, 23(4): 609-617.
- Mura, T., 1987. *Micromechanics of defects in solids*. Nijhoff, Dordrecht etc., 587 pp.
- Muskhelishvili, N.I., 1953. *Some basic problems of the mathematical theory of elasticity*. Noordhoff Groningen, 704 pp.
- Passchier, C.W., 1987. Stable Positions of Rigid Objects in Noncoaxial Flow - a Study in Vorticity Analysis. *Journal of Structural Geology*, 9(5-6): 679-690.
- Passchier, C.W. and Trouw, R.A.J., 1996. *Microtectonics*. Springer, Berlin [etc.], 289 pp.
- Pennacchioni, G., Di Toro, G. and Mancktelow, N.S., 2001. Strain-insensitive preferred orientation of porphyroclasts in Mont Mary mylonites. *Journal of Structural Geology*, 23(8): 1281-1298.
- Ramsay, J.G. and Huber, M.I., 1983. *Strain analysis*. Academic Press, London, 307 pp.
- Ru, C.Q. and Schiavone, P., 1997. A circular inclusion with circumferentially inhomogeneous interface in antiplane shear. *Proceedings of the Royal Society of London Series A - Mathematical Physical and Engineering Sciences*, 453: 2551-2572.
- Schmid, D.W. and Podladchikov, Y.Y., 2002a. Analytical solutions for deformable inclusions in general shear. *Geophysical Journal International*, submitted.
- Schmid, D.W. and Podladchikov, Y.Y., 2002b. Mantled porphyroclast gauges. *Journal of Structural Geology*, submitted.
- Shen, H., Schiavone, P., Ru, C.Q. and Mioduchowski, A., 2001. Stress analysis of an elliptic inclusion with imperfect interface in plane elasticity. *Journal of Elasticity*, 62(1): 25-46.
- Simpson, C. and Wintsch, R.P., 1989. Evidence for Deformation-Induced K-Feldspar Replacement by Myrmekite. *Journal of Metamorphic Geology*, 7(2): 261-275.
- Snoke, A.W., Tullis, J. and Todd, V.R., 1998. *Fault-related rocks : a photographic atlas*. Princeton University Press, Princeton, N.J., 617 pp.

ten Grotenhuis, S.M., Passchier, C.W. and Bons, P.D., 2002. The influence of strain localisation on the rotation behaviour of rigid objects in experimental shear zones. *Journal of Structural Geology*, 24(3): 485-499.

APPENDIX – MATLAB SCRIPT SUPPLEMENT TO FIGURE 4

```

=====
% PLOT_STABLE_POS.M
%
% Plot stable clast inclinations in shear zones according to the
% equivalent void theory and to Ghosh & Ramberg, 1976
%
% 2002, Dani Schmid
=====

%INITIALIZE FIGURE
figure(1)
colormap(gray)
clf
hold on

%VARIOUS sr VALUES AFTER GHOSH & RAMBERG 1976, sr = pure shear rate / simple shear rate
Sr = [-5, -1, -.2, +5, +1, +.2];

%ASPECT RATIOS
R = 1:.001:21;

%NEW VOID THEORY
angle = asin(1./sqrt(2*R+2))/pi*180;
void = plot(R, angle, '-r');
set(void, 'LineWidth', 2);

%STABLE FIELD BOUNDARY FOR GHOSH AND RAMBERG 1976
stable_bdry = -atan(R)/pi*180;
stable_bdry(stable_bdry<0) = stable_bdry(stable_bdry<0)+180;
stable_bdry = -stable_bdry+90;
plot(R, +stable_bdry, 'b');
fill([R, max(R), min(R)], [+stable_bdry, 0, 0], 'b');
fill([R, max(R), min(R)], [-stable_bdry, 90, 90], 'b');

%PLOT STABILITY CURVES FOR sr VALUES
for sr=Sr
    %THETA_5 eqn. 8b, GHOSH & RAMBERG 1976
    theta_5 = atan(-sr*(R.^2-1)-sqrt(sr^2.*(R.^2-1).^2-R.^2));
    theta_5(:, imag(theta_5)~=0) = NaN;
    theta_5 = real(theta_5);
    theta_5 = theta_5/pi*180;
    theta_5(theta_5<0) = theta_5(theta_5<0)+180;

    %TRANSLATE ANGLES INTO OUT SCHEME
    theta_5 = -theta_5+90;

    %SOLID IS STABLE - DASHED IS INSTABLE
    stable = plot(R, +theta_5, '-k');
end

%ADJUST PLOT
set(gca, 'Xlim', [1, max(R)]);
set(gca, 'Xtick', [1:2:max(R)]);
set(gca, 'Ylim', [-90, 90]);
set(gca, 'Ytick', [-90, -45, 0, 45, 90])
grid on

xlabel('Aspect Ratio')
ylabel('Inclination')
legend('VOID THEORY', 'GHOSH&RAMBERG fields of stable positions',...
'GHOSH&RAMBERG Examples of stable positions', 4)
title('STABLE INCLINATIONS IN SHEAR ZONES')

```

CHAPTER 6: FOLDING OF FINITE LENGTH LAYERS

(This chapter will be submitted “Journal of Geophysical Research” by Daniel W. Schmid, Yuri Yu. Podladchikov, and Fernando O. Marques)

ABSTRACT

Folding of finite length ductile and elastic layers embedded in a Newtonian viscous matrix are investigated and compared to conventional folding experiments, such as folding of an infinite layer or a finite layer in direct contact to lateral boundaries. Thin plate approximation combined with the complex potential method is used throughout the analysis. For power law layers, the infinite layer expression for the dominant wavelength remains valid, but the growth rate is greatly decreased for high viscosity contrast cases. This decrease helps to explain the apparent absence of periodic waveforms with very large wavelength to thickness ratio in nature. These findings are verified by 2D finite element simulations. In the elastic case, a set of new dependencies quantifying folding is revealed. A weak relationship between dominant wavelength and strain rate is established and verified by laboratory experiments over a controlling parameter range of ten orders of magnitude. The importance of the finite length of the folding layer is controlled by a dimensionless parameter D_a that is equal to the effective viscosity contrast divided over aspect ratio of the layer. If $D_a \gg 1$ the aspect ratio of the layer has a substantial influence on the folding process. Conversely, if $D_a \ll 1$ the classical "infinite" setup can be used without loss of accuracy even if the layer length is finite. All folding modes and the corresponding applicability ranges are summarized in an overview table. Appropriate quantification of folding modes is important for scaling of laboratory experiments, for deducing strain and rheological contrasts from natural folds and for identification of folding as a leading strain accommodation mode.

INTRODUCTION

Folding theories elaborate on the original setup chosen by Leonhard Euler in the early 18th century (Euler, 1744) who developed the theory for an elastic bar, surrounded by a much less competent matrix (air), and subjected to compression and/or moments, directly applied to the lateral boundaries. Substantial and important modifications of Euler's theory contributed to our understanding of how folds develop in nature. The features accounted for by these modifications include: finite competence contrast between layer and matrix, different combinations of layer and matrix rheologies, layer parallel shortening due to compression, finite amplitude effects, gravity and erosion, finite width matrix material, i.e., channels, three dimensional folds, and interaction in multi-layered systems. References can be found in textbooks such as Price and Cosgrove (1990) and Johnson and Fletcher (1994). A recent addition to the existing theories was made by Schmalholz and Podladchikov (2000; 2001) who developed a theory that predicts finite amplitude folding in pure shear up to 50 percent shortening and allows rheology independent strain estimates for fold geometries.

However, two principal features of natural folds have not been investigated: i) real folds are observed in layers of finite length and ii) usually there are no rigid walls that directly apply boundary conditions onto the lateral layer ends. This statement is scale independently valid: from small veins to subducting slabs. For example Sherwin and Chapple (1968) made measurement on the prototype of folds in layers of finite length where no rigid walls are present: quartz veins embedded in slate. This paper stimulated much research to explain the observed natural preference of small wavelengths to thickness ratios. Such ratios suggest small (<100) viscosity contrasts, in contradiction to laboratory measurements that show variability of the viscosity of natural rocks over many orders of magnitudes (Biot, 1961).



Figure 1

Extremity of a folded quartz vein, Almugraf, Portugal.

In this paper we investigate in two dimensions the folding of finite length layers embedded in a less competent matrix and subjected to pure shear far-field flow. The rheology of the matrix is assumed to be Newtonian, but we investigate the behavior of Newtonian, power-law and elastic layers. The basis of our approach is that a finite length layer can be approximated as an elongated ellipse, for which we can perform the basic state analysis that yields all necessary values for the classical linear stability analysis of folding.

BASIC STATE ANALYSIS

The indispensable requirement for the study of folding instability is the understanding of the basic state. The basic state has the same boundary conditions, material properties and geometrical configuration as the folding model, but no perturbation that could grow is present. In the “classical” basic state a layer is embedded in a weaker matrix and the entire system is subjected to layer-parallel compression, directly applied through rigid lateral boundaries onto matrix and layer (Figure 2). Knowing the boundary conditions and the material rheologies, one may deduce all components of strain (rates) and stresses throughout the system.

The basic state of the finite length layer is notably different (Figure 3). The layer is isolated within the surrounding matrix and has no direct contact to the boundaries of the box. Consequently the values of stress and strain (rate) within the system are not a priori known, even if rheology, geometry, and boundary conditions are given. Approximating the finite length layer by an ellipse simplifies the problem, because several analytical solutions exist for elliptical inclusions in a matrix subjected to general shear flows. Elliptical inclusions have an exceptional property that under homogenous boundary conditions (e.g., pure shear far-field flow), all stress and strain (rate) components within the inclusions are constant with respect to space and can be completely described by a single value. Examples are pressure (p), layer-parallel stress (σ_{xx}), and total layer parallel strain rate ($\dot{\epsilon}_{xx}$). The origin of this observation is often attributed to Eshelby (1957; 1959) who developed an analytical theory that allows to find the complete solution for the three dimensional ellipsoidal inclusion subjected to far field boundary conditions. In two dimensions, this property was already noted by Hardiman (1954). Constant values inside the inclusion additionally simplify the analysis of finite length layer folding, as it allows for straightforward combination of our basic state analysis with the “classical” folding analysis that also relies on constant values.

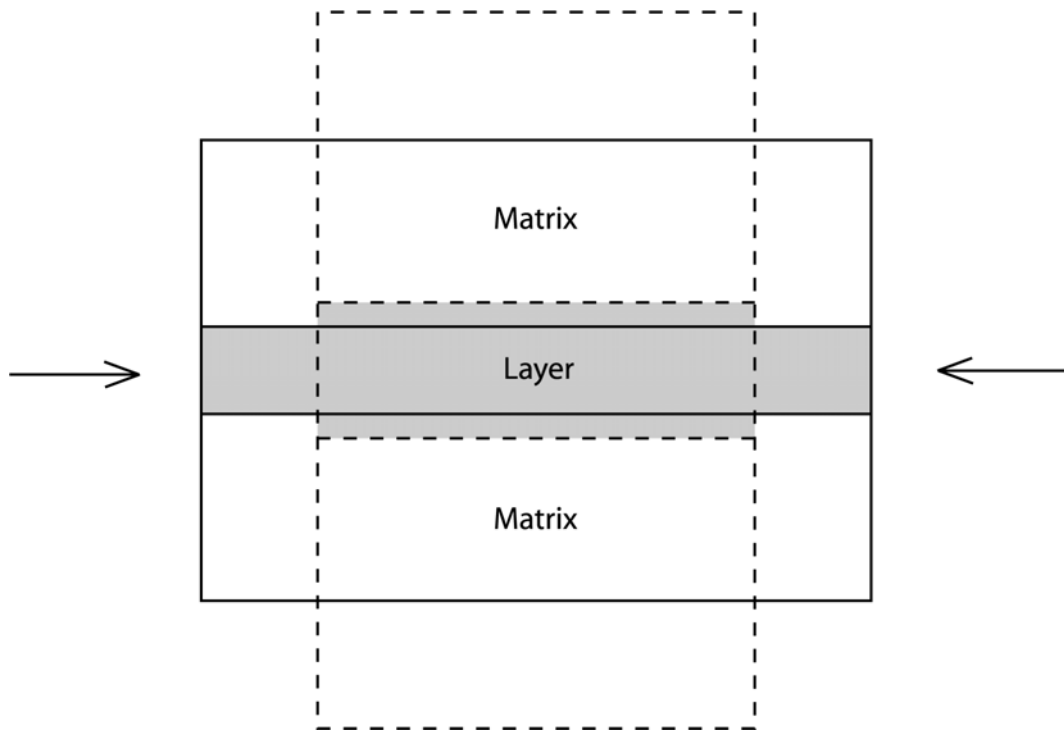


Figure 2

"Classical" basic state configuration, after Smith (1977).

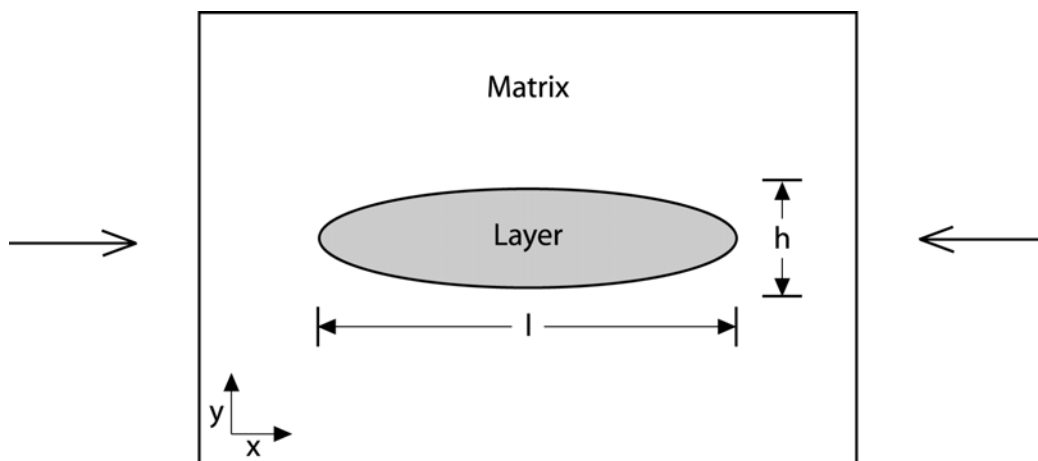


Figure 3

Illustration of a finite length layer subject to horizontal compression.

Note that a typical real layer is likely to have a larger aspect ratio and the bounding box would be much larger with respect to the layer. h and l are the layer thickness and length, respectively.

SOLUTION WITH MUSKHELISHVILI'S METHOD

In order to derive the analytical expression of the background state we employ the method of Muskhelishvili (1953). This method allows finding analytical solutions for a wide range of problems of two-dimensional viscous flow and elasticity. Solutions are given in terms of complex potentials $\phi(z)$ and $\psi(z)$, where z is the complex coordinate. Once these complex potentials are obtained the following basic formulae allow extraction of the desired parameters in the case of incompressible viscous materials:

$$\frac{\sigma_{xx} + \sigma_{yy}}{2} = 2\Re(\phi'(z)) \quad (1)$$

$$\frac{\sigma_{yy} - \sigma_{xx}}{2} + i\sigma_{xy} = \bar{z}\phi''(z) + \psi'(z) \quad (2)$$

$$v_x + iv_y = \frac{\phi(z) - z\overline{\phi'(z)} - \overline{\psi(z)}}{2\mu} \quad (3)$$

where $i = \sqrt{-1}$, μ the material viscosity, x and y are the usual Cartesian coordinates (Figure 3) that relate to the complex coordinate through $z = x + iy$, v_x and v_y are the horizontal and vertical velocities, respectively, and σ_{xx} , σ_{yy} and σ_{xy} are the components of the total stress tensor. The over-bar means conjugation and $\Re(\)$ the real part.

The complete analytical solution for the inside of an arbitrary inclined elliptical inclusion with finite viscosity contrast to the matrix, subjected to horizontal pure shear far-field flow is

$$\phi(z) = \left(\frac{2\mu_m r^2 (\mu_l - \mu_m)}{(\mu_l + \mu_m)r^4 - \mu_l + \mu_m} \cos(2\alpha) - i \frac{2\mu_l r^2 (\mu_l - \mu_m)}{(\mu_l + \mu_m)r^4 + \mu_l - \mu_m} \sin(2\alpha) \right) \dot{\epsilon} z \quad (4)$$

$$\psi(z) = \left(\frac{-4\mu_l \mu_m r^4}{(\mu_l + \mu_m)r^4 - \mu_l + \mu_m} \cos(2\alpha) - i \frac{4\mu_l \mu_m r^4}{(\mu_l + \mu_m)r^4 + \mu_l - \mu_m} \sin(2\alpha) \right) \dot{\epsilon} z \quad (5)$$

α is the angle of long axis inclination measured from the x -axis (positive values are counter-clockwise), $\dot{\epsilon}$ is the far field strain rate ($\dot{\epsilon} = \partial v_x / \partial x$), μ_l is the layer viscosity,

μ_m the matrix viscosity, and r is a function of the ellipse aspect ratio, $a = l/h$, and can be determined through:

$$r = \frac{\sqrt{(a+1)(a-1)}}{a-1} \quad (6)$$

Eqns. (4) and (5) are only valid inside the elliptical inclusion; the expressions for the outside are more complex since the matrix does not exhibit the constant value property. However, in the thin layer approximation of folding analysis only the layer internal values matter and consequently we focus on these. For now we will assume that the inclusion is oriented parallel to the applied pure shear (Figure 3). Therefore we set $\alpha = 0$ and eqns. (4) and (5) simplify to:

$$\phi(z) = \frac{2\mu_m r^2 (\mu_l - \mu_m)}{(\mu_l + \mu_m)r^4 - \mu_l + \mu_m} \dot{\epsilon} z \quad (7)$$

$$\phi(z) = \frac{-4\mu_l \mu_m r^4}{(\mu_l + \mu_m)r^4 - \mu_l + \mu_m} \dot{\epsilon} z \quad (8)$$

VISCOUS LAYER IN VISCOUS MATRIX

The above expressions are derived for the viscous inclusion in a viscous matrix. The key parameters needed for the analysis of fold growth are the horizontal stress, σ_{xx} , the horizontal deviatoric stress, τ_{xx} , and the horizontal strain rate, $\dot{\epsilon}_{xx}$, in the layer. Combining eqns. (1) and (2), σ_{xx} can be extracted through

$$\sigma_{xx} = \Re(2\phi'(z) - \bar{z}\phi''(z) - \psi'(z)) \quad (9)$$

which yields

$$\sigma_{xx} = 2 \frac{\mu_m (a+1)(-a\mu_m + \mu_m + 2a\mu_l)}{a^2 \mu_m + \mu_m + 2a\mu_l} \dot{\epsilon} \quad (10)$$

Note that this σ_{xx} is only determined up to a constant, therefore a (lithostatic) pressure component may be added without influencing the results.

$\dot{\epsilon}_{xx}$ can be deduced from eqn. (3) as

$$\dot{\varepsilon}_{xx} = \frac{(a+1)^2 \mu_m}{(a^2+1)\mu_m + 2a\mu_l} \dot{\varepsilon} \quad (11)$$

These two expressions exhibit familiar limits. Setting $a \rightarrow \infty$ in σ_{xx} we obtain

$$\sigma_{xx} = 4\mu_l \dot{\varepsilon} - 2\mu_m \dot{\varepsilon} \quad (12)$$

If in addition the viscosity of the layer is significantly higher than that of the matrix we can omit the second term to get $4\mu_l \dot{\varepsilon}$, which is the total horizontal stress value used in the classical viscous folding theory (Biot et al., 1961).

On the other hand, if $\mu_l \rightarrow \infty$ in eqn. (10) then we get

$$\sigma_{xx} = 2\mu_m (1+a) \dot{\varepsilon} \quad (13)$$

which is identical to the result Mandal et al (2001) obtained based on Jeffery's (1922) theory. For $a \rightarrow \infty$ this expression yields the background value, $\dot{\varepsilon}$, as the horizontal strain rate in the layer, $\dot{\varepsilon}_{xx}$. This is equivalent to applying the boundary conditions through a rigid wall directly onto the layer.

The infinitely rigid inclusion is not deformable and consequently eqn. (11) yields $\dot{\varepsilon}_{xx} = 0$ for $\mu_l \rightarrow \infty$.

The limit values of σ_{xx} and $\dot{\varepsilon}_{xx}$ either checkable versus intuition or published results. However, in order to check the validity also for intermediate cases we have employed a finite element code. The elements are triangular Crouzeix-Raviart elements with continuous (bubble node enriched), quadratic basis functions for the velocities and discontinuous linear basis functions for pressure. The incompressibility constraint is taken care of by Uzawa iterations (Cuvelier et al., 1986). In all performed checks the deviations between analytical and numerical results were less than 1%, which confirms the validity of the derived expressions over the entire range of viscosity contrasts and aspect ratios.

The complexity of the derived expressions for σ_{xx} and $\dot{\varepsilon}_{xx}$ can be reduced through the introduction of the dimensionless parameter D_a

$$D_a = \frac{\mu_l}{\mu_m} \frac{1}{a} \quad (14)$$

Using D_a we can approximate σ_{xx} and $\dot{\epsilon}_{xx}$ as:

$$\sigma_{xx} \approx 4\mu_l \frac{1}{1+2D_a} \dot{\epsilon} \quad (15)$$

$$\dot{\epsilon}_{xx} \approx \frac{1}{1+2D_a} \dot{\epsilon} \quad (16)$$

Thus, the horizontal deviatoric stress, τ_{xx} , inside the finite length layer is

$$\tau_{xx} \approx 2\mu_l \frac{1}{1+2D_a} \dot{\epsilon} \quad (17)$$

D_a is useful because it readily allows analyzing the competing effects of the aspect ratio, a , versus the viscosity contrast, μ_l / μ_m . Two distinct limits can be characterized. If $D_a \ll 1$, the layer has a much larger aspect ratio than the viscosity contrast to the matrix and all the classical values of folding analysis are recovered (proven in the following). If $D_a \gg 1$, the aspect ratio of the finite length layer is smaller than the viscosity contrast and new expressions are obtained, which govern new folding modes. The quality of the D_a -approximations is displayed in Figure 4, showing that the errors introduced by the approximated form are generally negligible for realistic aspect ratios.

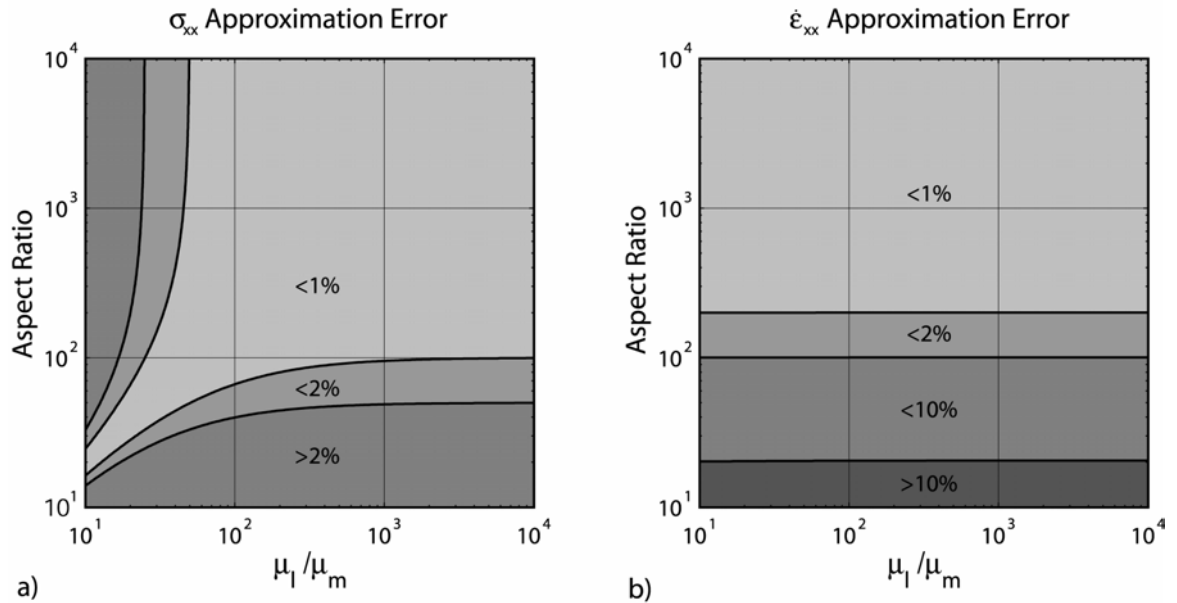


Figure 4

a) Error of σ_{xx} approximation versus viscosity contrast and aspect ratio

b) Error of $\dot{\epsilon}_{xx}$ approximation versus viscosity contrast and aspect ratio.

POWER-LAW LAYER IN VISCOUS MATRIX

Laboratory measurements show that real rocks almost never have a Newtonian rheology, but exhibit non-linear power-law behavior. In order to take the corresponding effects into account we introduce a power-law material layer. Since we use the thin plate approximation in the following analysis of fold growth we can ignore shear deformations, and thus introduce the power-law rheology for the layer as:

$$|\tau_{xx}| = B |\dot{\epsilon}_{xx}|^{\frac{1}{n}} \quad (18)$$

where n is the power-law exponent and B is a material constant. For the folding analysis the horizontal strain rate in the layer can be split into a mean and a fiber component (Timoshenko and Woinowsky-Krieger, 1959)

$$\dot{\epsilon}_{xx} = \dot{\epsilon}_B + \dot{\epsilon}_F \quad (19)$$

where $\dot{\epsilon}_B$ is the value of the mean layer-parallel strain rate caused by the shortening and $\dot{\epsilon}_F$ is the fiber strain rate caused by flexure of the layer (Schmalholz and Podladchikov, 2000). Substituting eqn. (19) into (18) and expanding the nonlinear eqn. (18) by a second order Taylor series around $\dot{\epsilon}_{xx} = \dot{\epsilon}_B$ yields the following linear approximation for the horizontal deviatoric stress:

$$\tau_{xx} = 2\mu_e \dot{\epsilon}_B + 2\frac{\mu_e}{n} \dot{\epsilon}_F \quad (20)$$

where μ_e is the effective viscosity of the layer, which is defined by

$$\mu_e = \frac{B}{2} \dot{\epsilon}_B^{\left(\frac{1}{n}-1\right)} \quad (21)$$

In the case of a Newtonian layer, $n = 1$, we get $B = 2\mu_l$ and therefore $\mu_e = \mu_l$.

The expressions for σ_{xx} , τ_{xx} and $\dot{\epsilon}_{xx}$ which we derived for a Newtonian layer embedded in a likewise matrix remain applicable, by replacing μ_l by μ_e . Since we are interested in the most general solution form, we will use power-law rheology in the following, from which the Newtonian case can be deduced. The fiber strain rate, $\dot{\epsilon}_F$, will be determined in the linear stability analysis of the folding instability. The mean

layer-parallel strain rate, $\dot{\varepsilon}_B$, is identical to the basic state $\dot{\varepsilon}_{xx}$ and, therefore, the effective viscosity can be related to the far field strain rate, $\dot{\varepsilon}$, through the following implicit equation

$$\mu_e = \frac{B}{2} \left(\frac{1}{1+2D_a} \dot{\varepsilon} \right)^{\left(\frac{1}{n}-1\right)} \quad (22)$$

ELASTIC LAYER IN VISCOUS MATRIX

Above we performed the basic state analysis for an incompressible viscous layer in an incompressible viscous matrix, albeit the method of Muskhelishvili was derived originally for elastic problems. Since the infinitesimal (all) viscous and (all) elastic problem are identical (e.g., Eshelby, 1957) this could be done without further complication. However, this is not the case for the elastic finite length layer in the viscous matrix. The problem must be reduced to one of only one type of rheology. This is possible through the use of the correspondence principle (Biot, 1954) done here by the introduction of an effective viscosity. The behavior of the incompressible elastic inclusion is hereby translated into one of a viscous inclusion with corresponding (effective) viscosity. The same technique was essentially already employed in the treatment of the power-law layer.

First we express the elastic rheology, due to our focus of interest, only in terms of horizontal deviatoric normal components:

$$\tau_{xx} = 2G\varepsilon_{xx} \quad (23)$$

where G the shear modulus and ε_{xx} the horizontal strain. Taking the time derivative of eqn. (23) we can write:

$$\frac{\partial \tau_{xx}}{\partial t} = 2G \frac{\partial \varepsilon_{xx}}{\partial t} = 2G \dot{\varepsilon}_{xx} \quad (24)$$

Substituting eqns. (16) and (17) as a function of $\mu_e(t)$ into eqn. (24) results in an ordinary differential equation for the unknown effective viscosity of the elastic layer, $\mu_e(t)$. Assuming that at time $t=0$ the elastic layer is unstrained, the initial effective viscosity is $\mu_e(0) = 0$. Consequently the effective viscosity is

$$\mu_e(t) = -\frac{1}{2}a\mu_m + \frac{1}{2}a\mu_m \exp\left(\frac{2Gt}{a\mu_m}\right) \quad (25)$$

Through the introduction of this effective viscosity the results of the viscous basic state analysis become applicable to the elastic case, by performing the substitution (25) throughout and taking care of the time dependence of the effective viscosity. The D_a number for the elastic case is therefore:

$$D_a = \frac{\mu_e(t)}{\mu_m} \frac{1}{a} \quad (26)$$

and the general expression for σ_{xx} in the elastic beam (eqn. (15)) becomes

$$\sigma_{xx}(t) = 4\mu_e(t) \frac{1}{1+2D_a} \dot{\epsilon} \quad (27)$$

We point out that the somewhat complicated effective viscosity expressed in eqn. (25), can be further simplified through a second order Taylor series expansion around $t=0$, which results in

$$\mu_e(t) = Gt \quad (28)$$

Although much simpler, the maximum error introduced in the entire D_a range is less than 25% (Figure 5), which is acceptable for this study. In addition, the errors are restricted to a small range around $D_a = 1$.

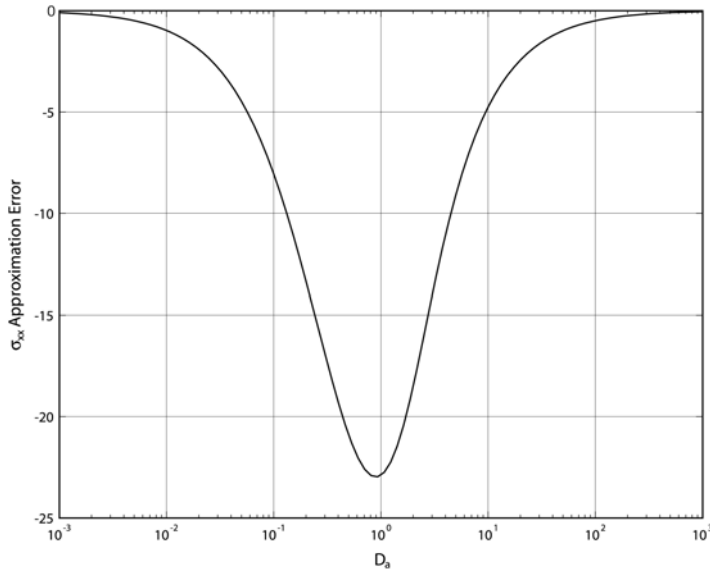


Figure 5
Error in $\sigma_{xx}(t)$ caused by the $\mu_e(t) = Gt$ approximation.

LINEAR STABILITY ANALYSIS

Having derived the basic state expressions we can investigate the development of folds in finite length layers by means of the so called “linear stability analysis”. The interface between layer and matrix is now assumed to be perturbed and we employ the bending equation (Biot, 1961) in order to analyze the growth of these perturbations.

VISCOUS LAYER IN VISCOUS MATRIX

The behavior of a power-law viscous layer in a Newtonian matrix is determined by

$$\frac{\mu_e h^3}{3n} \frac{\partial^5 w}{\partial x^4 \partial t} + \sigma_{xx} h \frac{\partial^2 w}{\partial x^2} + q_m = 0 \quad (29)$$

Here q_m is the vertical component of the stress exerted by the matrix onto the layer boundary and w is the deflection of the layer. Assuming a sinusoidal perturbation, we can express w as:

$$w = A(t) \sin(kx) \quad (30)$$

where $A(t)$ is the amplitude of the sinusoidal perturbation with time and k is the wavenumber, related to the wavelength λ by:

$$k = \frac{2\pi}{\lambda} \quad (31)$$

We choose q_m to represent two adjacent viscous half spaces (Biot, 1961).

$$q_m = 4\mu_m k \frac{\partial w}{\partial t} \quad (32)$$

Different expressions for q_m , covering a wider range of cases can be found in Schmalholz et al. (2002). Substituting eqns. (32) and (30) into (29) results in an ordinary differential equation for $A(t)$ which has the following solution

$$A(t) = A(0) \exp\left(\frac{3hkn}{\mu_e h^3 k^3 + 12\mu_m n} \sigma_{xx} t\right) \quad (33)$$

where $A(0)$ is the initial amplitude of the perturbation. Eqn. (33) shows the well known result that the amplification of initial perturbations is exponential with time (see Schmalholz and Podladchikov (2000) for finite amplitude behavior). The part of the exponent in front of t is termed growth rate, α :

$$\alpha = \frac{3hkn}{\mu_e h^3 k^3 + 12\mu_m n} \sigma_{xx} \quad (34)$$

Since all initial perturbations, independent of the wavelength, are exponentially amplified, it is necessary to determine the wavelength at which the growth rate is maximum. This is done by taking the derivative of α versus k , setting it to zero and solving for k . The only positive solution of k yields

$$\lambda = 2\pi \sqrt[3]{\frac{\mu_e}{6n\mu_m} h} \quad (35)$$

Interestingly, the dominant viscous wavelength does not depend on D_a and is therefore insensitive to the finiteness of the layer.

Plugging eqn. (35) into (34) and using the general expression for σ_{xx} (eqn. (15)), the general viscous maximum growth rate is given by

$$\alpha = \frac{1}{1+2D_a} \left(\frac{4n}{3} \frac{\mu_e}{\mu_m}\right)^{2/3} \dot{\epsilon} \quad (36)$$

Eqns. (35) and (36) show the typical effect of a power-law layer, i.e., with increasing power-law exponent n the wavelength decreases, but the growth rate increases.

Viscosity Contrast Smaller Than Aspect Ratio – Classical Limit

As already mentioned the Da parameter is useful to distinguish competing effects of aspect ratio and viscosity contrast. In the case of a very long layer $Da \rightarrow 0$ and consequently we can directly obtain the classical growth rate expression

$$\alpha = \left(\frac{4n}{3} \frac{\mu_e}{\mu_m} \right)^{2/3} \dot{\epsilon} \quad (37)$$

Viscosity Contrast Larger Than Aspect Ratio

On the other hand, if the viscosity contrast is significantly larger than the aspect ratio then $Da \gg 1$ and eqn. (36) simplifies to

$$\alpha = \frac{1}{2D_a} \left(\frac{4n}{3} \frac{\mu_e}{\mu_m} \right)^{2/3} \dot{\epsilon} \quad (38)$$

Using the definition of D_a (eqn. (14)) this evaluates to

$$\alpha = \frac{l}{h} \frac{(2n^2)^{1/3}}{3} \left(\frac{\mu_e}{\mu_m} \right)^{-1/3} \dot{\epsilon} \quad (39)$$

This result is important because the growth rate shows an inverse proportionality to the effective viscosity contrast, i.e., long wavelength/high-viscosity contrast folds are suppressed, a feature reported from natural folds (Sherwin and Chapple, 1968) but not inherent to the “classical” theories.

ELASTIC LAYER IN VISCOUS MATRIX

The behavior of an elastic beam in a viscous matrix is determined by

$$\frac{Gh^3}{3} \frac{\partial^4 w}{\partial x^4} + \sigma_{xx} h \frac{\partial^2 w}{\partial x^2} + q_m = 0 \quad (40)$$

Using the same expressions for w and q_m as for the viscous case, we can solve eqn. (40) for the dominant elastic wavelength and maximum growth rate

$$\lambda = 2\pi \sqrt{\frac{G}{\sigma_{xx}}} h \quad (41)$$

$$\alpha = \frac{1}{6\mu_m} \sqrt{\frac{\sigma_{xx}^3}{G}} \quad (42)$$

These are the classical expressions, which are valid if σ_{xx} is constant.

We have seen in the basic state analysis that the effective viscosity, eqn. (25), and the horizontal stress, eqn. (27), of the elastic layer are time dependent. Thus, it is not admissible to substitute the time-dependent σ_{xx} into eqns. (41) and (42), and it is therefore necessary to derive the corresponding expressions, with the time dependency taken into account:

$$\lambda = 2\pi \frac{D_a}{\sqrt{\varepsilon(-1 + e^{-2D_a} + 2D_a)}} h \quad (43)$$

$$\alpha = \frac{\mu_e}{6\mu_m} \frac{\varepsilon^{3/2}(-1 + e^{-2D_a} + 2D_a)}{D_a^3} \quad (44)$$

The effective viscosity used in these expressions is the simplified form, eqn. (28), which can be written in terms of bulk strain ε , i.e., assuming constant far-field strain rate:

$$\mu_e = Gt = \frac{G\varepsilon}{\dot{\varepsilon}} \quad (45)$$

This can be used to simplify eqns. (43) and (44) to

$$\lambda = 2\pi \left(\frac{1 + D_a}{2\varepsilon} \right)^{1/2} h \quad (46)$$

$$\alpha = \frac{\mu_e}{6\mu_m} \left(\frac{2\varepsilon}{1 + D_a} \right)^{3/2} \quad (47)$$

The errors introduced through these simplifications are small; in the case of the dominant wavelength expression the maximum error in the entire D_a range is less than

7% (Figure 6). Therefore, we perform the remaining analysis with the simplified expressions. As for the viscous case we distinguish the small and the large D_a limits.

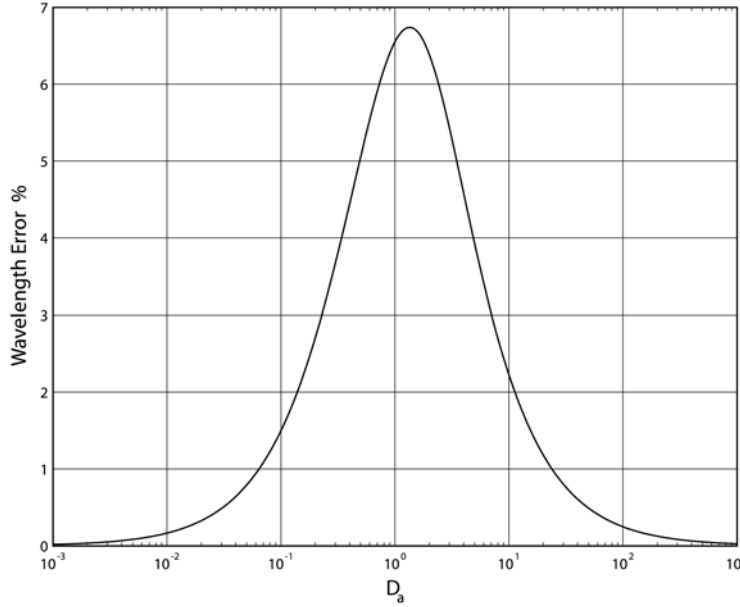


Figure 6
Error in the dominant wavelength expression due to the usage of the simplified form (eqn. (46)).

Effective Viscosity Contrast Smaller Than Aspect Ratio

Elastic layers with aspect ratios that are larger than the effective viscosity contrast are characterized by $D_a \ll 1$. The corresponding dominant wavelength and maximum growth rate are

$$\lambda = 2\pi \left(\frac{1}{2\varepsilon} \right)^{1/2} h \quad (48)$$

$$\alpha = \frac{\sqrt{2}}{3} \frac{\mu_e}{\mu_m} \varepsilon^{3/2} \quad (49)$$

These expressions are very close the classical expressions, eqns. (41) and (42), if the following relationship between total horizontal stress and strain is taken into account:

$$\sigma_{xx} = 4G\varepsilon_{xx} \quad (50)$$

Eqn. (50) is valid for the classical elastic beam. Rewriting and substituting $\varepsilon = \varepsilon_{xx}$ yields

$$\frac{1}{2\varepsilon} = \frac{2G}{\sigma_{xx}} \quad (51)$$

Hence, our small D_a limit expressions for the dominant wavelength and maximum growth rate differ from the classical expressions only by a factor of $\sqrt{2}$ and $2^{-3/2}$, respectively. These differences are due to the time-dependency of σ_{xx} .

Effective Viscosity Contrast Larger Than Aspect Ratio

In the second limit of the finite length elastic layer, the effective viscosity contrast is larger than the aspect ratio, i.e., $1 \ll D_a$. In this case the expressions are

$$\lambda = 2\pi \left(\frac{D_a}{2\varepsilon} \right)^{1/2} h \quad (52)$$

$$\alpha = \frac{\mu_e}{6\mu_m} \left(\frac{2\varepsilon}{D_a} \right)^{3/2} \quad (53)$$

Substituting the definition of D_a we can write

$$\lambda = 2\pi \left(\frac{G}{2a\mu_m\dot{\varepsilon}} \right)^{1/2} h \quad (54)$$

$$\alpha = \frac{\sqrt{2}}{3} \left(\frac{\mu_e}{\mu_m} \right)^{-1/2} (a\varepsilon)^{3/2} \quad (55)$$

Transition From Small to Large D_a - Wavelength Locking

Folding in finite length elastic layers embedded in a viscous matrix is complicated through the varying effective viscosity. While in viscous-viscous folding the D_a number is constant and given by the experimental setup, this is not true for the elastic-

viscous case. Assuming sufficient strain, the D_a number will go from zero to very large values, which is due to the ever increasing effective viscosity contrast, cf. eqns. (25) and (28). One can imagine the elastic layer as an initially unloaded spring, embedded in a viscous medium. With increasing deformation of the viscous medium the spring will get continuously loaded, which makes it progressively more difficult to further deform the spring as it becomes harder in an “effective viscosity” sense. Thus, sufficient strain assumed, every finite length elastic layer will record folding in the small and the large D_a number domain. In addition, the dominant wavelength expression of the small D_a domain is a function of the bulk strain, which makes it difficult to identify one single dominant wavelength that results from folding in this domain. We can resolve this problems by introducing a parameter \tilde{A} , which controls the wavelength locking. This term refers to the stage at which the fold has developed a significant amplitude that locks the wavelength selection process. Since elastic materials are very strain sensitive we expected that the wavelength locking takes place in the early stages of fold development. Wavelength locking is therefore very different from the frequently discussed “fold locking” concept that refers to the final stages of fold development during which the active amplification has come to an end (e.g., Biot, 1961; Ramsay, 1974; Cobbold, 1976). The definition of \tilde{A} is

$$\tilde{A} = \ln(A(t) / A(0)) \quad (56)$$

If the folds are locked in the small D_a domain, we can set \tilde{A} equal the corresponding amplification expression, eqn. (49)

$$\tilde{A} = \frac{\sqrt{2}}{3} \frac{\mu_e}{\mu_m} \varepsilon^{3/2} = \frac{\sqrt{2}}{3} \frac{G}{\mu_m \dot{\varepsilon}} \varepsilon^{5/2} \quad (57)$$

This can be solved for the corresponding bulk strain, ε , at which locking takes place:

$$\varepsilon = \left(\frac{\sqrt{2}}{3} \frac{\tilde{A} \mu_m \dot{\varepsilon}}{G} \right)^{2/5} \quad (58)$$

Plugging the resulting expression for ε into the small D_a dominant wavelength expression, eqn. (48), we obtain the wavelength that will be inherent to the fold throughout the rest of the deformation:

$$\lambda = \pi \left(\frac{8}{3} \frac{G}{\tilde{A} \mu_m \dot{\epsilon}} \right)^{1/5} \quad (59)$$

The dominant wavelength expression of the large D_a domain, eqn. (54), does not depend on the bulk strain it is therefore not necessary to introduce the wavelength locking concept for large D_a numbers.

TABLE 1 - SUMMARY OF FOLDING MODES

	Case	Amplification	Dominant Wavelength	Condition	Parameters
DUCTILE LAYER	General	$\left(\frac{4n}{3} \frac{\mu_e}{\mu_m}\right)^{2/3} \frac{\varepsilon}{1+2D_a}$		$2\pi \left(\frac{1}{6n} \frac{\mu_e}{\mu_m}\right)^{1/3} < a$	$D_a = \frac{\mu_e}{\mu_m a}$
	Large Aspect Ratio Classical Limit	$\left(\frac{4n}{3} \frac{\mu_e}{\mu_m}\right)^{2/3} \varepsilon$	$2\pi \left(\frac{1}{6n} \frac{\mu_e}{\mu_m}\right)^{1/3} h$	$a > \max \left(\begin{array}{c} \frac{\mu_e}{\mu_m} \\ 2\pi \left(\frac{1}{6n} \frac{\mu_e}{\mu_m}\right)^{1/3} \end{array} \right)$	$\mu_e = \frac{B}{2} \dot{\varepsilon}^{\left(\frac{1}{n}-1\right)}$ $a = \frac{l}{h}$
	Small, Finite Aspect Ratio	$a \left(\frac{9}{2n^2} \frac{\mu_e}{\mu_m}\right)^{-1/3} \varepsilon$		$2\pi \left(\frac{1}{6n} \frac{\mu_e}{\mu_m}\right)^{1/3} < a < \frac{\mu_e}{\mu_m}$	
ELASTIC LAYER	General	$\frac{\sqrt{2}}{3} \frac{\mu_e}{\mu_m} \left(\frac{\varepsilon}{1+D_a}\right)^{3/2}$	$2\pi \left(\frac{1+D_a}{2\varepsilon}\right)^{1/2} h$	$2\pi \left(\frac{1+D_a}{2\varepsilon}\right)^{1/2} < a$	$D_a = \frac{\mu_e}{\mu_m a}$
	Large Aspect Ratio	$\frac{\sqrt{2}}{3} \frac{\mu_e}{\mu_m} \varepsilon^{3/2} = \frac{\sqrt{2}}{3} \frac{G}{\mu_m \dot{\varepsilon}} \varepsilon^{5/2} = \tilde{A}$	$\pi \left(\frac{2}{\varepsilon}\right)^{1/2} h = \pi \left(\frac{8}{3\tilde{A}} \frac{G}{\mu_m \dot{\varepsilon}}\right)^{1/5}$	$a > \max\left(\frac{\mu_e}{\mu_m}, \sqrt{2\pi\varepsilon}^{-1/2}\right)$	$\mu_e = Gt = G \frac{\varepsilon}{\dot{\varepsilon}}$ $a = \frac{l}{h}$
	Small, Finite Aspect Ratio	$\frac{\sqrt{2}}{3} \left(\frac{\mu_e}{\mu_m}\right)^{-1/2} (a\varepsilon)^{3/2} = \frac{\sqrt{2}}{3} \left(\frac{G}{\mu_m \dot{\varepsilon}}\right)^{-1/2} a^{3/2} \varepsilon$	$\pi \left(\frac{2}{a} \frac{G}{\mu_m \dot{\varepsilon}}\right)^{1/2} h$	$\left(2\pi^2 \frac{G}{\mu_m \dot{\varepsilon}}\right)^{1/3} < a < \frac{\mu_e}{\mu_m}$	

TABLE 2 - USED SYMBOLS

$A(t)$	Amplitude of interface perturbation at time t
$A(0)$	Initial amplitude of interface perturbation ($t = 0$)
μ_m	Matrix viscosity
μ_e	Effective viscosity of layer (elastic or power-law)
n	Power-law exponent of viscous layer material
$\mu_e(t)$	Time dependent effective viscosity of elastic beam
η	Effective viscosity contrast
G	Shear modulus of elastic beam
a	Layer aspect ratio
l	Layer length
h	Layer thickness
$\dot{\varepsilon}$	Bulk (far-field) pure shear strain rate
ε	Bulk strain
σ_{xx}	Layer parallel total stress (without lithostatic pressure)
τ_{xx}	Layer parallel deviatoric stress
$\dot{\varepsilon}_{xx}$	Layer parallel strain rate
ε_{xx}	Layer parallel strain
D_a	Parameter controlling folding domain
t	Time
k	Wavenumber
λ	Wavelength
\tilde{A}	Wavelength locking parameter

DISCUSSION

VISCOUS LAYER IN VISCOUS MATRIX

Dominant Wavelength

A prominent feature in folding of a finite length viscous layer is that the dominant wavelength selection is insensitive to the aspect ratio of the isolated layer and the corresponding expression is identical to the classical formula. The reason is that the dominant wavelength selection does not depend on the layer parallel stress, σ_{xx} , which is just a multiplier in eqn. (34).

Maximum Growth Rate Spectra

Besides the dominant wavelength the second important quantity is the normalized maximum growth rate, $\alpha / \dot{\varepsilon}$, which is the coefficient in front of the bulk matrix strain, ε , in the amplification expression. The maximum growth rate exhibits drastic changes depending on the competing effects of effective viscosity contrast and aspect ratio, Figure 7. These competing effects are characterized by the D_a number. In the small D_a number limit, the aspect ratio is much larger than the viscosity contrast. This is the classical case for which the theory predicts infinitely increasing maximum growth rate values with increasing viscosity contrasts. Natural folds, in layers of finite length, will not exhibit this behavior. Instead, for large viscosity contrast, they will be controlled by the large D_a number limit, in which case the maximum growth rate actually decreases with increasing viscosity contrast. Introducing the effective viscosity contrast (η):

$$\eta = \frac{\mu_e}{\mu_m} \quad (60)$$

we can determine the D_a value at which the transition from the small to the large D_a number limit happens, by differentiating the general, normalized maximum growth rate

$$\frac{\alpha}{\dot{\varepsilon}} = \frac{1}{1 + 2\frac{\eta}{a}} \left(\frac{4n}{3} \eta \right)^{2/3} \quad (61)$$

versus η , equating to 0 and solving for η . This yields, independently of the power-law exponent,

$$\eta^* = a \quad (62)$$

where the * means critical value. The corresponding D_a is

$$D_a^* = 1 \quad (63)$$

However, besides $D_a > 1$, there is a second restriction for the applicability of the large D_a number limit. Namely, for large viscosity contrasts, the length of the layer may simply be too small to accommodate even one dominant wavelength. This limit is specified through

$$2\pi \left(\frac{1}{6n} \eta \right)^{1/3} \leq a \quad (64)$$

In terms of the presented maximum growth rate versus viscosity contrast plot we can determine this applicability limit, by substituting eqn. (64) into the normalized maximum growth rate of the large D_a limit:

$$\frac{\alpha}{\dot{\varepsilon}} = \left(\frac{2n^2}{9} \right)^{1/3} a \eta^{-1/3} \quad (65)$$

which yields

$$\frac{\alpha}{\dot{\varepsilon}} = \frac{2\pi}{3} n^{1/3} \quad (66)$$

In order to make the diagram (Figure 7) as general as possible, the growth rates are additionally normalized by $n^{2/3}$. Thus, the entire plot becomes independent of the power-law exponent, with the exception of the large D_a limit size limitation, eqn. (66), which is

$$\frac{\alpha}{\dot{\varepsilon}} = \frac{2\pi}{3} n^{-1/3} \quad (67)$$

This result is logical, since higher power-law exponents cause shorter dominant wavelengths and therefore more folds can be hosted onto a layer of given length.

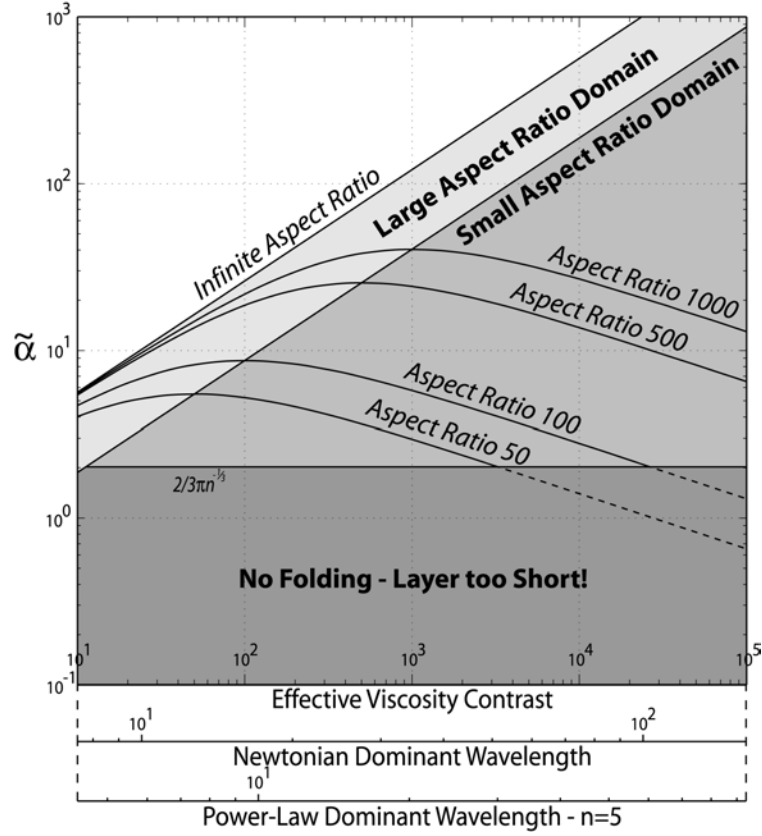


Figure 7

Normalized maximum growth rates, $\tilde{\alpha} = \alpha / \dot{\epsilon} / n^{2/3}$, versus effective viscosity contrast. Domain characterization and four specific examples of layers with different aspect ratios. The plot is power-law exponent independent with the exception of the size of the “No Folding” field, which is here given for a Newtonian rheology, $n=1$. The additional horizontal scales show the dominant wavelengths that correspond to the effective viscosity contrasts.

The characteristic effect of the transition from the small to the large D_a regime is also evident in Figure 8, where the maximum growth rate is contoured in the aspect ratio – viscosity contrast space. As in Figure 7, the maximum growth rate is normalized by $\dot{\epsilon}$ as well as $n^{2/3}$. Thus, Figure 8 is applicable independently of the power-law exponent. The exception is again the boundary to the field where the dominant wavelength longer than the layer itself. This boundary line is given through the dominant wavelength expression, which is dependent on n , and when normalized by $n^{2/3}$ becomes

$$a = 2\pi \left(\frac{1}{6}\eta \right)^{1/3} n^{-1} \quad (68)$$

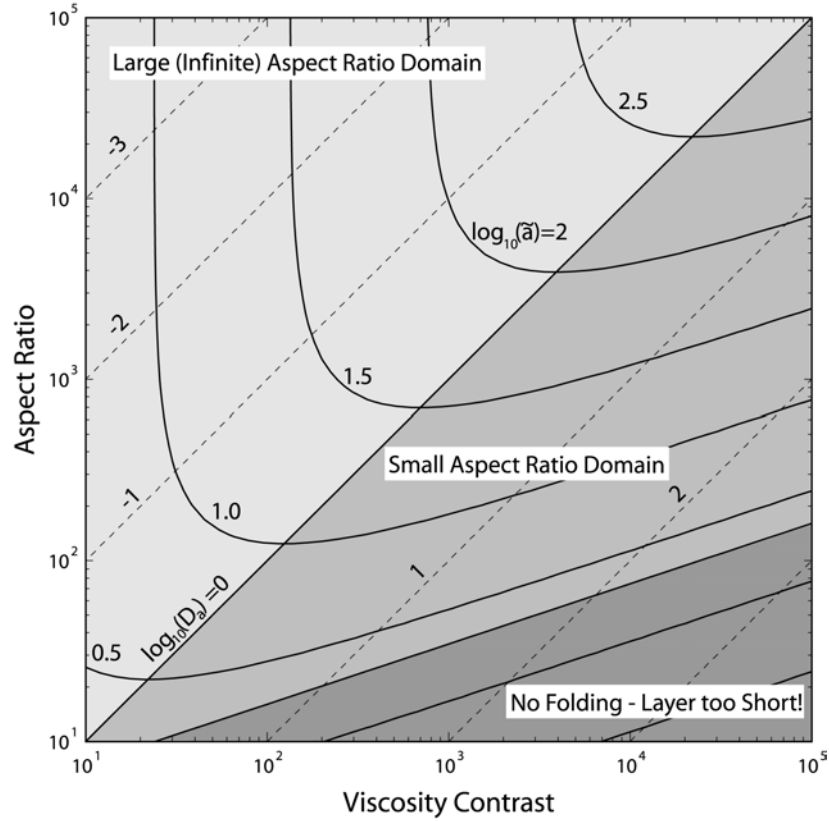


Figure 8

\log_{10} contour plot of the normalized maximum growth rate, $\tilde{\alpha}$, versus aspect ratio and viscosity contrast. Since $\tilde{\alpha} = \alpha / \dot{\epsilon} / n^{2/3}$ the plot is power-law exponent independent, with the exception of the “No Folding” field, which is given for a Newtonian layer.

In the classical analysis small growth rate values such $2/3\pi n^{-1/3}$ (Figure 7) could be ignored, because it can be argued that layer shortening would overprint the folding (e.g., Sherwin and Chapple, 1968). However, the folding of finite length layers exhibits two different timescales, one related to the matrix shortening and a second related to the layer shortening. Since in the large D_a domain, the layer experiences only a fraction of the matrix shortening, the growth rate may still be sufficient to compete the layer shortening and develop significant folds. The relationship between far-field, matrix shortening and layer shortening in the large D_a domain is (cf. eqn. (16))

$$\dot{\epsilon} = 2D_a \dot{\epsilon}_{xx} \tag{69}$$

Consequently, the growth rates in the large D_a domain are $2D_a$ -times larger, when normalized over the appropriate strain rate, i.e., the layers own strain rate instead of the far field $\dot{\epsilon}$. Hence, the seemingly small growth rates must be taken into account in the folding analysis.

Complete Growth Rate Spectra

The difference between the two timescales can also be analyzed by looking at the complete (not only maximum) growth rate spectra. For this we substitute the general expression for σ_{xx} , eqn. (15), into the complete viscous growth rate expression, eqn. (34):

$$\frac{\alpha}{\dot{\epsilon}} = \left(\frac{3hkn}{\mu_e h^3 k^3 + 12\mu_m n} \right) \frac{4\mu_e}{1+2Da} \quad (70)$$

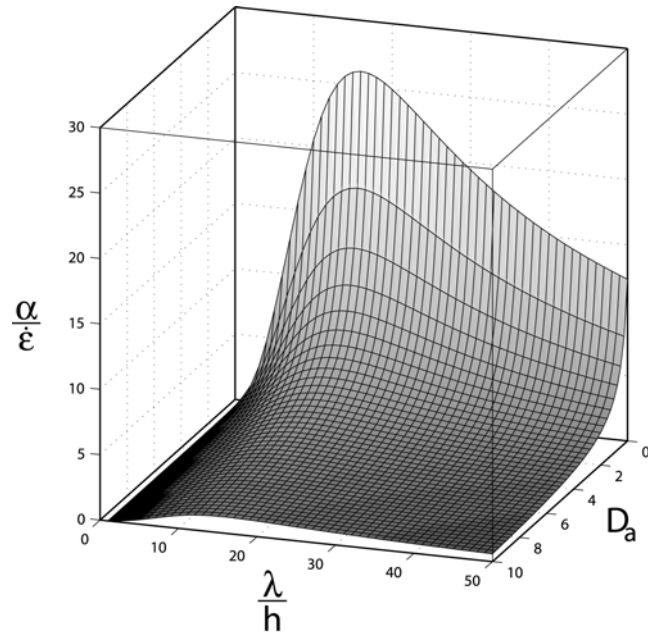
Using h to normalize the length parameters, and eqn. (31) to introduce the normalized wavelength, $\tilde{\lambda} = \lambda/h$, eqn. (70) becomes

$$\frac{\alpha}{\dot{\epsilon}} = \left(\frac{3\pi n \tilde{\lambda}^2}{4\pi^3 \mu_e + 6\mu_m n \tilde{\lambda}^3} \right) \frac{4\mu_e}{1+2Da} \quad (71)$$

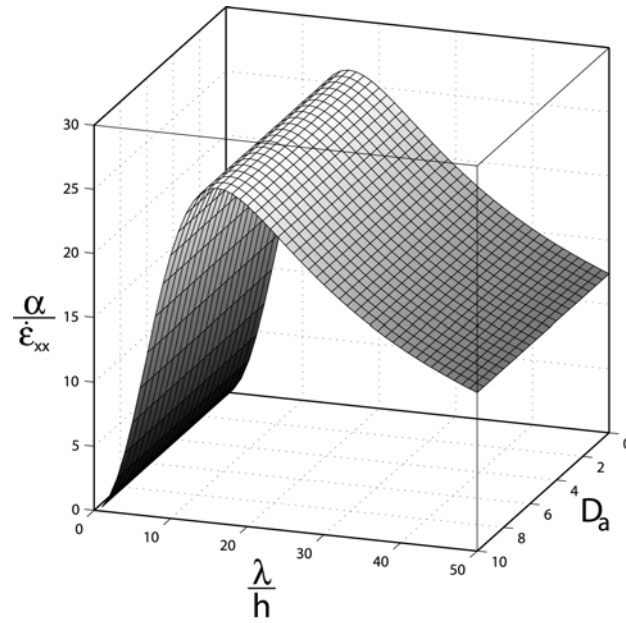
If we normalize eqn. (71) by the layer strain rate value, $\dot{\epsilon}_{xx}$, eqn. (16), we obtain

$$\frac{\alpha}{\dot{\epsilon}_{xx}} = \left(\frac{3\pi n \tilde{\lambda}^2}{4\pi^3 \mu_e + 6\mu_m n \tilde{\lambda}^3} \right) 4\mu_e \quad (72)$$

This expression is identical to the classical growth rate spectra, which are independent of the aspect ratio and D_a . The difference of eqns. (71) and (72) is illustrated in Figure 9. The small growth rates of Figure 9a) cannot be ignored, since they are as large as the classical ones, if normalized by the appropriate strain rate. However, the amount of bulk strain required to build folds of the same amplitude is $2D_a$ -times larger. The reason to use the normalization in eqn. (71) is because $\dot{\epsilon}$ is known beforehand, while $\dot{\epsilon}_{xx}$ is not.



a)



b)

Figure 9

Complete growth rate spectra for Newtonian layer with viscosity contrast 100:1 in the $\lambda/h - D_a$ -space.

a) Normalized over far field strain rate $\dot{\epsilon}$.

b) Normalized over layer strain rate $\dot{\epsilon}_{xx}$.

Finite Strain Experiments

In order to verify the folding characteristics of a finite length viscous layer up to large deformations, we performed numerical experiments (a short description of the code used can be found in the section “Basic State Analysis-Viscous Layer in Viscous Matrix”). We present three experiments, which are all Newtonian with a viscosity contrast of 100:1 (Figure 11). The aspect ratio is varied in order to change the D_a number. As already discussed, the dominant wavelength does not depend on D_a , but the growth rate expression, eqn. (61), yields decreasing values with increasing D_a number, i.e., smaller aspect ratios. Given viscosity contrast, the maximum D_a number is limited by

$$\max(D_a) = \frac{\mu_e}{\mu_m \lambda} \quad (73)$$

which is the expression for the smallest aspect ratio that can still accommodate one dominant wavelength.

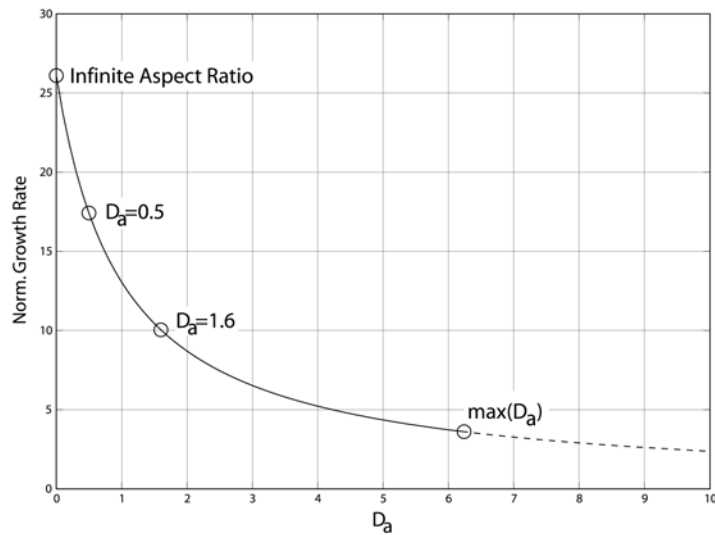


Figure 10

Normalized growth rate ($\alpha/\dot{\epsilon}$) versus D_a for Newtonian layer with viscosity contrast 100:1. The three points on the left correspond to the experiments in Figure 11. The last point, which is followed by the dotted line, represent the maximum possible D_a for the given viscosity contrast.

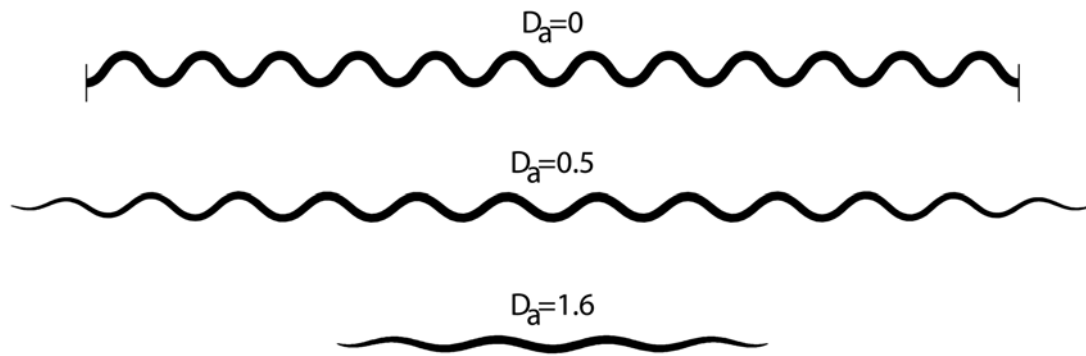


Figure 11

Folding in finite length layers. Viscosity contrast is always 100:1. Bulk shortening in all three experiment is 33%.

Figure 11 shows three fold experiments with the same layer-matrix viscosity contrast and the same amount of bulk shortening (33%). The D_a number increases from top to bottom, 0 (boundaries directly connected to the layer), 0.5 and 1.6. For comparison the initial length of the $D_a = 0$ and the $D_a = 0.5$ layers was set equal. Since the dominant wavelength in viscous-viscous folding is not sensitive to D_a , all three fold interfaces had the same initial perturbation.

The fold amplitudes in these experiments show how the growth rate decreases with increasing D_a number, with respect to the bulk strain and strain rate. The folds in the $D_a = 0$ configuration have, at 33% percent shortening, almost gone through the entire field of active amplification (Schmalholz and Podladchikov, 2000) and developed significant amplitudes. The $D_a = 0.5$ folds have a considerably lower growth rate and are consequently less pronounced. This layer “feels” less compression than the equivalent $D_a = 0$, which can also be seen from the fact that the $D_a = 0.5$ fold train is still longer, although their initial layer lengths were identical. Another verification of the folding theory is that the folds towards the tips are less developed than in the center of the layer. This is due to the initial perturbation which was put on the entire layer with a fixed wavelength. The required wavelength to thickness ratio was tuned to fit the center of the layer. Due to its elliptical shape the thickness of the layer decreases towards the

tips. Consequently, the wavelength to thickness ratio of the perturbation near the tips is larger than the dominant value, and hence the folds grow slower (cf., Figure 9). Interestingly, the folded quartz vein in Figure 1 shows the same behavior.

Applicability of Finite Strain Theory

The question arises, whether the finite amplitude solution and strain map, developed by Schmalholz and Podladchikov (2000; 2001), are valid for folds in layers of finite length. Their technique is consistently based on layer-strain and layer-amplification. Therefore the applicability of their results is not diminished by the finiteness of the layer length. However, the strain estimates resulting from the strain map are only a valid approximation for the layer and will underestimate the bulk (overall) matrix strain which is usually of great interest in nature. However, with the theory developed here it is possible to translate the layer strain into the larger bulk matrix strain. The corresponding expression can be derived with eqn. (16) as:

$$\varepsilon = (1 + 2D_a) \varepsilon_{xx} \quad (74)$$

In nature the value of D_a can be evaluated from simple geometrical parameters: the aspect ratio can be measured directly and the effective viscosity contrast can be determined by the competence estimation method developed by Schmalholz and Podladchikov (2001).

Relevance to Natural Folds

Natural folds show a preference for small wavelength to thickness ratios (Sherwin and Chapple, 1968). This observation implied that Biot's theory of viscous folding (Biot, 1961) is not applicable because the resulting wavelength to thickness ratios require such small viscosity contrasts that the corresponding growth rates would be too small to develop folds. Further theoretical investigations, and additions such as layer parallel shortening (Sherwin and Chapple, 1968) and power-law materials (Fletcher, 1974; Smith, 1975) were thus developed to explain small wavelength to thickness ratios. However, these theories explain why small wavelength to thickness ratios are possible, but no known theory explains why large wavelength to thickness ratios are not observed in nature, supposedly having much larger growth rates. Variations in material properties of natural rocks are vast and therefore large effective viscosity contrasts are likely to be

the general case rather than the exception. Hence, large wavelength to thickness ratios should be commonly observed, because this is intrinsic to all existing theories.

Our theoretical development explains for the first time a mechanism that suppresses large wavelength to thickness ratios. We simply re-analyzed the most fundamental part of the analysis of folding: the basic state. Our basic state is a layer of finite aspect ratio, which clearly must be the case in nature. While for large enough aspect ratios (compared to the viscosity contrast), the classic theory is recovered, this is not case if the aspect ratio is small. In this new mode, the layer does not “get” the layer parallel stress, σ_{xx} , from a force directly applied to its ends, but from the matrix that is deforming faster than the layer and exerting shear stresses all along the layer. Our theory does not invalidate previous arguments such as layer parallel shortening, but it is important to realize the influence of the finiteness of the layer length on the folding behavior as a first order effect.

Ending the Small Viscosity Contrast Paradox

Arguably, natural layers admissible for fold amplification are likely to have aspect ratios less than 1000. For example veins have aspect ratios in the range 100-500 (e.g., Vermilye and Scholz, 1995). It is hard for natural processes “to prepare” a long layer, having maximum of deviation from perfect plane smaller than half of the layer thickness. Larger amplitudes of initial perturbation move folding out of the exponential amplification, where dominant folding frequencies are expected to develop, into large amplitude mode characterized by weak wavelength selectivity and by kinematic dominance of initial heterogeneities (Schmalholz and Podladchikov, 2000). For example, 1 km long 1 m thick layer should not deviate more than half a meter from a perfect plane, nowhere within its 1 km length! It is shown here that classical folding theories are not applicable for the finite layers having aspect ratio less than 1000 if viscosity contrasts are greater than 1000. Therefore, the lack of natural fold trains indicating large viscosity contrasts is due to inapplicability of the classical theories rather than due to absence of large viscosity contrasts in natural setting. This conclusion basically resolves the long-standing paradoxical discrepancy between laboratory measurements and field observations.

ELASTIC LAYER IN VISCOUS MATRIX

From the above discussion of the viscous-viscous case, it follows that our theory is closely related to the classical theory, developed by Biot, especially in the small D_a domain. For the elastic layer in a viscous matrix, we have shown in the linear stability analysis that the small D_a limit is closely related to the corresponding classical expression. However, the classical expressions for the dominant wavelength and growth rate of an elastic layer embedded in a viscous matrix, eqns. (41) and (42), leave the layer parallel stress, σ_{xx} , as an unknown. Since σ_{xx} must change throughout the folding of an elastic layer (progressive loading) and the dominant wavelength expression depends on σ_{xx} , it is unclear which value for σ_{xx} should be used for the dominant wavelength and growth rate expressions. Indeed, for geological problems σ_{xx} may be used as a fitting parameter between natural folds and theory (Turcotte and Schubert, 1982). Our theory directly determines σ_{xx} and relates it to the far-field strain rates. The far-field strain rates are assumed to be constant and not influenced by the folding process and should therefore be easy to determine.

Similarity to the Viscous-Viscous Case

The viscous-viscous folding of finite length layers has two characteristics: 1) the wavelength does not depend on D_a , and 2) the growth rate has, for given aspect ratio, a maximum at the domain transition, $D_a = 1$. While the first is not the case for the finite length elastic layer, the growth rates show indeed a similar behavior. If we define the growth rate as the coefficient in front of $\varepsilon^{3/2}$ in the elastic amplification expression, then we also obtain a maximum at the domain transition. For small D_a numbers, the growth rate increases with the first power of the increasing effective viscosity contrast, and for large D_a the growth rate decreases with the square root of the effective viscosity contrast (Figure 12). As for the viscous-viscous case, three domains exist: small D_a number, large D_a number, and “No Folding”. The distinctive growth rate behavior and domain characterization can also be seen on the contoured plot of the growth rate versus aspect ratio and viscosity contrast (Figure 13).

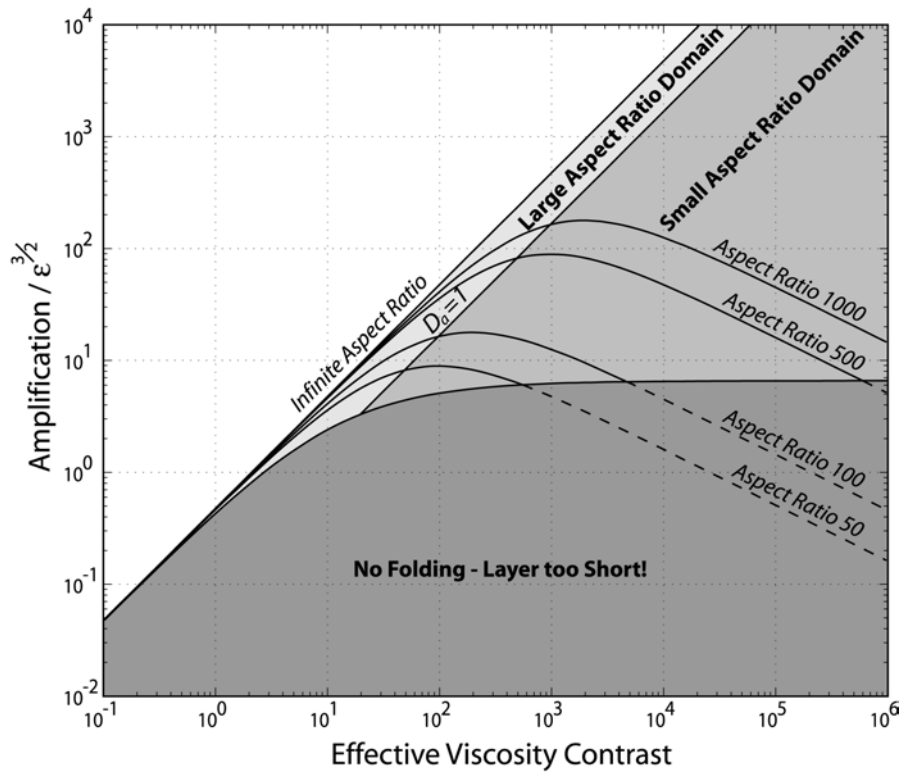


Figure 12

Maximum growth rate, $\tilde{\alpha} = \text{Amplification} / \varepsilon^{3/2}$, versus effective viscosity contrast, and domain characterization.

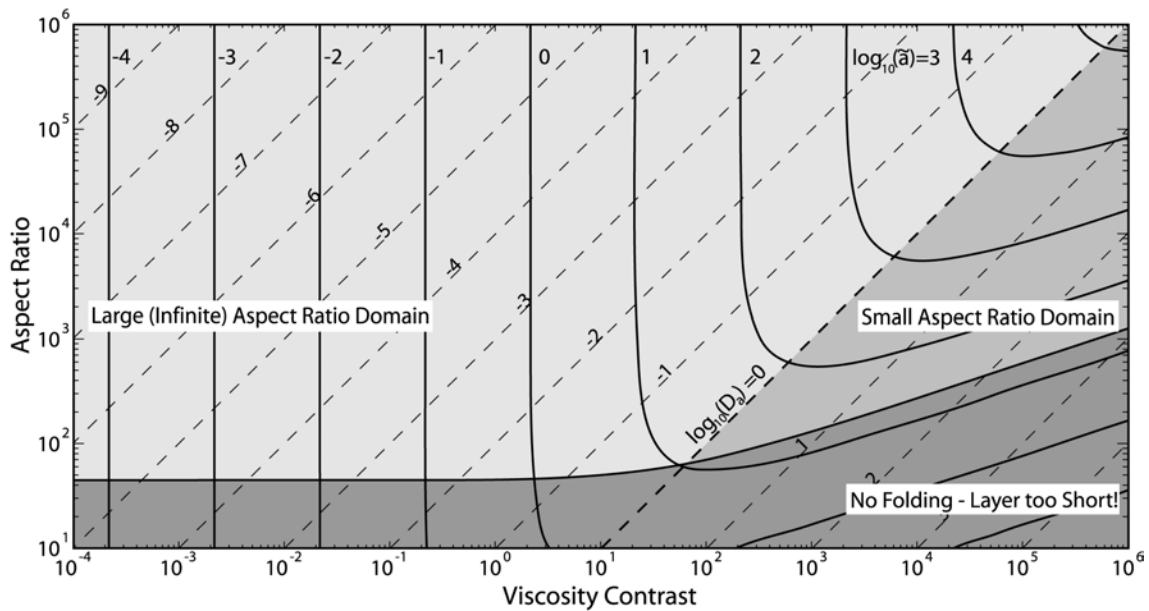


Figure 13

\log_{10} contour plot of the maximum growth rate, $\tilde{\alpha} = \text{Amplification} / \varepsilon^{3/2}$, versus aspect ratio and effective viscosity contrast. The “No Folding” field is bulk strain dependent and here given for $\varepsilon = 0.01$.

The “No Folding” domain in Figures 12 and 13 means that the aspect ratio of the layer is too small to accommodate even one dominant wavelength. Within the scope of this work we have not determined what exactly happens if a layer is configured to lie in the “No Folding” domain. Three different possibilities exist: 1) non-dominant wavelengths, which fit onto the layer amplify, 2) Euler beam buckling takes place, or 3) no folding. Analogue experiments point to the third possibility.

Comparison to Analogue Experiments

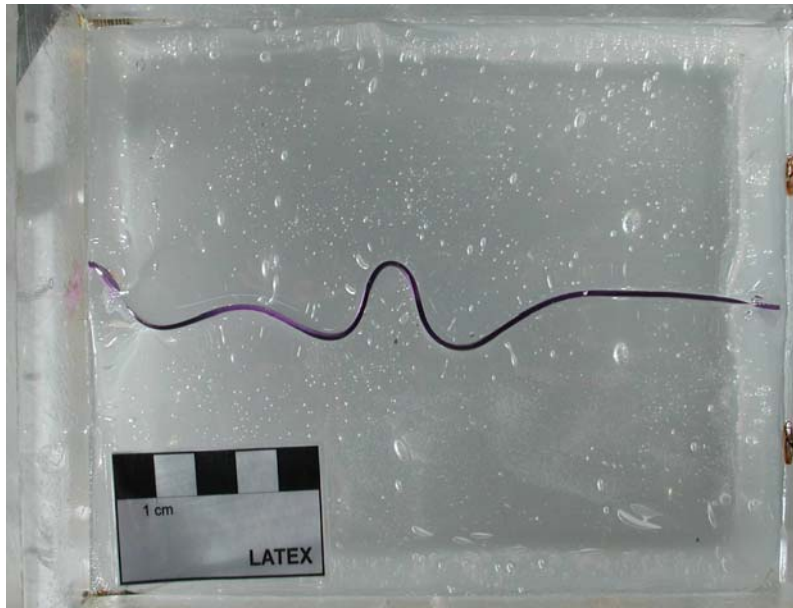
The folding of finite length elastic layers is, due to the constantly changing effective viscosity, growth rates, dominant wavelengths and domain transitions, of considerable complexity. The derivation of the relevant formulae uses several simplifications, which should only affect the domain transition values, around $D_a \approx 1$. In order to test the presented theory, we performed analogue experiments, which give insight into the domain transition and especially the approximate order of magnitude of the yet undetermined wavelength locking parameter in the small D_a domain, \tilde{A} .

The experiments were performed under constant velocity pure shear. A strip of elastic material was embedded in a Polydimethylsiloxane (PDMS) matrix with an approximate viscosity of $5e4$ [Pas]. The strips were made of either Plasticine, Cellophane or Aluminum foil. The physical parameters of these strips are given in Table 3. It is notable that metal foils are amongst the oldest materials used in the experimental folding literature as already Smoluchowski (1909) used tin foil and beaten gold in the experimental verifications of his theoretical results. Pictures of the characteristic behavior of the three materials are shown in Figures 14 to 16.

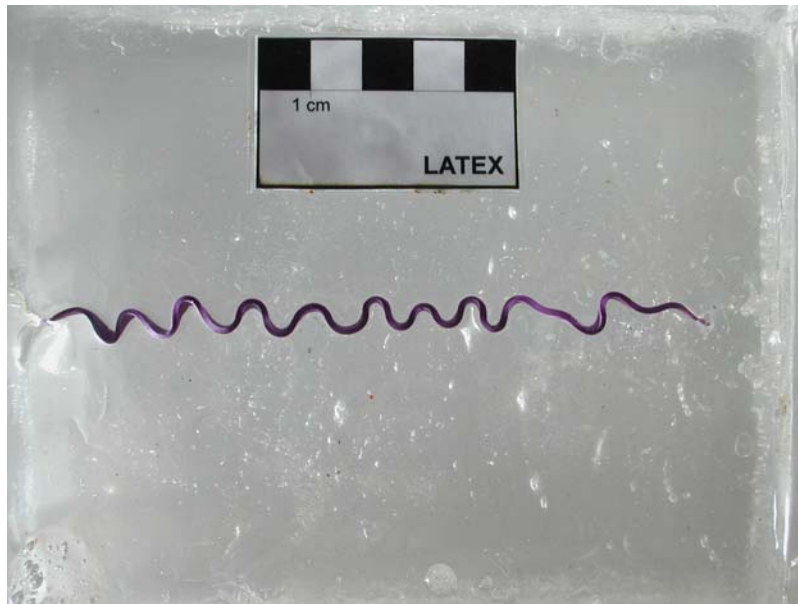
Table 3

Material Properties

	Plasticine	Cellophane	Aluminum Foil
G [Pa]	1.62e-4	1.76e+8	1.13e+11
h [m]	1e-3	4e-5	1e-5
l [m]	0.2	0.2	0.2



a)



b)

Figure 14

Plasticine experiments in the small D_a domain with identical geometrical configuration.. The influence of the bulk strain rate on the wavelength is clearly visible.

a) $\dot{\epsilon} = 1.9e^{-4}s^{-1}$

b) $\dot{\epsilon} = 3.6e^{-2}s^{-1}$



Figure 15

Cellophane experiment at $\dot{\epsilon} = 1.9e^{-4}s^{-1}$ (compare to Figure 14a).



Figure 16

Aluminum experiment at $\dot{\epsilon} = 4.5e^{-4}s^{-1}$. Few localized folds take up all the strain.

Our theory has no means of determining if a material actually locks the folds in the small D_a number domain or if they are chiefly formed in the large D_a domain. Yet, for any given material and aspect ratio a few experiments are sufficient to determine the slope on a log-log fold arc length versus strain rate plot. If the arc length decreases with $\dot{\epsilon}^{1/5}$ then the folds were determined in the small D_a domain and the wavelength locking amplitude \tilde{A} and the D_a number can be determined. On the other hand if the arc length decreases only with $\dot{\epsilon}^{1/2}$ then the folds were formed in the large D_a number domain.

Figure 17 summarizes the analogue experiments and makes a comparison to the theory. It is evident that all plasticine, cellophane and most of the aluminum experiments exhibit the same 1/5 slope, which attributes the folding to the small D_a domain. While plasticine and cellophane have the same locking parameter, the aluminum foil shows a smaller locking parameter. Consequently, less amplification is needed to lock the fold development in the aluminum. This may be attributed to the fact that with the aluminum it is difficult to maintain a smooth, undisturbed surface when the experiment is set up. Additionally the aluminum is much thinner than the cellophane and especially the plasticine and it is therefore likely to have large initial perturbations relative to its thickness. This and further problems with the aluminum experiments are described in detail in the “Appendix”.

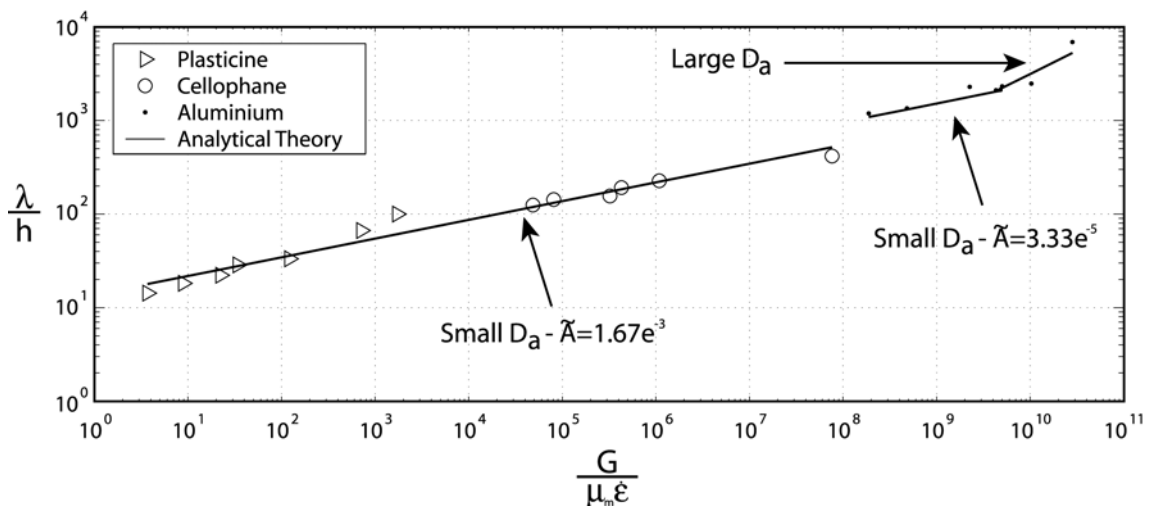


Figure 17

Analogue experiments versus analytical theory.

Translating these values of \tilde{A} into bulk matrix strain, results in values within the range of $5e^{-2}$ to $5e^{-4}$ for plasticine and cellophane, and values of the order e^{-6} for aluminum foil. These values are extremely small and show how fast a finite length elastic layer “decides” upon what the dominant wavelength should be.

Unfortunately, the large D_a number domain is only represented by two points from the aluminum foil experiments. In addition, these two points are actually just transitional values (i.e., $D_a = 1.1$ and $D_a = 2.0$). More experiments are required to prove our theoretical investigation of the existence of a second elastic folding domain. However, it seems that the last data point of the aluminum series cannot be explained by the continuation of the small D_a domain as the discrepancy would be too big. Furthermore, the theoretical large D_a -domain dominant wavelength value corresponds quite well with the mentioned experimental data point, which is encouraging because the dominant wavelength in the large D_a domain is solely dependent on material properties and no fitting “fudge” factor like \tilde{A} can be used to improve the match between theory and experiment.

CONCLUSIONS

We have shown that the finiteness of the length of a layer has a first order influence on folding. For the viscous-viscous case the present theory explains why large wavelength to thickness ratios are not favoured. In the case of the elastic layer in the viscous matrix we have eliminated the need to guess the layer parallel stress, σ_{xx} , and we have shown that the dominant wavelength expression is weakly (to the power 1/5) dependent on the bulk strain rate, which was previously not recognized.

The derivation presented is based on the assumption that the compression is layer parallel. However, the results of the basic state analysis can be easily generalized, as the presented solution in terms of complex potentials is already derived for inclined pure shear. For any inclination, the required layer values can be determined and the linear stability analysis performed. Yet, if there is an angle between layer and pure shear then the layer will also rotate and the folding will be in competition to the rotation. Since the

rotation will move the layer from compression into fields of extension, the layer has only restricted time to develop folds. If an additional simple shear component exists, then the finite length layer may continuously rotate (Jeffery, 1922) and therefore undergo progressive shortening and extension. In order to complete this study, it is therefore essential to combine the general shear Muskhelishvili solution with the linear stability analysis of folding which will yield a theoretical analysis of one of the most common (folding) situations in nature: the finite length layer in general shear.

ACKNOWLEDGEMENTS

This research was supported by the ETH Zurich, grant TH 0-20650-99. It is a contribution to GEOMODELS (PCTI/CTA/32742/99 and POCTI/CTA/38695/2001). The experiments were performed in the LATTEX facilities. We wish to thank Jean-Pierre Burg, James Connolly, Boris Kaus, and Stefan Schmalholz for helpful and inspiring discussions. Toby Thain is acknowledged for providing the plugin that was used to measure the fold arc length free of charge under www.telegraphics.com.au/sw.

REFERENCES

- Biot, M.A., 1954. Theory of Stress-Strain Relations in Anisotropic Viscoelasticity and Relaxation Phenomena. *Journal of Applied Physics*, 25(11): 1385-1391.
- Biot, M.A., 1961. Theory of Folding of Stratified Viscoelastic Media and Its Implications in Tectonics and Orogenesis. *Geological Society of America Bulletin*, 72(11): 1595-1620.
- Biot, M.A., Ode, H. and Roever, W.L., 1961. Experimental Verification of the Theory of Folding of Stratified Viscoelastic Media. *Geological Society of America Bulletin*, 72(11): 1621-&.
- Cobbold, P.R., 1976. Fold shapes as functions of progressive strain. *Phil. Trans. R. Soc. London*, A283(129-138).
- Cuvelier, C., Segal, A. and Steenhoven, A.A., 1986. Finite element methods and Navier-Stokes equations. Reidel, Dordrecht a. o., XVI, 483 pp.
- Eshelby, J.D., 1957. The Determination of the Elastic Field of an Ellipsoidal Inclusion, and Related Problems. *Proceedings of the Royal Society of London Series a- Mathematical and Physical Sciences*, 241(1226): 376-396.
- Eshelby, J.D., 1959. The Elastic Field Outside an Ellipsoidal Inclusion. *Proceedings of the Royal Society of London Series a- Mathematical and Physical Sciences*, 252(1271): 561-569.

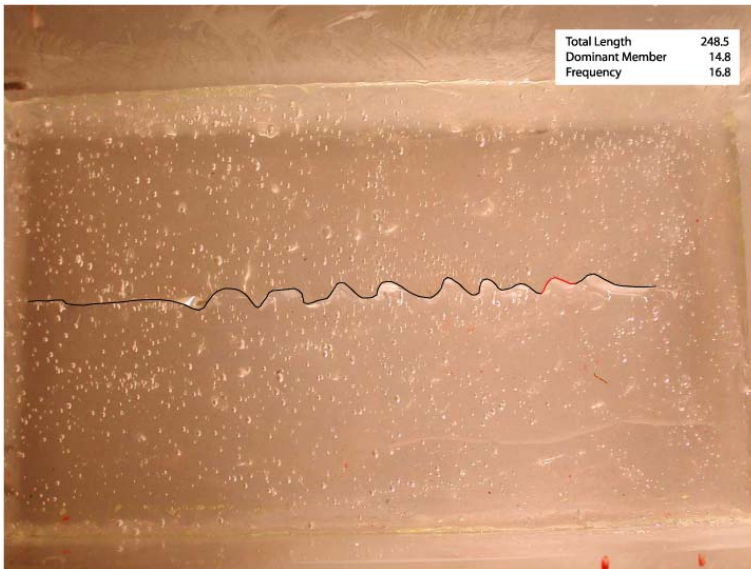
- Euler, L., 1744. Methodus inveniendi lineas curvas maximi minimive proprietate gaudentes sive solutio problematis isoperimetrici latissimo sensu accepti. Marcum-Michaellem Bousquet & Socios., Lausanne & Genève.
- Fletcher, R.C., 1974. Wavelength selection in the folding of a single layer with power-law rheology. *Am. J. Sci.*, 274(11): 1029-1043.
- Hardiman, N.J., 1954. Elliptic Elastic Inclusion in an Infinite Elastic Plate. *Quarterly Journal of Mechanics and Applied Mathematics*, 7(2): 226-230.
- Jeffery, G.B., 1922. The motion of ellipsoidal particles immersed in a viscous fluid. *Proceedings of the Royal Society of London*, A102: 161-179.
- Johnson, A.M. and Fletcher, R.C., 1994. *Folding of viscous layers*. Columbia University Press, New York.
- Mandal, N., Chakraborty, C. and Samanta, S.K., 2001. Controls on the failure mode of brittle inclusions hosted in a ductile matrix. *Journal of Structural Geology*, 23(1): 51-66.
- Muskhelishvili, N.I., 1953. *Some basic problems of the mathematical theory of elasticity*. Noordhoff Groningen, 704 pp.
- Price, N.J. and Cosgrove, J.W., 1990. *Analysis of Geological Structures*. Cambridge University Press, Cambridge.
- Ramsay, J.G., 1974. Development of Chevron Folds. *Geological Society of America Bulletin*, 85(11): 1741-1754.
- Schmalholz, S.M. and Podladchikov, Y.Y., 2000. Finite amplitude folding: transition from exponential to layer length controlled growth (vol 179, pg 363, 2000). *Earth and Planetary Science Letters*, 181(4): 619-633.
- Schmalholz, S.M. and Podladchikov, Y.Y., 2001. Strain and competence contrast estimation from fold shape. *Tectonophysics*, 340(3-4): 195-213.
- Schmalholz, S.M., Podladchikov, Y.Y. and Burg, J.-P., 2002. Control of folding by gravity and matrix thickness: Implications for large-scale folding. *Journal of Geophysical Research B: Solid Earth*, 107(1): 1-16.
- Sherwin, J.A. and Chapple, W.M., 1968. Wavelengths of Single Layer Folds - a Comparison between Theory and Observation. *American Journal of Science*, 266(3): 167-179.
- Smith, R.B., 1975. Unified Theory of Onset of Folding, Boudinage, and Mullion Structure. *Geological Society of America Bulletin*, 86(11): 1601-1609.
- Smith, R.B., 1977. Formation of Folds, Boudinage, and Mullions in Non-Newtonian Materials. *Geological Society of America Bulletin*, 88(2): 312-320.
- Smoluchowski, M., 1909. Versuche über Faltungserscheinungen schwimmender elastischer Platten. *Akad. Wiss. Krakau. Math. Kl.*: 727-734.
- Timoshenko, S.P. and Woinowsky-Krieger, S., 1959. *Theory of Plates and Shells*. McGraw-Hill Book Company, Auckland.
- Turcotte, D.L. and Schubert, G., 1982. *Geodynamics applications of continuum physics to geological problems*. Wiley, New York, ix, 450 pp.
- Vermilye, J.M. and Scholz, C.H., 1995. Relation between Vein Length and Aperture. *Journal of Structural Geology*, 17(3): 423-434.

APPENDIX

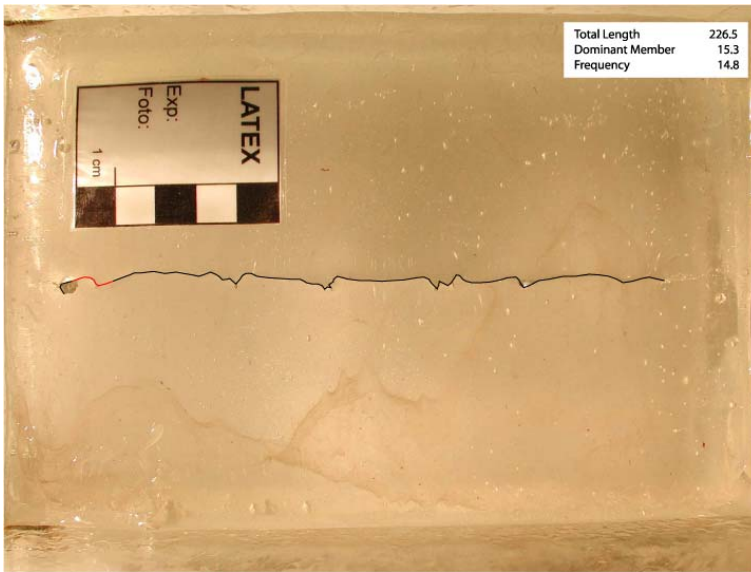
ALUMINIUM FOIL EXPERIMENTS

The analogue experiments with aluminum foil embedded in PDMS showed a tendency to amplify only a few folds to a large amplitude before other parts of the layer started to develop folds. The reason for this may be that the aluminum foil is difficult to handle, and it is hard to maintain a perfectly smooth surface while putting the foil into the PDMS. Additionally, the foil already has a certain structure when rolled off the roll. Since the fold amplification is exponential, small irregularities in the initial layer perturbation can cause significant differences in the finite amplitude behavior, especially strain localization. These types of problems seem to be characteristic for thin metal foils; Smoluchowski (1909) already observed similar troubles with beaten gold.

The wavelength used to compare to the theory is therefore taken to be the arc length of the “dominant member”. The dominant member is the fold that seems representative for the entire fold train. In order to illustrate which arc length was chosen to be the dominant member and how the folds develop into the finite amplitude stage, we present here the analyzed finite amplitude pictures from all aluminum experiments. The black line is always the digitized aluminum foil and the red line the dominant member.



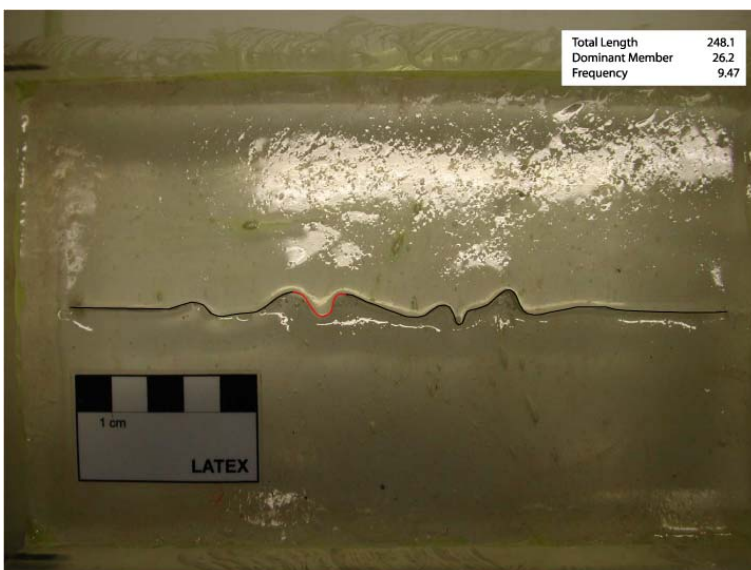
a) $\dot{\epsilon} = 1.2e-2$



b) $\dot{\epsilon} = 4.7e-3$



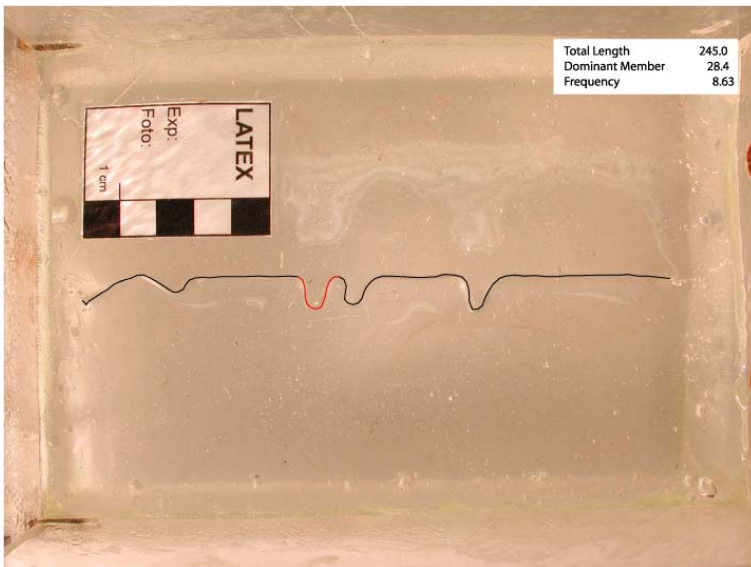
c) $\dot{\epsilon} = 1.0e-3$



d) $\dot{\epsilon} = 5.25e-4$



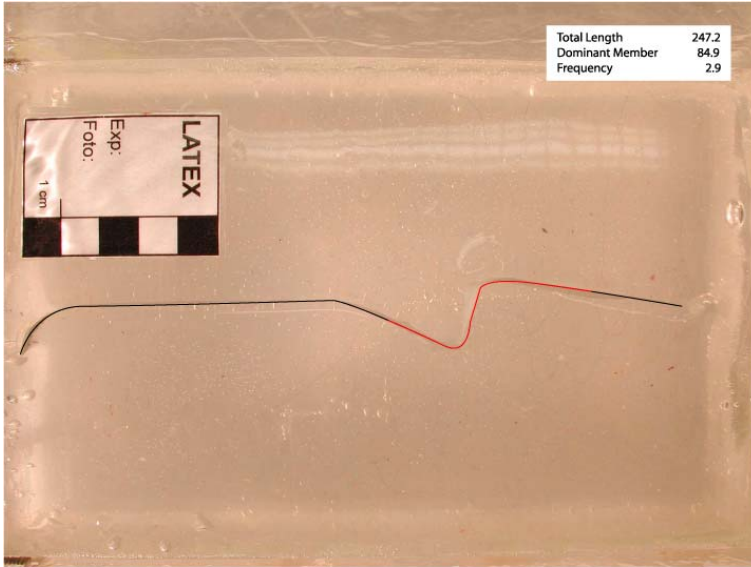
e) $\dot{\epsilon} = 4.7e-4$



f) $\dot{\epsilon} = 4.5e-4$



g) $\dot{\epsilon} = 2.2e-4$



h) $\dot{\varepsilon} = 5.8e-5$

CHAPTER 7: NUMERICAL MODELING OF SINGLE LAYER FOLDING IN GENERAL SHEAR

NOTE: Due to the media content this paper should be viewed in the PDF version (on the companion CD) where all the movies can be played. This hardcopy version is merely printed for reasons of completeness.

ABSTRACT

Asymmetric folds are by far the majority of natural folds. Nevertheless, they are, in comparison to their symmetric counterparts, not adequately studied and the asymmetry causing processes are still under speculation. Intuitive argumentations suggest that rotational deformation drives asymmetry. Yet, previous analytical, analogue, and numerical experiments have not been able to identify this as the cause for fold asymmetry. Based on fully dynamic, two-dimensional numerical modeling we show how combined layer parallel pure and simple shear results in asymmetric folds. Comparison to the kinematic and dynamic fold development under pure shear only fosters our understanding of the lifetime of a fold, from its initial to the final (radiator) stages. We find that fold asymmetry is mainly a passive phenomenon. We outline how this passive character allows for the construction of a shear strain map. Such a map, in combination with the strain map developed by Schmalholz and Podladchikov (2001), would allow determining competence contrast, shortening strain as well as shear strain directly in the field from simple geometrical parameters.

INTRODUCTION

Folding is one of the main mechanisms by which layered rocks accommodate shortening. Consequently folds have been, for many years, the focus of research in structural geology. The subject is well studied from analytical (e.g., Biot, 1961; Ramberg, 1963; Chapple, 1968; Smith, 1975; Johnson and Fletcher, 1994; Schmalholz and Podladchikov, 2000), analogue modeling (e.g., Ghosh, 1966; Cobbold, 1975; Abbassi and Mancktelow, 1992) and numerical modeling (e.g., Dieterich, 1970; Manz and Wickham, 1978; Hudleston and Lan, 1994; Zhang et al., 1996; Mancktelow, 1999; Schmalholz and Podladchikov, 1999) points of view. However, there is no “complete dataset” for the most classical case of folding, i.e., a single competent layer embedded in a viscous matrix, subjected to layer parallel compression. By “complete dataset” we mean kinematic parameters such as velocity, strain rate and strain, as well as dynamic parameters such as stress and pressure *throughout the fold development*. Despite the sound mechanical understanding of the folding process, structural geology mainly relies on kinematic concepts such as flexural slip folding or shear folding (Ramsay and Huber, 1987; Twiss and Moores, 1992) and on geometrical classifications such as the dip isogon (Ramsay, 1967). This kinematic approach certainly has its eligibility since, in geological studies, the only preserved quantity of the process is the geometrical configuration. However, in order to verify the applicability of the kinematic approach it is necessary to verify these concepts versus dynamic continuum mechanics models, which is why we provide here the complete dataset for six different numerical experiments.

Another point which we address in this paper is the asymmetry of folds, which most natural folds exhibit. It is intuitively accepted that the asymmetry is caused by simple shear superposed onto a pure shear shortening. Yet, infinitesimal analytical theories show that simple shear has no influence on the folding process (Treagus, 1973; Johnson and Fletcher, 1994, p.62). This observation is supported by analogue experiments (Ghosh, 1966; Manz and Wickham, 1978). In addition there is some doubt whether the vergence of folds (Bell, 1981) can be used as a reliable indicator for the direction of the simple shear component of the far-field flow. For example Reches and Johnson (1976) and Pfaff and Johnson (1989) have reported kink fold asymmetries opposite to the bulk simple shear component, and Krabbendam and Leslie (1996) explained asymmetric

multilayer folds in the Scottish Highland with a simple shear component that is opposite to the vergence. The numerical experiments by Anthony and Wickham (1978) contribute to this confusion in that their folds develop a weak asymmetry, but the long limb thickens and the short limb thins (with respect to each other), which is against our intuitive understanding of asymmetric fold development. We want to resolve this confusion (or maybe contribute to it) by demonstrating under which conditions asymmetric folds develop in single layers and we reestablish the use of fold vergence as a reliable indicator of the simple shear sense.

MODEL DESCRIPTION

The model developed for this study solves the Stokes equations for incompressible flow of Newtonian fluids in the absence of body forces such as gravity. In indicial notation, the Eulerian formulation of the basic equations is (Mase, 1970):

The continuity equation

$$v_{i,i} = 0 \tag{1}$$

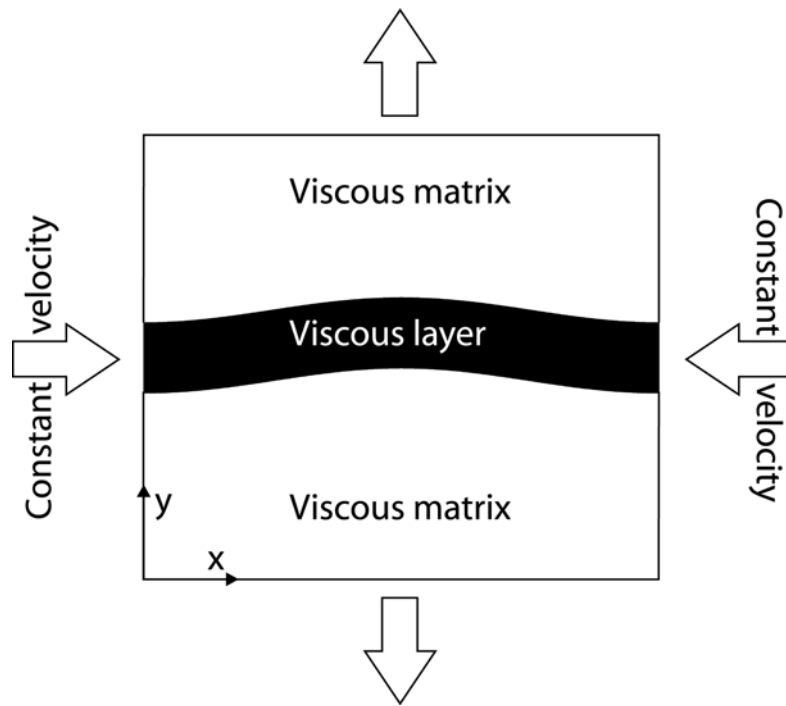
The equations of motion

$$\sigma_{ij,j} = 0 \tag{2}$$

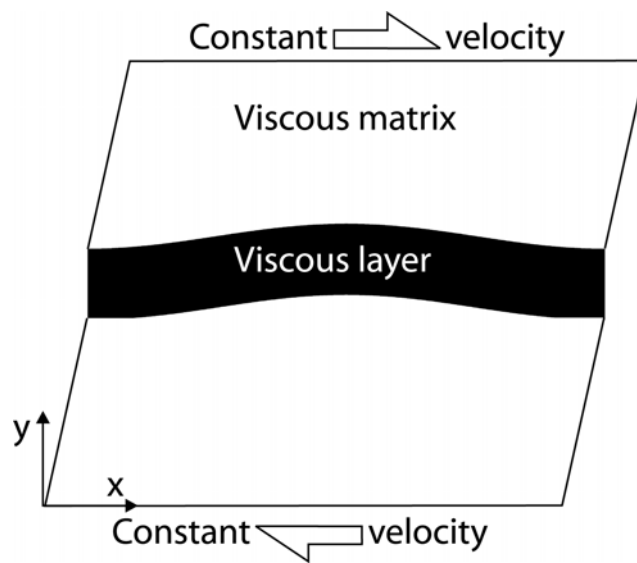
the constitutive equations for incompressible Newtonian fluids

$$\sigma_{ij} = -p\delta_{ij} + \mu(v_{i,j} + v_{j,i}) \tag{3}$$

where v_i , σ_{ij} , p , δ_{ij} , μ are the velocity, total stress tensor, pressure, Kronecker delta and viscosity, respectively. Eqns. (1) to (3) form a closed system of partial differential equations and thus can be solved for the unknown velocities. The numerical method used is a mixed finite difference / spectral method, already successfully applied to study high amplitude folding in Schmalholz and Podladchikov (2000) and documented in detail by Schmalholz et al. (2001). With this method the periodic nature of folds is taken into account by applying a spectral expansion in the direction of the periodicity (x-direction in Figure 1), in the other, orthogonal direction, a conservative finite difference method with a staggered grid (Canuto et al., 1988) is used.



a)



b)

Figure 1

Model setup - a competent layer is embedded in a weaker matrix.

a) Pure shear

b) Simple shear and its effect on the lateral boundaries.

The model setup follows the classical way of embedding a competent layer in a weaker matrix. This system is then subjected to layer parallel pure shear with constant velocity boundary conditions relative to a fixed spatial point (Figure 1). The simple shear boundary condition is similar to Ghosh (1966) and identical to Johnson and Fletcher (1994) but is different to previous numerical work (Anthony and Wickham, 1978). Namely, we apply a constant velocity at the top and bottom of the numerical box and periodic boundary conditions at the lateral boundaries. Contrasting constant shear rate (rigid lateral wall) boundary conditions (for simple shear), this avoids strong boundary effects. The effect of the employed simple shear boundary condition is depicted symbolically in Figure 1b, where the weak matrix accommodates much more shear strain than the competent layer.

In the initial configuration of all presented experiments the thickness (h) to wavelength (λ) ratio was set according to Biot's theory (1961):

$$\frac{\lambda}{h} = 2\pi \sqrt[3]{\frac{\mu_l}{\mu_m}} \quad (4)$$

where μ_l and μ_m are the viscosity of the layer and the matrix, respectively. In order to allow for fold growth the layer was sinusoidally perturbed with an amplitude of 1/50 of the layer thickness.

VISUALIZATION

Six different parameters are visualized for every individual experiment: material, active flow, maximum shear strain rate, strain, maximum shear stress and pressure. These are explained in detail below:

MATERIAL

Simply a visualization of the geometrical evolution of the fold by means of the viscosity distribution. Red (layer) is more competent than blue (matrix).

ACTIVE FLOW

Since the pure and simple shear background components of the flow are well known (e.g., Ramsay and Huber, 1983) and overprint the actual shape changing active flow, it is custom (Ramberg, 1963; Cobbold, 1975) to visualize only the active flow (also termed perturbation or secondary flow). The active flow is simply the total flow minus the pure and simple shear background components. Instead of using arrows, it is advantageous to use streamlines to plot the active flow. The streamlines are contour lines of the stream function ψ , which is defined as

$$v_1 = -\psi_{,2} \quad (5)$$

$$v_2 = \psi_{,1} \quad (6)$$

Streamlines are useful because in steady state they are trajectories of individual material particles that are moved by the flow. An example of how velocity vectors translate into the stream function and streamlines is given by the comparison in Figure 2a) and b). The vortex structure, especially if complex, can be more intuitively captured through the stream function plot. Red (positive) values symbolize clockwise rotating vortices, blue (negative) values counter-clockwise rotation. The contour lines are tangential to the velocity vectors.

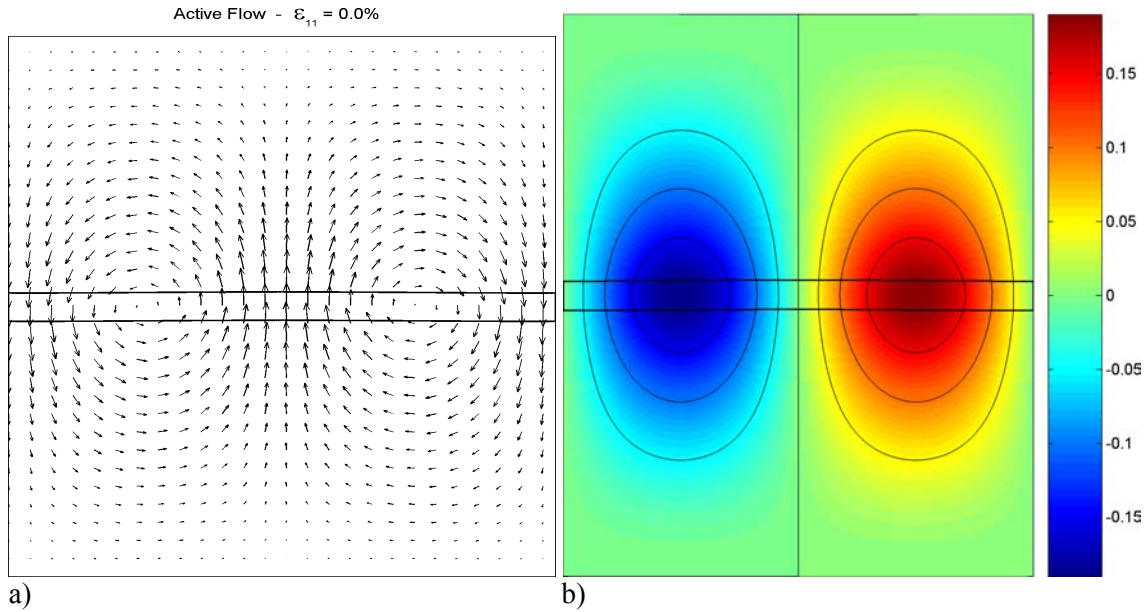


Figure 2

Different ways of visualizing the active flow field caused by a layer in pure shear with a small perturbation and a viscosity contrast of 100:1.

a) Arrows, b) Stream function and Streamlines

EFFECTIVE STRAIN RATE

The maximum shear strain rate, also termed effective strain rate, $\dot{\epsilon}_E$, at a point is described with a coordinate frame independent measure, the square root of the second invariant (e.g, Ranalli, 1995).

$$\dot{\epsilon}_E = \left(\frac{1}{2} \dot{\epsilon}_{ij} \dot{\epsilon}_{ij} \right)^{1/2} \quad (7)$$

LONGITUDINAL STRAIN

The position of a so called neutral line or surface of a fold, where the extension is zero, is often discussed in the folding literature (e.g., Ramsay and Huber, 1987; Price and Cosgrove, 1990; Twiss and Moores, 1992) and is an important concept for analytical folding theories which may or may not take shear deformation across the layer into

account. Therefore, we measure the accommodated strain by means of the longitudinal strain along initially horizontal lines (Ramsay and Huber, 1983, p.285). This measure is zero for originally horizontal lines that maintain their length, negative if they are shortened and positive if they are stretched. The zero contour is drawn in white. The strain measure method implemented is based on a passive square grid that is moved with the total velocity field. Since the original grid does not follow the geometry of the problem, i.e., crosscuts the initial fold geometry that has a small perturbation, some squares overlap the layer-matrix interface and therefore record a strain mixture. This is a minor drawback that only concerns the fold-matrix interface. The use of a Eulerian grid for strain recording, based on the cumulated strain rate tensor, could improve this.

EFFECTIVE STRESS

The definition of the maximum shear stress, or effective stress, σ'_E , at a point is analogous to the maximum shear strain rate defined as the square root of the second invariant.

$$\sigma'_E = \left(\frac{1}{2} \sigma'_{ij} \sigma'_{ij} \right)^{1/2} \quad (8)$$

where σ'_{ij} is the deviatoric stress tensor ($\sigma'_{ij} = \sigma_{ij} + p\delta_{ij}$). For two different cases the maximum shear stress can be interpreted as a measure of proximity to failure: i) fold and matrix are pressure insensitive plastic materials (e.g., von Mises), and ii) the fold thickness is negligible compared to the depth at which the fold is located in the lithosphere.

PRESSURE

Since the set of Stokes equations determines the pressure only up to a constant, any constant (lithostatic) value may be added to the presented values without influence on the results. As a consequence, the pressure perturbation can take both, negative and positive values, which is naturally not the case for the complete pressure.

RESULTS

A total of six complete experiments are documented on the following pages, four pure shear and two experiments where pure and simple shear parallel to the layer act contemporaneously. The initial setup and the boundary condition follow the description in Figure 1. In order to see the results it is necessary to have the QUICKTIME plugin that can be downloaded freely from www.apple.com/quicktime.

In order to focus on the interesting part of the experiments some matrix was clipped and therefore the vertical boundaries do not represent the physical boundaries of the experiments. Another point worth explaining is that in order to make optimal use of the available space, the area is not kept constant in the movies, which is not the case in the actual experiments. A last point that might cause confusion is the lateral periodicity. Especially in the general shear experiments parts of the folds leave the box on the right side and come back in on the left side. One must imagine the displayed data as a TV screen section of an infinitely long fold train. On new widescreen TVs the picture would look like Figure 3.

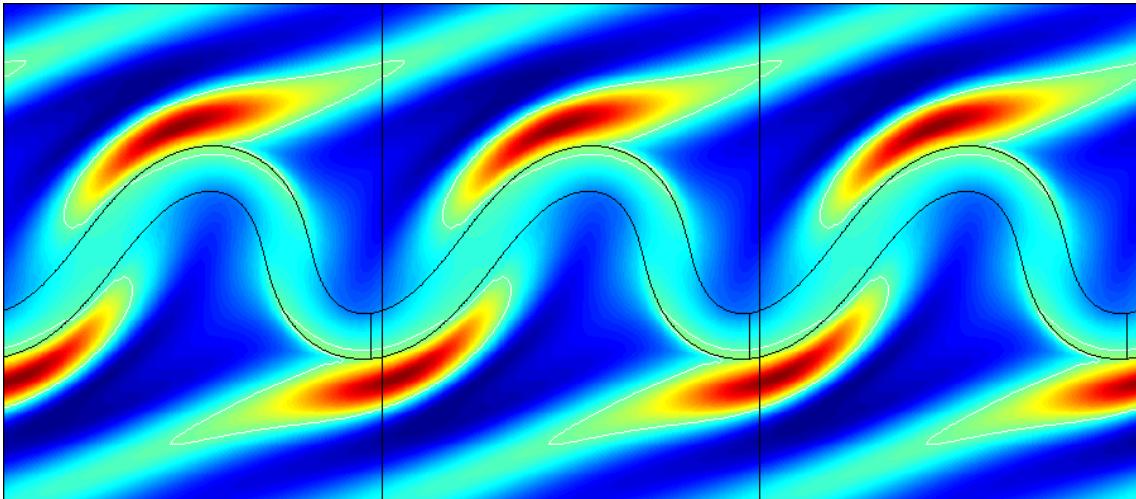
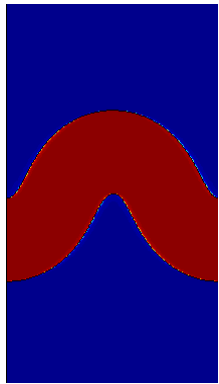
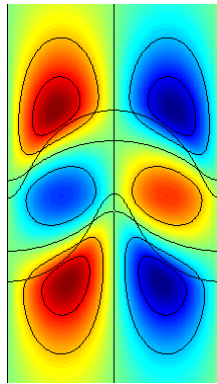
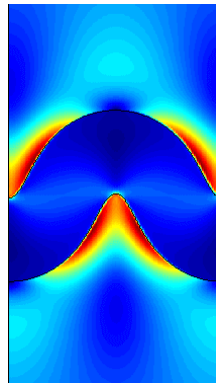
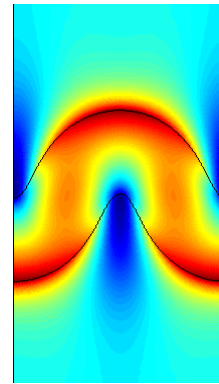
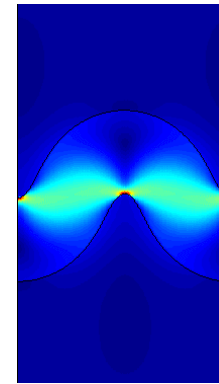
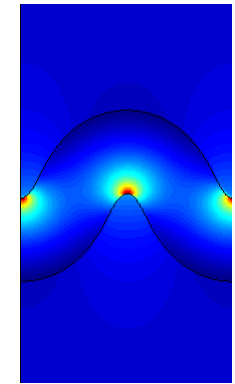
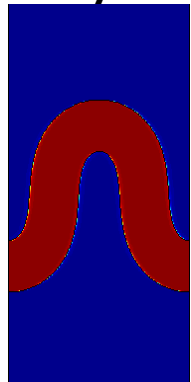
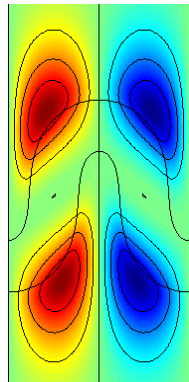
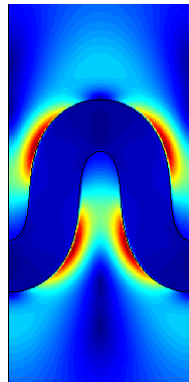
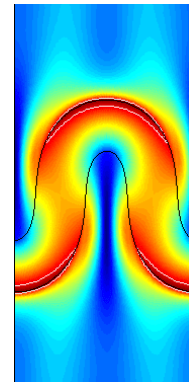
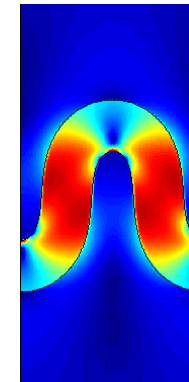
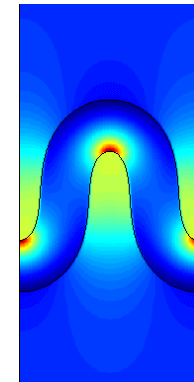


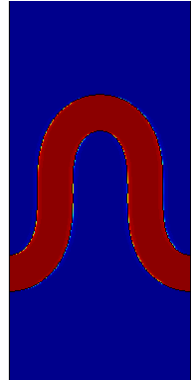
Figure 3

Lateral periodicity demonstrated with the example of longitudinal strain of a layer with viscosity contrast 50:1, subjected to general shear. $\epsilon_{xx} = 38.9$, $\gamma = 2.77$

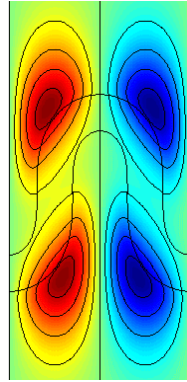
PURE SHEAR

Viscosity Contrast 25:1MaterialActive FlowEff. Strain RateLong. StrainEff. StressPressure**Viscosity Contrast 50:1**MaterialActive FlowEff. Strain RateLong. StrainEff. StressPressure

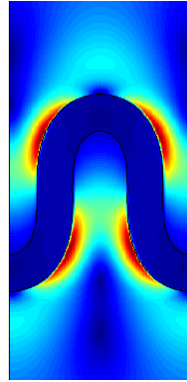
Viscosity Contrast 100:1



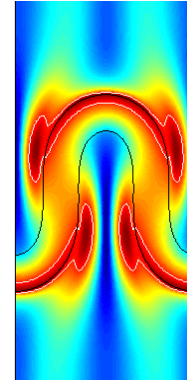
Material



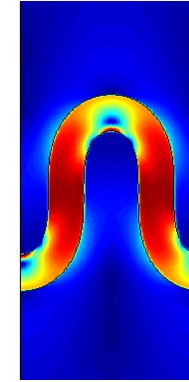
Active Flow



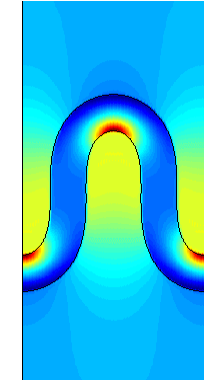
Strain Rate



Strain

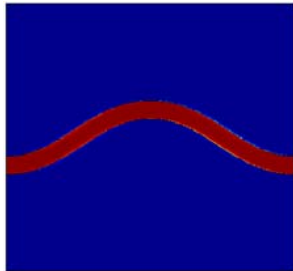


Stress

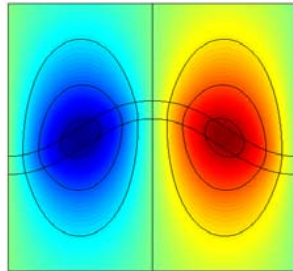


Pressure

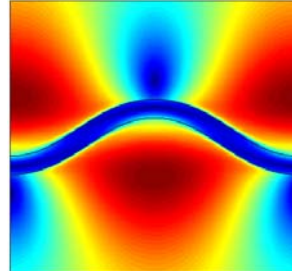
Viscosity Contrast 200:1



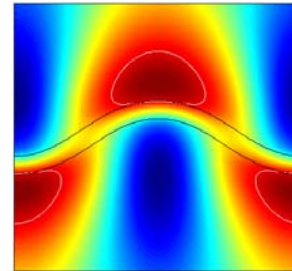
Material



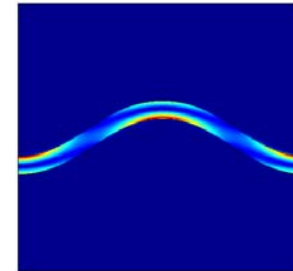
Active Flow



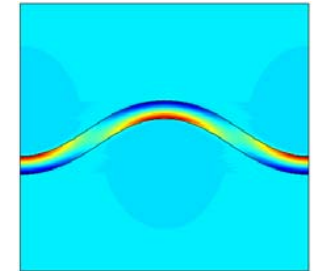
Strain Rate



Strain

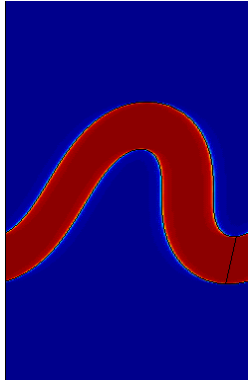
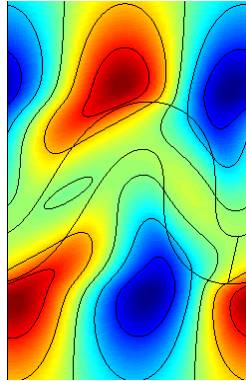
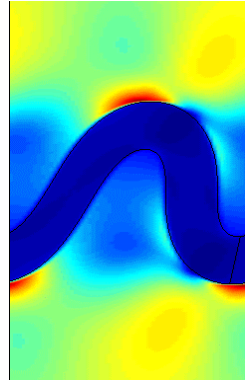
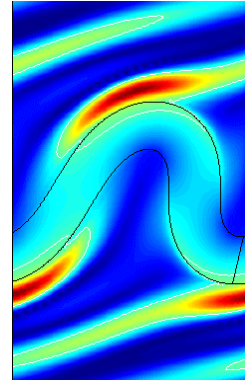
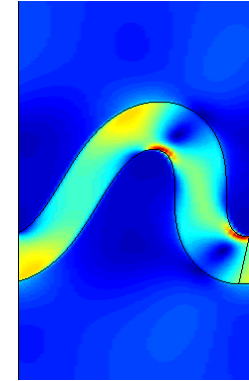
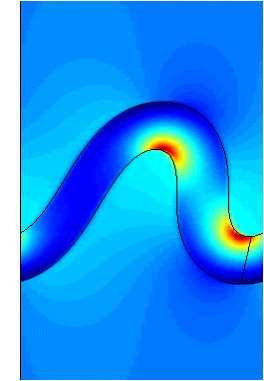
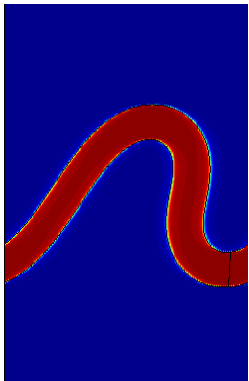
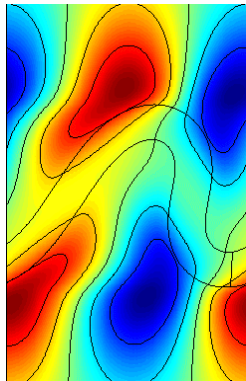
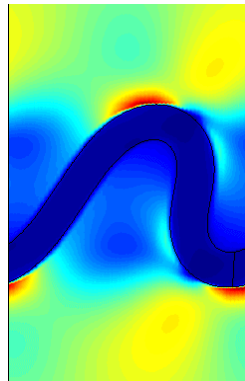
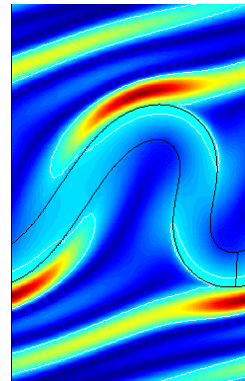
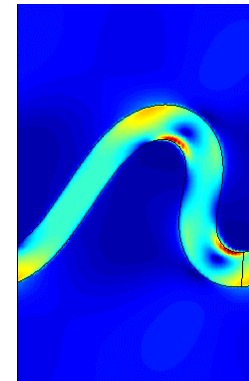
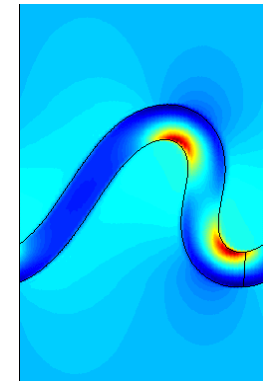


Stress



Pressure

COMBINED PURE AND SIMPLE SHEAR

Viscosity Contrast 50:1MaterialActive FlowEff. Strain RateLong. StrainEff. StressPressure**Viscosity Contrast 100:1**MaterialActive FlowEff. Strain RateLong. StrainEff. StressPressure

DISCUSSION AND INTERPRETATION OF PURE SHEAR EXPERIMENTS

Four different pure shear experiments are presented where the viscosity contrast varies from 25:1, 50:1, 100:1 to 200:1. The numerical resolution used was 2000 finite difference points by 64 spectral harmonics.

GEOMETRICAL EVOLUTION AND ACTIVE FLOW FIELD

Subjected to lateral compression, the layer starts to amplify the initially small perturbation and develop into a fold. This is best seen in the active flow field plots, which for all four viscosity contrasts initially consists of two amplifying vortexes (Figure 5). According to Biot's theory the growth rate increases with increasing viscosity contrast according to

$$\frac{\alpha}{\dot{\epsilon}} = \left(\frac{4 \mu_l}{3 \mu_m} \right)^{2/3} \quad (9)$$

The growth rate describes how many times faster the instability grows compared to the purely passive, kinematic amplification, which is due to the background pure shear. The relevant growth rate spectra are shown in Figure 4. The growth rate for a fold with viscosity contrast 200:1 is approximately 4 times larger than for a fold with viscosity contrast 25:1. Since the amplification initially follows an exponential law, the effect of the different growth rates is tremendous.

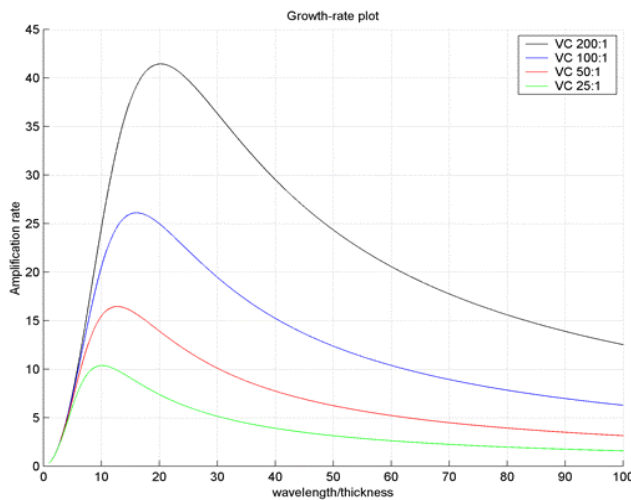


Figure 4
Biot growth rate spectra for
different viscosity contrasts.

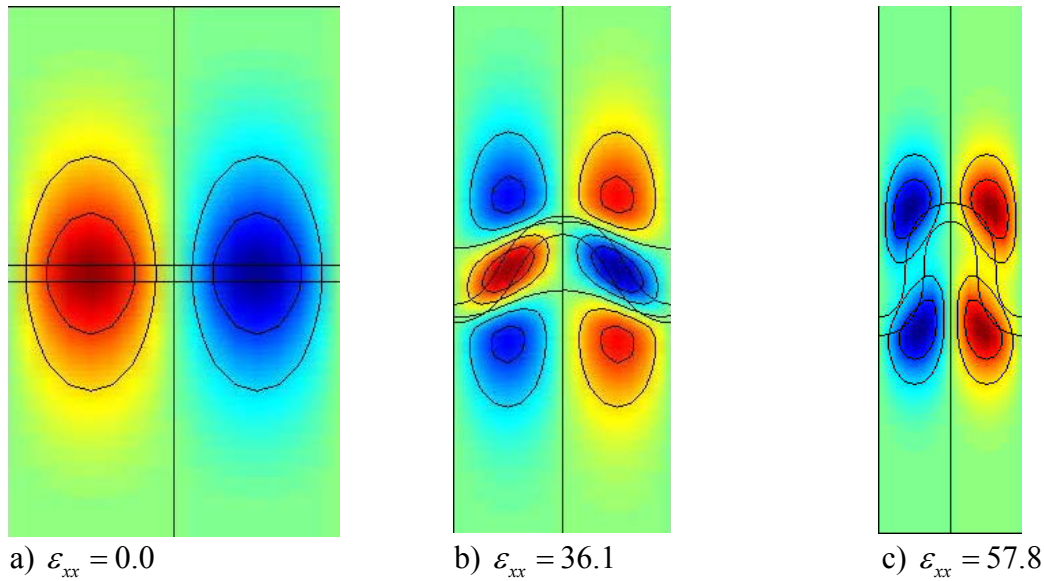


Figure 5

The characteristic active flow vortex pattern of the evolution of a single layer fold. The viscosity contrast is 200:1.

The increase in the vigor of the amplification is reflected in the size of the vortices compared to the thickness of the layer. Namely, the vortex size grows with increasing viscosity contrast. This follows the analytical and experimental considerations of Ramberg (1961) who found that the “contact strain”, i.e., the region over which the matrix records the deformation caused by the folding of a nearby layer, is limited to about one initial wavelength on either side of the layer. Since the initial wavelength increases according to eqn. (4), the region of contact strain increases also and it is to be expected that the size of the active flow field enlarges. Active flow plots for initial stages were shown previously by Ramberg (1963) in his analytical work and by Cobbold (1975) in experimental work.

The two initial active flow vortices drive the amplification and development of folds. Infinitesimal folding theories state that the growth of the fold is exponential. Clearly, this can only be the case for small strains and it has been shown by Schmalholz and Podladchikov (2000) that the fold development goes from exponential into a layer-length controlled growth mode. This decreases the fold growth rate and is captured here by the steady shrinkage of the amplifying vortices with increasing strain, which leads to a complete breakdown of the two amplifying vortices into a six vortex pattern (Figure

5b). The task of this new vortex structure is to act against the passive pure shear stretching, as the layer tries to maintain its length. Therefore the top and bottom row of vortices rotate against the fold, in an attempt to compensate the pure shear stretching. The middle row of vortices accommodates further horizontal shortening through rotating the limbs into a steeper orientation. Once the limbs are vertical, the middle row of vortices disappears and a four vortex structure tries to prevent the layer from passive stretching. Yet, the counter-rotating vortex structure is not strong enough to overprint stretching of the fold into a “radiator stage” (Schmalholz and Podladchikov, 1999). It is interesting, that folds in layers with strong viscosity contrasts go much faster, in terms of bulk strain, through the 2-6-4 vortex behavior. This is again related to their higher growth rates that leads to much larger amplification for given strain, compared to less competent layers.

Folds with larger viscosity contrast do not just grow faster and build up larger amplitudes; they also show less internal deformation. A fold of viscosity contrast 200:1 for example remains a parallel fold (Ramsay and Huber, 1987) up to high amplitude stages. A fold with viscosity contrast 25:1 accommodates much of the shortening by layer parallel thickening and internal shear deformation. This can be well observed in the maximum shear strain rate movies. This has been recognized for a long time and Sherwin and Chapple (1968) have provided corrections for the analytical theories.

The fold development behavior described here is not new. It follows the descriptions of fold life times given by several previous authors (e.g., Ramsay, 1974; Cobbold, 1976). Yet, the evolution of the active flow field vortex structure, which is important to understand fold process, has not been analyzed elsewhere.

EFFECTIVE SHEAR STRAIN RATE AND LONGITUDINAL STRAIN

As already discussed in the geometrical evolution section the weak layer shows much more internal deformation than a strong layer. This is also manifested in a comparison of maximum shear strain rate plots for different viscosities, for example 25:1 versus 200:1. While the strong layer stays dark blue (very little shearing) over most of the shortening, the weak layer shows during the first 50% of shortening strong internal shearing and large internal variations in shear strain rate. While the outer hinges are

regions of relatively little shear straining, the inner hinges and the limbs record much higher maximum shear strain rates. However, due to its relative incompetence, the matrix records the highest values of maximum shear strain rates throughout the folding process. The location of the maximum shear strain rates in the matrix is always, independent from strain and viscosity contrast, in the inner hinge region where the matrix is squeezed away by the approaching limbs.

The measured strain gives the information if originally horizontal lines, which basically is the case for the initial configuration of the layer, are stretched or shortened. In the case of the very weak layer (viscosity contrast 25:1), all elongations recorded within 60% shortening, are negative, i.e., all lines are shorter than they were originally. This can again be explained by the massive layer parallel shortening, that occurs because of the small growth rates compared to the kinematic background deformation. With increasing viscosity contrast and strain, regions of extension come into existence. As expected from geometrical considerations, the location where this extension takes place is in the outer hinge region (e.g., Ramsay and Huber, 1987). However, generally geometric constructions overestimate size and the amplitude of the extensional field at the outer hinge of the layer.

EFFECTIVE SHEAR STRESS AND PRESSURE

As already pointed out in the section “Visualization” the maximum shear stress and the maximum shear strain rate are closely related. In fact we can express one through the other by

$$\sigma'_E = 2\mu\dot{\epsilon}_E \quad (10)$$

where μ is the viscosity of the point for which σ'_E and $\dot{\epsilon}_E$ are valid. Although they contain redundant information, the example in Figure 6 shows that none is obsolete. The maximum shear strain rate shows the regions where the material undergoes maximum shear straining, which is the matrix material between the limbs, close to the hinges. At this location the matrix must contemporaneously accommodate the laterally approaching hinges and expel material from the core. On the other hand, the maximum shear stress visualizes the proximity to failure.

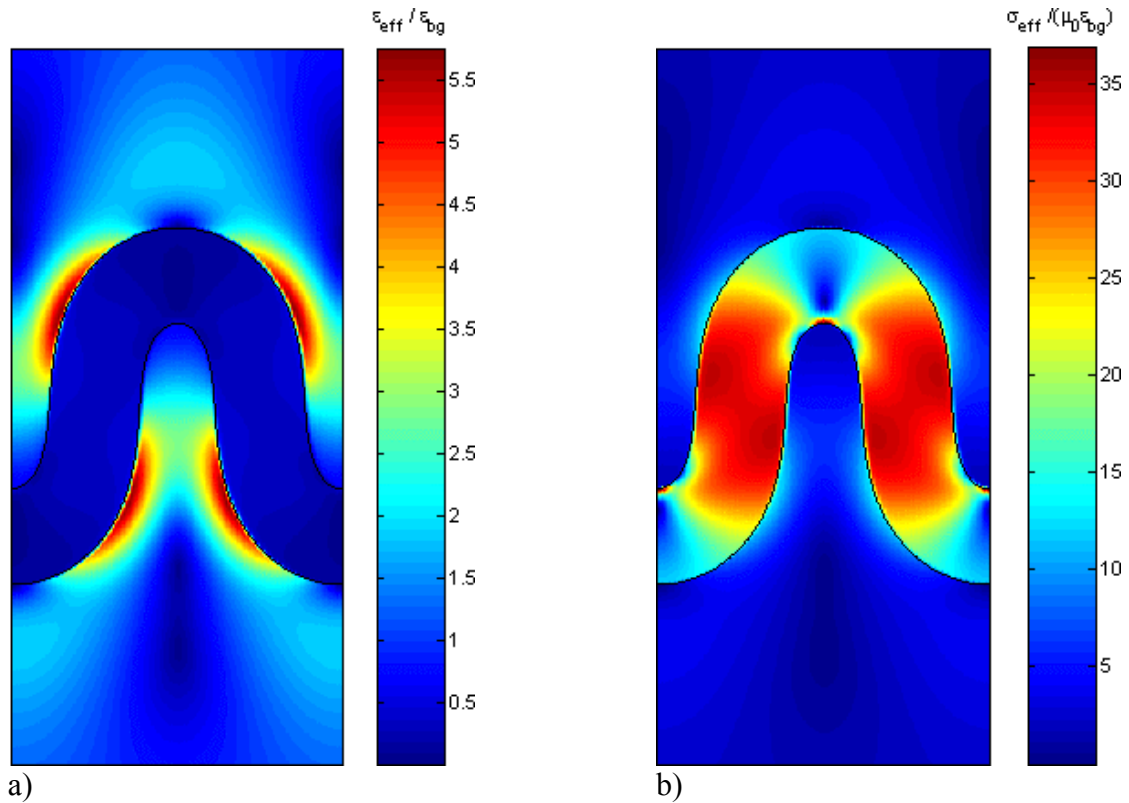


Figure 6

Comparison of maximum shear strain rate (a) versus maximum shear stress (b).

Viscosity contrast is 50:1. Bulk shortening 63%.

At this high amplitude stage the limbs are closest to failure, because they are stretched by the pure shear kinematics, which overprints the described counter-rotating active flow vortices. Due to the large differences in viscosity it is impossible to understand the different meaning of $\dot{\epsilon}'_E$ and σ'_E , if only one of them is displayed.

The finite strain evolution of $\dot{\epsilon}'_E$ and σ'_E is as follows: $\dot{\epsilon}'_E$ is mainly matrix related and continuously records growing values with increasing strain. σ'_E is layer related and has a maximum at intermediate strain values. Starting from the initial stage where the layer exhibits an almost constant value, σ'_E keeps increasing with increasing strain. These maximum values are restricted to the inner hinges. Once the two vortex pattern starts to become smaller, the σ'_E values decrease. The final stage (Figure 6) is related to the breakdown of the six vortex pattern. The σ'_E maxima become large in extent (the entire limb region), yet the values are much smaller than the maxima that occurred during the

limb stretching and even smaller than the initial values. Hence, if σ'_E is used as a measure of failure proximity, the fold would have yielded much earlier.

The remaining dynamic parameter is pressure. In terms of maximum values its evolution is similar to the maximum shear stress. The entire layer is initially under a pressure that is equivalent to $2\mu_1\dot{\epsilon}$ (Biot, 1961). In the next stage the maximum pressure progressively increases, but is restricted to the inner hinges. However, once the four vortex stage is reached the pressure behavior starts resembling more the maximum shear strain rate, in that the maxima are found within the matrix. This is due to the fact that the matrix is trapped within the fold core.

DISCUSSION AND INTERPRETATION OF GENERAL SHEAR EXPERIMENTS

Two different experiments with combined pure and simple shear are presented where the viscosity contrast is 50:1 and 100:1, respectively. The numerical resolution used was 2000 finite difference points by 64 spectral harmonics. The shear stress to normal stress ratio in the undisturbed matrix was set to be 5:1. The direction of the simple shear component top to the right.

GEOMETRICAL EVOLUTION AND ACTIVE FLOW FIELD

The most noticeable effect of the additional simple shear component on the active flow field is that still two amplifying vortexes exist, but they are inclined against the applied simple shear. As long as the two vortex pattern exists there is almost no visible component of asymmetric fold shape. Once the vortexes become weaker, the folds develop a vergence which accords with the applied simple shear. Hence, the development of fold asymmetry is a passive, geometrical process. It may be compared to the final stage of the pure shear single layer folds where the background pure shear component stretches the limbs and the active flow tries to prevent this. In a similar fashion the active flow acts against the movement of the passive simple shear component, without success.

The development of fold asymmetry is limited by the lateral space. This becomes progressively more restricted as more shortening is accommodated. The individual folds, implicit in the assumption of lateral periodicity, force themselves back into the “radiator stage” in which the asymmetry remains visible due to the thickness differences in the limbs. This thickness difference stems from the fact that the fore limb is shortened, while the back limb is being stretched by the simple shear (Figure 9). Note, that this stretching and extension are mostly relative, overprinted by the overall pure shear shortening. An absolute extension of originally horizontal lines in the limbs indeed occurs first in the back limb, but only in the very late stages where the background pure shear already stretches the limbs.

The flow pattern evolution is, due to the asymmetry, much more complex, but follows the 2-6-4 vortex pattern. In general it seems that despite the formation of asymmetric folds, the folding in combined pure and simple shear is very similar to the pure shear only case. If this is the case the finite amplitude theory of Schmalholz and Podladchikov (2000) should be applicable to the asymmetric case as well. Their theory successfully describes the single layer fold development in pure shear at least up to threefold shortening. In order to compare our results to their theory we must define wavelength and amplitude of asymmetric folds. Our method of measuring is depicted in Figure 7.

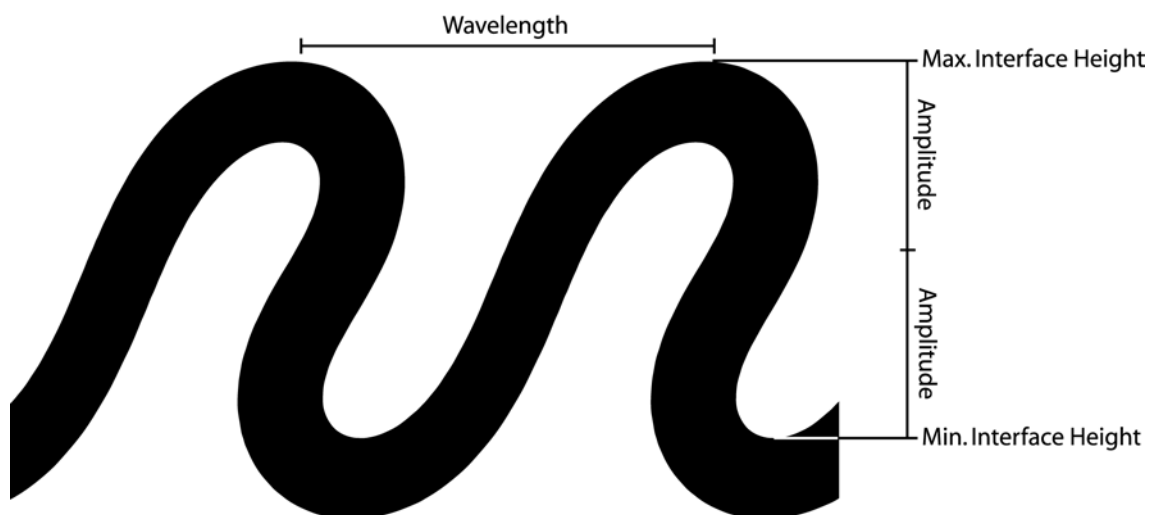
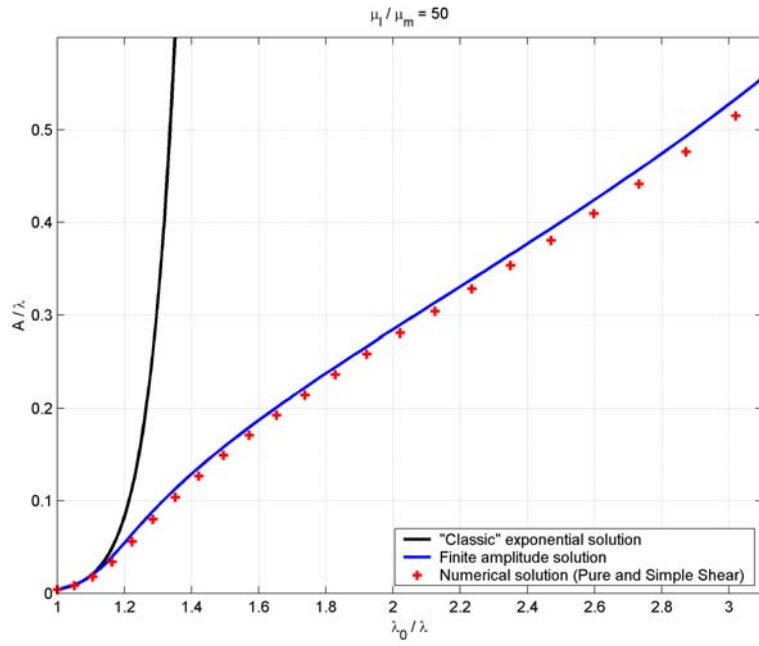
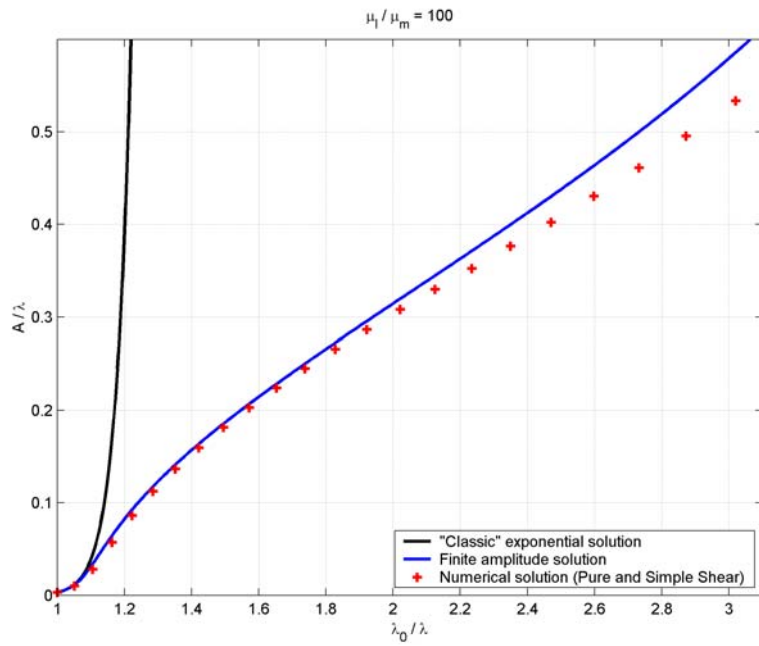


Figure 7

Wavelength and amplitude measurement for comparison with finite amplitude theory.



a)



b)

Figure 8

Comparison of combined pure & simple shear experiments to the exponential solution and to the finite amplitude solution of Schmalholz & Podladchikov.

a) Viscosity contrast 50:1

b) Viscosity contrast 100:1

The direct comparison of the numerical runs to the theory is shown in Figure 8. Both experiments show excellent agreement with the finite amplitude theory. In contrast and as shown by Schmalholz and Podladchikov (2000) the infinitesimal, exponential solution is only valid for small amounts of shortening. The applicability of the finite amplitude theory serves as the basis for the strain and competence contrast estimation method developed by Schmalholz and Podladchikov (2001), which allows to deduce the competence contrast and the strain accommodated by a fold by means of two simple geometrical parameters: the amplitude to wavelength ratio and the layer thickness to wavelength ratio. We can therefore conclude that the strain and competence contrast estimation method is also applicable to asymmetric folds, which was uncertain before.

The remaining key unknown in the field is the amount of accommodated bulk shear strain, which is due to the simple shear component of the flow. Combining the values that the strain map yields and fold asymmetry it is possible to determine the shear strain. The method of measuring the fold asymmetry (A) is depicted in Figure 9. The corresponding mathematical expression to quantify the asymmetry is

$$Asymmetry = \frac{BackLimb}{ForeLimb} - 1 \quad (11)$$

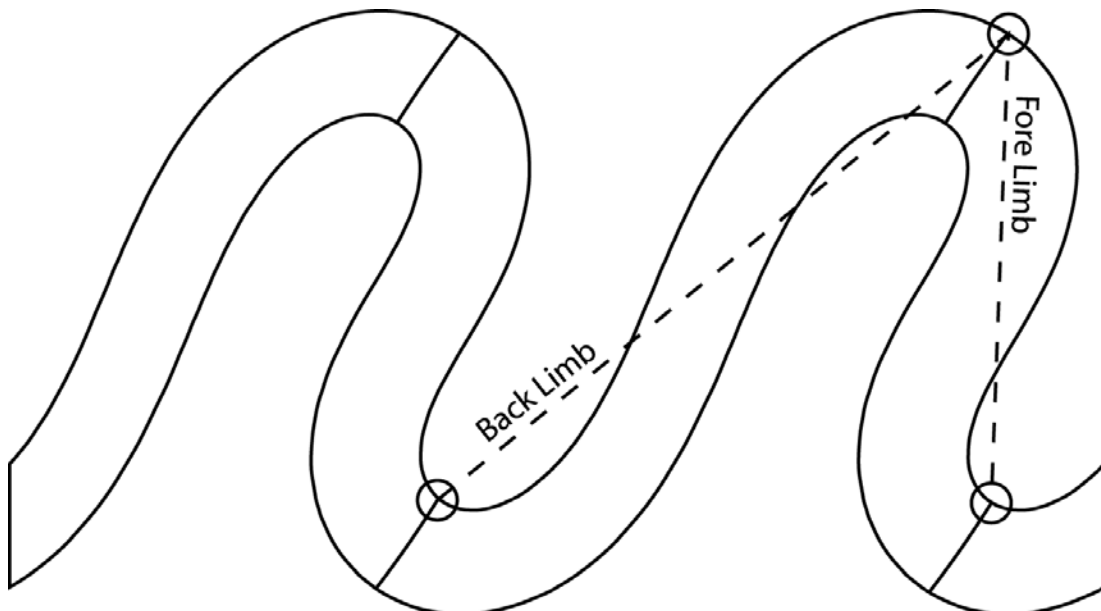


Figure 9
Fold asymmetry measurement method.

The results from the two experiments performed are depicted in Figure 10. Interestingly the two measured data lines almost collapse, although their viscosity contrasts differ by a factor two. The use of Figure 10 is to determine overall simple shear component. Given a natural fold, the strain map can be used to estimate the accommodated shortening and the viscosity contrast. This information together with the asymmetry data allows to deduce the shear strain, as explained with one example in Figure 10. Due to the character of the curve always two values are possible. The larger value is related to the approaching of the neighboring folds and therefore associated with large shortening strains. Therefore it is possible resolve this ambiguity.

The shear strain plot presented in Figure 10 is only based on two experiments. In order to develop it into a useful tool, a systematic investigation of viscosity contrasts and pure to simple shear rate ratios is needed. Additionally it should be verified how different rheologies, such as power-law and viscoelasticity influence the results.

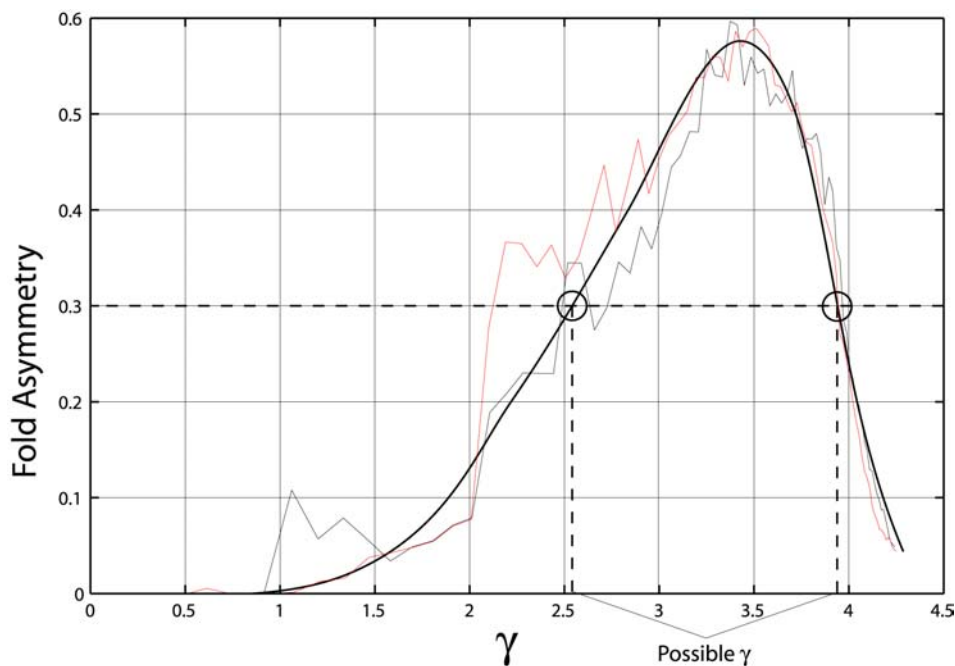


Figure 10

First version of a shear strain map. Thick line is fitted, thin lines are from the two simple shear experiments. The dashed line shows how a measured fold asymmetry value can be used to infer possible shear strain amounts. (The noise in the two original signals stems from using a somewhat crude method to determine the second derivative, which represents the curvature and is needed to identify the hinge.)

EFFECTIVE SHEAR STRAIN RATE AND LONGITUDINAL STRAIN

Both, maximum shear strain rate and longitudinal strain differ significantly from the pure shear only case. The main reason is that, from the start, the undisturbed matrix shows five fold higher effective strain rates (according to our setup of simple to pure shear ratio). This largely overprints the fold development. Consequently, the recorded strains are much larger in the matrix. As a result, extension starts within the matrix, not the outer hinge, and at much smaller shortenings than required in pure shear only experiments. With increasing strain the field of extension enlarges and progressively incorporates parts of the layer, firstly the outer hinge. Soon afterwards the entire back limb is in extension. It must be noted that for folds in general shear the use of longitudinal strain of originally horizontal lines is only sub-optimal. In pure shear only it is to be expected that one of the principal axes of the strain ellipsoid follows the deformation of originally horizontal lines. This is unlikely to be the case for folding in general shear. Therefore the applied method may fail to capture any maximum or minimum extension at a point.

EFFECTIVE SHEAR STRESS AND PRESSURE

In the initial phase of pure shear dominance and strong amplification, both, maximum shear stress and pressure are almost identical to the pure shear only case. With progressive asymmetry of the fold geometry the two parameters deviate from the pure shear only case. However, the general characteristics of where minima and maxima occur and how large their amplitudes are, are overall preserved.

CONCLUSIONS

We provide with this work key examples of single layer fold development up to very high amplitude stages. The chief kinematic and dynamic parameters are analyzed and should be used for tuning the classical, geometry or kinematics, based methods. We have focused on the developed of asymmetric folds and analyzed how the asymmetry

influences the fold development. We demonstrated that combinations of pure and simple shear lead to asymmetric folds if the appropriate set of boundary conditions is used. However, the asymmetry does not grow as an instability but is mainly a kinematic effect that becomes possible at relatively large amplitude stages, where the active fold amplification decays. Consequently, parameters such as effective stress and pressure deviate in general shear only slightly from the pure shear case. This explains why first order analytical theories that are strictly valid only for the initial stages are not sensitive to the layer parallel simple shear component and is in agreement with the argumentation outlined by Johnson and Fletcher (1994). We show that the vergence of the folds and the limb thickness ratios can be used as shear sense indicators. Opposite senses of fold vergence reported by Reches and Johnson (1976) are related to multilayers and restricted to kinking. Argumentations put forward by Krabbendam and Leslie (1996) are related to purely passive deformation of already existing folds and are only relevant if several deformation phases can be identified.

An advantageous consequence of the passive nature of the fold asymmetry development is that the pure shear based finite amplitude theory and the strain map developed by Schmalholz and Podladchikov (2000; 2001) is applicable to asymmetric folds. Since the strain map yields the competence contrast and the amount of layer parallel shortening, the only undetermined parameter is the shear strain. Based on the few experiments available we have shown that it is possible to use the fold asymmetry to infer the bulk shear strain. However, a systematic study of competence contrast and simple shear to pure shear ratios is needed to develop a complete shear strain map. The combination of such a shear strain map with the aforementioned strain map will result in a major tool for field geology, because for the first time strain reconstructions could be performed with simple geometrical parameters, but based on a solid continuum mechanistic foundation.

REFERENCES

- Abbassi, M.R. and Mancktelow, N.S., 1992. Single layer buckle folding in non-linear materials-I: Experimental study of fold development from an isolated initial perturbation. *Jou. Struct. Geol.*, 14(1): 85-104.
- Anthony, M. and Wickham, J., 1978. Finite-element simulation of asymmetric folding. *Tectonophysics*, 47(1-2): 1-14.
- Bell, A.M., 1981. Vergence - an Evaluation. *Journal of Structural Geology*, 3(3): 197-202.
- Biot, M.A., 1961. Theory of Folding of Stratified Viscoelastic Media and Its Implications in Tectonics and Orogenesis. *Geological Society of America Bulletin*, 72(11): 1595-1620.
- Canuto, C., Hussaini, M.Y., Quarteroni, A. and Zang, T.A., 1988. *Spectral Methods in Fluid Dynamics*. Springer series in computational physics. Springer, Berlin Heidelberg.
- Chapple, W.M., 1968. A mathematical theory of finite-amplitude rock-folding. *Geol.Soc.Am.Bull.*, 79: 47-68.
- Cobbold, P.R., 1975. Fold propagation in single embedded layers. *Tectonophysics*, 27: 333-351.
- Cobbold, P.R., 1976. Fold shapes as functions of progressive strain. *Phil. Trans. R. Soc. London*, A283(129-138).
- Dieterich, J.H., 1970. Computer experiments on mechanics of finite amplitude folds. *Can. J. Earth Sciences*(7): 467-476.
- Ghosh, S.K., 1966. Experimental tests of buckling folds in relation to strain ellipsoid in simple shear deformations. *Tectonophysics*, 3: 169-185.
- Hudleston, P.J. and Lan, L., 1994. Rheological controls on the shape of single-layer folds. *J. Struct. Geol.*, 16(7): 1007-1021.
- Johnson, A.M. and Fletcher, R.C., 1994. *Folding of viscous layers*. Columbia University Press, New York.
- Krabbendam, M. and Leslie, A.G., 1996. Folds with vergence opposite to the sense of shear. *Journal of Structural Geology*, 18(6): 777-781.
- Mancktelow, N.S., 1999. Finite-element modelling of single-layer folding in elasto-viscous materials: the effect of initial perturbation geometry. *J. Struct. Geol.*, 21(2): 161-177.
- Manz, R. and Wickham, J., 1978. Experimental analysis of folding in simple shear. *Tectonophysics*, 44: 79-90.
- Mase, G.E., 1970. *Continuum Mechanics*. Schaum's Outline Series. McGraw-Hill, New York.
- Pfaff, V.J. and Johnson, A.M., 1989. Opposite Senses of Fold Asymmetry. *Engineering Geology*, 27(1-4): 3-38.
- Price, N.J. and Cosgrove, J.W., 1990. *Analysis of Geological Structures*. Cambridge University Press, Cambridge.
- Ramberg, H., 1961. Contact strain and folding instability of a multilayered body under compression. *Geol. Rdsch.*, 51: 405-439.
- Ramberg, H., 1963. Fluid dynamics of viscous buckling applicable to folding of layered rocks. *Bull. Am. Ass. Petr. Geol.*, 47(3): 484-505.
- Ramsay, J.G., 1967. *Folding and fracturing of rocks*. International series in the earth and planetary sciences. McGraw-Hill, New York, 568 pp.
- Ramsay, J.G., 1974. Development of Chevron Folds. *Geological Society of America Bulletin*, 85(11): 1741-1754.
- Ramsay, J.G. and Huber, M.I., 1983. *Strain analysis*. Academic Press, London, 307 pp.
- Ramsay, J.G. and Huber, M.I., 1987. *Folds and fractures*. Academic Press, London, XI, [392] 1987. pp.
- Ranalli, G., 1995. *Rheology of the Earth*. Chapman & Hall, London [etc.], 413 pp.
- Reches, Z. and Johnson, A.M., 1976. Theory of Concentric, Kink and Sinusoidal Folding and of Monoclinial Flexuring of Compressible, Elastic Multilayers .6. Asymmetric Folding and Monoclinial Kinking. *Tectonophysics*, 35(4): 295-334.
- Schmalholz, S.M. and Podladchikov, Y., 1999. Buckling versus folding: Importance of viscoelasticity. *Geophysical Research Letters*, 26(17): 2641-2644.

- Schmalholz, S.M. and Podladchikov, Y.Y., 2000. Finite amplitude folding: transition from exponential to layer length controlled growth (vol 179, pg 363, 2000). *Earth and Planetary Science Letters*, 181(4): 619-633.
- Schmalholz, S.M. and Podladchikov, Y.Y., 2001. Strain and competence contrast estimation from fold shape. *Tectonophysics*, 340(3-4): 195-213.
- Schmalholz, S.M., Podladchikov, Y.Y. and Schmid, D.W., 2001. A spectral/finite difference method for simulating large deformations of heterogeneous, viscoelastic materials. *Geophys. J. Int.*, In press.
- Sherwin, J.A. and Chapple, W.M., 1968. Wavelengths of Single Layer Folds - a Comparison between Theory and Observation. *American Journal of Science*, 266(3): 167-179.
- Smith, R.B., 1975. Unified Theory of Onset of Folding, Boudinage, and Mullion Structure. *Geological Society of America Bulletin*, 86(11): 1601-1609.
- Treagus, S.H., 1973. Buckling Stability of a Viscous Single-Layer System, Oblique to Principal Compression. *Tectonophysics*, 19(3): 271-289.
- Twiss, R.J. and Moores, E.M., 1992. *Structural Geology*. W. H. Freeman and Company, New York.
- Zhang, Y., Hobbs, B.E. and Ord, A., 1996. Computer simulation of single-layer buckling. *J. Struct. Geol.*, 18(5): 643-655.

CHAPTER 8: MULTILAYER FOLDING

“It is apparent, however, that the theory of folding of single layers tells us almost nothing about most folds, which are in rocks consisting of many, interlayered, stiff and soft beds, that is, consisting of multilayers”. (Johnson and Ellen, 1974)

“Certain classical fold forms, such as kink and box folds, are conspicuously absent in the multilayers analyzed in this paper” (Johnson and Pfaff, 1989)

ABSTRACT

Multilayer folding is the dominant folding mode in nature, but due to the overwhelming possible parameters space many questions concerning the folding of multilayers are not answered from theoretical and practical viewpoints. For example it is not clear if there is a distinct multilayer folding mode at all or if there is just a smooth transition from welded, effective single layer to real single layer folding. We show analytically that such a folding mode exists and explain why it dominates the folding in natural rocks. Another question that we address is the formation of kink bands. Explicitly resolving the basic characteristics of a relatively simple model configuration with a numerical code we show that kinking is a dominating mechanism in the folding of simple multilayered Newtonian fluids subjected to general shear in the proximity of a no-slip base. This renders anisotropic, non-linear, and elasto-plastic rheologies unnecessary and consequently changes the way process controlling mechanisms are deciphered from natural folds.

INTRODUCTION

The first citation at the beginning of this chapter stems from Johnson and Ellen (1974), which was the first of an entire series of papers about folding that resulted in Johnson's book "Styles of Folding" (1977). Indeed, given the abundance of folds in multilayered strata compared to the rare occasion that one actually discovers a single layer fold in nature, it seems unjustified that single layer folding attracted so much attention. However, it is obvious that due to their geometrical simplicity single layer folds are the easiest to tackle by means of analogue, numerical and analytical modeling. Furthermore, single layer folding may be taken as a special case of multilayer folding, which, due to its easy accessibility, can serve as the fundament of multilayer folding theories. The majority of analytical studies for multilayer folding are based on the thick-plate formulation (Ramberg, 1963; Ramberg, 1970; Johnson and Pfaff, 1989; Cruikshank and Johnson, 1993). The thick-plate assumption has the advantage, over the thin-plate (Biot, 1961), that layer deformation and interaction are automatically taken care of, and various boundary conditions can be introduced (e.g., Schmalholz et al., 2002). This may be the reason why no systematic analysis of the most simple multilayer case exists: only two different materials, competent layers and weaker matrix, embedded in two infinite matrix half-spaces and subjected to layer parallel pure shear. What are the dominant wavelengths and maximum growth rates for such a system? How do they depend on layer-interlayer spacing, viscosity contrast, and number of layers?

The second citation is from Johnson and Pfaff (1989) and points out some of the symptomatics of previous multilayer folding research. Kink folds or box folds are common in natural multilayers, but can only be reproduced in experiments if anisotropic (Cobbold et al., 1971) or/and non-linear (Latham, 1985) materials are used. Theoretical considerations conclude that conventional materials cannot be used to model kinking and Cosserat continua (Adhikary et al., 1999) or other special formulations (Hunt et al., 2000) must be introduced. Common to these formulations is that, instead of modeling the layers explicitly, it is assumed that they can be treated as a homogenous, anisotropic material. This goes back to Biot (1965) who employed the same method when he originally investigated the development of *internal instabilities* in the folding in a multilayer stack. The question, which we ask here, is if all this complexity is really

necessary? Maybe a much simpler setup, such as simple multilayered Newtonian fluids subjected to general shear, can also develop kinks?

In order to answer the raised first order questions, we must use adequate tools. Due to the geometrical non-linearity of the studied system and the fact that folding is a finite strain phenomenon, only a combination of analytics and numerics, that incorporates the entire non-linear interaction, can tackle the problem. Following previous work we apply the thick plate theory to analytically investigate the folding of the *simple* multilayer stack. The reason for this is that the thin-plate theories generally do not incorporate the to be expected shear deformations. More general effective thin-plate approaches require a priori knowledge of the morphology of the multilayer response, i.e., welded multilayer folding can be handled by the “leaf spring model” (McNutt et al., 1988; Burov and Diament, 1995). The purpose of this paper is to establish the morphological multilayer folding modes in a wide parameter range. Therefore it is preferable to apply a thick-plate theory for infinitesimal stages and numerical simulations of the complete Stokes equations for the non-linear finite amplitude stages.



Figure 1
Folding in multilayer stacks, Almugraf, Portugal.

METHODS

Both methods that we use are described elsewhere and therefore not documented in detail here. The linear stability analysis performed with the thick-plate approximation is explained in Johnson and Pfaff (1989). The numerical code used for the finite amplitude behavior under general shear is a descendant of a previous code that is documented in Schmalholz et al. (2001). It is based on a mixed finite difference/spectral formulation, whereby in the direction orthogonal to the layer a finite difference scheme is used and in the layer parallel direction a spectral expansion is employed that makes use of the lateral periodicity, which is intrinsic to the problem. This new code version has several improvements implemented. While the transformation of the input signal to the frequency space is still based on an analytical Fourier transform, the necessary convolutions for the signal multiplication in frequency space are now based on Fast Fourier Transforms (Cooley and Tukey, 1965) which increases the performance significantly. In addition, a full cosine and sine signal implementation is used now, that allows to study combined effects of pure and simple shear. Therefore the bandwidth had to be increased because the system only converges if a complex conjugate system is formed that contemporaneously solves for the $+k$ -th and the $-k$ -th harmonic. The implementation of the layer parallel simple shear uses a constant velocity boundary condition at the top and the bottom, which is different to the constant lateral shear strain rate (rigid wall) boundary conditions usually employed in analogue (e.g., Cobbold et al., 1971; Manz and Wickham, 1978) or numerical modeling (Anthony and Wickham, 1978). This avoids strong boundary effects that are disturbing the analysis of the model. The combination of constant pure shear rate and constant simple shear stress boundary conditions results in a set of velocity boundary conditions that are shown in Figure 2.

The materials used here are simple Newtonian fluids in the absence of gravity. This does not mean that the results are not applicable to large-scale tectonics. Schmalholz et al. (2002) have derived the conditions for which gravity is important and have shown for several large-scale tectonic examples that gravity had no controlling influence on the folding process.

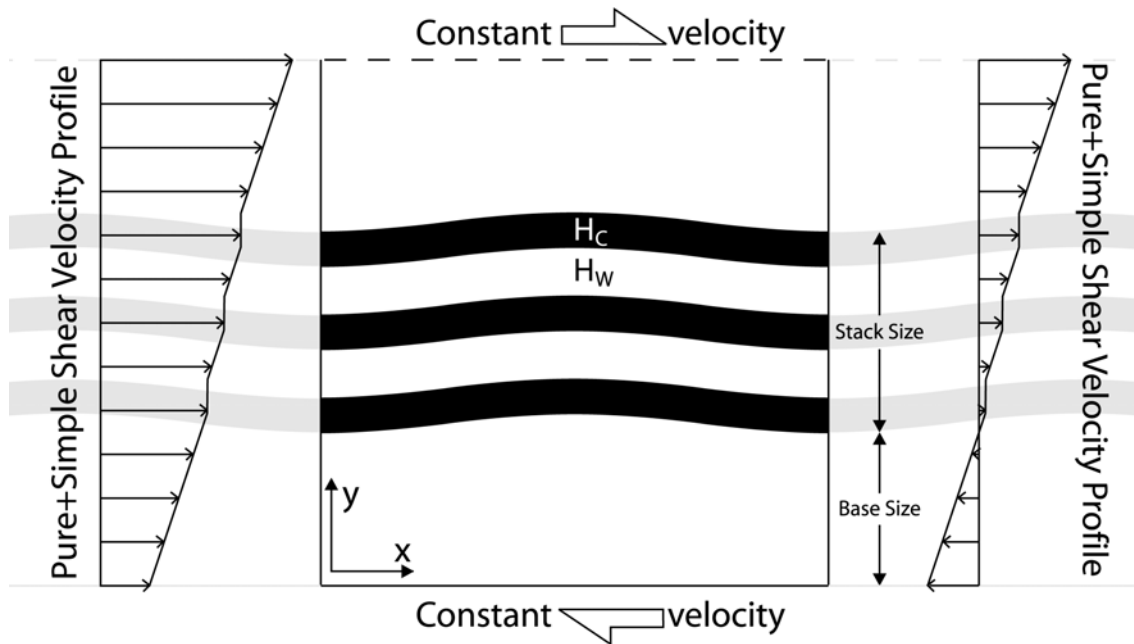


Figure 2

Multilayer setup: a number of layers are subjected to combined layer parallel pure and simple shear. In the horizontal direction periodicity is assumed. The thick-plate analysis assumes an infinite half space above and below the layer stack. In the numerical model the layer stack can be close to a no-slip base. The thickness of the competent (black) layer is H_C , the thickness of the weak interlayer is H_W . In the thick-plate experiments the amplitude of the initial perturbation is determined by the eigenvalue analysis, in the numerical experiments the layers were individually perturbed with a random red noise with amplitude $H_C/50$.

THICK PLATE LINEAR STABILITY ANALYSIS

The basic equations for the thick plate analysis result in a complex system that must be analyzed with eigenvalue analysis in order to determine dominant wavelength and growth rate of the multilayer stack (Ramberg, 1970). If we take Figure 2 as an example and specify the viscosity contrast, the eigenvalue analysis will yield an eigenvalue and a set of eigenvectors. The eigenvectors determine the relative amplitudes, with which the interfaces must be perturbed so that the stack amplifies fastest, for the given wavelength. The growth rate is determined by the eigenvalue. To determine the maximum possible growth rate an eigenvalue analysis must be performed for the all possible wavelengths. As pointed out in the introduction single layer folding is an end-member case of multilayer folding. The expected result of the linear stability analysis is depicted in Figure 3. If the individual layers are very close to each other, the effect of the weak interlayer will become negligible and the stack will fold as an effective single layer. On the other hand if the individual layers are too far apart then no interaction takes place anymore and the individual layer behaves as a normal single layer. It can be expected that the distance where the mutual layer influence becomes negligible is about one dominant wavelength, as determined by Ramberg (1961) with his contact strain theory. The interesting region of layer-interlayer thickness ratio (H_C/H_W) is in-between this two end member cases. Is there a smooth transition from one limit to the other, or is there a third folding mode?

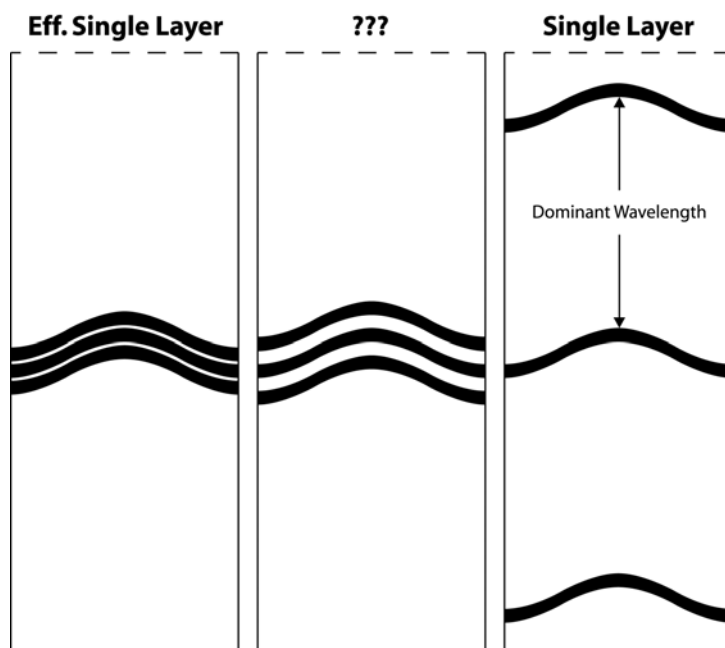


Figure 3
Expected result of linear
stability analysis (see text for
explanation).

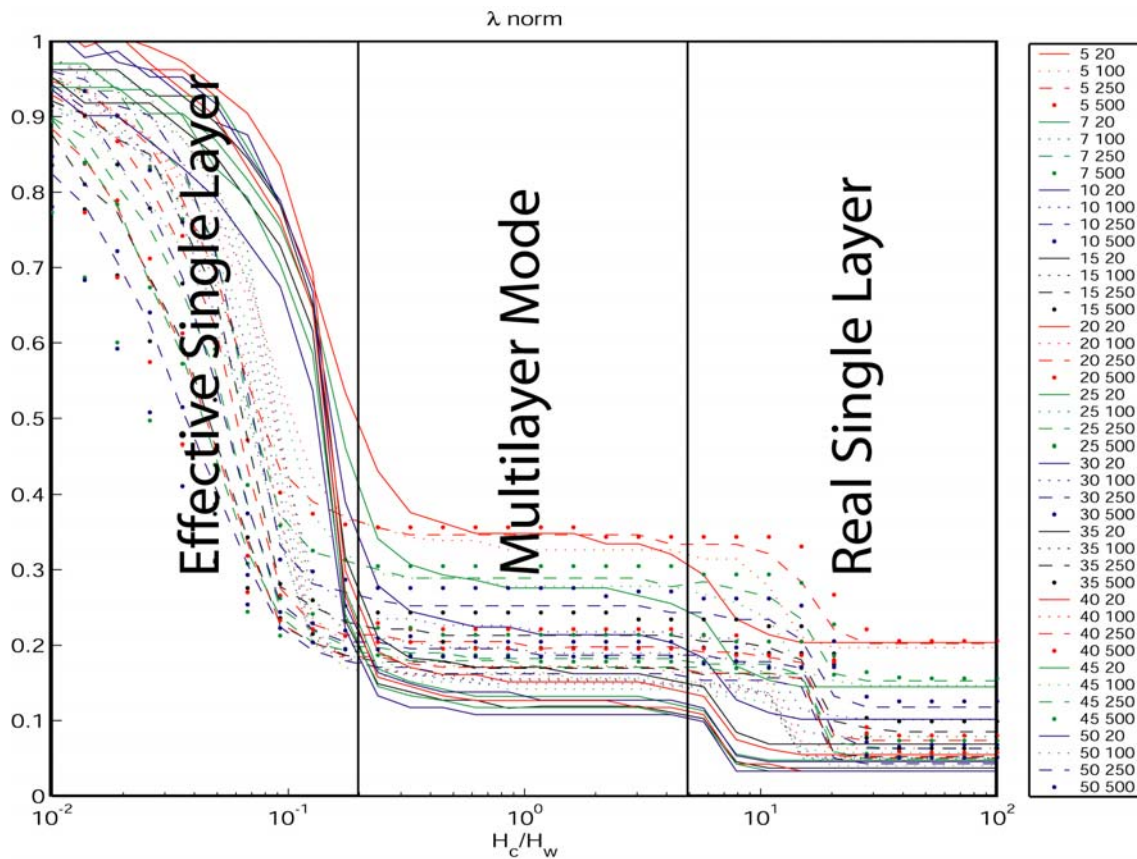


Figure 4

Normalized dominant wavelength versus layer-interlayer thickness ratio. Colors are related to number of layers, line styles to viscosity contrasts.

The answer, given in Figure 4, is clear: there is a third mode, which is a true multilayer mode. The dominant wavelengths are normalized by the dominant wavelength of the effective single layer. Naturally, the effective and the real single layer are related, but since the effective single layer is thicker than the individual (real) layer the normalized values go from 1 in the *effective single layer domain* (small H_c/H_w values) to smaller dominant wavelengths values in the *real single layer domain* (large H_c/H_w values). In-between this two there is a third plateau that is centered on $H_c/H_w = 1$, independently of viscosity contrasts and number of layers.

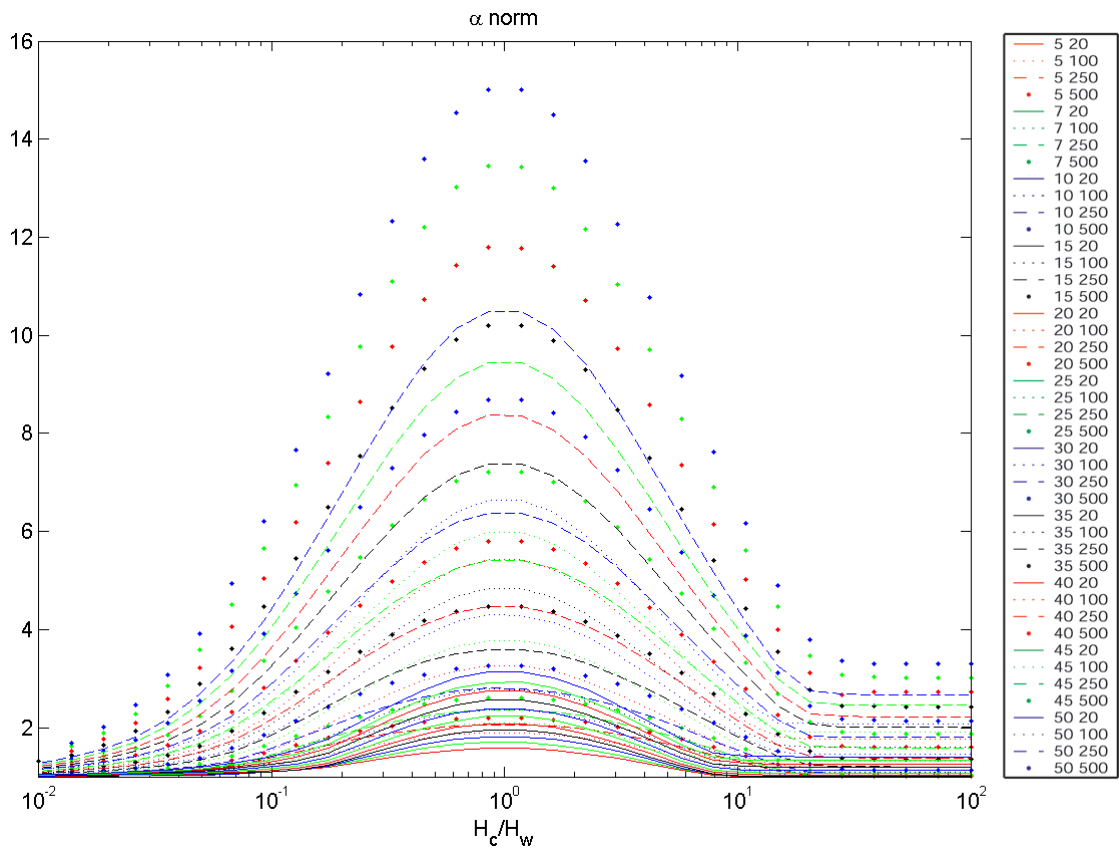


Figure 5

Normalized maximum growth rate versus layer-interlayer thickness ratio.

However, this third plateau is only of interest if the corresponding growth rates are significant compared to the background, kinematic shortening. The corresponding plot is shown in Figure 5. The normalization used is again the value of the effective single layer. It is clear that the effective single layer and the real single layer should have the same growth rates, which is reflected in the near one values in the two domains. The growth rates that correspond to the described third plateau are significantly larger than the single layer values. Thus, the third plateau represents an important folding mode.

The third folding mode is especially interesting because it has shorter dominant wavelength to thickness ratios than the effective single layer. This could be another explanation for the natural preference of small wavelength to thickness ratios which is in contradiction to the large viscosity contrast variations (Sherwin and Chapple, 1968).

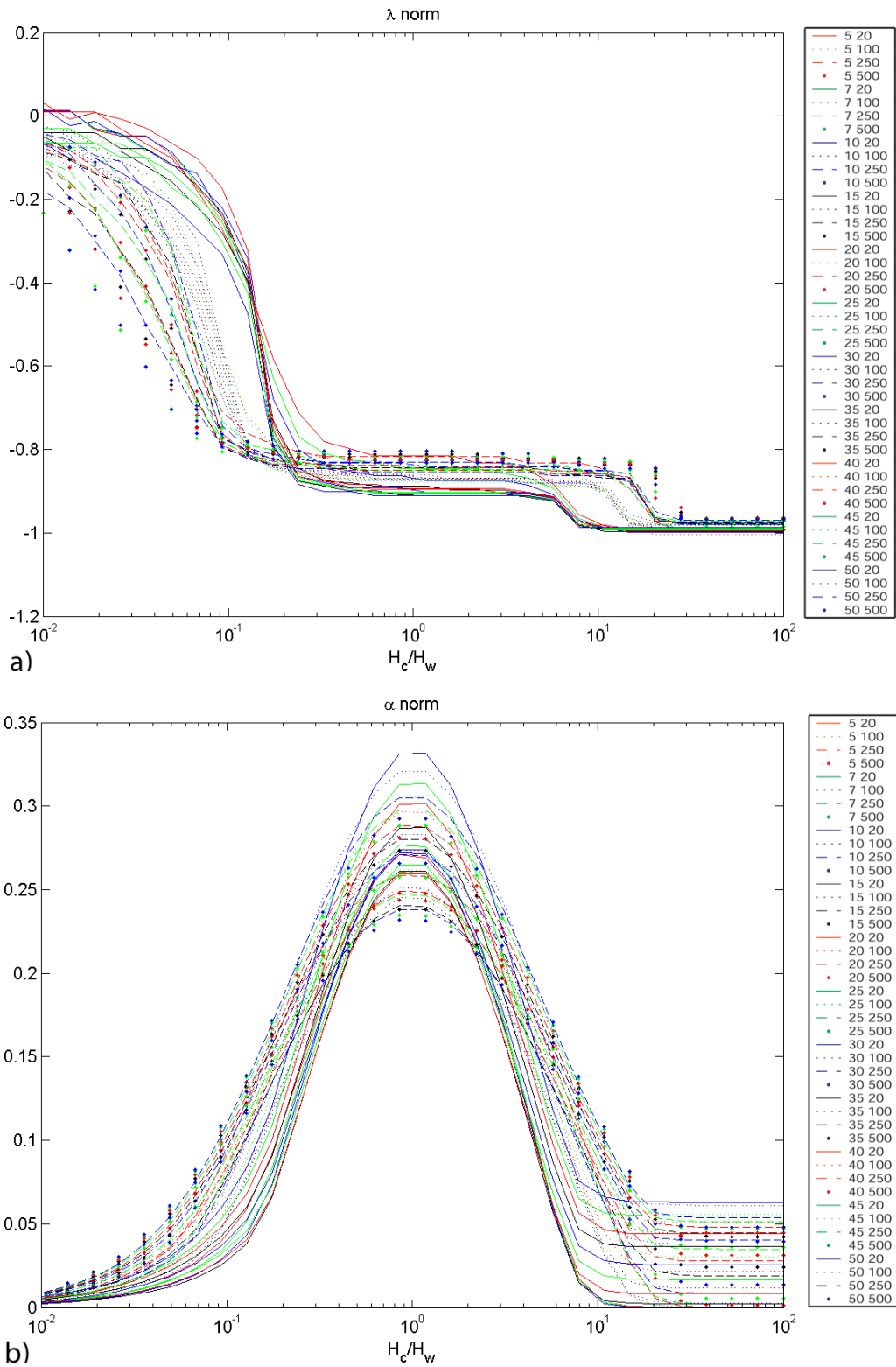


Figure 6

Improved normalization, which reduces the dependency on viscosity contrast and number of layers. a) Dominant wavelength b) Maximum growth rate.

The results in Figure 4 and Figure 5 are normalized by the corresponding value of the effective single layer. Although similar, the resulting curves differ significantly and it is preferable to develop an improved normalization that results in a single curve that is valid for the entire parameter range studied. If such a curve can be found the controlling parameters can be identified and the mechanism of the folding process can be better understood. The proposed normalizations for the maximum growth rate (α) and the dominant wavelength (λ) are:

$$\tilde{\alpha} = (\alpha - 1) \frac{\mu_c}{\mu_w} \exp\left(-\frac{\ln(n)}{2\pi}\right) \quad (1)$$

$$\tilde{\lambda} = \frac{(\lambda - 1)}{\left(\frac{n-1}{n}\right)} \quad (2)$$

where μ_c and μ_w are the viscosity of the competent and weak materials, respectively, and n is the number of layers.

The corresponding plots are given in Figure 6. These simple normalizations are reasonably effective in reducing the curve variability and can be used to derive an analytical expression for folding in the complex parameter space described here. For example the maximum growth rate common to all layer configurations is (Figure 6b) $\tilde{\alpha} \approx 1/4$. Therefore we can rearrange eqn. (1) to obtain the maximum growth rate expression that is valid for any number of layers in the entire range of viscosity contrasts:

$$\alpha = 1 + \frac{\mu_c}{4\mu_w} \exp\left(\frac{\ln(n)}{2\pi}\right) \quad (3)$$

For improved visualization of the effect of viscosity contrast we select two datasets, 5 and 50 competent layers, and plot $\tilde{\lambda}$ and $\tilde{\alpha}$ in the $H_c/H_w - \mu_c/\mu_w$ space (Figure 7). We can clearly identify the three different folding mode domains, which are separated by sharp transitions. Thus, the used normalizations reduce the complexity of the described multilayer folding to determining the straight lines that separate the three fields.

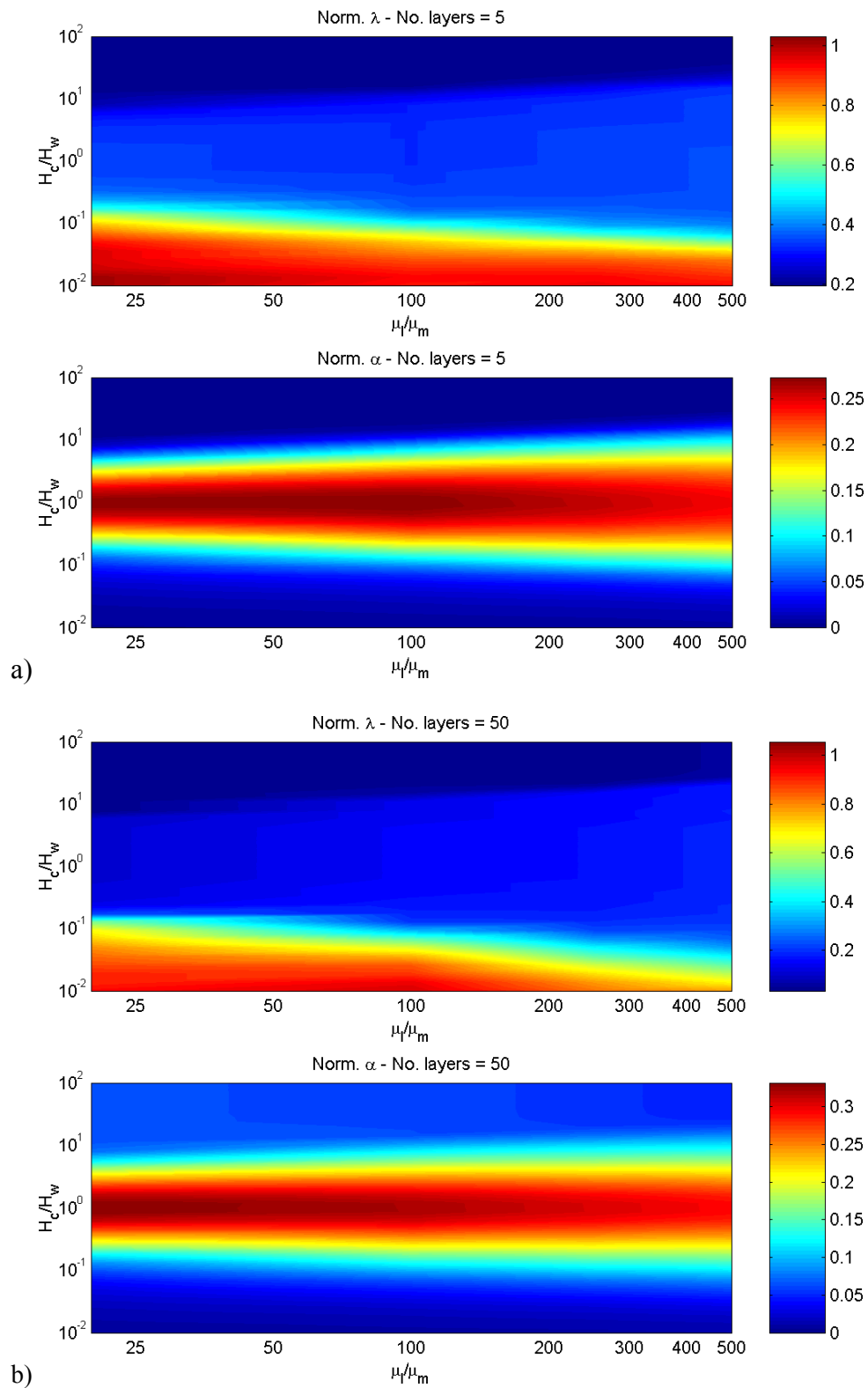


Figure 7

Visualization of the viscosity contrast effect in the $H_C / H_W - \mu_C / \mu_W$ space for 5 and 50 competent layers.

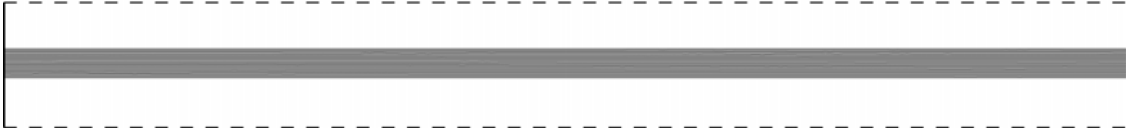
NUMERICAL ANALYSIS OF FINITE AMPLITUDE MORPHOLOGY

To study the finite amplitude fold morphology we applied the described finite difference/spectral code. We present here a few specific cases, which allow us to generate the “Fold Morphology Table”. In all cases the viscosity contrast is 50:1 and 21 competent layers are modeled. The thickness ratio of competent to incompetent layers is always 2:1, which is in the region of the multilayer folding mode, described in the section “Thick Plate Linear Stability Analysis”. Therefore complex interaction is expected, which differs significantly from single layer folding. All layer interfaces were given an initial red noise perturbation with amplitude $H_C/50$. The red noise was generated by cumulating a pseudo random signal and subsequently removing the linear trend. Compared to the thick plate analysis two additional factors were analyzed: contemporaneous simple shear and the influence of a no-slip base. The far-field simple shear stresses in the matrix were set to tenfold the pure shear values. If present, the no-slip base is at the bottom of the box and its proximity is specified the h_b/h_s parameter, which is the ratio of the base size to the stack size (Figure 2). The numerical resolution used was 2000 finite difference points by 128 spectral harmonics. For each case several snapshots are given at different amounts of total shortening (ϵ_{xx}) and shear strain (γ). γ is defined as the total shear displaced divided by the original box height.

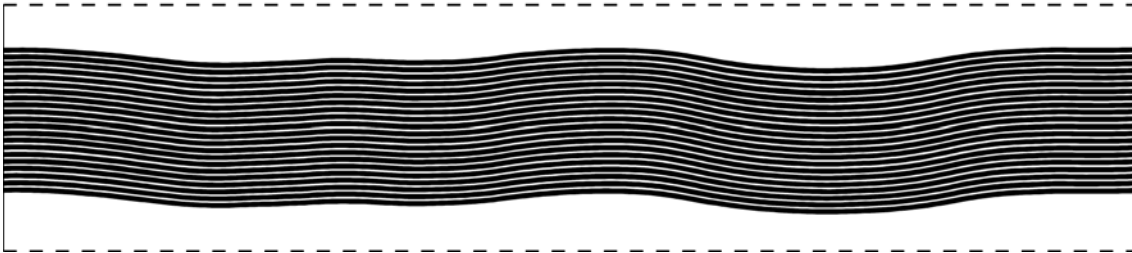
Multilayer folding in the absence of the base is not very different in pure shear only and combinations of pure and simple shear. An initial dominant wavelength is selected and amplified. However, before 50% shortening is achieved the exponential amplification decreases strongly and it becomes more favorable to fold the stack on a larger wavelength that can accommodate further strain. The development of fold asymmetry can also be attributed to these late stages. The progressive decrease of the stack to base distance leads to an increased sharpness of the finite amplitude folds. While the pure shear only experiments develop chevron like folds the general shear results in the formation of kink bands. Figure 10 shows an interesting phenomenon of this kink development. The presence of a no-slip base causes the fold asymmetry to grow with much smaller shortening strains. This early development prevents the accommodation of further strain because this would require stretching of the short limb. Therefore the fold “tries” to develop a second hinge in long limb that grows against the applied simple shear.

Case 1

a) Initial situation



b) $\varepsilon_{xx} = 44.3$, $\gamma = 0$



c) $\varepsilon_{xx} = 79.7$, $\gamma = 0$

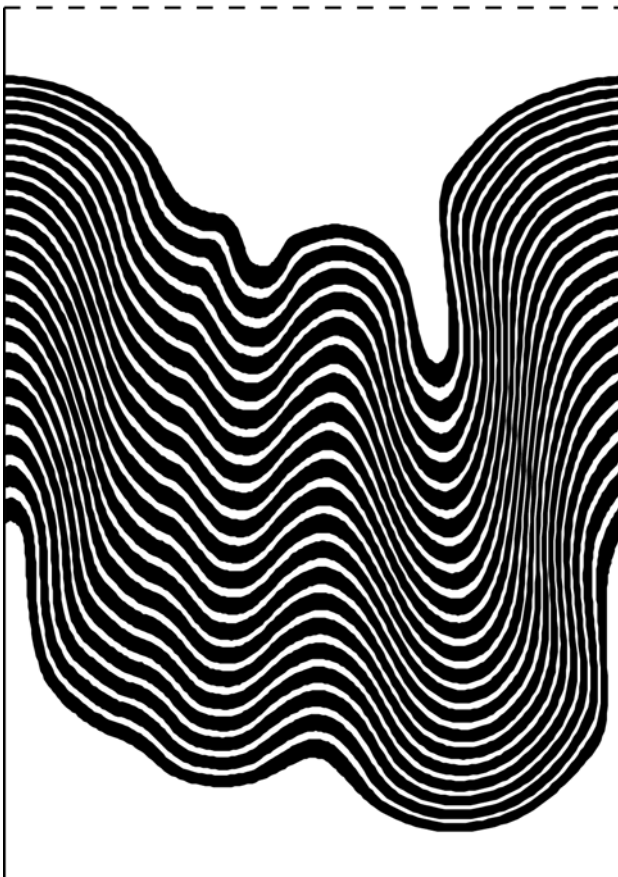


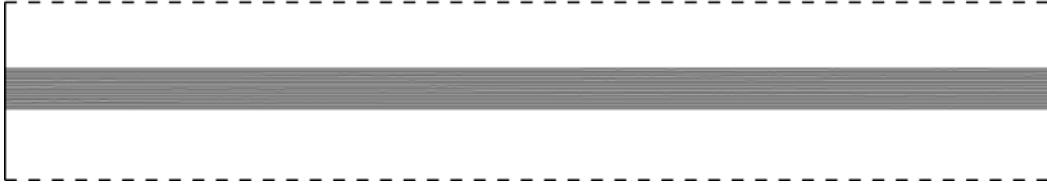
Figure 8

*Folding of a 21 layer stack
subjected to pure shear,
embedded in viscous half
spaces.*

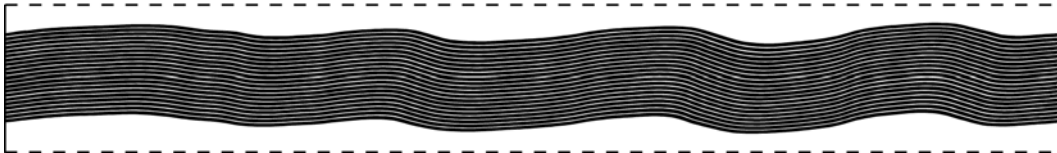
$$\mu_c / \mu_w = 50, h_c / h_w = 2$$

CASE 2

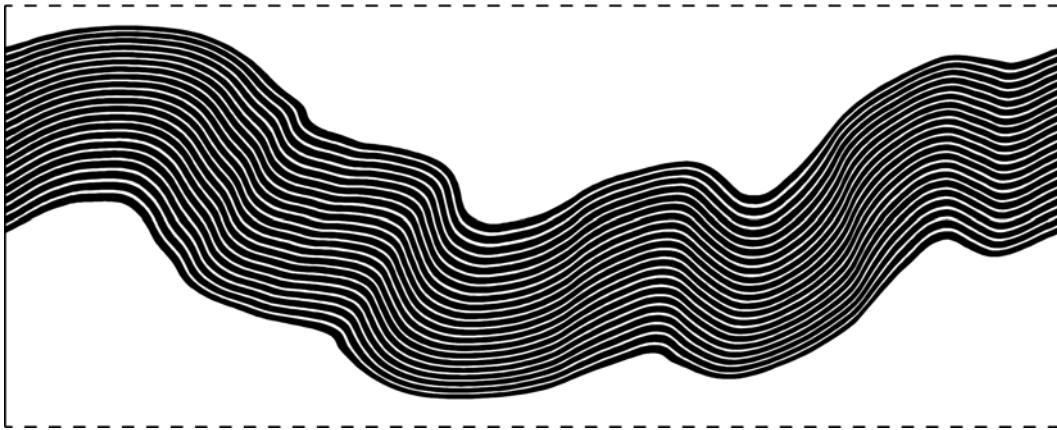
a) Initial situation



b) $\varepsilon_{xx} = 31.9, \gamma = 4.65$



c) $\varepsilon_{xx} = 54.5, \gamma = 6.69$



d) $\varepsilon_{xx} = 76.8, \gamma = 7.61$

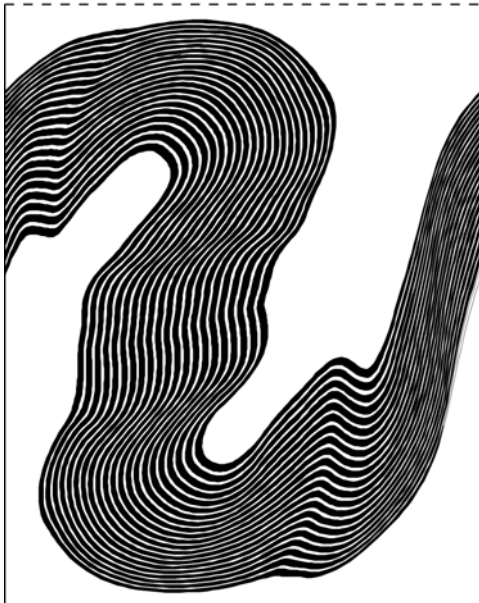


Figure 9

*Folding of a 21 layer stack
subjected to general shear,
embedded in viscous half
spaces.*

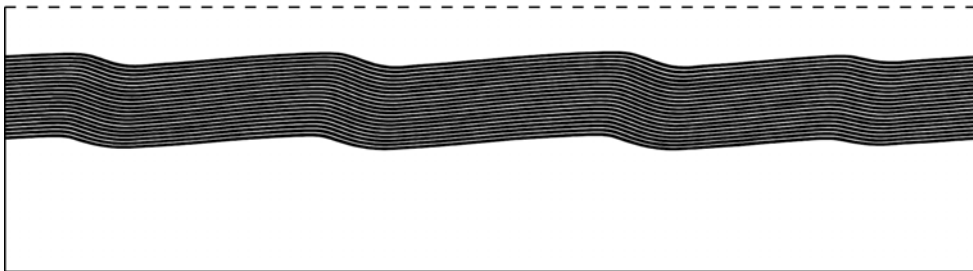
$$\mu_c / \mu_w = 50, h_c / h_w = 2$$

CASE 3

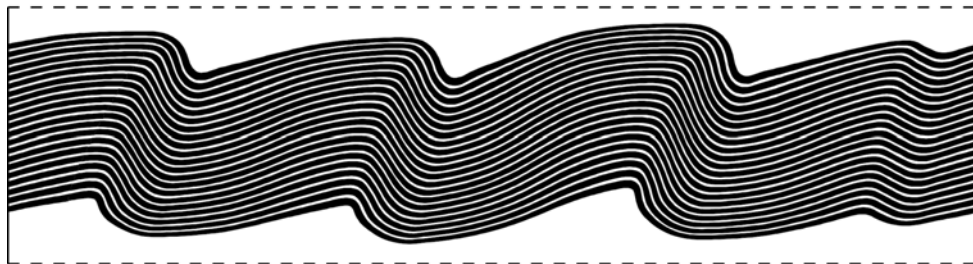
a) Initial Situation



b) $\varepsilon_{xx} = 32.7, \gamma = 4.8$



c) $\varepsilon_{xx} = 53.7, \gamma = 6.85$



d) $\varepsilon_{xx} = 71.4, \gamma = 7.98$

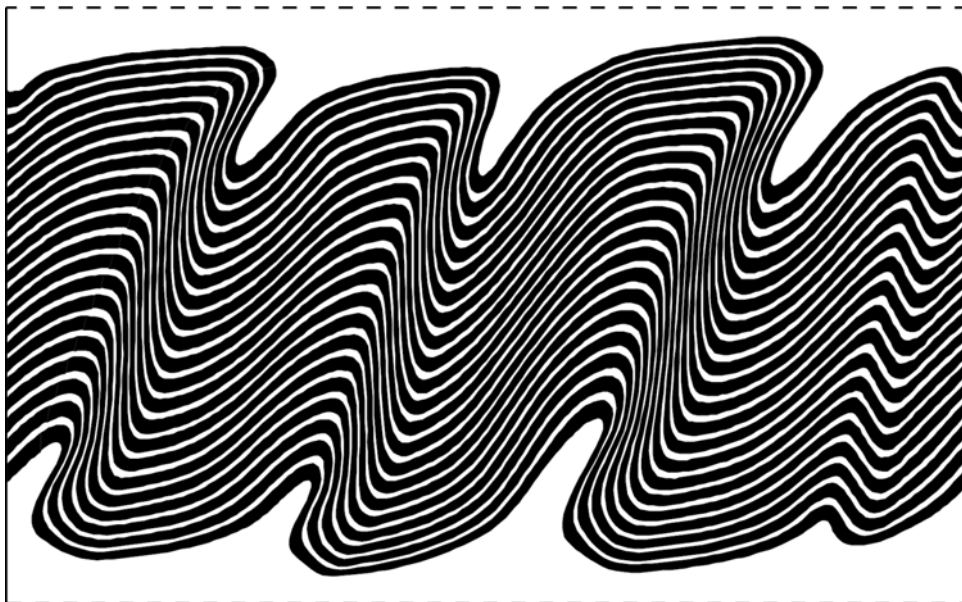


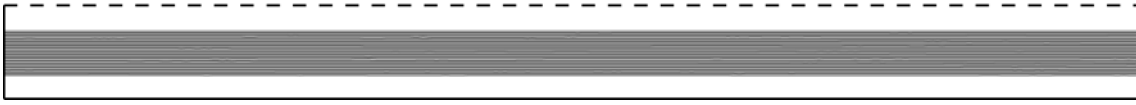
Figure 10

Folding of a 21 layer stack subjected to general shear with a no-slip base close.

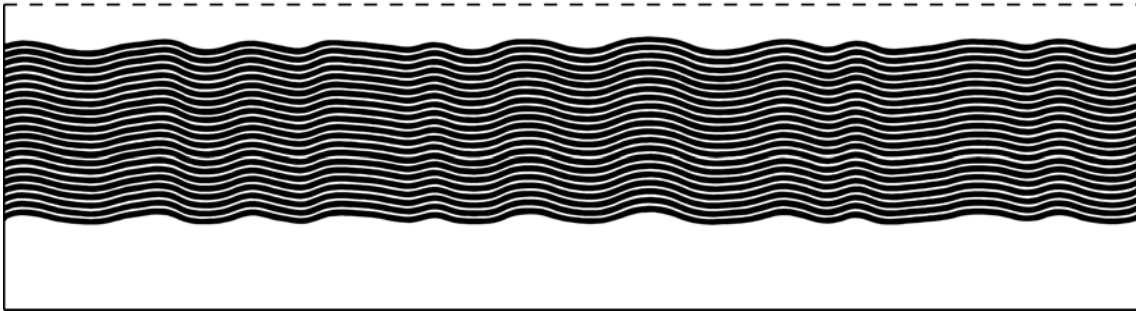
$$\mu_c / \mu_w = 50, h_c / h_w = 2, h_b / h_s = 3/2$$

CASE 4

a) Initial Situation



b) $\varepsilon_{xx} = 49.7, \gamma = 0$



c) $\varepsilon_{xx} = 79.7, \gamma = 0$

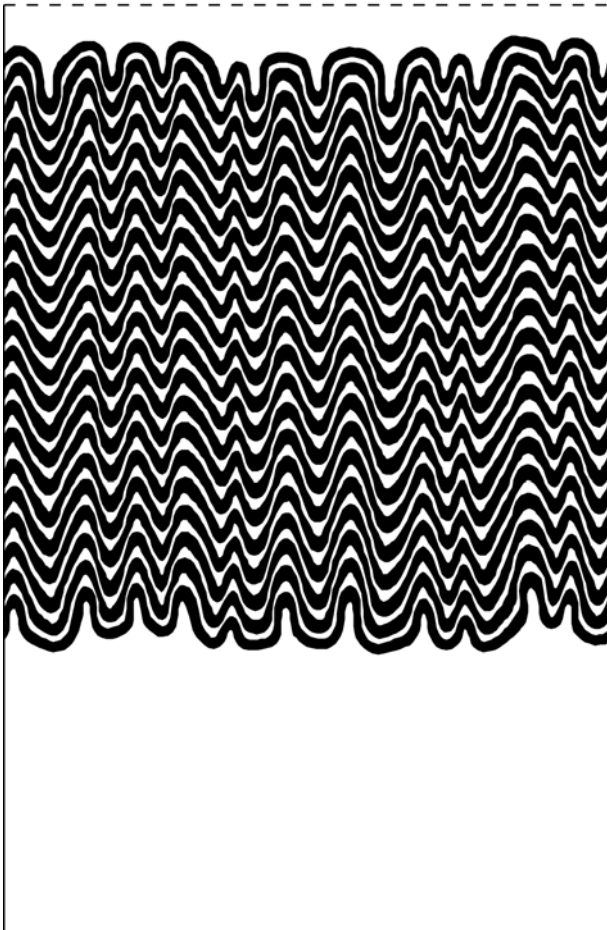


Figure 11

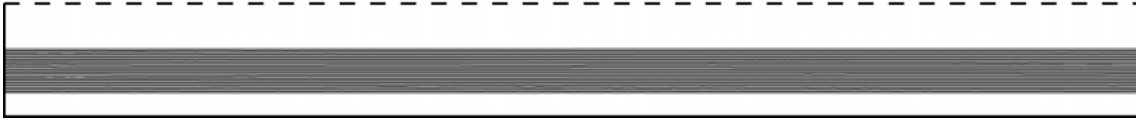
*Folding of a 21 layer stack
subjected to pure shear with a no-
slip base very close.*

$$\mu_c / \mu_w = 50, h_c / h_w = 2,$$

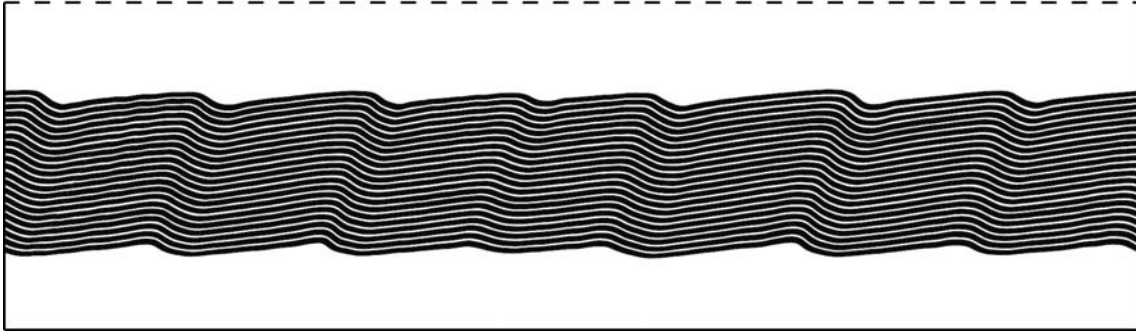
$$h_b / h_s = 1/2$$

CASE 5

a) Initial Situation



b) $\varepsilon_{xx} = 46.3, \gamma = 6.27$



c) $\varepsilon_{xx} = 57.9, \gamma = 7.22$

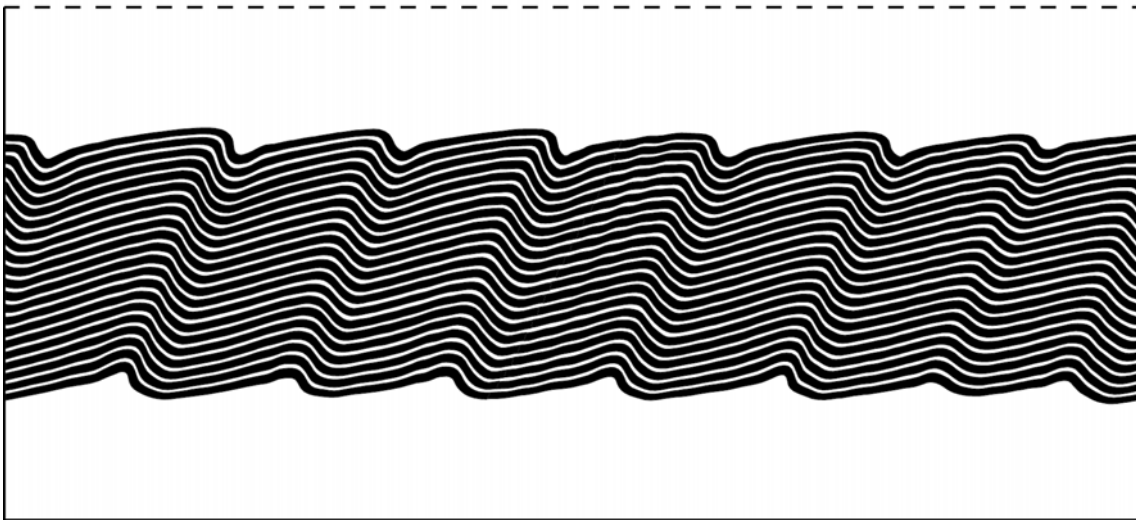
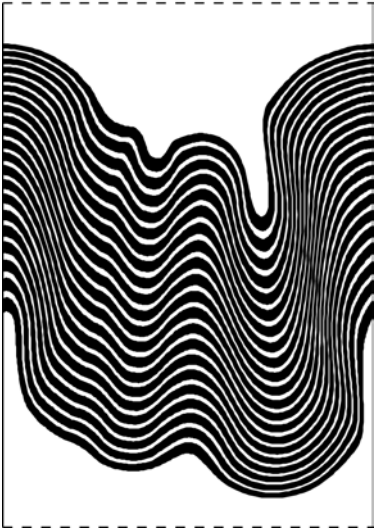

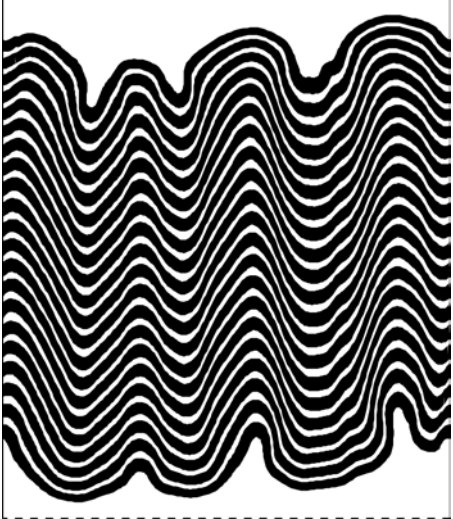
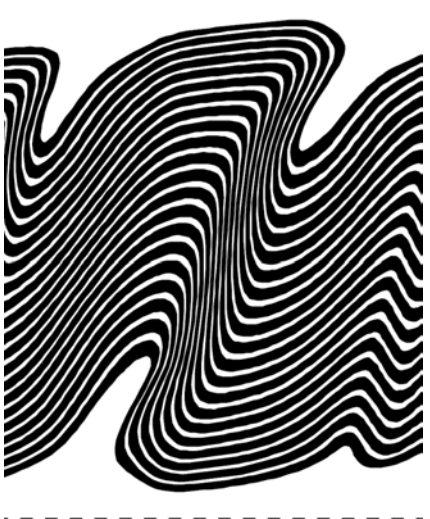
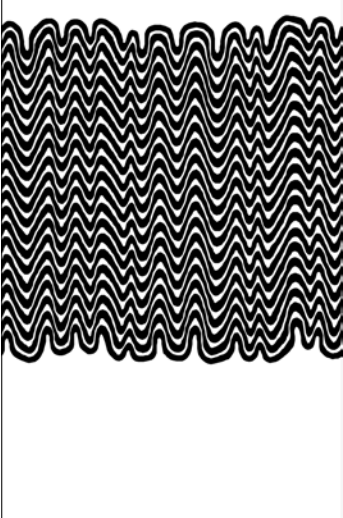
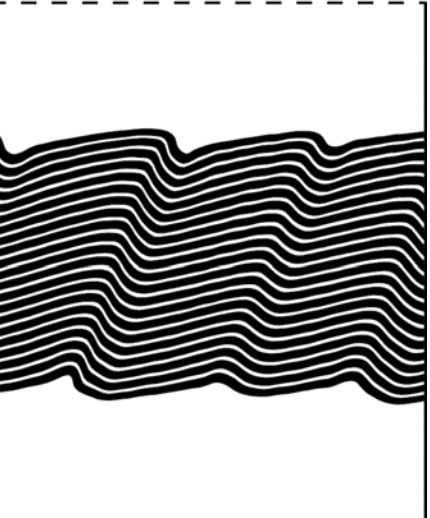


Figure 12

Folding of a 21 layer stack subjected to general shear with a no-slip base very close.

$$\mu_c / \mu_w = 50, h_c / h_w = 2, h_b / h_s = 1/2$$

FOLD MORPHOLOGY TABLE

	Pure Shear	General Shear
No Base		
Base / Stack = 3/2		
Base / Stack = 1/2		

DISCUSSION AND CONCLUSIONS

The key finding of our thick plate analysis is the identification of a distinct third folding mode that is a true multilayer mode. This mode occurs if the thickness ratio of competent to incompetent layer thickness is approximately 1:1, independently of the number of layers and the viscosity contrast. It exhibits growth rates that are significantly faster than single layer growth rates and may explain why single layer folding is rare in nature. In addition this mode exhibits small wavelength to stack thickness ratios, which agrees with natural observations.

Our study of finite amplitude multilayer folding is maybe the only existing example where a large number of layers with initial randomly perturbed interfaces are explicitly modeled with a fully dynamic code, as opposed to effective property approximations. The characteristic effect of the presence of a rigid base is to suppress the pure shear folding mode. Therefore, the multilayer stack in this situation becomes more sensitive to the contemporaneous simple shear and the kinking mode becomes the dominant and fold morphology determining process. However, the observed kinking is not the outcome of prescribed geometry but the true result of a relatively simple model configuration. We found that simple shear, the presence of a base, and the number of layers exert a chief influence on the kink formation. Additionally we demonstrate that kinking is possible if Newtonian rheology is used, rendering anisotropic, non-linear, and elasto-plastic rheologies as not necessary conditions for kinking. In other words: the observation of kinking in the field cannot be used as an indicator for low-grade / brittle conditions.

The results presented here establish the applicability ranges of previously developed single layer folding theories. Welded mode and independent mode both can be described as effective single layers. Similar and concentric folding modes are characterized by penetrative deformation. Transition to the kinking mode, facilitated by simple shear and the proximity to the base, exhibits a switch to strong strain partitioning and large, weakly deformed areas within the multilayer stacks. The quasi-rigid body behavior of these areas may be similar to the clast behavior in general shear or folding of the finite length competent layers, studied in the previous chapters. Detailed elaboration of this issue is the topic of ongoing studies outside the scope of this work.

REFERENCES

- Adhikary, D.P., Muhlhaus, H.B. and Dyskin, A.V., 1999. Modelling the large deformations in stratified media - the Cosserat continuum approach. *Mechanics of Cohesive-Frictional Materials*, 4(3): 195-213.
- Anthony, M. and Wickham, J., 1978. Finite-element simulation of asymmetric folding. *Tectonophysics*, 47(1-2): 1-14.
- Biot, M.A., 1961. Theory of Folding of Stratified Viscoelastic Media and Its Implications in Tectonics and Orogenesis. *Geological Society of America Bulletin*, 72(11): 1595-1620.
- Biot, M.A., 1965. *Mechanics of Incremental Deformations*. John Wiley & Sons, Inc., New York.
- Burov, E.B. and Diament, M., 1995. The Effective Elastic Thickness (T-E) of Continental Lithosphere - What Does It Really Mean. *Journal of Geophysical Research-Solid Earth*, 100(B3): 3905-3927.
- Cobbold, P.R., Cosgrove, J.W. and Summers, J.M., 1971. Development of Internal Structures in Deformed Anisotropic Rocks. *Tectonophysics*, 12(1): 23-&.
- Cooley, J.W. and Tukey, J.W., 1965. An Algorithm for Machine Calculation of Complex Fourier Series. *Mathematics of Computation*, 19(90): 297-&.
- Cruikshank, K.M. and Johnson, A.M., 1993. High-Amplitude Folding of Linear-Viscous Multilayers. *Journal of Structural Geology*, 15(1): 79-94.
- Hunt, G.W., Peletier, M.A. and Wadee, M.A., 2000. The Maxwell stability criterion in pseudo-energy models of kink banding. *Journal of Structural Geology*, 22(5): 669-681.
- Johnson, A.M., 1977. Styles of folding : mechanics and mechanisms of folding of natural elastic materials. *Developments in geotectonics ; 11*. Elsevier Scientific Pub. Co. ; distributors for the U.S. and Canada Elsevier North-Holland, Amsterdam ; New York, xx, 406 pp.
- Johnson, A.M. and Ellen, S.D., 1974. Theory of Concentric, Kink, and Sinusoidal Folding and of Monoclinial Flexuring of Compressible, Elastic Multilayers. *Tectonophysics*, 21(4): 301-339.
- Johnson, A.M. and Pfaff, V.J., 1989. Parallel, Similar and Constrained Folds. *Engineering Geology*, 27(1-4): 115-180.
- Latham, J.P., 1985. The Influence of Nonlinear Material Properties and Resistance to Bending on the Development of Internal Structures. *Journal of Structural Geology*, 7(2): 225-236.
- Manz, R. and Wickham, J., 1978. Experimental analysis of folding in simple shear. *Tectonophysics*, 44: 79-90.
- McNutt, M.K., Diament, M. and Kogan, M.G., 1988. Variations of Elastic Plate Thickness at Continental Thrust Belts. *Journal of Geophysical Research-Solid Earth and Planets*, 93(B8): 8825-8838.
- Ramberg, H., 1961. Contact strain and folding instability of a multilayered body under compression. *Geol. Rdsch.*, 51: 405-439.
- Ramberg, H., 1963. Fluid dynamics of viscous buckling applicable to folding of layered rocks. *Bull. Am. Ass. Petr. Geol.*, 47(3): 484-505.
- Ramberg, H., 1970. Folding of laterally compressed multilayers in the field of gravity, I. *Physics of the Earth and Planetary Interiors*, 2(4): 203-232.
- Schmalholz, S.M., Podladchikov, Y.Y. and Burg, J.-P., 2002. Control of folding by gravity and matrix thickness: Implications for large-scale folding. *Journal of Geophysical Research B: Solid Earth*, 107(1): 1-16.
- Schmalholz, S.M., Podladchikov, Y.Y. and Schmid, D.W., 2001. A spectral/finite difference method for simulating large deformations of heterogeneous, viscoelastic materials. *Geophys. J. Int.*, In press.
- Sherwin, J.A. and Chapple, W.M., 1968. Wavelengths of Single Layer Folds - a Comparison between Theory and Observation. *American Journal of Science*, 266(3): 167-179.

ACKNOWLEDGEMENTS

The first and biggest thanks go to Yuri. He made a dream come true that I had since I was a kid: I wanted to be a modeler. In the mid-80s I had read somewhere about what one can do with Finite Elements. Computer maniac as I was, I was convinced that if I had such kind of tools the world would be mine. Now, with Yuri's big help, I have developed different kinds of codes myself, including Finite Elements. I still think that they are the most elegant numerical method to solve problems, but I also had to learn that it is not done with the Finite Elements alone: physics, mechanics and math must also be understood. So Yuri had to teach all the things I had forgotten or never learned in the previous twenty something years. I thank him for his endless patience, for his motivation and energy. He also has the gift to make the weirdest things enjoyable, for example learning Muskhelishvili's method. But Yuri is not only a great supervisor; he is also a good friend. Our collaboration was not only scientific, we also worked together many evenings in WigWam and related places, be it in Zürich or somewhere else in Europe. This was great fun, although we still haven't found the meaning of life!

I thank my official Doktorvater: Jean-Pierre. Although a "who cares?" comes quickly over his lips, as a provocation and motivation, he actually does care a lot. Whenever I was in need for something - scientific, administrative, or personal - I found his office door wide open and he would take his time until the problem was solved. Jean-Pierre's advanced introductory course to French culture was always great fun and much appreciated.

Although I did a modeling PhD I occasionally left my office, most often not to do field work, but to collaborate with people. In the early days I went two times to the Swiss Center for Scientific Computing in Manno where I could always count on the hospitality of Djordje Maric. Later we started working together with Fernando O. Marques in Lissabon. He had invited Yuri to collaborate with him, but things somehow didn't get started. So, one day we found two airplane tickets in our mail and shortly afterwards we flew to Portugal. Fernando showed us some of his analogue experiments and I was amazed, because one was the bigger puzzle than the other. He has a sixth sense

to discover scientific riddles which is paired with his unbelievable enthusiasm. To a large extent he is responsible (in a good way!) how my thesis came along. Fernando - for this and your hospitality a big: agradecimentos muito. Then, in autumn last year, we (Boris and me) wanted to work together with Dave Yuen and Oleg Vasilyev in the US. Unfortunately we were supposed to arrive there on the 11. September, 2001. While Boris never made it to the US at all, I got stuck in LA for a week, but finally made it down to Missouri. However, there troubles were not over as I got hit by a car and my hotel went bankrupt and got sealed with my stuff still in there... Anyways, I would like to thank Dave and Oleg for supporting me during this difficult time.

During my PhD time I had three siblings: Boris, Katja and Stefan. They are the ones that save you when you have your lows, they also stop you if you have your highs, they stimulate you and make the endless hours in front of the computer bearable. There are many more people to thank: actual and former members of the institute from all over the world who helped me, opened my eyes for other ways of thinking, countries, cultures and let me enjoy many adventures with them (yes, Mohammed I'll finally come to Egypt!). However, I think the most important thing is that all these people somehow share the spirit of the institute as we know it. I don't know where it is - maybe somewhere hidden in the walls of the building, maybe it is the sum of the people, and maybe it is a few individuals that care - thanks a lot and keep those crazy parties, SOLA and Friday beers going!

In the NO building I also met Hil. Anti-American as I was we didn't have an easy start when I first showed up in her office. But somehow she has her way of changing things, never with brute force as I would, but at a steady peace. Since the 22.2.2002 we are married. Thanks so much for loving me, supporting me, and bearing me even when I don't deserve it!

I also want to thank my family. I love my mum and my two little sisters, Beatrice and Yvonne. My parents never tried to interfere with what I was aiming at. They always let me go my way. They always supported me, even when they didn't have much. I cannot express how grateful I am to you.

CURRICULUM VITAE

Name: Schmid, Daniel Walter
Date and place of birth: 22. December, 1973, Kingston, Jamaica
Citizenship: Swiss
Bürgerort: Full-Reuenthal
Civil Status: Married

Education

1989-1993 Kantonsschule Baden, Typus C
1993-1998 Department of Earth Science, ETH Zürich
Diploma work “Numerical modeling of Newtonian material under pure and simple shear”.
1995-1996 Department of Earth Sciences, University of Liverpool
Erasmus exchange student.
1998-2002 Department of Earth Science, ETH Zürich
PhD thesis in the structural geology and tectonics group.